Towards a mechanistic understanding of nanoparticle behavior using zebrafish

Arias Alpizar, G.

Towards a Mechanistic Understanding of Nanoparticle Behavior *using* Zebrafish

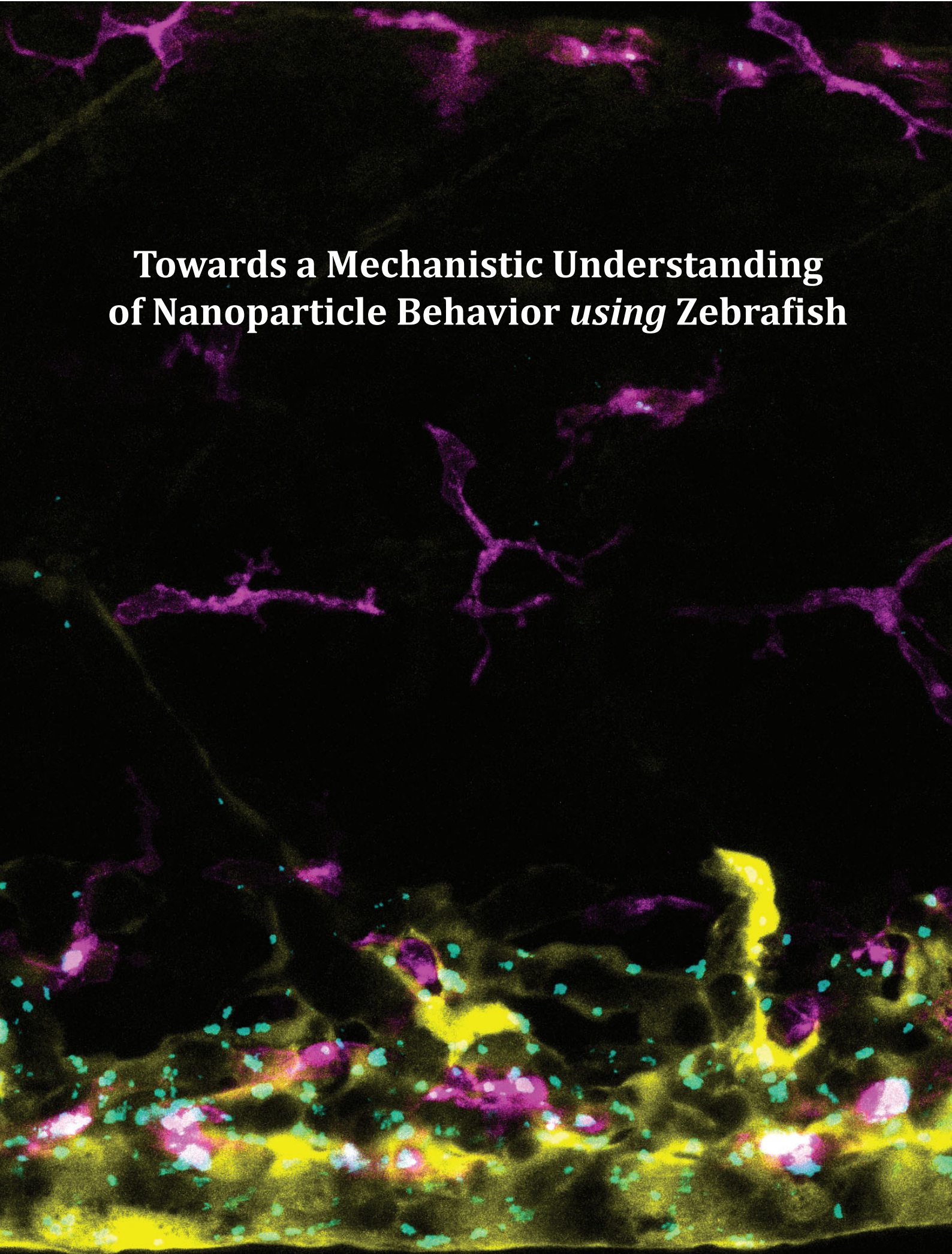

M. Gabriela Arias Alpízar

Towards a Mechanistic Understanding of Nanoparticle Behavior *using* Zebrafish

---

M. Gabriela Arias Alpízar

Ph.D. Thesis, Leiden University, November 2021

Promotiecommissie

Promotor:	Prof. dr. A. Kros		LIC, Leiden University
	Prof. dr. H.P. Spaink		IBL, Leiden University
Co-promotor:	Dr. J. Bussmann		LACDR, Leiden University
Overige leden:	Prof. dr. H. S. Overkleeft	(voorzitter)	LIC, Leiden University
	Prof. dr. W. Jiskoot	(secretaris)	LACDR, Leiden University
	Prof. dr. J.M.F.G. Aerts		LIC, Leiden University
	Prof. dr. A.H. Meijer		IBL, Leiden University
	Prof. dr. E. Mastrobattista		Utrecht University
	Prof. dr. A. Salvati		University of Groningen

ISBN: 978-94-6421-513-7

Printed by Ipskamp printing

Cover design: M. Gabriela Arias Alpízar

About the cover: In front, the caudal region of the zebrafish containing lipid nanoparticles (LNPs, cyan) and expressing GFP (yellow) in the scavenging endothelial cells after 24 h of *i.v.* administration. Macrophages in magenta. In the back, tissue exposed macrophages (magenta) containing LNPs (cyan) and expressing GFP (yellow).

Towards a Mechanistic Understanding of Nanoparticle Behavior *using* Zebrafish

Proefschrift

ter verkrijging van
de graad van doctor aan de Universiteit Leiden,
op gezag van rector magnificus prof.dr.ir. H. Bijl,
volgens besluit van het college voor promoties
te verdedigen op Donderdag 4 November 2021
klokke 13:45 uur

Door

María Gabriela Arias Alpízar
geboren te San José, Costa Rica
op 22 april 1984

“Para empezar un gran proyecto, hace falta valentía.
Para terminar un gran proyecto, hace falta perseverancia”

To Valeria, Bernal, my parents and Sebastian,
for being an inspiration.

Table of Content **Pages**

Chapter 1

General Introduction & Scope of the thesis

Image: Fluorescently labelled nanoparticles (cyan) intravenously injected in a zebrafish embryo. Endothelial cells (green) showing the intersegmental vessels and dorsal aorta.

1.1 Nanomedicine at a glance

Nanomedicine refers to the application of nanotechnology in the development of devices and therapeutics to benefit diagnosis and/or treatments.[1] This field has been motivated by the concept of targeted drug delivery, which intends to enhance the therapeutic efficacy and safety profile by protecting the cargo (*i.e.* drugs, genetic material) from external degradation, controlling its delivery, and thereby helping to minimize the side effects.

Due to their various characteristics, nanoparticles are believed to be suitable systems for different commercial applications[2] from sensing,[3] detection of proteins,[4] imaging,[5] to vaccine development,[6] and drug/gene delivery[7-10] purposes. In the last ~50 years a myriad of materials and techniques have been applied to the design, characterization, and production of different types of nanosystems. Despite the variety of applications, it can be surprising that commercialized products are very limited, suggesting that nanoparticles are not 'the magic bullet' that were initially expected to be. This urgently called for further investigation, or a change in the investigation approach to be performed, and maybe a reassessment in the capabilities of nanoparticles.

The development of more efficient nanoparticles will definitely contribute to the clinical success. However, it requires a thorough understanding of the nano-systems used and their performance *in vivo*. Mechanistically, nanoparticles mimic the behavior and uptake of natural agents, such as viruses, to deliver a cargo. Viruses are known to enter the body, travel in the bloodstream, find the target tissue and be taken up by the cell. Subsequently, degradation of the "shell" and release of the cargo occur.[11] Furthermore, the immune system recognizes both viruses and nanoparticles as intruders and tries to remove them from the organism to maintain homeostasis. In other words, similar to viruses, nanoparticles need to pass different barriers to reach the intended place; these series of events can only be observed simultaneously in a living organism, where all the organs and systems are present and dynamic interactions take place. In this respect, translation of nanomedicines (see page 14-16) is one of the greatest barrier to the clinics, therefore models that help to understand the fundamental behavior *in vivo* of such particles are required.

Classification of nanocarriers

Depending on the material used for their preparation, nanoparticles can be classified into two main groups: organic and inorganic. The first class includes biodegradable and non-toxic materials such as polymeric dendrimers (*i.e.* micelles, vesicles), hydrogels, proteins and lipid-based delivery systems. The inorganic group consists mainly of non-toxic metal-based particles (*e.g.* gold, aluminum, zinc), coated quantum dots, and mesoporous silica. In this classification, the nanoparticle type that has demonstrated the highest success in the clinic and commercialization is the lipid-based nanoparticles. Therefore, they are described and used as research platforms in this thesis.

Lipid-based nanoparticles comprise the most well-studied systems for drug delivery and one of the most commonly used strategies in nanomedicine. Their characteristics of biocompatibility, biodegradability, low toxicity, and ease of production, makes them versatile and attractive materials for drug delivery.[12] Three main groups can be mentioned as lipid-based nanoparticles: lipid micelles, liposomes, and lipid nanoparticles (LNPs). Micelles are simple structures formed by amphiphilic lipids (preferably of conical shape) in an aqueous solution that, above the critical micelle concentration, self-assemble into a micellar system with a hydrophobic core.[13] They are characterized by a high dynamic inherent nature and therefore, are found mostly combined with polymer blocks as delivery systems.[14] In contrast to micelles, liposomes and more recently LNPs have demonstrated more versatility by reaching clinical applications.[15] Liposomes are composed of amphipathic lipids that, mimicking biological membranes, self-assemble into spherical vesicles forming a bilayer and an aqueous core (**Figure 1**). This feature allows entrapment of hydrophilic or lipophilic compounds, protection of the cargo against degradation and lowers their apparent toxicity. To achieve targeting, the outer layer of the lipid-based nanoparticles can be functionalized by coupling of ligands, antibodies, polymers, proteins, *etc*. thereby tuning the *in vivo* behavior. Characteristics like rigidity is mainly dependent on the acyl/alkyl chain length and saturation, while surface charge is defined by charges present in the lipid head group. These properties, together with size and stability, will also affect pharmacokinetics of liposomes *in vivo* and subsequent interactions with cells. Hence, the physicochemical properties can be used to tune lipid-based nanoparticle *in vivo* fate and cellular uptake.

Some of the challenges that have been overcome with liposomes as a delivery platform in diagnostics and clinics are: reduction of toxicity, improvement of the

therapeutic index of delivered drugs,[9] protection of sensitive materials (*e.g.* DNA, RNA, oligonucleotides, cytosine arabinose) from early inactivation or degradation,[16, 17] and enhancement of the pharmacokinetic profile.[10, 18] Gene delivery, however, is more difficult to achieve due to limitations in the stability, safety and delivery of nucleic acids. This modality aims to regulate gene expression by successfully delivering nucleic acids to a particular tissue of interest. Hence, downregulation of genes could be achieved by small interfering RNA (siRNA), microRNA (mRNA) or antisense oligonucleotides (ASOS). In contrast, increase and correction of the gene expression are mediated by messenger RNA (mRNA), small activating RNA (saRNA), DNA, splicing-mediated ASOS or as a result of the use of a more complex gene technique, clustered regularly interspaced short palindromic repeat-associated protein 9 (CRISR/Cas9).[19]

Nucleic acids have been chemically modified to solve the challenging tasks of stability and reduction of side effects, for example, synthetic RNA molecules were modified to regulate immune responses and suppress inflammatory responses.[20-22] From the nanotechnology perspective, development of non-viral vector based delivery systems contributes in the protection of the cargo to circumvent some of the biological barriers and ensure the biological activity of the nuclei acid-based drugs once target site is reached. Encapsulation of nucleic acids into the core of a nanocarrier prevents intravascular degradation (*e.g.* breakdown by serum nucleases) and rapid renal clearance due to its small size. Furthermore, due to the negative charge and hydrophilic nature, naked nucleic acids have a poor ability to cross cell membranes. Thus, nanocarriers are required to promote endocytosis leading to cargo delivery in the cytosol (RNA) or the nucleus (DNA) of the targeted tissue. Intracellular barriers, like endosomes, also limit the efficacy of the desired therapy. Consequently, strategies to overcome this barrier successfully result in the development of cationic lipids that facilitate the entrapment of DNA/RNA and promote endosomal escape.[23-25] Incorporation of these lipids has led to the development of a new generation lipid-based nanoparticles, known as lipid nanoparticles (LNPs).

LNPs were developed as an strategy to deliver nucleic acid-based therapeutics and to improve the encapsulating capacity of lipid-based delivery systems. Compared to liposomes, LNPs are more complex solid lipid-based nanoparticles with a monolayer outer membrane and a non-aqueous hydrophobic core.[26] Typically, LNPs incorporate at least four components: helper lipids (*i.e.* cholesterol and phospholipids), ionizable lipids (*i.e.* DLinDMA, DLinKC2DMA,

DLinMC3DMA), the genetic material of interest (*i.e.* DNA/RNA), and a polyethylene glycol (PEG) lipid.[27, 28] Structurally, cholesterol, the helper lipid and the ionizable lipid in complex with the genetic material form a lipid core, coated by a pegylated surface (**Figure 1**). Rapid mixing of these components in an ethanol solution with an aqueous buffer (at pH 4), in a 1:3 ratio, is normally achieved employing microfluidic systems.[26] In that way, and commonly in a nitrogen to phosphate ratio (N/P) of ~6, efficient entrapment of the genetic cargo can be reached (>50 %), quantified by using a fluorescent dye (*e.g.* RiboGreen assay).[29] This results in a homogenous population of small LNPs (<100 nm), with a solid complex core and a surface rich in helper and PEG-lipids.

As a gene delivery system, the *in vivo* efficacy of the LNP relies mainly on the delivery efficiency and the stability of the cargo; whereas the potency of such a system firmly depends on the ionizable and PEG-lipids used.[30-32] The ionizable lipid is an essential component in the encapsulation of LNPs, as it is cationic at low pH (*e.g.* pH 4). This allows association between the negatively charged nucleic acids and the cationic lipid mediated by electrostatic interactions, upon mixing. In addition, once the LNPs are internalized in the cytoplasm, the acidic pH of the endosomes induces protonation of the ionizable lipid resulting in membrane destabilization and consequent release of the cargo, promoting a required endosomal escape.[33] The PEG-lipid primary function is to support the self-assembly; however, it also influences the nanoparticle size and the dissociation rate.[30, 31] Size of LNPs depends on the amount of lipid-PEG during assembly, increase in PEG-lipids concentration leads to decreased LNP size. For instance, incorporation of 1 and 5 mol% results in LNPs with a diameter of 44,5 and 22,4 nm respectively.[31] Furthermore, since the PEG-lipid resides preferentially on the outer monolayer of the LNP, its rate of dissociation *in vivo* impacts the release of the cargo and the activity of the nanosystem.[32]

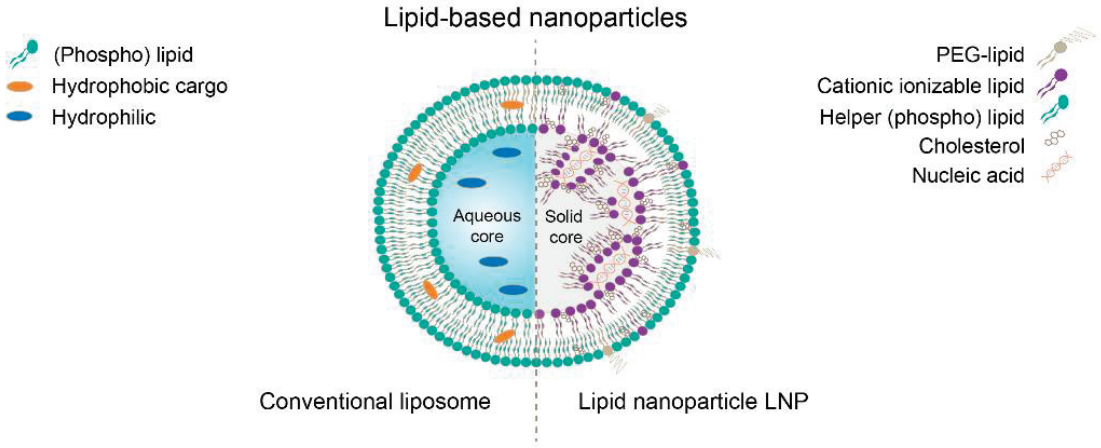

Figure 1. Lipid-based nanoparticles platforms. On the left side, schematic representation of a conventional liposome composed of lipid molecules with a hydrophilic head group and a hydrophobic tail that self-assemble to form a bilayer containing an aqueous core. This characteristic allows the encapsulation of hydrophobic or hydrophilic cargos. On the right side, a lipid nanoparticle (LNP) formed by a combination of lipids (cationic ionizable, helper, PEG) entrapping nucleic acids in a solid (non-aqueous) core.

Clinically approved (lipid-based) drug delivery systems

The potential of the lipid-based drug delivery systems has been demonstrated by delivering anticancer agents, antibiotics, combinations of drugs, and many more. Clinically approved lipid-based nanoparticles are reviewed in reference [15]. Although different routes have been used in the administration of approved formulations, the intravenous (*i.v.*) application is the most commonly used route. Approved liposomes *i.v.* administered are summarized in **Table 1**.

The first liposomal formulation approved (in Europe) in the 90s was Ambisome®,[34] containing amphotericin B, an antibiotic used against acute fungal infections. Later, two similar formulations (Abelcet®[35] and Amphotec®[36]) were approved to treat aspergillosis. Besides fungal infections, drugs loaded liposomes were developed to treat various forms of cancer. Liposomal formulations such as Myocet®,[37] Doxyl®,[18] LipoDox®,[38] DaunoXome®,[39] Vyxeos®,[40] Marqibo®[41, 42], and Onyvide®[43] were approved due to prolonged circulation times and tumor extravasation of the entrapped and protected cytotoxic drugs: doxorubicin (*i.e.* breast, ovarian cancer), daunorubicin and cytarabine (*i.e.* Kaposi's sarcoma), vincristine (*i.e.* acute leukemia) and irinotecan (*i.e.* adenocarcinoma of the pancreas). In 2012, one more formulation was approved, Mepact®, and commercialized for the treatment of osteosarcoma associated with chemotherapy. These liposomes deliver mifamurtide, which

Table 1. Clinically approved *i.v.* administered liposomes.
(Adapted from references [44, 45]).

Formulation	Lipid composition	Cargo	Indication
Ambisome®	DSPC, DSPG, Cho (2:0.8:1)	Amphotericin -B	Fungal infections (*i.e.* aspergillosis)
Abelcet®	DMPC, DMPG (7:3)		
Amphotec®	Cholesteryl sulfate		
Doxyl®/ Caelyx® LipoDox®	HSPC, Cho, PEG2k-DSPE (56:39:5)	Doxorubicin	Kaposi's sarcoma, breast and ovarian cancer
Myocet®	POPC, Cho (2:1)		Breast cancer
DaunoXome®	DSPC, Cho (2:1)	Daunorubicin	Kaposi's sarcoma, leukemia
Vyxeos®	DSPC, DSPG, Cho (7:2:1)	Daunorubicin + cytarabine	Acute myeloid leukemia
Marqibo®	Sphingomyelin, Cho (60:40)	Vincristine	Acute lymphoblastic leukemia
Mepact®	DOPS, DOPC (3:7)	Mifamurtide	Osteosarcoma
Onyvide®	DSPC, Cho, PEG-2K-DSPE (3:2:0.015)	Irinotecan	Adenocarcinoma of the pancreas
Visudyne®	DMPC, EPG (1:8)	Verteporfin	Age-related macular degeneration, myopia, ocular histoplasmosis

Abbreviations: Cho, cholesterol; DMPC, 1-α-dimyristoylphosphatidylcholine; DMPG, 1-α dimyristoylphosphatidylglycerol; DOPC, 1,2-dioleoyl-*sn*-glycero-3-phosphocholine; DOPS, 1,2-dioleoyl-*sn*-glycero-3- phosphatidylserine; DSPC, 1,2-distearoyl-*sn*-glycero-3-phosphocholine; HSPC, hydrogenated soy phosphatidylcholine; DSPG, 1,2-distearoyl-*sn*-glycero-3-phosphoglycerol; EPC, egg phosphatidylcholine; EPG, egg phosphatidyl-glycerol; PEG 2k-DSPE, polyethylene glycol 2000-1,2-distearyl-*sn*-glycero-3-phosphati-dylethanolamine; POPC, 1-palmitoyl-2-oleoyl-glycero-3-phosphocholine.

binds to toll-like receptors 4 stimulating an immune response mediated by macrophages and generating an antitumor activity.[46] In a different context than cancer, the liposomal formulation containing the photosensitizer verteporfin, was developed to decrease the risk of vision loss.[47] Visudyne® approved for photodynamic therapy to treat subfoveal choroidal neovascularization due to age-related macular degeneration.

LNPs have only recently obtained approval as a drug delivery platform, **Table 2**. Onpattro® (Patisiran) is the pioneer in the LNPs-based RNA therapeutics. Approved in 2018, Onpattro® uses small interfering RNA (siRNA) to treat polyneuropathies caused by a genetic disease named amyloidogenic transthyretin (TTR) amyloidosis.[33] This treatment silences the TTR mutated gene by delivering siRNA to hepatocytes. Targeting of this liver cell type is mediated by the binding of apolipoprotein-E to the cell surface which subsequently guide the LNPs to the low-density lipoprotein receptor (LDLR) family members.[48] Other LNP siRNA-based therapies have reached the clinical trials;[49] for instance TKM-080301 is a formulation for solid tumors or lymphomas. The antineoplastic activity of this formulation, which silence the overexpression of polo-like kinase 1 (PLK1) in tumor cells, was demonstrated so far in xenograft models and preclinical studies.[50, 51]

In addition, the great potential of LNPs has been demonstrated recently in the development of non-viral vaccines[52] due to its ability to deliver vaccine antigens and express proteins upon cytoplasmic mRNA delivery. In this context, LNPs technology is under investigation of various immunization approaches against viruses (*e.g.* influenza,[53] Zika virus,[54] HIV-1[55], cytomegalovirus[56]) and for cancer immunotherapies.[57] Compared to conventional vaccine platforms, using live attenuated and inactivated viruses, LNPs not only decrease the risk of potential infection, but also offers the possibility to be applied in non-infectious diseases (*e.g.* cancer). Moreover, the rapid development and manufacturing scalability are exemplified by the recent approval (in emergency cases by FDA) of mRNA-based vaccines for the prevention of the pandemic COVID-19, highlighting the versatility of this technology. Comirnaty® (also called BNT162b2)[58] and Moderna COVID vaccine®[59] (mRNA-1273) encode a mutant viral spike (S) protein of SARS-CoV-2. These LNPs formulations are used as a carrier of the mRNA to facilitate efficient intracellular delivery and to avoid extracellular degradation by RNAses.[60] After intramuscular injection, LNPs are taken up by cells via endocytosis and ultimately mRNA is delivered in the cytosol. As a result, the S protein is produced and translated into a functional protein to finally induce the adaptive immune response and formation of antibodies against the

virus. Due to the ease of design, LNPs technology promises a more personalized genetic therapy for the future, where a large variety of diseases can be effectively treated.

Table 2. Clinically approved LNPs (December 2020).

Formulation	Lipid composition	Route of administration	Cargo	Indication
Onpattro®/Patisiran	DSPC, Cho, DLin-MC3-DMA*, DMG-PEG2k	*i.v.*	TTR siRNA	TTR-mediated amyloidosis
Comirnaty®/BNT162b2	DSPC, Cho, ALC-0315*, ALC-0159	*i.m.*	mRNA	SARS-CoV-2
Moderna COVID-19 vaccine® /mRNA-1273	DSPC, Cho, SM-102*, DMG-PEG2k			

Abbreviations: ALC-0315, (4- hydroxybutyl) azanediyl)bis (hexane-6,1-diyl)bis (2-hexyldecanoate), ALC-0159, 2-[(polyethylene glycol)-2000]-N,N-ditetra- decylacetamide. DLin-MC3-DMA, heptatriaconta-6,9,28,31-tetraen-19-yl-4- (dimethylamino) butanoate; DMPG, 1-α dimyristoylphosphatidylglycerol; DSPC, distearoylphosphatidylcholine; PEG2k-DMG, polyethylene glycol 2000; SM-102, heptadecan-9-yl 8-((2-hydroxyethyl)(6-oxo-6-(undecyloxy)hexyl)amino)octanoate. *i.m.* intramuscular, *i.v.* intravascular.
* ionizable lipid.

Translation of nanomedicines

Successful clinical translation of new medicines is a challenging task.[61] So far, there are many nanotechnology-based systems under clinical development, but very low success has been seen. A critical step for this process resides in the early stages of research. During these stages, careful selection of nanoparticles, within the infinite catalog of possible designs, is vital. Drug delivery systems with a robust design, stable, effective and non-toxic are essential to succeed and have a strong first preclinical data. Improvements in the initial stages of research will help in increasing the clinical success rate, for instance, more predictive models, targeted drug delivery technologies and a thorough understanding of the behavior and the route of nanoparticles in a living system.

In short, once formulated and after entering the body, intravenously injected nanoparticles have to overcome several barriers to reach the desired target. In the bloodstream, serum proteins and biomolecules interact and/or adsorb on the surface of the nanoparticles. This phenomena, known as 'protein corona' is a dynamic process impacting in the biological location and cellular uptake of the particles.[62, 63] Despite the efforts in the challenging task of protein corona analysis, the effect on nanoparticle composition and protein corona has not been fully elucidated. Several proteins are believed to help in the recognition of specific cellular receptors and eventually promote cellular internalization.[64, 65] For example, apolipoproteins such as apolipoprotein-E, that binds to the clinical formulation Onpattro®,[66, 67] facilitates the interaction with LDL receptors expressed on hepatocytes.

Besides interaction with proteins in the bloodstream, nanoparticle behavior is determined by their physicochemical properties. The chemical composition,[68] shape,[69, 70] size,[71, 72] stiffness,[73] hydrophobicity,[74, 75] and surface charge[76, 77] combined determine the biodistribution, cellular entry and circulation life time of nanoparticles. Precise control of these properties, by changing the particle composition, tuning the size, and/or exposing functional groups to the surface, allows one to tailor nanoparticle fate. It is important to note that study on the direct effect of an individual parameter in the biological identity of nanoparticles, in some cases, is challenging to assess *in vivo*. This is due to the complexity of the dynamic processes encountered by nanoparticles after systemic administration. In short, the material's chemical composition will define the nanoparticle surface properties, and thereby, corresponding interactions with different components in its surrounding. Shape is known to affect the curvature and surface contact with membranes, as well as phagocytosis by macrophages.[68] Nanoparticle size influences the renal clearance (limit 5,5 nm),[78] cellular internalization and engulfment of macrophages (>200 nm).[79] Diameter size of around 100 nm have shown prolonged circulation life-time and relatively low uptake by macrophages.[80] In fact, a 50 nm diameter is speculated as a recommended size since these particles favor kinetics and cellular uptake in comparison to particles of the same chemistry.[31, 72, 81] Stiffness influences circulation life-time, for example, softer nanogels circulate longer as to the stiffer counterpart, attributed to their capabilities of deformability.[73] Hydrophobicity is believed to improve cellular internalization of nanoparticles due to the increased enthalpic interaction with membranes.[74, 75] Likewise, cationic surface charge promotes endocytosis *via* interaction with negatively charged residues on the cellular surface membrane. Nevertheless, its use is limited by the associated cellular

toxicity.[82-84] This property leads to non-specific cellular internalization. In contrast, neutral (zwitterionic) surface charge, results in free circulation,[85] avoiding interactions and maximizing the exposure of nanoparticles to different tissues and cell types. Whereas negatively charged nanoparticles are characterized by a poor pharmacokinetic profile, preferentially found in liver and spleen, after rapid removal from circulation.[86]

Despite this flexibility in design, nanoparticles typically accumulate in non-desired tissues (also known as off-target) affecting the efficacy of the delivery system. This process is dominated by the reticuloendothelial system (RES), consisting of specialized cells: Kupffer cells (lining the sinusoids of the liver and the spleen) and fenestrated liver sinusoidal endothelial cells (LSECs). Due to the high endocytic capacity of these cells, RES main function is to maintain the body homeostasis by removing macromolecules from circulation and tissues, including pathogens (*e.g.* bacteria and viruses) and other foreign substances.[87-89] The ability to design nanomaterials that can selectively target or evade RES will contribute in the development of improved nano-therapies.

Clinical translation of nanomedicines has been primarily observed with lipid-based nanoparticles approach, however, many challenges remain.[90, 91] Although some general concepts about the influence of shape, size, surface charge on the fate of the nanoparticles are known, to which extend each of these properties affect the *in vivo* behavior? What are the optimal properties for a drug delivery system? How can we apply this knowledge to obtain the desired targeting? These are questions that are not fully understood. For these reasons and because of the poor predicting power of cell culture based-studies in nanomedicine, a model to screen multiple nano-systems is highly desired. Ideally, this model allows tracking of the particles *in vivo*, contributes to understand how the nanoparticle properties affect the *in vivo* fate, improves the design of delivery systems and potentially the success rate in the future medical applications.

1.2 Zebrafish as an animal model in the field of nanomedicine

The zebrafish *(Danio rerio)* is a teleost, non-mammalian vertebrate animal that originated from tropical freshwater. It was first used as a biological model by George Streisinger in the early 1980s,[92] since then the zebrafish has gained increased attention in research due to the wide range of advantageous features and is now one of the most studied animal models. The small size (from 0,7 µm in a single cell stage to 4 mm as larvae), high fecundity, ease of husbandry, relatively low cost of maintenance, external fertilization, and rapid development are only a few of the characteristics that attract researchers to select this animal for research studies.

As an experimental animal, zebrafish are extensively used in the area of developmental biology, regeneration, drug discovery, toxicity, cancer, inflammation, and molecular genetics. The comparison of fundamental and cellular events between zebrafish and mammals is supported by a known conservation in developmental and physiological processes among vertebrate species. For instance, lipid uptake/metabolism, and lipid transport are conserved and shows high similarity to humans.[93] Studies in this area can be performed on embryonic stages since most of the organs in the gastrointestinal tract are established at 2-4 days post-fertilization (dpf).[94, 95] The liver, however, is one of the organs that shows its full functionality about 120 hpf,[96] while the kidney shows glomerular filtration since 48 hpf a complete renal anatomy with glomerular and tubular filtration processing at 96 hpf.[97] Conservation at the genomic level was further confirmed in 2010s with the identification of 26206 protein-coding genes[98] and the sequence of the complete zebrafish genome.[99] These genes revealed the close relation of the zebrafish genome with that of mammals, having a 70% similarity with humans. Whereas 82% of human genes associated with diseases have a zebrafish orthologue.[99, 100] Genes associated with neurological disorders, cardiovascular disease, cancer, and vascular disorders have been identified and characterized in the zebrafish.[98, 99] In addition, comparative transcriptomic studies of different organs such as the heart,[101] liver,[102] lungs-swim bladder,[103] kidney,[104] or pancreas[105] between different species have demonstrated the good correlation of zebrafish analysis with higher organisms. Overall, this data support the functional conservation of genes and pathways between zebrafish and mammals and allow, to a certain extent, extrapolation of data obtained by zebrafish analysis.

Zebrafish key features for the development of efficient nanomedicines

Compared to other *in vivo* models, such as rodents, two particular characteristics make this organism suitable and attractive for research in nanotechnology: the optical transparency that offers the embryonic stages allows visualization and imaging, and the external fertilization facilitates the genetic manipulation (**Figure 2**). The combination of both characteristics provides a suitable strategy to shed light on the cellular mechanism involved in nanoparticle behavior.

The transparency of *Danio rerio* together with a variety of *in vivo* imaging techniques enables a non-invasive assessment of many biological processes through evaluation of the dynamics of fluorescent probes (*i.e.* proteins, synthetic dyes, quantum dots, *etc*.). The zebrafish development, for instance, has been tracked by microscopy and computational approaches resulting in a high-resolution map of embryogenesis in time.[106] Furthermore, incorporation of fluorescent dyes to nanoparticles allows the study of nanoparticle biodistribution after systemic administration by tracking their dynamics and fate in a whole living animal.[107] In this context, nanoparticles affinity for specific tissues can be visualized in detail providing information about cellular interactions involved in the underlying mechanism.

A range of tools are available to study nanomedicine biodistribution and nanoparticle-cell interaction zebrafish at the molecular level. This includes transgenic lines expressing fluorescent reporter proteins controlling promoter sequences for marked cell types,[108] mutants, antibodies, probes used to study mRNA expression of genes, *etc*. Established transgenic lines facilitate studies since it avoids non-specific labeling as a result of typical immunostaining of cells; such as *kdrl* and *mpeg1* lines expressing fluorescent proteins in endothelial cells and macrophages respectively. These two are of particular interest because nanoparticles, after parenteral administration, interact with: blood proteins in circulation, endothelial cells lining the vasculature, and blood resident macrophages. Tg(*kdrl:*eGFP)*s843* [109] allows visualization of the vascular system and therefore quantification of nanomaterials in circulation over time (*e.g.* to determine pharmacokinetic values such as half-life), extravasation, and endocytosis by specific type of endothelial cells. Whereas the transgenic Tg(*mpeg1:*mCherry)*gl23* [110] line label macrophages enabling the dynamic study of nanoparticles phagocytosed by macrophages. Other transgenic lines with possible applications in studying nanomedicine behavior are shown in **Table 3**.

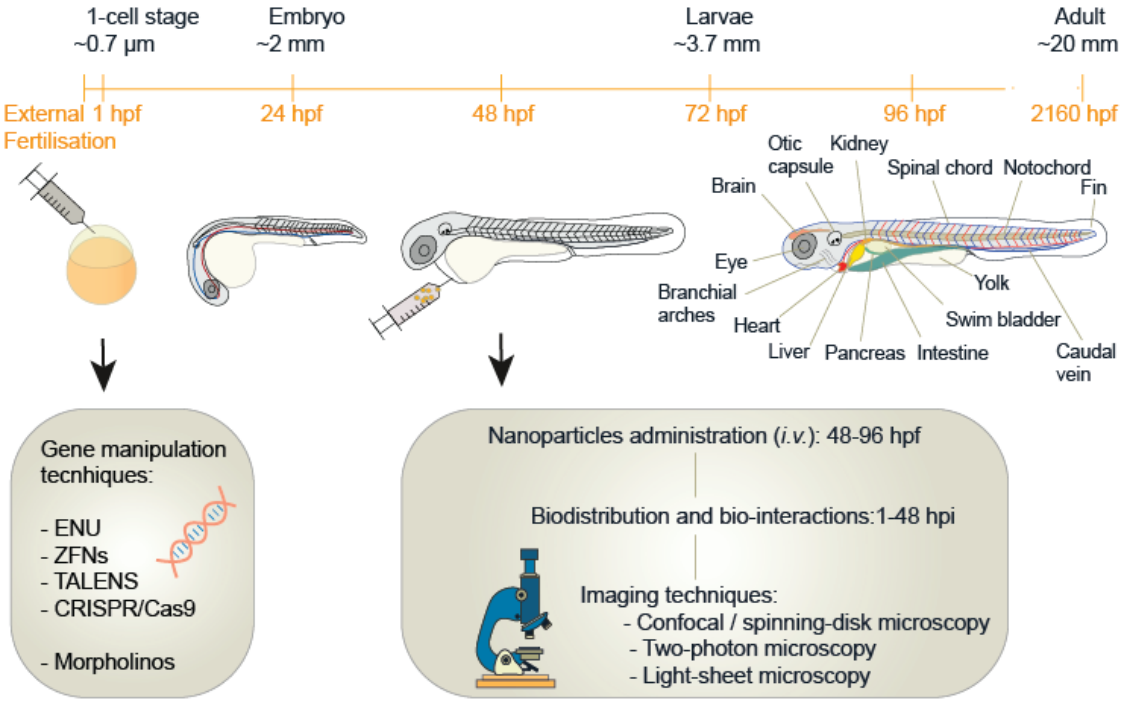

Figure 2. Development of the zebrafish and important features for nanomedicine. Timeline showing the zebrafish development from external fertilization (0 hours) up to 2160 hours post fertilization (hpf). Gene modification is performed at 0-0,75 hpf, in a 1-cell stage. Some of the techniques known for gene manipulation that have been applied in zebrafish to knockout genes are: ENU, ZFNs, TALENS and CRISPR/Cas9. Morpholinos are known to transiently knockdown genes of interest. At 24 hpf, the zebrafish embryo has a body length of about 2 mm. At this stage the circulatory system starts to develop. At 48 hpf, the embryo continue growing, circulatory systems is more develop, most of the organs are established. From this stage, fluorescently labeled nanoparticles can be *i.v.* administrated. Biodistribution of the nanoparticles can be tracked and bio-nano interactions can be studied with the help of different microscopy techniques such as confocal, spinning-disk confocal, two-photon, light-sheet. The main organs and other parts of the zebrafish are indicated in a larvae of about 96 hpf. The larvae continue growing until reaching the adult stage at 2160 hpf (3 months).

Furthermore, external fertilization of the zebrafish facilitates genetic manipulation. This characteristic provides the possibility to develop disease models and study the influence of a candidate gene in a disease state. In nanomedicine, this feature can also be applied to understand the mechanisms of nanoparticle-receptor interaction associated mediating uptake. The first attempt to modify a zebrafish gene was performed in the 90s employing chemical mutagenesis through a point mutation induced by *N*-ethylnitrosourea (ENU).[111] This methodology, based on forward genetics, carries a mutation for the next generation and requires large screenings to determine phenotypic changes to be

further studied. Later, genetics evolved to more developed reverse approaches enabling random (*Tol2* transposons)[112] and targeted insertions of exogenous DNA into the genome. Zinc finger nucleases (ZFNs) and transcription activator-like effector nucleases (TALENS) have also been used to mutate specific genes in the zebrafish.[113, 114] More recently, CRISPR/Cas9 appeared as an efficient gene-editing technique due to its ability to induce double-strand breaks within an identified genomic location (similar to ZFNs and TALENS) and its potential for targeting multiple genomic regions.[95, 115-117] Co-injection of single guide RNA (sgRNA) -including a 20 nucleotides target sequence- along with Cas9 mRNA in a single cell stage of a zebrafish zygote could result in a mutant carrier. After identifying the founder carrying the mutation and some crosses for new generations, a homozygous mutant may be available for further studies.

Table 3. Selected fluorescent transgenic lines of interest for the evaluation of nanomedicines.

Transgenic line	Marker	Application in nanomedicine
*kdrl:*eGFP [109], *kdrl:*mCherry, *kdrl:*mTurquoise *fli-1:*eGFP, [118] *gata1:*dsRed [119]	Endothelial cells (vascular system)	▪ Nanoparticles in circulation/ circulation life time of nanoparticles ▪ Extravasation of nanoparticles ▪ Endocytosis of nanoparticles by endothelial cells
*mpeg1:*mCherry, *mpeg1:*GFP [110]	Macrophages	▪ Sequestration of nanoparticles by macrophages ▪ Targeting of macrophages
*cldn5a:*GFP [120]	BBB and choroid plexus	▪ Targeting of brain endothelial cells ▪ Extravasation
l-fabp: GFP [121]	Hepatocytes	▪ Uptake of nanoparticles by liver
*live1:*dsRed [122]	Lymphatic endothelial cells	▪ Lymphatic uptake
*wt1b:*GFP [123]	Pronephros	▪ Kidney uptake ▪ Blood filtration of nanoparticles

Abbreviations: BBB, blood brain barrier; SECs, sinusoidal endothelial cells.

Site-specific modifications are identified by genotyping (sequencing or fluorescent PCR) followed by phenotypic analysis. In addition, transient knockdown of a targeted gene with morpholinos is also applied in zebrafish.[124] This strategy relies on the use of synthetic oligo, antisense morpholino, that inhibits the translation of a complementary mRNA by preventing initiation or splicing. Although it is a fast and low cost, high inconsistencies (up to 80%)[125] in phenotypes due to off-targeting inhibition in the use of morpholinos compared to a knockout made its efficacy questionable in respect to false positives.

The advantages of the zebrafish in nanotechnology are evident, useful and in principle provide a great addition compared to other models. The tools available in zebrafish research and advances in new technologies in other related fields, such as imaging and genetics, could offer constant improvement and increase its potential.

State-of-the-art of the zebrafish in the study of nanoparticles

While it is evident that the zebrafish share many cellular and physiological mechanisms with mammals and that they possess attractive characteristics to be preferred as a model in many research areas. It was not until very recently that this model started to be used to study nanomedicines.[126-128] A search in Pubmed reveals the limited amount of publications per year in the last decade indicating that despite the already highlighted zebrafish features, the model is relatively new and has not been deeply explored. Compared to the total amount of publications in zebrafish in 2019, 3,8% of the publications included nanoparticles research and less than 1% represented studies in nanomedicine. Such a difference can be explained by the application of the zebrafish in the toxicological analysis of nanoparticles. In addition, an important contribution of this organism in the study of cancer (already reviewed in references [126, 129, 130] and therefore not discussed in this thesis), gene therapy, and phagocytic by macrophages have been reported.

As a model in toxicology, zebrafish is useful due to their sensitivity to chemical exposure during early stages and the amenability to monitor phenotypical changes. Nanoparticle toxicology studies in the zebrafish, as a relevant alternative to rodents, has been recently reviewed.[131-133] It relies mainly on the toxicity assessment after direct exposure of the zebrafish to water containing nanoparticles.[132] This allows the study of molecular mechanism, functional changes and transcriptional gene alterations.[134, 135] Markers associated with intestinal inflammatory responses, for example, were used to study the toxicity

of metal and polystyrene nanoparticles.[135] This type of administration, however, should consider variability in the absorption, dosages, as well as stability of the nanoparticles. Therefore, toxicology experiments after systemic administration are also recommended.

In the study of gene therapy mediated by non-viral delivery systems,[136] zebrafish embryos, combined with fluorescent materials (DNA, mRNA, small interfering siRNA), enables visualization of genetic material delivered by nanoparticles and functional activity. Not only gene silencing[137, 138] has been demonstrated with zebrafish embryos but also mRNA transcribing fluorescent proteins. A pilot study using a non-delivery system, LNPs, as nanocarriers showed delivery of genetic encapsulated mRNA, and fluorescent expression (eGFP) as a delivery readout.[139] Important research efforts have been the focus in the development of new LNPs,[140, 141] the potential of the zebrafish to assess these nano-sized technologies and to further understand the interactions between the vector and their host could pave the way to better translations of gene therapies in higher organisms. With the help of fluorescent genetic material (DNA, small interfering siRNA,) the transfer and expression of exogenous genes in specific cell-type can be investigated in zebrafish. In this context, silencing of specific genes by siRNA-mediated delivery in the study of cardiac diseases seems to be the more explored area within gene therapy in adult zebrafish. For instance, polymer and dendrimer-based nanoparticles showed functional siRNA delivery by mediating silencing of specific genes in the heart.[142, 143] In addition to the functional assessment, more recently the distribution of polyamidoamine dendrimer-based nanoparticles in endothelial cells, cardiomyocytes, leucocytes, and macrophages were quantified.[144]

In recent years, *Danio rerio* has gained attention as an attractive research model. Surprisingly, the relatively low amount of studies in the field of nanomedicine reflects that, in this context, it is a model that remains rather unexplored. Although high conservation between zebrafish and mammals is known, a potential challenge in terms of translation due to differences in specific mechanisms, gene duplication, absence of proteins, differences in development, can be foreseen and need to be taken into consideration.

1.3. Scope and motivation of the thesis

Nanoparticles composed of lipids have shown to improve the therapeutic effect of various drugs; however, there is clearly room for improvement. This thesis aims to improve the mechanistic understanding and the fundamental *in vivo* behavior of nanostructures after *i.v.* administration. This is achieved by applying the zebrafish as a model organism to study fundamental aspects of nanoparticles distribution and provides the possibility to identify cellular interactions and mechanism of clearance *in vivo.* Motivation relies mainly on the potential that nanoparticles have as a delivery vehicle and the lack of *in vivo* information about the bio-nano interaction involved. Therefore, this thesis starts with the basics, establishing a zebrafish model, assessing the influence of surface properties on the behavior of nanoparticles *in vivo* and identifying key biological interactions with liver cell types in a molecular level (**Chapter 2-3**). Next, the scope is changed to design nano-systems that target specific cell types (**Chapter 4-6**).

After an introduction to the field of nanomedicine and zebrafish as a general *in vivo* model in **Chapter 1**, we established the zebrafish as a model to study nanoparticles in **Chapter 2** and showed that fluorescent nanoparticle biodistribution can be tracked and visualized in embryonic zebrafish. In addition, by applying the gene-editing technique CRISPR/Cas9 to zebrafish, **Chapter 2** revealed the identification of Stabilin-2, an important scavenger receptor that recognizes and removes macromolecules and a range of nanoparticles from circulation. Stabilin-2 is expressed in a subset of endothelial cells in the zebrafish, named as scavenging endothelial cells, functionally homolog to LSECs in mammals. However, other receptor, were also involved in the clearance of anionic nanoparticles by the liver, since part of particles studied were not influenced by Stabilin-2. In **Chapter 3**, we continued investigating the clearance of these nanoparticles by studying additional scavenger receptors expressed in LSECs. Here, the generation and characterization of a single Stabilin-1 and a double Stabilin zebrafish mutant lead to unravel the role of Stabilin-1 in the uptake of nanoparticles. Stabilin-1 was identified as responsible for the clearance and uptake of small anionic nanoparticles (6-30 nm). In addition, we revealed that together with Stabilin-2, Stabilin-1 contributes in the clearance of bacterial lipopolysaccharide from circulation and anionic nanoparticles of about 100 nm size.

Preceded by an understanding of the fundamental behavior of nanoparticles, this thesis changed the scope to investigate nanomedicine able to target specific cell

types or with control over nanocarriers-cell interaction. To date, several strategies have been employed to design nano-systems capable of delivering cargo triggered by an external stimulus. These systems offer a better spatiotemporal control for delivery of the cargo. In **Chapter 4**, using light as an external trigger, we developed liposomes capable of switching the surface charge *in situ* and *in vivo*, changing from a near-neutral circulating liposomes to a cationic formulation, resulting in the intracellular uptake and delivery of an impermeable cargo. Switching of the surface charge occurs due to the incorporation of a photoactive lipid into the liposomes, as one of the two components of this simple formulation. Simultaneous interactions of the liposomes with endothelial cells and macrophages were shown to be dependent on the transition of the surface charge. This behavior, as well as endocytosis and payload delivery was visualized in the zebrafish embryo in real time.

In **Chapter 5**, a serendipitously found liposomal formulation is studied and characterized. This PAP3 formulation consist of two lipids (DSPC and DOaG) and, to our surprise, accumulate in brain endothelial cells in the zebrafish. Physicochemical characterization of these liposomes, including cryo-transmission electron microscopy (CryoTEM), revealed an uncommon phase-separated 'parachute' morphology, which correlates with the specific targeting *in vivo.* Structurally, the DOaG lipid resemble diacylglycerol (DAG, known to perturb lamellar membranes structure) and in combination with DSPC, form a hydrophobic 'bleb' as a result of a phase separation. Mechanistically, PAP3 liposomes in zebrafish hijack an endogenous triglyceride lipase-mediated pathway of plasma lipid transport and metabolism to selectively target, and be taken up by, endothelial cells *in vivo* which express endothelial lipase (*LIPG*) in embryonic stages. In mice, liposome predominantly accumulate within the liver and spleen, matching with the high expression of endothelial lipase within these metabolic organs.

Using the concepts learned in previous studies on how the liposomes distribute according to their physicochemical properties, we describe in **Chapter 6** a rationally designed LNP formulation able to preferentially target hepatic RES. Here, mRNA was preferentially delivered using an anionic LNP (srLNP) formulation. Biodistribution of srLNPs and cytoplasmic delivery of the mRNA was successfully shown in zebrafish and we demonstrated the selective expression of a fluorescent protein in hepatic cell types at cellular resolution. Mechanistically, we revealed that targeting of SECs is mediated by scavenger receptors Stabilin-1 and Stabilin-2. Furthermore, translation in mice confirmed the srLNP biodistribution, uptake, cytosolic delivery and protein expression of

hepatic RES mice cells. This proves the importance of understanding the mechanism of the designed delivery systems and the ability of the zebrafish model to predict and optimize nanoparticle formulations.

In **Chapter 7** a step-by-step description of a protocol used throughout this thesis is provided. This ensures reproducibility of the experiments performed, such as intravenous injection, imaging and analysis of nanoparticles in the zebrafish.

In **Chapter 8,** the obtained results are discussed in general terms, in the context of nanomedicine, and includes concluding remarks.

1.4. Abbreviations

ALC-0315	(4- hydroxybutyl) azanediyl)bis (hexane-6,1-diyl)bis (2-hexyldecanoate)
ALC-0159	2-[(polyethylene glycol)-2000]-N,N-ditetra-decylacetamide
BBB	blood brain barrier
Cho	cholesterol
CRISPR/Cas9	clustered regularly interspaced short palindromic repeat/Cas9
CryoTEM	Cryo-transmission electron microscopy
CV	caudal vein
DAG	diacylglycerol
DLin-MC3-DMA	amino lipid dilinoleylmethyl-4-dimethylaminobutyrate
DMPC /G	1-α-dimyristoylphosphatidylcholine / glycerol
dpf	day(s) post fertilization
DOPC /S	1,2-dioleoyl-*sn*-glycero-3-phosphocholine / serine
DSPC /G	1,2-distearyl-*sn*-glycero-3-phosphocholine / glycerol
DSPE	1,2-distearyl-*sn*-glycero-3-phosphatidylethanolamine
ENU	*N*-ethylnitrosourea
EPC/G	egg phosphatidylcholine/glycerol
hpi	hour(s) post injection
HSPC	hydrogenated soy phosphatidylcholine
i.m./ i.v.	intramuscularly / intravenously
LDL	low density lipoproteins
LNP	lipid nanoparticle
LSECs	liver sinusoidal endothelial cells
PEG	polyethylene glycol
PLGA	poly(lactic-co-glycolic)
POPC	1-palmitoyl-2-oleoyl-glycero-3-phosphocholine
RES	reticuloendothelial system
SEC	scavenger endothelial cells
sgRNA/siRNA	single guide RNA / small interfering RNA
SM-102	heptadecan-9-yl 8-((2-hydroxyethyl) (6-oxo-6 (undecyloxy)hexyl amino)octanoate
TALENS	transcription activator-like effector nucleases
TTR	transthyretin
VLDL	very low density lipoproteins
ZFNs	zinc finger nuclease

1.5 References

1. Bawa, R., NanoBiotech 2008: Exploring global advances in nanomedicine. *Nanomedicine* **2009,** *5* (1), 5-7.
2. Salata, O., Applications of nanoparticles in biology and medicine. *J Nanobiotechnology* **2004,** *2* (1), 3.
3. Segev-Bar, M.; Haick, H., Flexible sensors based on nanoparticles. *ACS Nano* **2013,** *7* (10), 8366-8378.
4. Nam, J. M.; Thaxton, C. S.; Mirkin, C. A., Nanoparticle-based bio-bar codes for the ultrasensitive detection of proteins. *Science* **2003,** *301* (5641), 1884-1886.
5. Weissleder, R.; Elizondo, G.; Wittenberg, J.; Lee, A. S.; Josephson, L.; Brady, T. J., Ultrasmall superparamagnetic iron oxide: an intravenous contrast agent for assessing lymph nodes with MR imaging. *Radiology* **1990,** *175* (2), 494-498.
6. Heuts, J.; Jiskoot, W.; Ossendorp, F.; van der Maaden, K., Cationic Nanoparticle-Based Cancer Vaccines. *Pharmaceutics* **2021,** *13* (5).
7. Whitehead, K. A.; Dorkin, J. R.; Vegas, A. J.; Chang, P. H.; Veiseh, O.; Matthews, J.; Fenton, O. S.; Zhang, Y.; Olejnik, K. T.; Yesilyurt, V.; Chen, D.; Barros, S.; Klebanov, B.; Novobrantseva, T.; Langer, R.; Anderson, D. G., Degradable lipid nanoparticles with predictable in vivo siRNA delivery activity. *Nat Commun* **2014,** *5*, 4277.
8. Moon, J. S.; Lee, S. H.; Kim, E. J.; Cho, H.; Lee, W.; Kim, G. W.; Park, H. J.; Cho, S. W.; Lee, C.; Oh, J. W., Inhibition of Hepatitis C Virus in Mice by a Small Interfering RNA Targeting a Highly Conserved Sequence in Viral IRES Pseudoknot. *PLoS One* **2016,** *11* (1), e0146710.
9. Lopez-Berestein, G.; Fainstein, V.; Hopfer, R.; Mehta, K.; Sullivan, M. P.; Keating, M.; Rosenblum, M. G.; Mehta, R.; Luna, M.; Hersh, E. M.; et al., Liposomal amphotericin B for the treatment of systemic fungal infections in patients with cancer: a preliminary study. *J Infect Dis* **1985,** *151* (4), 704-710.
10. Gabizon, A.; Peretz, T.; Sulkes, A.; Amselem, S.; Ben-Yosef, R.; Ben-Baruch, N.; Catane, R.; Biran, S.; Barenholz, Y., Systemic administration of doxorubicin-containing liposomes in cancer patients: a phase I study. *Eur J Cancer Clin Oncol* **1989,** *25* (12), 1795-1803.
11. Dimitrov, D. S., Virus entry: molecular mechanisms and biomedical applications. *Nat Rev Microbiol* **2004,** *2* (2), 109-122.
12. Torchilin, V. P., Recent advances with liposomes as pharmaceutical carriers. *Nat Rev Drug Discov* **2005,** *4* (2), 145-160.
13. Chen, L. G.; Strassburg, S. H.; Bermudez, H., Micelle co-assembly in surfactant/ionic liquid mixtures. *J Colloid Interface Sci* **2016,** *477*, 40-45.
14. Nishiyama, N.; Kataoka, K., Current state, achievements, and future prospects of polymeric micelles as nanocarriers for drug and gene delivery. *Pharmacol Ther* **2006,** *112* (3), 630-648.
15. He, W.; Xing, X.; Wang, X.; Wu, D.; Wu, W.; Guo, J.; Mitragotri, S., Nanocarrier-Mediated Cytosolic Delivery of Biopharmaceuticals. *Advanced Functional Materials* **2020,** *30* (37), 1910566.
16. Ulrich, A. S., Biophysical aspects of using liposomes as delivery vehicles. *Biosci Rep* **2002,** *22* (2), 129-150.
17. Koller-Lucae, S. K.; Schott, H.; Schwendener, R. A., Interactions with human blood in vitro and pharmacokinetic properties in mice of liposomal N4-octadecyl-1-beta-D-arabinofuranosylcytosine, a new anticancer drug. *J Pharmacol Exp Ther* **1997,** *282* (3), 1572-1580.
18. Barenholz, Y., Doxil(R)--the first FDA-approved nano-drug: lessons learned. *J Control Release* **2012,** *160* (2), 117-134.
19. Weng, Y.; Li, C.; Yang, T.; Hu, B.; Zhang, M.; Guo, S.; Xiao, H.; Liang, X. J.; Huang, Y., The challenge and prospect of mRNA therapeutics landscape. *Biotechnology advances* **2020,** *40*, 107534.
20. Sioud, M.; Furset, G.; Cekaite, L., Suppression of immunostimulatory siRNA-driven innate immune activation by 2'-modified RNAs. *Biochem Biophys Res Commun* **2007,** *361* (1), 122-126.
21. Song, X.; Wang, X.; Ma, Y.; Liang, Z.; Yang, Z.; Cao, H., Site-Specific Modification Using the 2'-Methoxyethyl Group Improves the Specificity and Activity of siRNAs. *Mol Ther Nucleic Acids* **2017,** *9*, 242-250.
22. Khvorova, A.; Watts, J. K., The chemical evolution of oligonucleotide therapies of clinical utility. *Nat Biotechnol* **2017,** *35* (3), 238-248.

23. Semple, S. C.; Akinc, A.; Chen, J.; Sandhu, A. P.; Mui, B. L.; Cho, C. K.; Sah, D. W.; Stebbing, D.; Crosley, E. J.; Yaworski, E., et al., Rational design of cationic lipids for siRNA delivery. *Nat Biotechnol* **2010,** *28* (2), 172-176.
24. Semple, S. C.; Klimuk, S. K.; Harasym, T. O.; Dos Santos, N.; Ansell, S. M.; Wong, K. F.; Maurer, N.; Stark, H.; Cullis, P. R.; Hope, M. J.; Scherrer, P., Efficient encapsulation of antisense oligonucleotides in lipid vesicles using ionizable aminolipids: formation of novel small multilamellar vesicle structures. *Biochim Biophys Acta* **2001,** *1510* (1-2), 152-166.
25. Jayaraman, M.; Ansell, S. M.; Mui, B. L.; Tam, Y. K.; Chen, J.; Du, X.; Butler, D.; Eltepu, L.; Matsuda, S.; Narayanannair, J. K.; Rajeev, K. G.; Hafez, I. M.; Akinc, A.; Maier, M. A.; Tracy, M. A.; Cullis, P. R.; Madden, T. D.; Manoharan, M.; Hope, M. J., Maximizing the potency of siRNA lipid nanoparticles for hepatic gene silencing in vivo. *Angew Chem Int Ed Engl* **2012,** *51* (34), 8529-8533.
26. Leung, A. K.; Tam, Y. Y.; Chen, S.; Hafez, I. M.; Cullis, P. R., Microfluidic Mixing: A General Method for Encapsulating Macromolecules in Lipid Nanoparticle Systems. *J Phys Chem B* **2015,** *119* (28), 8698-8706.
27. Cullis, P. R.; Hope, M. J., Lipid Nanoparticle Systems for Enabling Gene Therapies. *Molecular Therapy* **2017,** *25* (7), 1467-1475.
28. Leung, A. K. K.; Hafez, I. M.; Baoukina, S.; Belliveau, N. M.; Zhigaltsev, I. V.; Afshinmanesh, E.; Tieleman, D. P.; Hansen, C. L.; Hope, M. J.; Cullis, P. R., Lipid nanoparticles containing siRNA synthesized by microfluidic mixing exhibit an electron-dense nanostructured core. *Journal of Physical Chemistry C* **2012,** *116* (34), 18440-18450.
29. Walsh, C.; Ou, K.; Belliveau, N. M.; Leaver, T. J.; Wild, A. W.; Huft, J.; Lin, P. J.; Chen, S.; Leung, A. K.; Lee, J. B.; Hansen, C. L.; Taylor, R. J.; Ramsay, E. C.; Cullis, P. R., Microfluidic-based manufacture of siRNA-lipid nanoparticles for therapeutic applications. *Methods Mol Biol* **2014,** *1141*, 109-120.
30. Chen, S.; Tam, Y. Y. C.; Lin, P. J. C.; Sung, M. M. H.; Tam, Y. K.; Cullis, P. R., Influence of particle size on the in vivo potency of lipid nanoparticle formulations of siRNA. *J Control Release* **2016,** *235*, 236-244.
31. Belliveau, N. M.; Huft, J.; Lin, P. J.; Chen, S.; Leung, A. K.; Leaver, T. J.; Wild, A. W.; Lee, J. B.; Taylor, R. J.; Tam, Y. K.; Hansen, C. L.; Cullis, P. R., Microfluidic Synthesis of Highly Potent Limit-size Lipid Nanoparticles for In Vivo Delivery of siRNA. *Mol Ther Nucleic Acids* **2012,** *1*, e37.
32. Mui, B. L.; Tam, Y. K.; Jayaraman, M.; Ansell, S. M.; Du, X.; Tam, Y. Y.; Lin, P. J.; Chen, S.; Narayanannair, J. K.; Rajeev, K. G.; Manoharan, M.; Akinc, A.; Maier, M. A.; Cullis, P.; Madden, T. D.; Hope, M. J., Influence of Polyethylene Glycol Lipid Desorption Rates on Pharmacokinetics and Pharmacodynamics of siRNA Lipid Nanoparticles. *Mol Ther Nucleic Acids* **2013,** *2*, e139.
33. Akinc, A.; Maier, M. A.; Manoharan, M.; Fitzgerald, K.; Jayaraman, M.; Barros, S.; Ansell, S.; Du, X.; Hope, M. J.; Madden, T. D.; Mui, B. L.; Semple, S. C.; Tam, Y. K.; Ciufolini, M.; Witzigmann, D.; Kulkarni, J. A.; van der Meel, R.; Cullis, P. R., The Onpattro story and the clinical translation of nanomedicines containing nucleic acid-based drugs. *Nature Nanotechnology* **2019,** *14* (12), 1084-1087.
34. Cornely, O. A.; Maertens, J.; Bresnik, M.; Ebrahimi, R.; Ullmann, A. J.; Bouza, E.; Heussel, C. P.; Lortholary, O.; Rieger, C.; Boehme, A., et al., Liposomal amphotericin B as initial therapy for invasive mold infection: a randomized trial comparing a high-loading dose regimen with standard dosing (AmBiLoad trial). *Clin Infect Dis* **2007,** *44* (10), 1289-1297.
35. Adedoyin, A.; Bernardo, J. F.; Swenson, C. E.; Bolsack, L. E.; Horwith, G.; DeWit, S.; Kelly, E.; Klasterksy, J.; Sculier, J. P.; DeValeriola, D.; Anaissie, E.; Lopez-Berestein, G.; Llanos-Cuentas, A.; Boyle, A.; Branch, R. A., Pharmacokinetic profile of ABELCET (amphotericin B lipid complex injection): combined experience from phase I and phase II studies. *Antimicrob Agents Chemother* **1997,** *41* (10), 2201-2208.
36. Schlossberg, D.; Samuel, R., AMPHOTEC (Amphotericin B Colloidal Dispersion – ABCD). 2017; pp 13-14.
37. Harris, L.; Batist, G.; Belt, R.; Rovira, D.; Navari, R.; Azarnia, N.; Welles, L.; Winer, E.; Group, T. D. S., Liposome-encapsulated doxorubicin compared with conventional doxorubicin in a randomized multicenter trial as first-line therapy of metastatic breast carcinoma. *Cancer* **2002,** *94* (1), 25-36.
38. Burade, V.; Bhowmick, S.; Maiti, K.; Zalawadia, R.; Ruan, H.; Thennati, R., Lipodox(R) (generic doxorubicin hydrochloride liposome injection): in vivo efficacy and bioequivalence versus Caelyx(R) (doxorubicin hydrochloride liposome injection) in human mammary carcinoma (MX-1) xenograft and syngeneic fibrosarcoma (WEHI 164) mouse models. *BMC Cancer* **2017,** *17* (1), 405.

39. Forssen, E. A.; Male-Brune, R.; Adler-Moore, J. P.; Lee, M. J.; Schmidt, P. G.; Krasieva, T. B.; Shimizu, S.; Tromberg, B. J., Fluorescence imaging studies for the disposition of daunorubicin liposomes (DaunoXome) within tumor tissue. *Cancer Res* **1996,** *56* (9), 2066-2075.
40. Tzogani, K.; Penttila, K.; Lapvetelainen, T.; Hemmings, R.; Koenig, J.; Freire, J.; Marcia, S.; Cole, S.; Coppola, P.; Flores, B.; Barbachano, Y.; Roige, S. D.; Pignatti, F., EMA Review of Daunorubicin and Cytarabine Encapsulated in Liposomes (Vyxeos, CPX-351) for the Treatment of Adults with Newly Diagnosed, Therapy-Related Acute Myeloid Leukemia or Acute Myeloid Leukemia with Myelodysplasia-Related Changes. *Oncologist* **2020,** *25* (9), e1414-e1420.
41. Shah, N. N.; Merchant, M. S.; Cole, D. E.; Jayaprakash, N.; Bernstein, D.; Delbrook, C.; Richards, K.; Widemann, B. C.; Wayne, A. S., Vincristine Sulfate Liposomes Injection (VSLI, Marqibo(R)): Results From a Phase I Study in Children, Adolescents, and Young Adults With Refractory Solid Tumors or Leukemias. *Pediatr Blood Cancer* **2016,** *63* (6), 997-1005.
42. Shah, N. N.; Cole, D. E.; Lester-McCully, C. M.; Wayne, A. S.; Warren, K. E.; Widemann, B. C., Plasma and cerebrospinal fluid pharmacokinetics of vincristine and vincristine sulfate liposomes injection (VSLI, marqibo(R)) after intravenous administration in Non-human primates. *Invest New Drugs* **2016,** *34* (1), 61-65.
43. FDA Approves Onivyde Combo Regimen for Advanced Pancreatic Cancer. *Oncology Times* **2015,** *37* (22), 8.
44. Gao, W.; Hu, C. M.; Fang, R. H.; Zhang, L., Liposome-like Nanostructures for Drug Delivery. *J Mater Chem B* **2013,** *1* (48), 6569-6585
45. Cullis, P. R.; Hope, M. J., Lipid Nanoparticle Systems for Enabling Gene Therapies. *Mol Ther* **2017,** *25* (7), 1467-1475.
46. Brard, C.; Piperno-Neumann, S.; Delaye, J.; Brugières, L.; Hampson, L. V.; Le Teuff, G.; Le Deley, M.-C.; Gaspar, N., Sarcome-13/OS2016 trial protocol: a multicentre, randomised, open-label, phase II trial of mifamurtide combined with postoperative chemotherapy for patients with newly diagnosed high-risk osteosarcoma. *BMJ Open* **2019,** *9* (5), e025877.
47. Photodynamic therapy of subfoveal choroidal neovascularization in age-related macular degeneration with verteporfin: one-year results of 2 randomized clinical trials--TAP report. Treatment of age-related macular degeneration with photodynamic therapy (TAP) Study Group. *Arch Ophthalmol* **1999,** *117* (10), 1329-1345.
48. Akinc, A.; Querbes, W.; De, S.; Qin, J.; Frank-Kamenetsky, M.; Jayaprakash, K. N.; Jayaraman, M.; Rajeev, K. G.; Cantley, W. L.; Dorkin, J. R., et al., Targeted delivery of RNAi therapeutics with endogenous and exogenous ligand-based mechanisms. *Molecular Therapy* **2010,** *18* (7), 1357-1364.
49. Wu, S. Y.; Lopez-Berestein, G.; Calin, G. A.; Sood, A. K., RNAi therapies: drugging the undruggable. *Sci Transl Med* **2014,** *6* (240), 240ps247.
50. Semple, S. C.; Judge, A. D.; Robbins, M.; Klimuk, S.; Eisenhardt, M.; Crosley, E.; Leung, A.; Kwok, R.; Ambegia, E.; McClintock, K.; MacLachlan, I., Abstract 2829: Preclinical characterization of TKM-080301, a lipid nanoparticle formulation of a small interfering RNA directed against polo-like kinase 1. *Cancer Research* **2011,** *71* (8 Supplement), 2829-2829.
51. Northfelt, D. W.; Hamburg, S. I.; Borad, M. J.; Seetharam, M.; Curtis, K. K.; Lee, P.; Crowell, B.; Vocila, L.; Fredlund, P.; Gilbert, M. J.; Mast, C. P.; Semple, S. C.; Judge, A. D.; MacLachlan, I.; Ramanathan, R. K., A phase I dose-escalation study of TKM-080301, a RNAi therapeutic directed against polo-like kinase 1 (PLK1), in patients with advanced solid tumors: Expansion cohort evaluation of biopsy samples for evidence of pharmacodynamic effects of PLK1 inhibition. *Journal of Clinical Oncology* **2013,** *31* (15_suppl), TPS2621-TPS2621.
52. Pardi, N.; Hogan, M. J.; Porter, F. W.; Weissman, D., mRNA vaccines — a new era in vaccinology. *Nature Reviews Drug Discovery* **2018,** *17* (4), 261-279.
53. Pardi, N.; Parkhouse, K.; Kirkpatrick, E.; McMahon, M.; Zost, S. J.; Mui, B. L.; Tam, Y. K.; Kariko, K.; Barbosa, C. J.; Madden, T. D.; Hope, M. J.; Krammer, F.; Hensley, S. E.; Weissman, D., Nucleoside-modified mRNA immunization elicits influenza virus hemagglutinin stalk-specific antibodies. *Nat Commun* **2018,** *9* (1), 3361.
54. Pardi, N.; Hogan, M. J.; Pelc, R. S.; Muramatsu, H.; Andersen, H.; DeMaso, C. R.; Dowd, K. A.; Sutherland, L. L.; Scearce, R. M.; Parks, R., et al., Zika virus protection by a single low-dose nucleoside-modified mRNA vaccination. *Nature* **2017,** *543* (7644), 248-251.
55. Pardi, N.; Secreto, A. J.; Shan, X.; Debonera, F.; Glover, J.; Yi, Y.; Muramatsu, H.; Ni, H.; Mui, B. L.; Tam, Y. K.; Shaheen, F.; Collman, R. G.; Kariko, K.; Danet-Desnoyers, G. A.; Madden, T. D.; Hope, M. J.;

Weissman, D., Administration of nucleoside-modified mRNA encoding broadly neutralizing antibody protects humanized mice from HIV-1 challenge. *Nat Commun* **2017,** *8*, 14630.
56. John, S.; Yuzhakov, O.; Woods, A.; Deterling, J.; Hassett, K.; Shaw, C. A.; Ciaramella, G., Multi-antigenic human cytomegalovirus mRNA vaccines that elicit potent humoral and cell-mediated immunity. *Vaccine* **2018,** *36* (12), 1689-1699.
57. Kreiter, S.; Vormehr, M.; van de Roemer, N.; Diken, M.; Lower, M.; Diekmann, J.; Boegel, S.; Schrors, B.; Vascotto, F.; Castle, J. C.; Tadmor, A. D.; Schoenberger, S. P.; Huber, C.; Tureci, O.; Sahin, U., Mutant MHC class II epitopes drive therapeutic immune responses to cancer. *Nature* **2015,** *520* (7549), 692-696.
58. Polack, F. P.; Thomas, S. J.; Kitchin, N.; Absalon, J.; Gurtman, A.; Lockhart, S.; Perez, J. L.; Pérez Marc, G.; Moreira, E. D.; Zerbini, C., et al., Safety and Efficacy of the BNT162b2 mRNA Covid-19 Vaccine. *New England Journal of Medicine* **2020,** *383* (27), 2603-2615.
59. Baden, L. R.; Stieh, D. J.; Sarnecki, M.; Walsh, S. R.; Tomaras, G. D.; Kublin, J. G.; McElrath, M. J.; Alter, G.; Ferrari, G.; Montefiori, D., et al., Safety and immunogenicity of two heterologous HIV vaccine regimens in healthy, HIV-uninfected adults (TRAVERSE): a randomised, parallel-group, placebo-controlled, double-blind, phase 1/2a study. *Lancet HIV* **2020,** *7* (10), e688-e698.
60. Tsui, N. B.; Ng, E. K.; Lo, Y. M., Stability of endogenous and added RNA in blood specimens, serum, and plasma. *Clin Chem* **2002,** *48* (10), 1647-1653.
61. Hay, M.; Thomas, D. W.; Craighead, J. L.; Economides, C.; Rosenthal, J., Clinical development success rates for investigational drugs. *Nat Biotechnol* **2014,** *32* (1), 40-51.
62. Aliyandi, A.; Zuhorn, I. S.; Salvati, A., Disentangling Biomolecular Corona Interactions With Cell Receptors and Implications for Targeting of Nanomedicines. *Front Bioeng Biotechnol* **2020,** *8*, 599454.
63. Cai, R.; Chen, C., The Crown and the Scepter: Roles of the Protein Corona in Nanomedicine. *Adv Mater* **2019,** *31* (45), e1805740.
64. Pattipeiluhu, R.; Crielaard, S.; Klein-Schiphorst, I.; Florea, B. I.; Kros, A.; Campbell, F., Unbiased Identification of the Liposome Protein Corona using Photoaffinity-based Chemoproteomics. *ACS Central Science* **2020,** *6* (4), 535-545.
65. Aggarwal, P.; Hall, J. B.; McLeland, C. B.; Dobrovolskaia, M. A.; McNeil, S. E., Nanoparticle interaction with plasma proteins as it relates to particle biodistribution, biocompatibility and therapeutic efficacy. *Adv Drug Deliv Rev* **2009,** *61* (6), 428-437.
66. Akinc, A.; Maier, M. A.; Manoharan, M.; Fitzgerald, K.; Jayaraman, M.; Barros, S.; Ansell, S.; Du, X.; Hope, M. J.; Madden, T. D.; Mui, B. L.; Semple, S. C.; Tam, Y. K.; Ciufolini, M.; Witzigmann, D.; Kulkarni, J. A.; van der Meel, R.; Cullis, P. R., The Onpattro story and the clinical translation of nanomedicines containing nucleic acid-based drugs. *Nat Nanotechnol* **2019,** *14* (12), 1084-1087.
67. Adams, D.; Gonzalez-Duarte, A.; O'Riordan, W. D.; Yang, C. C.; Ueda, M.; Kristen, A. V.; Tournev, I.; Schmidt, H. H.; Coelho, T.; Berk, J. L., et al., Patisiran, an RNAi Therapeutic, for Hereditary Transthyretin Amyloidosis. *N Engl J Med* **2018,** *379* (1), 11-21.
68. Walkey, C. D.; Olsen, J. B.; Guo, H.; Emili, A.; Chan, W. C., Nanoparticle size and surface chemistry determine serum protein adsorption and macrophage uptake. *J Am Chem Soc* **2012,** *134* (4), 2139-2147.
69. Yang, K.; Ma, Y. Q., Computer simulation of the translocation of nanoparticles with different shapes across a lipid bilayer. *Nat Nanotechnol* **2010,** *5* (8), 579-583.
70. Geng, Y.; Dalhaimer, P.; Cai, S.; Tsai, R.; Tewari, M.; Minko, T.; Discher, D. E., Shape effects of filaments versus spherical particles in flow and drug delivery. *Nat Nanotechnol* **2007,** *2* (4), 249-255.
71. Jiang, W.; Kim, B. Y.; Rutka, J. T.; Chan, W. C., Nanoparticle-mediated cellular response is size-dependent. *Nat Nanotechnol* **2008,** *3* (3), 145-150.
72. Chithrani, B. D.; Chan, W. C., Elucidating the mechanism of cellular uptake and removal of protein-coated gold nanoparticles of different sizes and shapes. *Nano Lett* **2007,** *7* (6), 1542-1550.
73. Zhang, L.; Cao, Z.; Li, Y.; Ella-Menye, J. R.; Bai, T.; Jiang, S., Softer zwitterionic nanogels for longer circulation and lower splenic accumulation. *ACS Nano* **2012,** *6* (8), 6681-6686.
74. Lin, J.; Miao, L.; Zhong, G.; Lin, C. H.; Dargazangy, R.; Alexander-Katz, A., Understanding the synergistic effect of physicochemical properties of nanoparticles and their cellular entry pathways. *Commun Biol* **2020,** *3* (1), 205.
75. Van Lehn, R. C.; Atukorale, P. U.; Carney, R. P.; Yang, Y. S.; Stellacci, F.; Irvine, D. J.; Alexander-Katz, A., Effect of particle diameter and surface composition on the spontaneous fusion of monolayer-protected gold nanoparticles with lipid bilayers. *Nano Lett* **2013,** *13* (9), 4060-4067.

76. Xiao, K.; Li, Y.; Luo, J.; Lee, J. S.; Xiao, W.; Gonik, A. M.; Agarwal, R. G.; Lam, K. S., The effect of surface charge on in vivo biodistribution of PEG-oligocholic acid based micellar nanoparticles. *Biomaterials* **2011,** *32* (13), 3435-3446.
77. Zhao, Z.; Ukidve, A.; Krishnan, V.; Mitragotri, S., Effect of physicochemical and surface properties on in vivo fate of drug nanocarriers. *Adv Drug Deliv Rev* **2019,** *143*, 3-21.
78. Choi, C. H.; Zuckerman, J. E.; Webster, P.; Davis, M. E., Targeting kidney mesangium by nanoparticles of defined size. *Proc Natl Acad Sci U S A* **2011,** *108* (16), 6656-6661.
79. Sonavane, G.; Tomoda, K.; Makino, K., Biodistribution of colloidal gold nanoparticles after intravenous administration: effect of particle size. *Colloids Surf B Biointerfaces* **2008,** *66* (2), 274-280.
80. Liu, D.; Mori, A.; Huang, L., Role of liposome size and RES blockade in controlling biodistribution and tumor uptake of GM1-containing liposomes. *Biochim Biophys Acta* **1992,** *1104* (1), 95-101.
81. Cabral, H.; Matsumoto, Y.; Mizuno, K.; Chen, Q.; Murakami, M.; Kimura, M.; Terada, Y.; Kano, M. R.; Miyazono, K.; Uesaka, M.; Nishiyama, N.; Kataoka, K., Accumulation of sub-100 nm polymeric micelles in poorly permeable tumours depends on size. *Nat Nanotechnol* **2011,** *6* (12), 815-823.
82. Goodman, C. M.; McCusker, C. D.; Yilmaz, T.; Rotello, V. M., Toxicity of gold nanoparticles functionalized with cationic and anionic side chains. *Bioconjug Chem* **2004,** *15* (4), 897-900.
83. Verma, A.; Stellacci, F., Effect of surface properties on nanoparticle-cell interactions. *Small* **2010,** *6* (1), 12-21.
84. Frohlich, E., The role of surface charge in cellular uptake and cytotoxicity of medical nanoparticles. *Int J Nanomedicine* **2012,** *7*, 5577-5591.
85. Arvizo, R. R.; Miranda, O. R.; Moyano, D. F.; Walden, C. A.; Giri, K.; Bhattacharya, R.; Robertson, J. D.; Rotello, V. M.; Reid, J. M.; Mukherjee, P., Modulating pharmacokinetics, tumor uptake and biodistribution by engineered nanoparticles. *PLoS One* **2011,** *6* (9), e24374.
86. Levchenko, T. S.; Rammohan, R.; Lukyanov, A. N.; Whiteman, K. R.; Torchilin, V. P., Liposome clearance in mice: the effect of a separate and combined presence of surface charge and polymer coating. *Int J Pharm* **2002,** *240* (1-2), 95-102.
87. Poisson, J.; Lemoinne, S.; Boulanger, C.; Durand, F.; Moreau, R.; Valla, D.; Rautou, P. E., Liver sinusoidal endothelial cells: Physiology and role in liver diseases. *J Hepatol* **2017,** *66* (1), 212-227.
88. Smedsrod, B.; Le Couteur, D.; Ikejima, K.; Jaeschke, H.; Kawada, N.; Naito, M.; Knolle, P.; Nagy, L.; Senoo, H.; Vidal-Vanaclocha, F.; Yamaguchi, N., Hepatic sinusoidal cells in health and disease: update from the 14th International Symposium. *Liver Int* **2009,** *29* (4), 490-501.
89. Seternes, T.; Sorensen, K.; Smedsrod, B., Scavenger endothelial cells of vertebrates: a nonperipheral leukocyte system for high-capacity elimination of waste macromolecules. *Proc Natl Acad Sci U S A* **2002,** *99* (11), 7594-7597.
90. Park, K., Facing the truth about nanotechnology in drug delivery. *ACS Nano* **2013,** *7* (9), 7442-7447.
91. Venditto, V. J.; Szoka, F. C., Jr., Cancer nanomedicines: so many papers and so few drugs! *Adv Drug Deliv Rev* **2013,** *65* (1), 80-88.
92. Streisinger, G.; Walker, C.; Dower, N.; Knauber, D.; Singer, F., Production of clones of homozygous diploid zebra fish (Brachydanio rerio). *Nature* **1981,** *291* (5813), 293-296.
93. Quinlivan, V. H.; Farber, S. A., Lipid Uptake, Metabolism, and Transport in the Larval Zebrafish. *Front Endocrinol (Lausanne)* **2017,** *8*, 319.
94. Goessling, W.; Sadler, K. C., Zebrafish: an important tool for liver disease research. *Gastroenterology* **2015,** *149* (6), 1361-1377.
95. Hwang, W. Y.; Fu, Y.; Reyon, D.; Maeder, M. L.; Tsai, S. Q.; Sander, J. D.; Peterson, R. T.; Yeh, J. R.; Joung, J. K., Efficient genome editing in zebrafish using a CRISPR-Cas system. *Nat Biotechnol* **2013,** *31* (3), 227-229.
96. Chu, J.; Sadler, K. C., New school in liver development: lessons from zebrafish. *Hepatology* **2009,** *50* (5), 1656-1663.
97. Drummond, I. A.; Davidson, A. J., Zebrafish kidney development. *Methods Cell Biol* **2010,** *100*, 233-260.
98. Collins, J. E.; White, S.; Searle, S. M.; Stemple, D. L., Incorporating RNA-seq data into the zebrafish Ensembl genebuild. *Genome Res* **2012,** *22* (10), 2067-2078.
99. Howe, K.; Clark, M. D.; Torroja, C. F.; Torrance, J.; Berthelot, C.; Muffato, M.; Collins, J. E.; Humphray, S.; McLaren, K.; Matthews, L., et al., The zebrafish reference genome sequence and its relationship to the human genome. *Nature* **2013,** *496* (7446), 498-503.

100. MacRae, C. A.; Peterson, R. T., Zebrafish as tools for drug discovery. *Nat Rev Drug Discov* **2015,** *14* (10), 721-731.
101. Shih, Y. H.; Zhang, Y.; Ding, Y.; Ross, C. A.; Li, H.; Olson, T. M.; Xu, X., Cardiac transcriptome and dilated cardiomyopathy genes in zebrafish. *Circ Cardiovasc Genet* **2015,** *8* (2), 261-269.
102. Lam, S. H.; Wu, Y. L.; Vega, V. B.; Miller, L. D.; Spitsbergen, J.; Tong, Y.; Zhan, H.; Govindarajan, K. R.; Lee, S.; Mathavan, S.; Murthy, K. R.; Buhler, D. R.; Liu, E. T.; Gong, Z., Conservation of gene expression signatures between zebrafish and human liver tumors and tumor progression. *Nat Biotechnol* **2006,** *24* (1), 73-75.
103. Zheng, W.; Wang, Z.; Collins, J. E.; Andrews, R. M.; Stemple, D.; Gong, Z., Comparative transcriptome analyses indicate molecular homology of zebrafish swimbladder and mammalian lung. *PLoS One* **2011,** *6* (8), e24019.
104. Sugano, Y.; Cianciolo Cosentino, C.; Loffing-Cueni, D.; Neuhauss, S. C. F.; Loffing, J., Comparative transcriptomic analysis identifies evolutionarily conserved gene products in the vertebrate renal distal convoluted tubule. *Pflugers Arch* **2017,** *469* (7-8), 859-867.
105. Tarifeno-Saldivia, E.; Lavergne, A.; Bernard, A.; Padamata, K.; Bergemann, D.; Voz, M. L.; Manfroid, I.; Peers, B., Transcriptome analysis of pancreatic cells across distant species highlights novel important regulator genes. *BMC Biol* **2017,** *15* (1), 21.
106. Keller, P. J.; Schmidt, A. D.; Wittbrodt, J.; Stelzer, E. H., Reconstruction of zebrafish early embryonic development by scanned light sheet microscopy. *Science* **2008,** *322* (5904), 1065-1069.
107. Campbell, F.; Bos, F. L.; Sieber, S.; Arias-Alpizar, G.; Koch, B. E.; Huwyler, J.; Kros, A.; Bussmann, J., Directing Nanoparticle Biodistribution through Evasion and Exploitation of Stab2-Dependent Nanoparticle Uptake. *ACS Nano* **2018,** *12* (3), 2138-2150.
108. Moro, E.; Vettori, A.; Porazzi, P.; Schiavone, M.; Rampazzo, E.; Casari, A.; Ek, O.; Facchinello, N.; Astone, M.; Zancan, I.; Milanetto, M.; Tiso, N.; Argenton, F., Generation and application of signaling pathway reporter lines in zebrafish. *Mol Genet Genomics* **2013,** *288* (5-6), 231-242.
109. Jin, S. W.; Beis, D.; Mitchell, T.; Chen, J. N.; Stainier, D. Y., Cellular and molecular analyses of vascular tube and lumen formation in zebrafish. *Development* **2005,** *132* (23), 5199-5209.
110. Ellett, F.; Pase, L.; Hayman, J. W.; Andrianopoulos, A.; Lieschke, G. J., mpeg1 promoter transgenes direct macrophage-lineage expression in zebrafish. *Blood* **2011,** *117* (4), e49-56.
111. Driever, W.; Solnica-Krezel, L.; Schier, A. F.; Neuhauss, S. C.; Malicki, J.; Stemple, D. L.; Stainier, D. Y.; Zwartkruis, F.; Abdelilah, S.; Rangini, Z.; Belak, J.; Boggs, C., A genetic screen for mutations affecting embryogenesis in zebrafish. *Development* **1996,** *123*, 37-46.
112. Suster, M. L.; Kikuta, H.; Urasaki, A.; Asakawa, K.; Kawakami, K., Transgenesis in zebrafish with the tol2 transposon system. *Methods Mol Biol* **2009,** *561*, 41-63.
113. Doyon, Y.; McCammon, J. M.; Miller, J. C.; Faraji, F.; Ngo, C.; Katibah, G. E.; Amora, R.; Hocking, T. D.; Zhang, L.; Rebar, E. J.; Gregory, P. D.; Urnov, F. D.; Amacher, S. L., Heritable targeted gene disruption in zebrafish using designed zinc-finger nucleases. *Nat Biotechnol* **2008,** *26* (6), 702-708.
114. Bedell, V. M.; Person, A. D.; Larson, J. D.; McLoon, A.; Balciunas, D.; Clark, K. J.; Neff, K. I.; Nelson, K. E.; Bill, B. R.; Schimmenti, L. A.; Beiraghi, S.; Ekker, S. C., The lineage-specific gene ponzr1 is essential for zebrafish pronephric and pharyngeal arch development. *Development* **2012,** *139* (4), 793-804.
115. Varshney, G. K.; Pei, W.; LaFave, M. C.; Idol, J.; Xu, L.; Gallardo, V.; Carrington, B.; Bishop, K.; Jones, M.; Li, M.; Harper, U.; Huang, S. C.; Prakash, A.; Chen, W.; Sood, R.; Ledin, J.; Burgess, S. M., High-throughput gene targeting and phenotyping in zebrafish using CRISPR/Cas9. *Genome Res* **2015,** *25* (7), 1030-1042.
116. Jao, L. E.; Wente, S. R.; Chen, W., Efficient multiplex biallelic zebrafish genome editing using a CRISPR nuclease system. *Proc Natl Acad Sci U S A* **2013,** *110* (34), 13904-13909.
117. Chang, N.; Sun, C.; Gao, L.; Zhu, D.; Xu, X.; Zhu, X.; Xiong, J. W.; Xi, J. J., Genome editing with RNA-guided Cas9 nuclease in zebrafish embryos. *Cell Res* **2013,** *23* (4), 465-472.
118. Delov, V.; Muth-Kohne, E.; Schafers, C.; Fenske, M., Transgenic fluorescent zebrafish Tg(fli1:EGFP)y(1) for the identification of vasotoxicity within the zFET. *Aquat Toxicol* **2014,** *150*, 189-200.
119. Tat, J.; Liu, M.; Wen, X. Y., Zebrafish cancer and metastasis models for in vivo drug discovery. *Drug Discov Today Technol* **2013,** *10* (1), e83-89.
120. van Leeuwen, L. M.; Evans, R. J.; Jim, K. K.; Verboom, T.; Fang, X.; Bojarczuk, A.; Malicki, J.; Johnston, S. A.; van der Sar, A. M., A transgenic zebrafish model for the in vivo study of the blood and choroid plexus brain barriers using claudin 5. *Biol Open* **2018,** *7* (2), bio030494.

121. Her, G. M.; Chiang, C. C.; Chen, W. Y.; Wu, J. L., In vivo studies of liver-type fatty acid binding protein (L-FABP) gene expression in liver of transgenic zebrafish (Danio rerio). *FEBS Lett* **2003,** *538* (1-3), 125-133.
122. Okuda, K. S.; Astin, J. W.; Misa, J. P.; Flores, M. V.; Crosier, K. E.; Crosier, P. S., lyve1 expression reveals novel lymphatic vessels and new mechanisms for lymphatic vessel development in zebrafish. *Development* **2012,** *139* (13), 2381-2391.
123. Perner, B.; Englert, C.; Bollig, F., The Wilms tumor genes wt1a and wt1b control different steps during formation of the zebrafish pronephros. *Dev Biol* **2007,** *309* (1), 87-96.
124. Ekker, S. C., Morphants: a new systematic vertebrate functional genomics approach. *Yeast* **2000,** *17* (4), 302-306.
125. Kok, F. O.; Shin, M.; Ni, C. W.; Gupta, A.; Grosse, A. S.; van Impel, A.; Kirchmaier, B. C.; Peterson-Maduro, J.; Kourkoulis, G.; Male, I.; DeSantis, D. F.; Sheppard-Tindell, S.; Ebarasi, L.; Betsholtz, C.; Schulte-Merker, S.; Wolfe, S. A.; Lawson, N. D., Reverse genetic screening reveals poor correlation between morpholino-induced and mutant phenotypes in zebrafish. *Dev Cell* **2015,** *32* (1), 97-108.
126. Sieber, S.; Grossen, P.; Bussmann, J.; Campbell, F.; Kros, A.; Witzigmann, D.; Huwyler, J., Zebrafish as a preclinical in vivo screening model for nanomedicines. *Adv Drug Deliv Rev* **2019,** *151-152*, 152-168.
127. Hayashi, Y.; Takamiya, M.; Jensen, P. B.; Ojea-Jimenez, I.; Claude, H.; Antony, C.; Kjaer-Sorensen, K.; Grabher, C.; Boesen, T.; Gilliland, D.; Oxvig, C.; Strahle, U.; Weiss, C., Differential Nanoparticle Sequestration by Macrophages and Scavenger Endothelial Cells Visualized in Vivo in Real-Time and at Ultrastructural Resolution. *ACS Nano* **2020,** *14* (2), 1665-1681.
128. Sieber, S.; Grossen, P.; Uhl, P.; Detampel, P.; Mier, W.; Witzigmann, D.; Huwyler, J., Zebrafish as a predictive screening model to assess macrophage clearance of liposomes in vivo. *Nanomedicine* **2019,** *17*, 82-93.
129. Gutierrez-Lovera, C.; Vazquez-Rios, A. J.; Guerra-Varela, J.; Sanchez, L.; de la Fuente, M., The Potential of Zebrafish as a Model Organism for Improving the Translation of Genetic Anticancer Nanomedicines. *Genes (Basel)* **2017,** *8* (12).
130. Evensen, L.; Johansen, P. L.; Koster, G.; Zhu, K.; Herfindal, L.; Speth, M.; Fenaroli, F.; Hildahl, J.; Bagherifam, S.; Tulotta, C.; Prasmickaite, L.; Maelandsmo, G. M.; Snaar-Jagalska, E.; Griffiths, G., Zebrafish as a model system for characterization of nanoparticles against cancer. *Nanoscale* **2016,** *8* (2), 862-877.
131. Johnston, H. J.; Verdon, R.; Gillies, S.; Brown, D. M.; Fernandes, T. F.; Henry, T. B.; Rossi, A. G.; Tran, L.; Tucker, C.; Tyler, C. R.; Stone, V., Adoption of in vitro systems and zebrafish embryos as alternative models for reducing rodent use in assessments of immunological and oxidative stress responses to nanomaterials. *Crit Rev Toxicol* **2018,** *48* (3), 252-271.
132. Haque, E.; Ward, A. C., Zebrafish as a Model to Evaluate Nanoparticle Toxicity. *Nanomaterials (Basel)* **2018,** *8* (7).
133. Chakraborty, C.; Sharma, A. R.; Sharma, G.; Lee, S. S., Zebrafish: A complete animal model to enumerate the nanoparticle toxicity. *J Nanobiotechnology* **2016,** *14* (1), 65.
134. Hu, H.; Li, Q.; Jiang, L.; Zou, Y.; Duan, J.; Sun, Z., Genome-wide transcriptional analysis of silica nanoparticle-induced toxicity in zebrafish embryos. *Toxicol Res (Camb)* **2016,** *5* (2), 609-620.
135. Brun, N. R.; Koch, B. E. V.; Varela, M.; Peijnenburg, W. J. G. M.; Spaink, H. P.; Vijver, M. G., Nanoparticles induce dermal and intestinal innate immune system responses in zebrafish embryos. *Environmental Science: Nano* **2018,** *5* (4), 904-916.
136. Yin, H.; Kanasty, R. L.; Eltoukhy, A. A.; Vegas, A. J.; Dorkin, J. R.; Anderson, D. G., Non-viral vectors for gene-based therapy. *Nat Rev Genet* **2014,** *15* (8), 541-555.
137. Cordeiro, M.; Carvalho, L.; Silva, J.; Saude, L.; Fernandes, A. R.; Baptista, P. V., Gold Nanobeacons for Tracking Gene Silencing in Zebrafish. *Nanomaterials (Basel)* **2017,** *7* (1).
138. Mauriello Jimenez, C.; Aggad, D.; Croissant, J. G.; Tresfield, K.; Laurencin, D.; Berthomieu, D.; Cubedo, N.; Rossel, M.; Alsaiari, S.; Anjum, D. H., et al., Photodynamic Therapy: Porous Porphyrin-Based Organosilica Nanoparticles for NIR Two-Photon Photodynamic Therapy and Gene Delivery in Zebrafish (Adv. Funct. Mater. 21/2018). *Advanced Functional Materials* **2018,** *28* (21), 1870143.
139. Patton, C.; Farr, G. H., 3rd; An, D.; Martini, P. G. V.; Maves, L., Lipid Nanoparticle Packaging Is an Effective and Nontoxic mRNA Delivery Platform in Embryonic Zebrafish. *Zebrafish* **2018,** *15* (3), 217-227.
140. Buck, J.; Grossen, P.; Cullis, P. R.; Huwyler, J.; Witzigmann, D., Lipid-Based DNA Therapeutics: Hallmarks of Non-Viral Gene Delivery. *ACS Nano* **2019,** *13* (4), 3754-3782.

141. Kulkarni, J. A.; Witzigmann, D.; Chen, S.; Cullis, P. R.; van der Meel, R., Lipid Nanoparticle Technology for Clinical Translation of siRNA Therapeutics. *Acc Chem Res* **2019,** *52* (9), 2435-2444.
142. Xiao, C.; Wang, F.; Hou, J.; Zhu, X.; Luo, Y.; Xiong, J. W., Nanoparticle-mediated siRNA Gene-silencing in Adult Zebrafish Heart. *J Vis Exp* **2018,** (137).
143. Diao, J.; Wang, H.; Chang, N.; Zhou, X. H.; Zhu, X.; Wang, J.; Xiong, J. W., PEG-PLA nanoparticles facilitate siRNA knockdown in adult zebrafish heart. *Dev Biol* **2015,** *406* (2), 196-202.
144. Wang, F.; Wang, X.; Gao, L.; Meng, L. Y.; Xie, J. M.; Xiong, J. W.; Luo, Y., Nanoparticle-mediated delivery of siRNA into zebrafish heart: a cell-level investigation on the biodistribution and gene silencing effects. *Nanoscale* **2019,** *11* (39), 18052-18064.

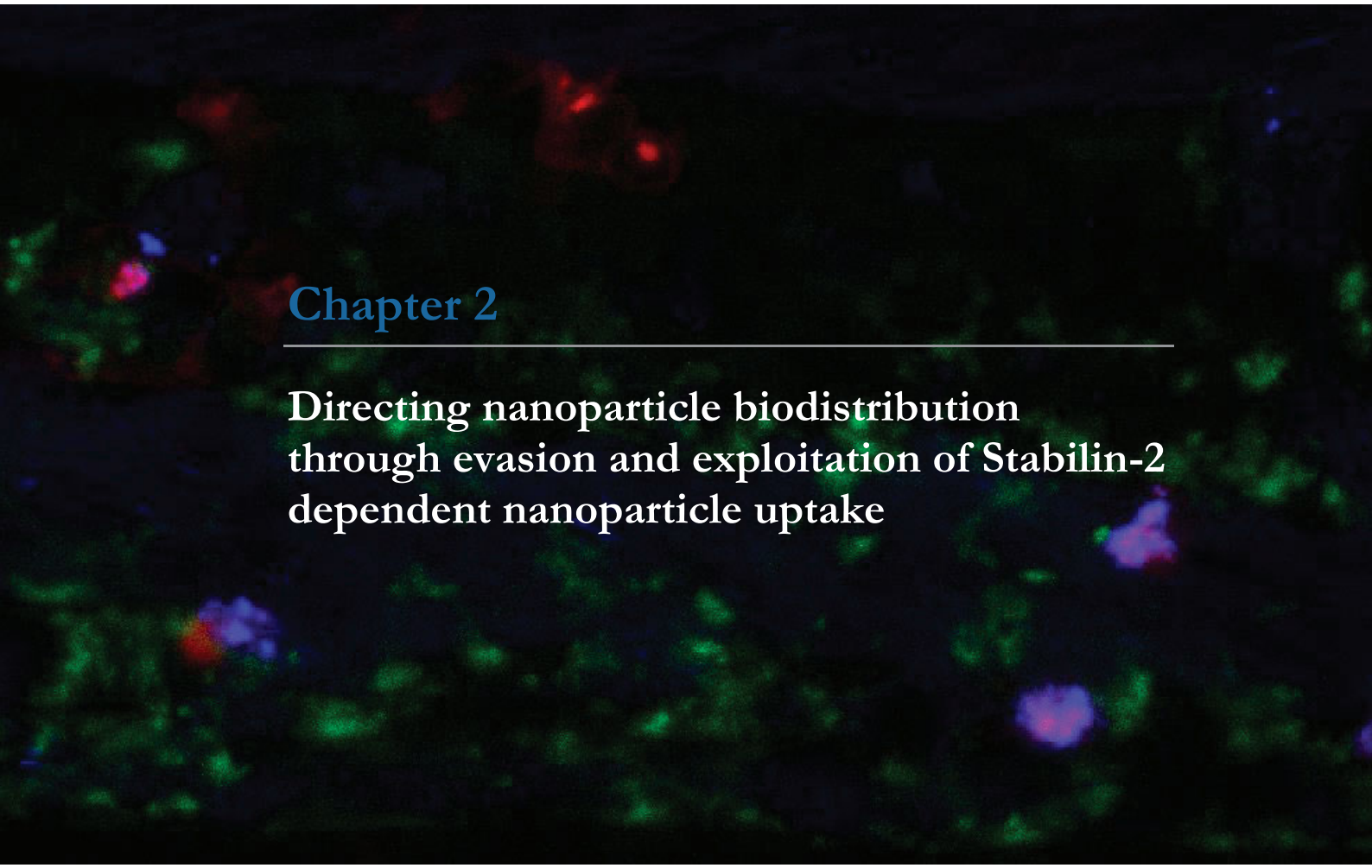

Chapter 2

Directing nanoparticle biodistribution through evasion and exploitation of Stabilin-2 dependent nanoparticle uptake

Published:

Campbell, F.; Bos, F. L*.; Sieber, S*.; **Arias-Alpizar, G***.; Koch, B. E.; Huwyler, J.; Kros, A.; Bussmann, J., Directing Nanoparticle Biodistribution through Evasion and Exploitation of Stab2-Dependent Nanoparticle Uptake. ACS Nano 2018, 12 (3), 2138-2150.

These authors contributed equally*

Image: Scavenging endothelial cells containing fluorescent hyaluronic acid and nanoparticles (blue), phagocytosed by macrophages (red).

2.1 Abstract

Up to 99% of systemically administered nanoparticles are cleared through the liver. Within the liver, most nanoparticles are thought to be sequestered by macrophages (Kupffer cells), although significant nanoparticle interactions with other hepatic cells have also been observed. To achieve effective cell-specific targeting of drugs through nanoparticle encapsulation, improved mechanistic understanding of nanoparticle–liver interactions is required. Here, we show the caudal vein of the embryonic zebrafish (*Danio rerio*) can be used as a model for assessing nanoparticle interactions with mammalian liver sinusoidal (or scavenger) endothelial cells (SECs) and macrophages. We observe that anionic nanoparticles are primarily taken up by SECs and identify an essential requirement for the scavenger receptor, Stabilin-2 (*stab2*) in this process. Importantly, nanoparticle–SEC interactions can be blocked by dextran sulphate, a competitive inhibitor of Stabilin-2 and other scavenger receptors. Finally, we exploit nanoparticle–SEC interactions to demonstrate targeted intracellular drug delivery resulting in the selective deletion of a single blood vessel in the zebrafish embryo. Together, we propose Stabilin-2 inhibition or targeting as a general approach for modifying nanoparticle–liver interactions of a wide range of nanomedicines.

2.2 Introduction

Cell-type specific targeting is a common goal in nanoparticle drug delivery. However, the inability to efficiently target subpopulations of cells, beyond the macrophages and monocytes of the mononuclear phagocyte system (MPS), has stymied progress of these technologies into clinical use.[1-4] Up to 99% of systemically administered nanoparticles, of all shapes, sizes, and chemical compositions are cleared through the liver.[5] While it is generally accepted that nanoparticles are taken up by liver-resident macrophages (Kupffer cells (KCs)),[6] the principal cell type of the MPS in the liver, significant nanoparticle interactions with other hepatic cells, including liver sinusoidal endothelial cells (LSECs), hepatocytes, and hepatic B-cells, have also been observed.[7-10] In these instances however, the cell-specific mechanisms underpinning these interactions have not been elucidated. A detailed understanding of exactly where and how nanoparticles are sequestered and cleared within the liver is crucial for the effective optimization of nanoparticle-mediated drug delivery.

The principle function of the liver is to maintain homeostasis. This includes the removal ("scavenging") of macromolecular and colloidal waste and pathogens from the blood. Within the liver, scavenging function is primarily associated with the hepatic sinusoids,[11] specialized blood vessels connecting the hepatic artery and portal vein (incoming blood flow) with the central vein (outgoing blood flow). In these vessels, scavenging function is facilitated by a >10-fold decrease in blood flow velocity.[12] Hepatic sinusoids are primarily composed of LSECs (~70%) and KCs (~20%).[13] Together these cells comprise the hepatic reticuloendothelial system (RES), a term originally proposed in the early 20th century by Aschoff[14] to include specialized cells that accumulated vital stains. Since then, the term RES has been largely superseded by the MPS, which in the liver sinusoid includes KCs but not LSECs.

Cells with a scavenging function similar to mammalian LSECs have been identified in all vertebrates examined. However, in teleost fish, sharks, and lampreys these cells have not been found in the liver, but are identified in various other organs.[15] Collectively, these cells are known as scavenger endothelial cells (SECs), a specialized endothelial cell type functionally defined as the major clearance site of endogenous macromolecules such as oxidized low-density lipoprotein (oxLDL) and hyaluronic acid (HA) from the blood.[11] Mammalian LSECs have also been implicated in clearance of blood-borne viruses from circulation[16-18] and are important cell-types of both the innate and adaptive immune system.[19, 20] In LSECs, clearance function is mediated through a

relatively small number of pattern-recognition endocytosis receptors.[11] Given the wide variety of macromolecules, colloids, and pathogens sequestered by LSECs, these receptors are clearly promiscuous with respect to potential binding partners. However, what general physicochemical properties direct materials to LSECs, to what extent are individual endocytosis receptors involved, and the significance of these interactions in the clearance of nanoparticles from circulation are not clearly defined.

Here, we show a specific part of the zebrafish embryonic vasculature displays functional homology to the mammalian liver sinusoid and includes macrophages/monocytes and functional SECs. Using this model, we are able to study which general properties of nanoparticles result in their uptake by each of these cell types after intravenous injection. For SECs, we reveal an important molecular mechanism required for nanoparticle clearance, involving the transmembrane receptor Stabilin-2, which can be both inhibited and exploited to guide cell-specific nanoparticle-mediated drug delivery.

2.3 Results

A Zebrafish Model for Liposome Biodistribution

Of the myriad nanoparticles reported as potential drug delivery vectors, liposomes are the most widely investigated and the major class of nanoparticles approved for clinical use.[21, 22] So far, the ability to predict the fate of liposomes following intravenous injection based on lipid composition alone has been limited. Furthermore, the opacity of mammalian models precludes comprehensive assessment of the dynamic behavior of liposomes *in vivo*. Recent studies have shown that the small and transparent zebrafish embryo allows for the direct observation of circulating nanoparticles, including liposomes, and their interactions with cells.[23-26] These studies show key aspects of nanoparticle behavior, including uptake by the MPS, are conserved between zebrafish and mammals. We therefore selected this model to identify the influence of lipid composition on liposome biodistribution and the mechanisms of liposome uptake by cells.

Three liposome formulations, either approved for clinical use or under development (Myocet, EndoTAG-1, and AmBisome),[27-29] were initially selected for intravenous injection into zebrafish embryos. These formulations were specifically chosen to assess the influence of contrasting nanoparticle surface

charge. Myocet is a neutral liposomal-doxorubicin formulation showing extravasation in tumors.[27] EndoTAG-1 is a positively charged liposomal-paclitaxel formulation targeting actively growing tumor blood vessels.[29] AmBisome is a negatively charged liposomal-amphotericin B formulation used to treat severe fungal infections.[28] Fluorescently labeled liposomes (~100 nm in diameter and without encapsulated drugs) based on the lipid composition of these formulations (**Supplementary Table 1**) were injected intravenously into the duct of Cuvier of zebrafish embryos at 54 h post-fertilization (hpf), a stage at which most organ systems are established. Injected embryos were imaged using confocal microscopy at 1, 8, 24, and 48 h post-injection (hpi) (**Figure 1a**), and confocal micrographs were generated for the entire embryo (whole organism level) as well as from a region caudal to the cloaca (tissue level) (**Figure 1b,d** and **Supplementary Figure 1**). We developed a quantification method to compare levels of circulating liposomes, extravasation, and accumulation in different blood vessel types between formulations (**Figure 1c,e–h** and **Supplementary Figure 2**). At 1 hpi, on a whole organism level, all three liposome were found associated with the blood vasculature and over time, the fluorescence associated with freely circulating liposomes within the lumen of the dorsal aorta, decayed exponentially (**Figure 1b,e**). At the tissue level however, clear differences in liposome biodistribution were observed (**Figure 1d**). Consistent with their behavior in mammals, neutral Myocet liposomes were mostly seen circulating within the blood vessel lumen. At 1 hpi, liposome translocation through the vessel wall (extravasation) was already evident, and between 1 and 8 hpi, co-localization with plasma-exposed macrophages was observed (**Figure 1d,g** and **Supplementary Figure 3**). Increasing the size of Myocet liposomes resulted in enhanced uptake by macrophages, whereas surface PEGylation—a strategy widely employed to limit nanoparticle clearance *in vivo*[30]—effectively inhibited phagocytotic uptake as described previously (**Supplementary Figure 3**).[23, 26]

For EndoTAG-1 and AmBisome, a large fraction of the injected dose was removed from circulation by 1 hpi and 8 hpi respectively, and these formulations were found associated with the vessel wall (**Figure 1e,h**). Strikingly however, anionic AmBisome liposomes associated only with ECs of a subset of blood vessels, namely the caudal vein (CV), the posterior and common cardinal veins (PCV and CCV), and the primary head sinus (PHS) as well as ECs within the caudal hematopoietic tissue (CHT-ECs) (**Figure 1d,f–h**).[31] These comprise the majority of venous ECs within the zebrafish embryo at this developmental stage.[32] Cationic EndoTAG-1 liposomes at 1 hpi associated with all ECs as expected[33] but at later time points remain associated only with venous ECs. AmBisome,

EndoTAG-1, and Myocet are each composed of various mixtures of (phospho)lipids and cholesterol. In these cases, lipid headgroup chemistries, fatty acid chain saturation and cholesterol content, will together combine to affect the overall physicochemical character of the formulated liposomes and consequently their *in vivo* fate.

To limit potential variation in liposome membrane composition, we next formulated and injected ~100 nm liposomes composed of the individual (phospho)lipids constituting AmBisome, EndoTAG-1, and Myocet (**Supplementary Figure 4** and **Table 1**). We also included liposomes composed of 1,2-dioleoyl-*sn*-glycero-3-phospho-(1′-*rac*-glycerol) (DOPG) and 1,2-dioleoyl-*sn*-glycero-3-phosphocholine (DOPC). In these experiments, injected cationic liposomes (measured zeta potential; >30 mV) initially associated with both arterial and venous ECs of the embryonic fish. All anionic liposomes (<−30 mV) associated with venous ECs alone, and the behavior of neutral liposomes was dependent on lipid fatty acid chain saturation, whereby "fluid" liposome membranes (*e.g.* DOPC), rich in unsaturated lipids, are freely circulating, whereas those composed of 'rigid', saturated lipids (*e.g.* 1,2-distearoyl-*sn*-glycero-3-phosphocholine (DSPC)) associated with venous ECs. Of these, liposomes composed of DSPC and DOPG associated with venous ECs of the CCV, PHS, PCV, CHT, and CV most strongly (**Figure 1i**, and **Supplementary Figure 4a,d**). Both these liposomes also accumulated in macrophages within the CHT and along the CCV (**Supplementary Figure 5**). Differential distribution of nanoparticles over blood vessel networks has previously been attributed to differences in flow patterns.[9, 25] However, when injections were performed in 4 day-old zebrafish embryos, both DOPG and DSPC liposomes preferentially associated with only a subset of venous ECs along the dorsal side of the PCV (dPCV) (**Figure 1j**). Liposome association with a subset of ECs in a single, straight blood vessel (where flow patterns are expected to be similar throughout) indicated dPCV ECs are a cell type distinct from ventral PCV (vPCV) ECs. Indeed, differentiation of dPCV and vPCV ECs has previously been observed during the induction of lymphatic differentiation and subintestinal vein angiogenesis,[34, 35] suggesting dPCV differentiation may lead to the expression of specific receptors by these ECs which in turn could mediate the selective binding of DOPG and DSPC liposomes.

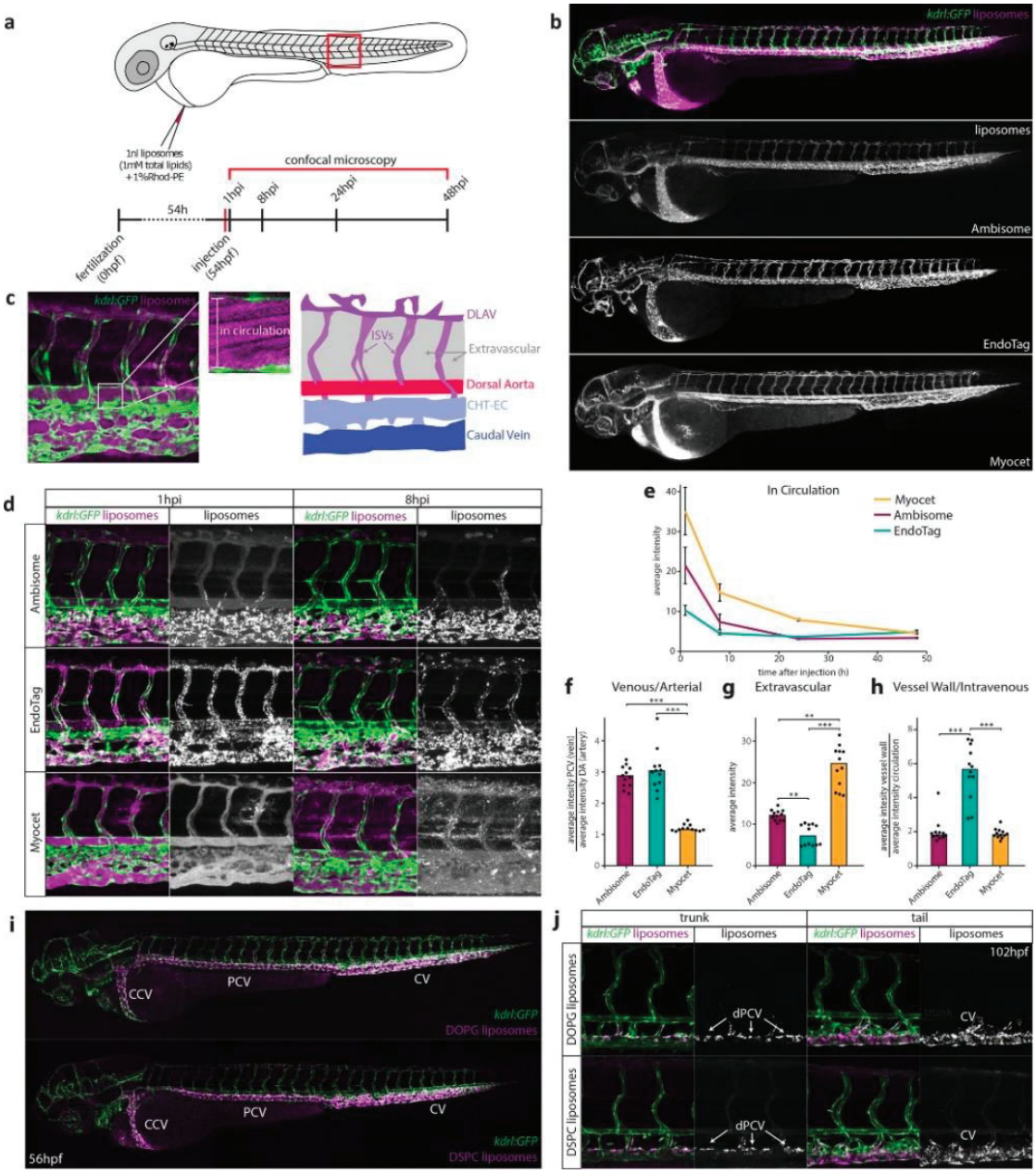

Figure 1. A zebrafish model for liposome biodistribution. (a) Schematic of liposome injection and quantification in zebrafish. Fluorescently labeled liposomes (1 mM total lipids containing 1 mol % Rhod-PE) were injected into the duct of Cuvier at 54 hpf. Confocal microscopy is performed in a defined region (boxed) caudal to the yolk extension at 1, 8, 24, and 48 h after injection. **(b)** Whole-embryo view of liposome distribution in *kdrl*:GFP transgenic embryos, 1 hpi with three different liposome formulations (AmBisome, EndoTAG-1, and Myocet). **(c)** High-resolution imaging allows quantification of liposomes in circulation (measured in the lumen of the dorsal aorta (white box)) and liposome association with different blood vessel types (see Supporting Information). CHT-EC: caudal hematopoietic tissue endothelial cells, DLAV: dorsal longitudinal anastomotic vessel. ISV: intersegmental vessel. **(d)** Tissue level view of liposome distribution in *kdrl*:GFP transgenic embryos, 1 h and 8 h after injection with three different liposome formulations and a single confocal section through the dorsal aorta

(DA) at 1 h after injection. **(e)** Quantification of liposome levels in circulation based on mean rhodamine fluorescence intensity in the lumen of the dorsal aorta at 1, 8, 24, and 48 h after injection (error bars: standard deviation.) n = 6 individually injected embryos per formulation per time point (in two experiments). **(f)** Quantification of liposome levels associated with venous *vs*. arterial endothelial cells based on rhodamine fluorescence intensity associated with caudal vein (CV) *vs.* DA at 8 h after injection. **(g)** Quantification of extravascular liposome levels based on rhodamine fluorescence intensity outside of the vasculature between the DLAV and DA at 8 h after injection. **(h)** Quantification of liposome levels associated with the vessel wall based on rhodamine fluorescence intensity associated with all endothelial cells relative to rhodamine fluorescence intensity in circulation at 1h after injection. **(f–h)** Bar height represents median values, dots represent individual data points, brackets indicate significantly different values (*: $p < 0.05$, **: $p < 0.01$, ***: $p < 0.001$) based on Kruskal–Wallis and Dunn's tests with Bonferroni correction for multiple testing. n=12 individually injected embryos per group (in 2 experiments). **(i)** Whole-embryo view of liposome distribution in *kdrl*:GFP transgenic embryos, 1 h after injection with DOPG and DSPC liposomes. Liposome accumulation for both formulations is observed in the primitive head sinus (PHS), common cardinal vein (CCV), posterior cardinal vein (PCV), and caudal vein (CV). **(j)** Tissue level view of liposome distribution in *kdrl*:GFP transgenic embryos, 1 h after injection with DOPG and DSPC liposomes at 102 hpf. Liposome accumulation is observed in the entire caudal vein (CV), but only on the dorsal side of the PCV (dPCV, arrows).

Identification of a Zebrafish EC Type Homologous to Mammalian LSECs

Selective association of liposomes with most venous ECs has not been observed in adult mammals. However, we hypothesized a more restricted subset of ECs in mammals could be functionally related to venous ECs of the embryonic zebrafish. To test this hypothesis, DOPG liposomes were injected intravenously into Tie2:GFP+ adult mice. In these mice, liposomes were removed from circulation within 1 hpi, and a striking accumulation was observed in the liver (**Figure 2a**). Within the liver, liposomes associated with Tie2:GFP+ sinusoidal ECs and with cells identified as KCs based on cell shape and intravascular localization (**Figure 2b**). No liposome accumulation was observed in hepatocytes or other analyzed organs. This suggested venous ECs and macrophages within the CHT and CV of the embryonic zebrafish were functionally homologous to LSECs and KCs of the mammalian liver and comprise the RES in zebrafish embryos. To confirm this, we injected colloidal lithium carmine (Li-Car), the most prominent vital stain originally used to define the mammalian RES, into zebrafish embryos. Making use of the inherent fluorescence of carminic acid,[36] we observed accumulation of this colloid in the same blood vessels (CV, CHT, PCV, and PHS) and subcellular structures within venous ECs and macrophages, in which DOPG and DSPC liposomes also accumulate (**Figure 2c**).

A small number of transmembrane receptors are selectively expressed in mammalian LSECs compared to other blood vascular ECs.[11] These include the scavenger receptors *Stabilin-1* and *-2*[37] and the mannose receptor *Mrc1.* Analysis of the expression patterns of their orthologs (*stab1, stab2* and *mrc1a*) in zebrafish embryos confirmed their restricted expression in venous ECs of the PHS, PCV, CHT, and CV as described previously.[38, 39] Importantly, expression of these genes becomes enriched in the dPCV, matching observed EC binding specificities of both DOPG and DSPC liposomes (**Supplementary Figure 6**). LSECs mediate the scavenging of macromolecular waste including oxLDL and HA through receptor-mediated endocytosis.[40] Therefore, we injected fluorescently labeled oxLDL and HA (fluoHA) and observed their rapid endocytosis, within the same subset of venous ECs (within the PHS, CCV, (d)PCV, and CV) (**Figure 2d,f**). Based on the conserved uptake of DOPG liposome, oxLDL, fluoHA, and Li-Car from circulation and expression of known LSEC markers by this venous EC subset in zebrafish embryos, we define them as SECs - homologous to mammalian LSECs. In contrast to DSPC and DOPG liposomes and to oxLDL, fluoHA uptake was specific to SECs, and no uptake was observed in macrophages (**Figure 2g**).

We next used fluoHA as a marker for endocytosis in SECs. Co-injection of fluoHA with DSPC or DOPG liposomes resulted in precise intracellular co-localization in all SECs of the embryonic fish, while in macrophages only liposome internalization was observed (**Figure 2h**, and **Supplementary Figure 7**). Intracellular co-localization in LSECs (but not KCs) of fluoHA and DOPG liposomes was conserved in the adult mouse liver (**Figure 2i**). These results demonstrated fluoHA endocytosis is a selective vital marker for SECs in vertebrates and offered a convenient method to study SEC differentiation in the developing zebrafish embryo (**Supplementary Figure 8**). Importantly, we found SECs were present at the earliest time point at which intravenous injection is possible (28 hpf). During embryonic and larval stages, SECs were maintained within the CV, but starting at 52 hpf became gradually restricted to the dPCV. No fluoHA uptake was observed in embryonic veins that develop during later stages, such as in the brain and subintestinal vasculature. These results show that SECs are one of the first EC subtypes to emerge during embryonic development and provide the first analysis of early embryonic SEC differentiation in any vertebrate.

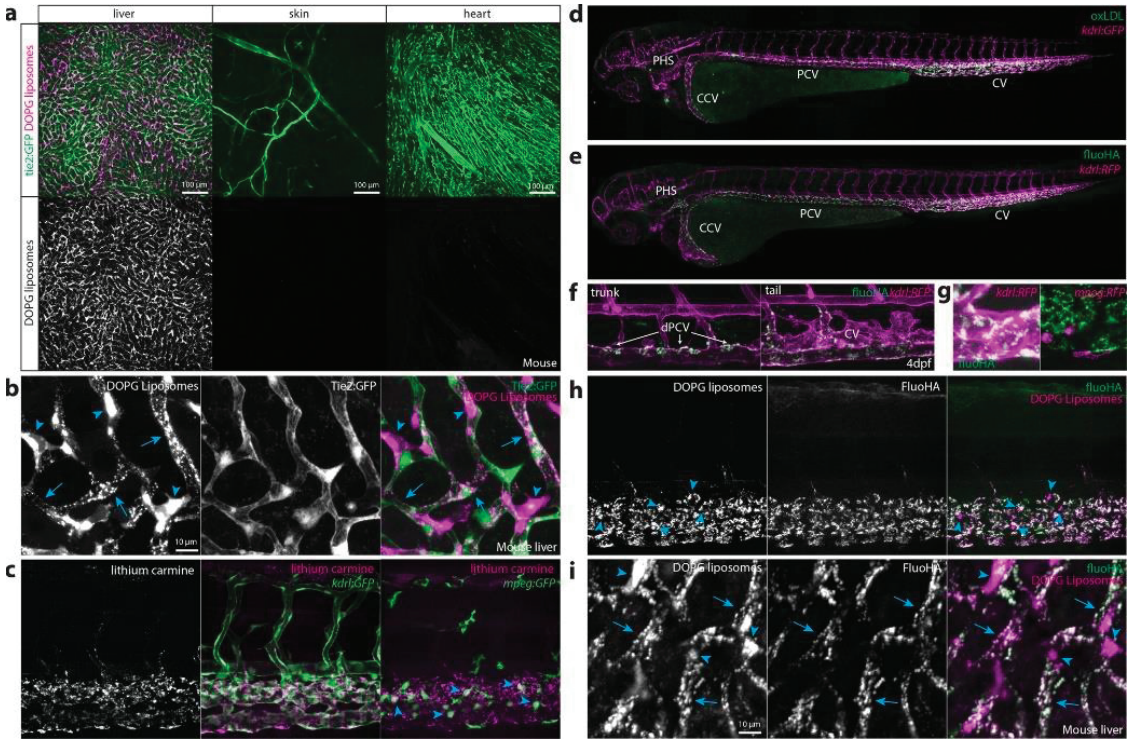

Figure 2. Identification of scavenger endothelial cells (SECs) in zebrafish embryos. **(a, b)** *Ex vivo* imaging of adult *Tie2*:GFP transgenic mouse organs, 1 h after injection with DOPG liposomes. **(a)** Liposome accumulation is observed in liver, but not in the ear skin or heart muscle. **(b)** Within the liver, DOPG liposomes are observed as punctae within *Tie2*:GFP+ sinusoidal ECs (arrows) as well as sinusoid-associated cells which based on shape and position were identified as KCs (arrowheads). **(c)** Tissue level view of lithium carmine distribution in *kdrl*:GFP and *mpeg*:GFP transgenic zebrafish embryos, 1 h after injection. Lithium carmine (carminic acid) fluorescence co-localizes both with kdrl:GFP+ endothelial cells in the caudal vein and *mpeg*:GFP+ monocytes/macrophages (arrowheads) within the CHT. **(d)** Whole-embryo view of fluorescent oxLDL distribution in *kdrl*:GFP transgenic embryos, 1 h after injection. Accumulation of oxLDL is observed in the PHS, CCV, PCV, and CV. **(e)** Whole-embryo view of fluoHA distribution in *kdrl:*RFP transgenic embryos, 1 h after injection. Accumulation of fluoHA is observed in the PHS, CCV, PCV, and CV. **(f)** Tissue level view of fluoHA distribution in *kdrl*:RFP transgenic embryos, 1 h after injection at 102 hpf. FluoHA accumulation is observed in the entire caudal vein (CV), but only on the dorsal side of the PCV (dPCV, arrows). **(g)** Tissue level view of fluoHA in *kdrl*:RFP and *mpeg*:RFP transgenic embryos. Co-localization of RFP expression and fluoHA is observed only within *kdrl:*RFP endothelial cells, but not *mpeg:*RFP monocytes/macrophages. **(h)** Tissue level view of co-injected fluoHA and DOPG liposomes, 1 h after injection reveals co-localization in SECs. Monocytes/ macrophages (arrowheads) take up DOPG but not fluoHA. **(i)** *Ex vivo* imaging of adult mouse liver, 1 h after injection with fluoHA and DOPG liposomes reveals widespread co-localization within sinusoidal ECs (arrows). KCs (arrowheads) take up DOPG liposomes only.

Stabilin-2 Is Required for Uptake of Liposomes and Other Nanoparticles by SECs

The precise intracellular co-localization of fluoHA with DOPG and DSPC liposomes in SECs indicated the use of a shared receptor for endocytosis. Importantly, one of the markers for SECs in zebrafish embryos and adult mammals, Stabilin-2, has been identified as the main HA clearance receptor in the mouse liver.[40]-*In vitro,* Stabilin-2 and its paralog Stabilin-1 have been shown to bind to a large variety of endogenous (mostly anionic) macromolecules[41] as well as phosphothiorate-modified antisense oligonucleotides (PS-ASO),[42] apoptotic cell bodies,[43] biotinylated albumin,[44] and carbon nanotubes.[45] *In vivo*, Stabilin-1 and Stabilin-2 were shown to mediate sequestration (but not uptake) by LSECs of aged erythrocytes in a phosphatidylserine-dependent manner.[46] Stabilin-1 and Stabilin-2 are both nonessential genes for development and normal physiology in mice, with mice lacking both Stabilin-1 and Stabilin-2 displaying deficient removal of nephrotoxic macromolecules from circulation.[37]

To test if stabilins were involved in liposome uptake by SECs, embryos were first pretreated with dextran sulfate - a competitive inhibitor of scavenger receptors, including *stab1* and *stab2*.[47, 48] Subsequent liposome injection (or co-injection) resulted in a striking loss of liposome uptake by SECs, offset by an increase in circulating liposomes, and particularly in the case of DOPG liposomes, an increase in macrophage uptake (**Figure 3a,b**). In contrast, injection of mannan, a competitive inhibitor of *mrc1a*,[49] did not inhibit liposome uptake by SECs (data not shown). To identify the specific role of *stab1* and *stab2* in liposome uptake, mutants for both genes were generated through CRISPR/Cas9-mediated mutagenesis. Here, we report the analysis of a *stab2* mutant line, in which we identified a 4nt deletion (*stab2*^{ibl2}), leading to a frameshift in the *stab2* coding sequence and a premature stop codon (C233X) (**Figure 3c** and **Supplementary Figure 9**). This mutation is predicted to remove most conserved *stab2* domains including all fasiclin domains, the HA binding Link domain, and the transmembrane and cytoplasmic segments. Homozygous *stab2*^{ibl2} mutants displayed a strong reduction of *stab2*, but not of *stab1* or *mrc1a,* mRNA expression indicating normal SEC differentiation and nonsense-mediated decay of *stab2*^{ibl2} mRNA (**Supplementary Figure 10**). *Stab2*^{ibl2} mutants survived throughout embryonic development without defects in either blood or lymphatic vascular systems, which were described previously for *stab2* morphants,[50, 51] and fertile adults were identified in normal Mendelian ratios (**Figure 3d,e**). Consistent with the increase in circulating HA levels observed in mouse Stab2 knockouts,[52] a complete loss of fluoHA uptake by SECs was observed in zebrafish

stab2^{ibl2} mutants, showing a conserved role for *stab2* in HA clearance in vertebrates (**Figure 3f**). Importantly, when either DOPG or DSPC liposomes were injected in *stab2*^{ibl2} mutants, a strong reduction of liposome endocytosis by SECs was observed, offset by an increase in circulating liposome levels and an increase in macrophage uptake (**Figure 3g,h**). Differential liposome uptake in neighboring venous ECs of embryos with a mosaic loss of *stab2* function indicated a cell-autonomous role of *stab2* function in liposome uptake by SECs (**Supplementary Figure 11**). For the original three liposome formulations screened, loss of *stab2* function affected AmBisome, but not Myocet or EndoTAG-1 biodistribution (**Figure 3i,k**). Since both AmBisome and EndoTAG-1 accumulated within SECs of wild-type embryos, *stab2*-mediated uptake by SECs appears dependent on specific physicochemical properties of liposomes and *stab2* does not function in the clearance of cationic liposomes.

In vivo, several other scavenger receptors with similar binding profiles to *stab2* are expressed,[11] not only on SECs but also on other endothelial cells and macrophages. Given the significant increase in circulating DOPG, DSPC, and AmBisome liposomes in *stab2*^{ibl2} mutants, *stab2* clearly plays a dominant role in removal of these liposomes from circulation compared to other scavenger receptors (including the structurally related *stab1*). Similarly, clearance of PS-ASOs was recently shown to be dominated by Stab2 in the mouse liver.[42] To test the generality of *stab2* function, several other polyanionic nanoparticles were injected in wild-type and *stab2*^{ibl2} mutant embryos as well as following dextran sulfate injection (**Figure 4a-l**). These included endogenous (DOPS liposomes, a model for apoptotic cell fragments), viral (Cowpea Chlorotic Mottle Virus-like particles, CCMV VLPs),[53] polymeric (polymersomes[54] and polystyrene beads), and inorganic (quantum dots, QDs) nanoparticles. All of these particles were endocytosed selectively by SECs in zebrafish embryos, and in all cases SEC endocytosis could be inhibited by dextran sulfate. However, not all nanoparticles were dependent on *stab2* for SEC endocytosis.

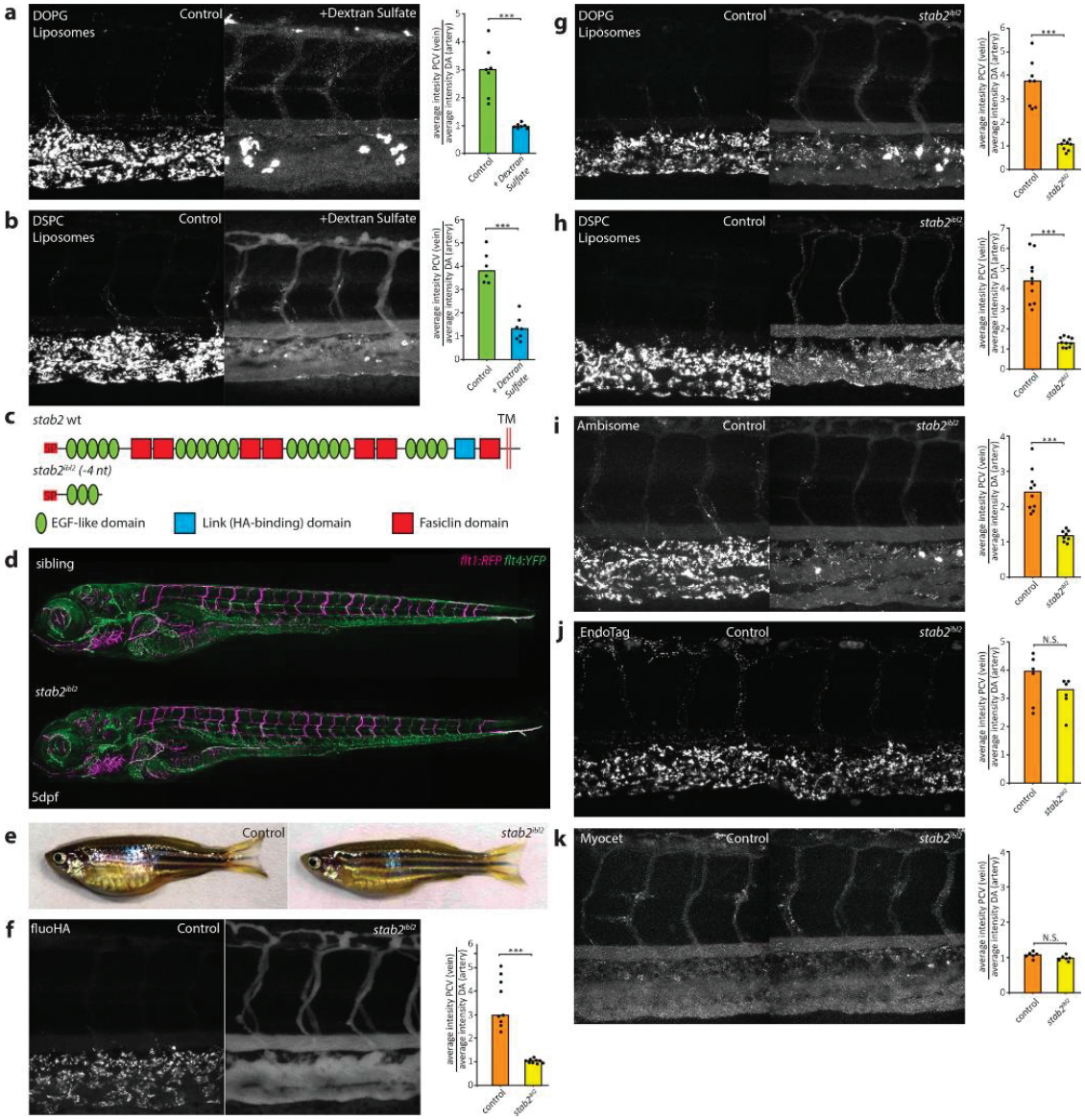

Figure 3. Stabilin-2 is required for anionic liposome uptake by SECs. **(a, b)** Tissue level view of DOPG and DSPC liposome distribution at 1 hpi in control and dextran sulfate injected embryos, with quantification of liposome levels associated with venous *vs*. arterial endothelial cells (ECs) based on rhodamine fluorescence intensity associated with CV *vs*. DA**. (c)** *stab2* domain structure predicted to be expressed from the wild-type *stab2* and the *stab2*^{ibl2} allele. **(d)** Whole-embryo view of *flt1*:RFP, *flt4:*YFP double transgenic embryos at 5 dpf to visualize blood vascular and lymphatic development. No defects were identified during (lymph)angiogenesis and vascular patterning in *stab2*^{ibl2} homozygous embryos compared to sibling controls**. (e)** Fertile adult females (*stab2*^{ibl2} homozygous and sibling controls) at 3 months post-fertilization. Tissue level view of fluoHA **(f)** DOPG **(g)**, DSPC **(h)**, AmBisome **(i)**, EndoTAG-1 **(j)**, and Myocet **(k)** liposome distribution at 1 hpi in *stab2*^{ibl2} and sibling control embryos, with quantification of liposome levels associated with venous *vs.* arterial ECs based on rhodamine fluorescence intensity associated with CV *vs*. DA. **(a, b, f–k)** Bar height represents median values, dots represent individual data points, and brackets indicate significantly different values (*: p<0.05, **: p<0.01, ***: p<0.001, N.S.: not significant) based on Mann–Whitney test. n=6-10.

Although uptake by SECs of DOPS liposomes, polymersomes, and polystyrene nanoparticles was strongly decreased in *stab2*^{ibl2} mutants, uptake of CCMV VLPs was only partly dependent on Stabilin-2 and QD uptake appeared *stab2*-independent. Alternatively, QD uptake by SECs is also mediated in part by *stab2*, but its function is masked in *stab2*^{ibl2} mutants through redundancy with other scavenger receptors (such as *stab1*) that can be inhibited by dextran sulfate. CCMV VLPs (28 nm) and QDs (<10 nm) were the smallest nanoparticles screened in this study, suggesting size may be an important determinant of scavenger receptor–nanoparticle interactions.

Targeted Liposomal Drug Delivery to SECs

Finally, to demonstrate we could extend the observed interaction of nanoparticles with SECs to cell-selective drug delivery, we encapsulated a model drug, clodronic acid, within DSPC liposomes (**Supplementary Table S2**). Clodronic acid requires active transport (endocytosis or phagocytosis) across the target cell membrane to illicit a cytotoxic effect.[55] Liposome-mediated intracellular delivery of clodronic acid into monocytes/macrophages is used extensively as a research tool to selectively remove these cell populations *in vivo*.[56] After 12–24 hpi, synchronous changes in the morphology of the CHT and caudal vein ECs were observed, followed by a gradual loss of *kdrl:*GFP endothelial cells or cell fragments and ultimately leading to the complete disappearance of the caudal vein between 24 and 48 hpi (**Figure 5a-d)**, The PCV and other cell types within the CHT, including *mpeg:*GFP macrophages (most of which are not exposed to circulating nanoparticles) as well as *mpx:*GFP neutrophils, were largely unaffected (**Supplementary Figure 12**). Injection of free clodronic acid (a control demonstrating the requirement of liposomal encapsulation) did not result in any observable changes to the venous endothelium. Similarly, injection of freely circulating DOPC-clodronic acid liposomes (a control demonstrating the requirement of selective nanoparticle uptake by SECs) did not affect the venous endothelium. The development of the dorsal aorta was unaffected by deletion of the CV and CHT, and blood supply to the caudal parts of the embryo was maintained through a rerouting of blood cells into the intersegmental vessels and dorsal longitudinal anastomotic vessel (DLAV). Embryos with a complete loss of the CV and CHT endothelial cells were agile and could survive at least until 6 dpf. Imaging of fluorescent DSPC-clodronic acid liposomes revealed selective *stab2*-dependent uptake by SECs analogous to empty DSPC liposomes (**Figure 5e**). Importantly, loss of *stab2* function as observed in *stab2*^{ibl2} mutant embryos

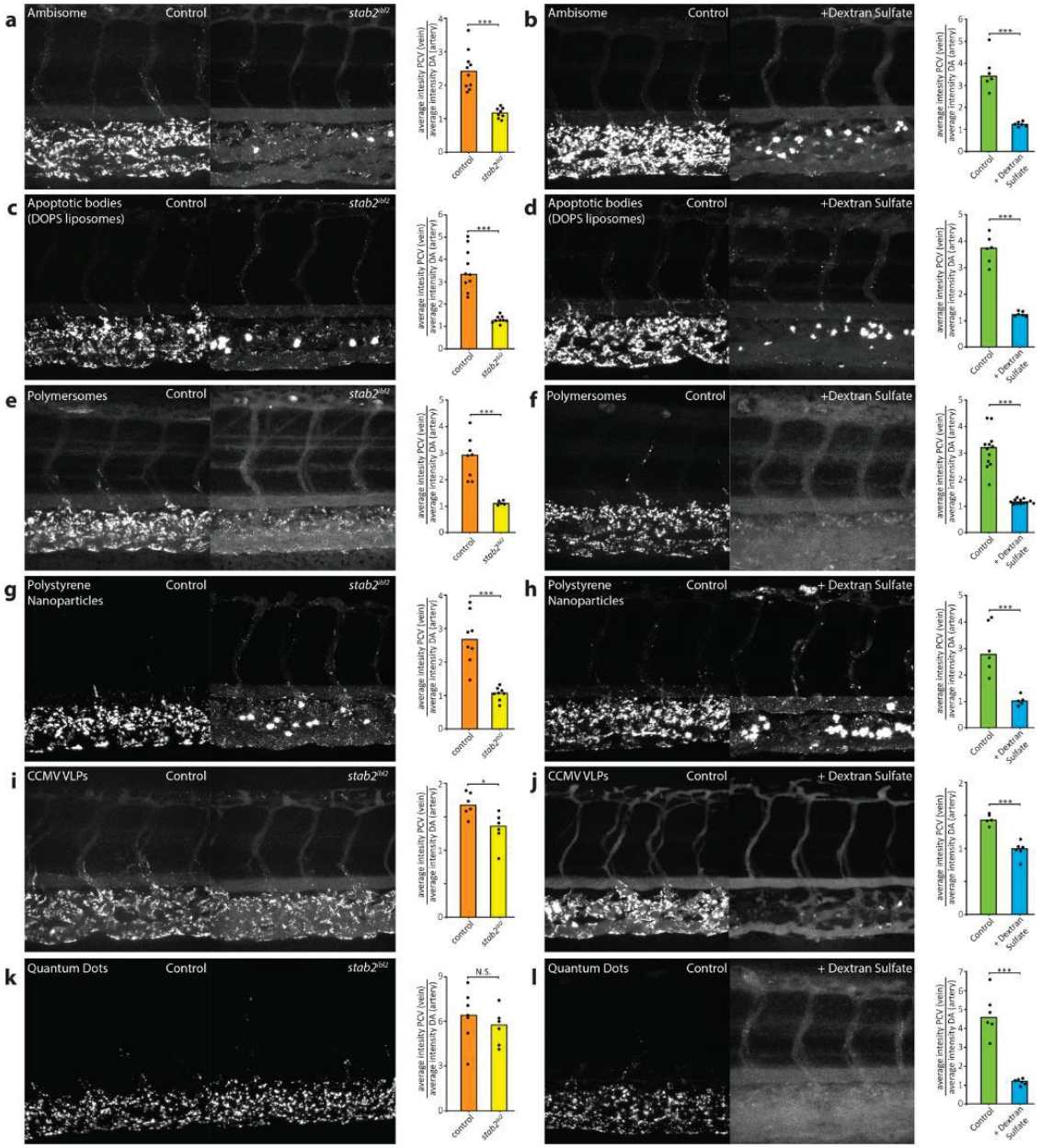

Figure 4. *stab2*-mediated scavenging of anionic nanoparticles *in vivo*. (a–i) Tissue level view of DOPS liposome **(a, b)**, PIB-PEG polymersome **(c, d)**, carboxylated polystyrene nanoparticle **(e, f)**, CCMV virus-like particle **(g, h)**, and carboxylated quantum dot **(i, j)** distribution at 1 hpi in *stab2*^{ibl2} and sibling control embryos **(a, c, e, g, i)** or control and dextran sulfate injected embryos **(b, d, f, h, j)**. Quantification of nanoparticle levels associated with venous vs arterial endothelial cells based on rhodamine fluorescence intensity associated with caudal vein vs DA. **(a–j)** Bar height represents median values, dots represent individual data points, and brackets indicate significantly different values (*: $p < 0.05$, **: $p < 0.01$, ***: $p < 0.001$, N.S.: not significant) based on Mann–Whitney test. n = 5–12 per group (in two experiments).

rescued the CV phenotype induced by injection of DSPC-clodronic acid liposomes (**Figure 5f-h**). These results identify Stabilin-2-mediated uptake of liposomes by SECs as a simple strategy for intracellular compound delivery to this cell type in zebrafish embryos.

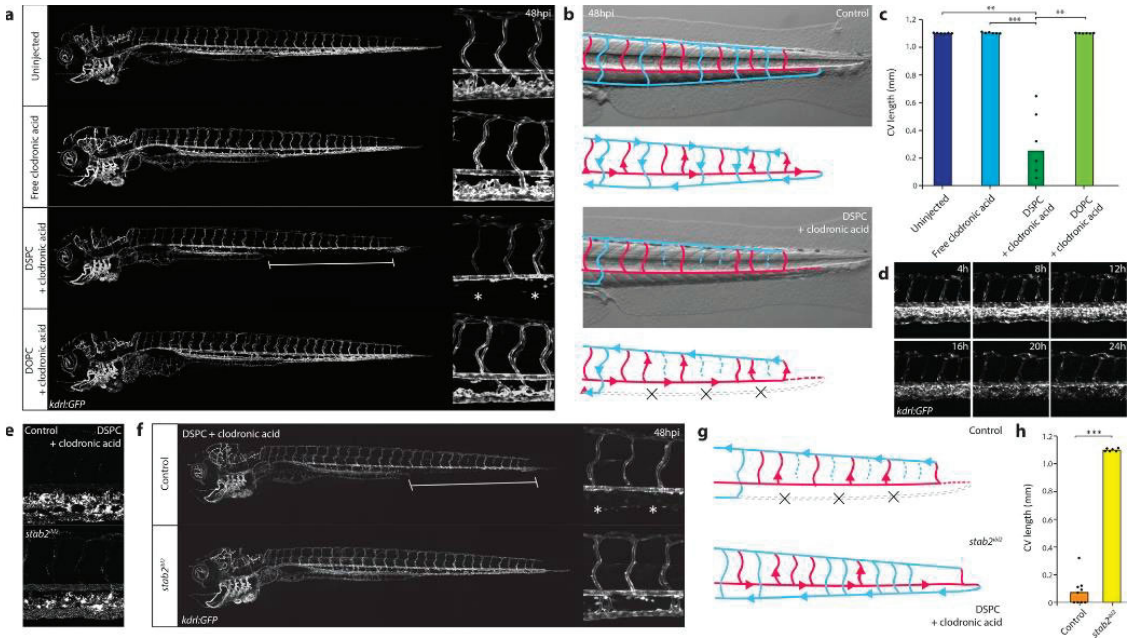

Figure 5. Nanoparticle-mediated SEC deletion. (a) Whole-embryo and tissue level views at 48 hpi of the blood vasculature in *kdrl:*GFP transgenic control embryos, embryos injected with 1 mg/mL clodronic acid, or embryos injected with liposomes containing 1 mg/mL clodronic acid (DSPC or DOPC liposomes). Complete deletion of the caudal vein is observed in embryos injected with DSPC liposomes containing clodronic acid (brackets and asterisks). **(b)** Schematic representation of blood flow in control embryos or embryos injected with DSPC liposomes containing 1 mg/mL clodronic acid. Blue indicates venous or capillary blood vessels, and red indicates arterial blood vessels. Arrowheads indicate direction of blood flow. The removal of the CV (dashed lines) leads to a rerouting of blood flow through the DLAV**. (c)** Quantification of PCV length in injected embryos. Bar height represents median values, dots represent individual data points, and brackets indicate significant values (**: $p < 0.01$, ***: $p < 0.001$) based on Kruskal–Wallis and Dunn's tests with Bonferroni correction for multiple testing. n = 6 individually injected embryos per group (in two experiments). **(d)** Progression of SEC deletion. Individual frames from Movie S2 in https://pubs.acs.org/doi/abs/10.1021/acsnano.7b06995, at indicated time points after injection of DSPC liposomes containing 1 mg/mL clodronic acid, injected into *kdrl:*GFP transgenic embryos. SEC fragmentation in this case is observed mostly between 12 hpi and 16 hpi, followed by a gradual loss of fluorescence or removal of cellular debris. **(e)** Tissue level view of distribution of DSPC liposomes containing 1 mg/mL clodronic acid at 1 hpi in *stab2*^{ibl2} and sibling control embryos. **(f)** Whole-embryo and tissue level views at 48 hpi of the blood vasculature in *kdrl*:GFP transgenic *stab2*^{ibl2} and sibling embryos. Embryos were injected with DSPC liposomes containing 1 mg/mL clodronic acid. Complete deletion of the caudal vein is observed in sibling control (brackets and asterisks), but not *stab2*^{ibl2} mutant embryos. **(g)** Schematic representation of blood flow in sibling control embryos or stab2ibl2 homozygous mutants, both injected with DSPC

liposomes containing approximately 1 mg/mL clodronic acid. Blue indicates venous or capillary blood vessels, and red indicates arterial blood vessels. Arrowheads indicate direction of blood flow (based on observations from Movie S3, that can be found in https://pubs.acs.org/doi/abs/10.1021/acsnano.7b06995). The removal of the CV (dashed lines) leads to a rerouting of blood flow through the DLAV in control embryos but not in *stab2*^{ibl2} homozygous mutants. **(h)** Quantification of PCV length in injected embryos. Bar height represents median values, dots represent individual data points, and brackets indicate significant values (***: $p < 0.001$) based on Mann–Whitney test.

2.4 Discussion and Conclusion

We show Stabilin-2 is an important (scavenger) receptor mediating the uptake of circulating nanoparticles by SECs. In particular, anionic nanoparticles, between 50 and 250 nm in size, are avidly taken up by SECs in a *stab2*-dependent fashion. Here, binding and uptake appear independent of material and functional properties of nanoparticles and are solely dependent on surface charge. Given the comparable sizes and surface charge of many blood-borne viruses,[16-18, 57] clearance of these circulating pathogens by LSECs is also potentially mediated by *stab2*. These findings, combined with the high expression of *stab2* by LSECs within the mammalian liver,[11] implicate SECs as an important cell-type in the binding, uptake, and clearance of administered nanoparticles. As such, we support the re-adoption of the RES, over the MPS, as the most accurate term to describe the specialized cellular components involved in nanoparticle clearance from circulation.[58]

The ultimate goal of many nanoparticle-based technologies is cell-type-specific targeting. Yet reported targeting efficiencies rarely surpass 1% of the total injected nanoparticle dose.[4] A major contributing factor has been off-target nanoparticle interactions within the mammalian liver.[5] By revealing the molecular basis of nanoparticle interactions with specific cells of the embryonic zebrafish, we have been able to demonstrate nanoparticle targeting of, and drug delivery to, specific cell types with homologues in the mammalian liver. In addition, we show these interactions can be effectively inhibited by dextran sulfate. As *stab2* is not essential for normal adult physiology,[37] this offers a simple method to extend circulation lifetimes of nanoparticles by minimizing potential off-target liver interactions.[59] This will likely be particularly beneficial in instances where active targeting of nanoparticles to cell types beyond the liver (*e.g.* cancer cells) is desired.

Importantly, the SEC/selective drug delivery we describe has not resulted from adding further complexity to nanoparticle designs. Instead, through systematic

screening of "simple" nanoparticles (*i.e.* liposomes composed of a single phospholipid), we have established what general properties and molecular mechanisms direct nanoparticles to specific cell types. The use of the embryonic zebrafish as a model organism, and the ability to visualize nanoparticle–cell interactions at high resolution in living organisms, has been essential in this process. We therefore propose that the embryonic zebrafish, with its established extensive genetic toolkit, is a valuable preclinical *in vivo* model allowing screening, optimization, and mechanistic understanding of nanoparticle biodistribution, predictive of their behavior in mammals.[26]

2.5 Materials and Methods

Reagents

Fluorescein-labeled hyaluronic acid (fluoHA) was prepared through conjugation of hyaluronic acid (100 kDa) with fluorescein isothiocyanate (Isomer I, Sigma-Aldrich) as previously described.[60] Additional fluoHA was provided as a kind gift from W. Jiskoot (Leiden University, The Netherlands). Colloidal Li-Car was prepared as previously described.[61] Rhodamine-loaded polymersomes on polyisobutadiene/ polyethylene glycol (PIB/PEG) block copolymers[54] were a kind gift from S. Askes and S. Bonnet (Leiden University, The Netherlands). Atto-647 labeled CCMV-virus-like particles (t = 3, 28 nm)[53] were a kind gift from M. de Ruiter and J. Cornelissen (Twente University, The Netherlands). Purchased reagents are described in the Supporting Information.

Liposome Preparation and Characterization

All liposomes (without encapsulated drugs) were formulated in ddH_2O at a total lipid concentration of 1 mM. Individual lipids, as stock solutions (1–10 mM) in chloroform, were combined at the desired molar ratios and dried to a film, first under a stream of N_2 and then >1h under vacuum. With the exception of Myocet 325 and 464 nm, lipid films were hydrated in 1 mL ddH_2O at >65 °C (with gentle vortexing if necessary) to form large/giant multilamellar vesicles. Large unilamellar vesicles were formed through extrusion above the T_m of all lipids (>65 °C, Mini-extruder with heating block, Avanti Polar Lipids, Alabaster, US). Hydrated lipids were passed 11 times through 2 × 400 nm polycarbonate (PC) membranes (Nucleopore Track-Etch membranes, Whatman), followed by 11 times through 2 × 100 nm PC pores. All liposomes were stored at 4 °C. With the exception of DSPC liposomes (significant aggregation after 1 week storage), all

liposomes were stable for at least 1 month. Myocet 325 and 464 nm liposomes were formulated by gentle hydration of lipid films at 35 °C (without vortexing). In the case of 464 nm Myocet liposomes, hydrated lipids were passed through a 800 nm PC membrane 7 times at 35 °C. In the case of 325 nm Myocet liposomes, hydrated lipids were passed through a 400 nm PC membrane 7 times at 35 °C. See **Supporting Information** for nanoparticle characterization methods and **Supplementary Table 1** for all lipid compositions, size, and zeta potentials of nanoparticles used in this study.

Clodronic Acid Encapsulation and Quantification

Lipid films (10 mM total lipids) were hydrated with ddH_2O containing 200 mg/mL^{-1} clodronic acid (1 mL) and formulated through extrusion as described for the corresponding "empty" liposomes. Unencapsulated clodronic acid was removed by size exclusion chromatography (illustra NAP Sephadex G-25 DNA grade premade columns (GE Healthcare) used according to the supplier's instructions). Eluted clodronic acid-encapsulated liposomes were diluted 2.5× during SEC and injected without further dilution. Quantification of encapsulated clodronic acid was determined by UV absorbance as previously reported.[62] Briefly, liposomes were first destroyed through a 1:1 dilution with 1% v/v Triton X-100 solution before further dilution into an acidic $CuSO_4$ solution (1:2.25:2.25; Liposome-Triton X-100 mix: 3 mM HNO_3: 4 mM $CuSO_4$). The concentration of clodronic acid was determined by UV absorbance (Cary 3 Bio UV–vis spectrometer) at 240 nm and quantified against a predetermined calibration curve (50 μM to 2.5 mM clodronic acid). All UV–vis absorbance measurements were taken at room temperature. Blanks were made using liposome solutions without encapsulated clodronic acid but prepared otherwise identically (including SEC procedure). The final encapsulated clodronic acid concentration varied between 0.9 and 1.7 mg mL^{-1} (see **Supplementary Table 2**).

Zebrafish Strains, in Situ Hybridization, and CRISPR/Cas9 Mutagenesis

Zebrafish (*Danio rerio*, strain AB/TL) were maintained and handled according to the guidelines from the Zebrafish Model Organism Database (http://zfin.org) and in compliance with the directives of the local animal welfare committee of Leiden University. Fertilization was performed by natural spawning at the beginning of the light period, and eggs were raised at 28.5 °C in egg water (60 ug/mL Instant Ocean sea salts). The following previously established zebrafish lines were used Tg(*kdrl:*GFP)^{s843},[63] Tg(*kdrl:*RFP-CAAX)^{s916},[38] Tg(*mpeg:*GFP)^{gl22},[64] Tg(*mpeg:*RFP-CAAX)^{ump2},[65] Tg(*flt1*^{enh}*:*RFP)^{hu5333},[66] Tg(*flt4*^{BAC}*:*YFP)^{hu7135},[67] and

Tg(*mpx:*GFP)^{uwm1}.[68] Whole-mount *in situ* hybridization was performed as described.[69]-Supplementary Table 3 lists primers for probe generation. Cloning-free sgRNAs for CRISPR/Cas9 mutagenesis were designed and synthesized as described.[70] sgRNAs (125 pg) and cas9 mRNA (300 pg) were co-injected into single-cell wild-type, albino or *flt4:*YFP*; flt1:*RFP transgenic embryos. Mutagenesis efficacy, founder identification, and genotyping were performed using CRISPR-STAT.[71] The nucleotide sequences and predicted *stab2* amino acid sequences in the *stab2*^{ibl2} line are shown in **Supplementary Figure 11** and **Table 3** for guide RNA sequences and genotyping primers. For mosaic analysis, heterozygous embryos (*stab2*$^{ibl/+}$) obtained from a cross between a *stab2*^{ibl2} homozygous parent and a *kdrl:*GFP (*stab2*$^{+/+}$) parent were co-injected with sgRNAs (125 pg) and cas9 mRNA (300 pg) to create second-hit mutations in the wildtype allele.

Zebrafish Intravenous Injections

Liposomal formulations were injected into 2 day old zebrafish embryos (52–56 hpf) using a modified microangraphy protocol.[72] Embryos were anesthetized in 0.01% tricaine and embedded in 0.4% agarose containing tricaine before injection. To improve reproducibility of microangiography experiments, 1 nl volumes were calibrated and injected into the sinus venosus/duct of Cuvier. We created a small injection space by penetrating the skin with the injection needle and gently pulling the needle back, thereby creating a small pyramidal space in which the liposomes and polymers were injected. Successfully injected embryos were identified through the backward translocation of venous erythrocytes and the absence of damage to the yolk ball, which would reduce the amount of liposomes in circulation. For injections at later stages (>80 hpf), 0.5 nL volumes were injected into the CCV. The following concentrations were injected: dextran sulfate (20 mg/mL), FluoHA (0.2 mg/mL), oxLDL (1 mg/mL), CCMV-VLP (1 mg/mL), QDs (1:25 dilution), lithium carmine (1:50 dilution), polymersomes (1 mg/mL), latex beads (1:10 dilution). Dextran sulfate was injected 20 min prior to nanoparticle injection.

Zebrafish Imaging and Quantification

For each treatment or time point, at least six individual embryos (biological replicates) using at minimum two independently formulated liposome preparations were imaged using confocal microscopy. Embryos were randomly picked from a dish of 20–60 successfully injected embryos (exclusion criteria were: no backward translocation of erythrocytes after injection and/or damage

to the yolk ball). Confocal z-stacks were captured on a Leica TCS SPE confocal microscope, using a 10× air objective (HCX PL FLUOTAR) or a 40× water-immersion objective (HCX APO L). For whole-embryo views, 3–5 overlapping z-stacks were captured to cover the complete embryo. Laser intensity, gain, and offset settings were identical between stacks and sessions. Images were processed and quantified using the Fiji distribution of ImageJ.[73, 74] Quantification (not blinded) of liposome biodistribution was performed on 40× confocal z-stacks (with an optical thickness of 2 µm/slice) as described in the **Supporting Information**.

Mouse Injections and Imaging

All experiments were performed in accordance with the guidelines of the Animal Welfare Committee of the Royal Netherlands Academy of Arts and Sciences, The Netherlands. Tg(*TIE2:*GFP)287Sato/J mice were sedated using isoflurane inhalation anesthesia (1.5–2% isoflurane/O_2 mixture). 100 µL of DOPG liposomes (10 mM DOPG + 1% Rhod-PE) diluted 1:5 in PBS were injected retro-orbitally with an insulin syringe (BD). After 1 h, mice were sacrificed, and organs were harvested and imaged *ex vivo* on glass bottom dishes. Images were taken with a Leica SP8 multiphoton microscope with a chameleon Vision-S (Coherent Inc.), equipped with four HyD detectors: HyD1 (<455 nm), HyD2 (455–490 nm), HyD3 (500–550 nm), and HyD4 (560–650 nm). Different wavelengths between 700 nm and 1150 nm were used for excitation; HA and Rhod-PE were excited with a wavelength of 960/1050 nm and detected in HyD3 and HyD4. All images were in 12 bit and acquired with a 25× (HCX IRAPO N.A. 0.95 WD 2.5 mm) water objective.

Statistical Analysis and Data Availability

Because of small sample sizes, nonparametric tests were used exclusively. For comparisons between two groups, two-tailed Mann–Whitney tests were performed. For comparisons between multiple groups, we used Kruskal–Wallis tests followed by two-tailed Dunn's tests with Bonferroni correction using the PMCMR package in R.[75] No statistical methods were used to predetermine sample size, but group sizes were >5 in order for the null distribution of the Kruskal–Wallis statistic to approximate the X^2 distribution (with k–1 degrees of freedom). With the exception of **Figure 1e**, graphs show all individual data points and the median. Confocal image stacks (raw data) are available from the corresponding authors upon reasonable request.

2.6 Abbreviations

CCMV VLP	cowpea chlorotic mottle virus derived virus-like particles
CHT	caudal hematopoietic tissue
CCV	common cardinal vein
CV	cardinal vein
dPCV	dorsal posterior cardinal vein
dpf	days post fertilization
DA	dorsal aorta
DLAV	dorsal longitudinal anastomotic vessel
DOPC	1,2-dioleoyl-sn-glycero-3-phosphocholine
DOPG	1,2-dioleoyl-*sn*-glycero-3-phospho-(1'-*rac*-glycerol)
DOPS	1,2-dioleoyl-sn-glycero-3phospho-L-serine
DSPC	1,2-distearoyl-*sn*-glycero-3-phosphocholine
DOTAP	1,2-dioleoyl-3-trimethylammonium-propane
ECs	endothelial cells
fluoHA	fluorescently labeled hyaluronic acid
hpi	hour(s) post injection
ISH	*in situ* hybridization
ISV	intersegmental vessels
KCs	Kupffer cells
Li-Car	lithium carmine
LSECs	liver sinusoidal endothelial cells
MPS	mononuclear phagocyte system
OxLDL	oxidized low-density lipoprotein
PCV	posterior cardinal vein
PHS	primitive head sinus
PIB-PEG	polyisobutylene-polyethylene glycol
POPC	1-palmitoyl-2-oleoyl-sn-glycero-3-phosphocholine
PS-ASO	phosphothiorate-modified antisense oligonucleotides
QDs	quantum dots
RES	reticuloendothelial system
SECs	scavenging endothelial cells
vPCV	ventral posterior cardinal vein

2.7 Supporting Information

Supplementary Table 1. Nanoparticle composition, size and zeta potential. For liposomes, size and polydispersity (PDI) ranges correspond to a least three independent formulations, with the exception of:

Formulation	Composition*	Size/nm	PDI	Zeta Potential/mV
Myocet	POPC:Cholesterol (55:45)	114.5 - 122.1	0.04 - 0.06	-15.8
AmBisome	DSPC: DSPG:Cholesterol (53:21:26)	118.8 - 133.7	0.05 - 0.07	-33.7
EndoTAG-1	DOTAP:DOPC (51.5:48.5)	109.6 - 114.3	0.03 - 0.05	+46.0
Myocet (325nm)	POPC:Cholesterol (55:45)	325.4[a]	0.22	-18.6
Myocet (465nm)	POPC:Cholesterol (55:45)	464.5[a]	0.24	-20.0
Myocet + PEG	POPC:Cholesterol:DOPE-mPEG2000 (50:41:9)	100.4 - 118.0	0.05 - 0.06	-11.8
100% DOPC	DOPC	114.8 - 118.4	0.07 - 0.09	-11.3
100% DSPC	DSPC	102.0 - 108.3	0.06 - 0.07	-3.4
100% DOPG	DOPG	114.0 - 121.8	0.03 - 0.07	-37.1
100% DSPG	DSPG	95.4 - 102.9	0.12 - 0.17	-45.9
100% DOTAP	DOTAP	101.8 - 114.8[b]	0.06 - 0.07	+35.6
100% POPC	POPC	108.0 - 111.4	0.07 - 0.08	-17.2
Polymersomes	PIB:PEG (1:0.75 mol ratio)	83.0	0.26	-24.0
Virus-like particles	90 CCMV capsid protein dimers	28.0	ND	-14.9[c]
Quantum Dots	CdSe core:ZnS shelt n-octylamine-modified poly acrylic acid (PnOAm-co-PAA) copolymer cap	≈ 5 x 12 (by TEM)	ND	-70.8
Latex beads	carboxylate-modified polystyrene	121.4	0.02	-51.0
* all lipsome formulations + 1mol% DOPE-LR/+1mol% DOPE-Atto633				

a. The sizes of both 'Myocet 325 nm' and 'Myocet 465 nm' liposomes varied significantly batch to batch.
b. Data for two independent formulations.
c. Zeta potential for unmodified (*i.e.* no conjugated dye) CCMV VLPs (t=3)
b. Data for two independent formulations only.

Supplementary Table 2. Liposome composition, size and encapsulated clodronic acid.

Formulation	Lipid Composition	Size/nm	PDI	Encapsulated Clodronate/ mgmL^{-1}
100% DOPC	DOPC	126.6	0.07	0.9
100% DSPC	DSPC	128.3 - 132.2[a]	0.06 - 0.09	1.21 - 1.72

a. Data for three separate formulations

Supplementary Table 3. Guide RNA sequences and primers.

Gene	Sequences (F: Forward, R: Reverse)
Stabilin1	
sgRNA	TAATACGACTCACTATAGGATCTGATGACTCCATTCCGTTTTAGAGCTAGAAATAGC
Genotyping	**F:** TGTAAAACGACGGCCAGTCACCACCTGTGAACTCATAAGC
	R: GTGTCTTCGTTATCATTCAGGAAACAGCA
In Situ hybridisation	**F:** GAGGTTGCCATGAAGAAGCCGAC
	R: GCAACAACCGAAGCCAAGTCTCC
Stabilin2	
sgRNA	TAATACGACTCACTATAGGCACACACTCCTCAAGCACGTTTTAGAGCTAGAAATAGC
Genotyping	**F:** TGTAAAACGACGGCCAGTCCTTTTTGAACTCACAAATGCTC
	R: GTGTCTTGTCATACACACAGCGGGTAGAG
In Situ hybridisation	**F:** CGCCTTCGGAACATCACTATCCAG
	R: CCTGCAGGAGCTCAAAGACTCCAC
Mrc1a	
In Situ hybridisation	**F:** TGTGGACTGATGGTAAAGGTGTCAGC
	R: CTCAGGACAGTTCCCTGGCATCTG

***Supplementary Figure 1. Confocal images of individual embryos that were used for image quantification.** Twelve (n=12) cellular views of Myocet, AmBisome and EndoTAG-1 liposome distribution in *kdrl:*GFP transgenic zebrafish embryos at 1,8, 24 and 48 hpi. For Myocet 48 hpi, n=11, and for EndoTAG-1 24 hpi and 48 hpi, n=6.

***For Supplementary Figure 1 and movies please go to:**
https://pubs.acs.org/doi/abs/10.1021/acsnano.7b06995.

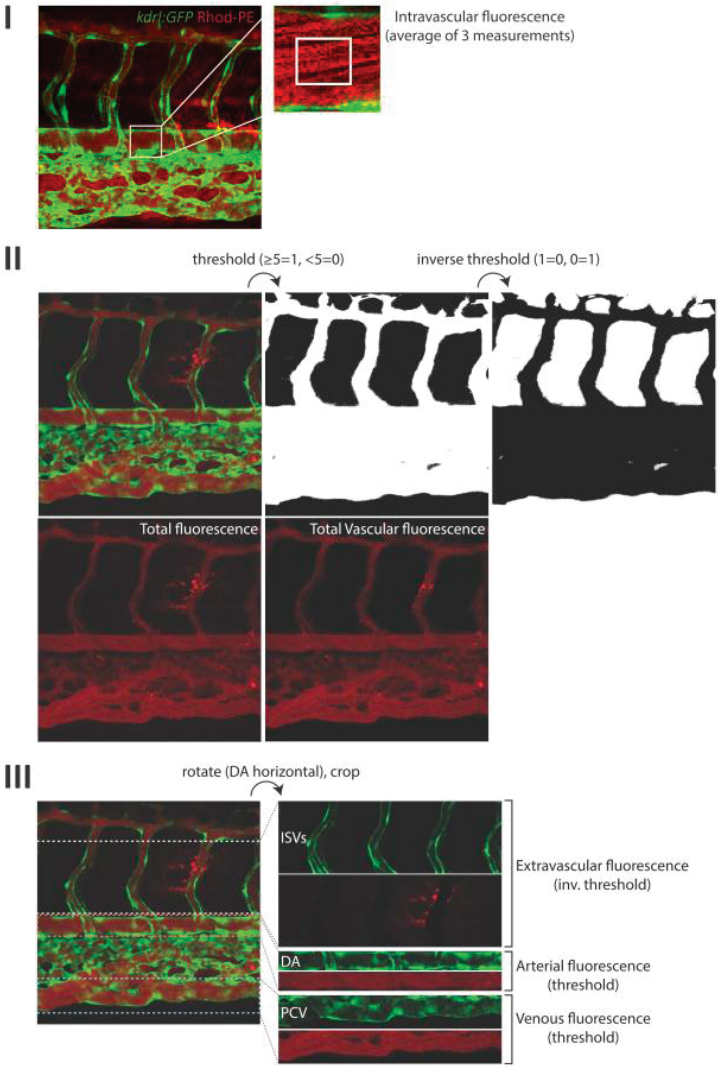

Supplementary Figure 2. Overview of quantification method as described in the Materials & Methods section. I. Quantification of intravascular fluorescence (liposomes in circulation). **II.** Quantification of total and total vascular fluorescence. **III.** Quantification of arterial, venous and extravascular fluorescence.

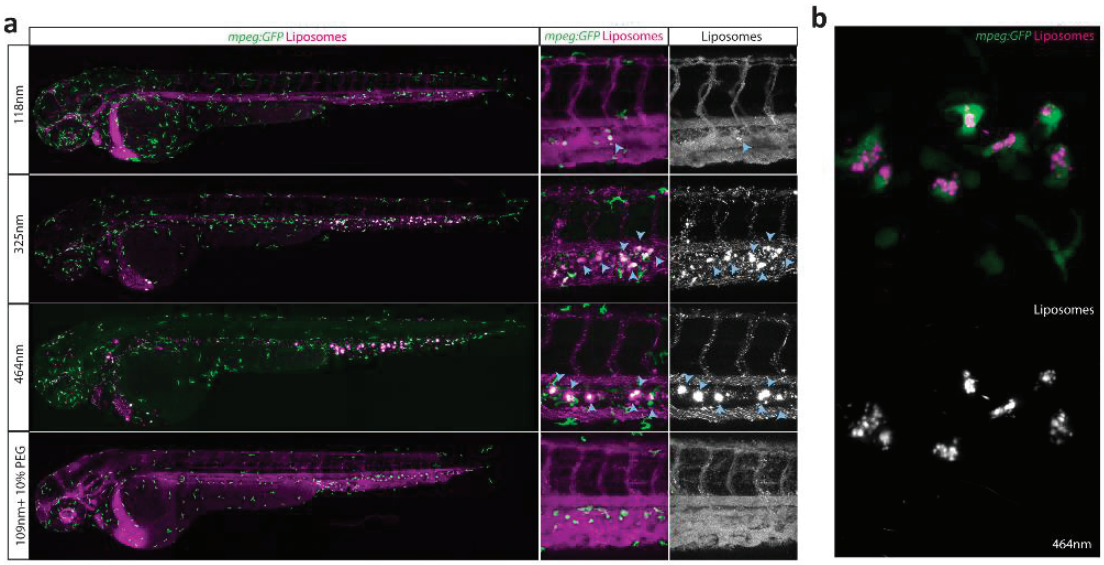

Supplementary Figure 3. Size-dependent uptake of neutral liposomes by monocytes/macrophages. (a) Whole-embryo and cellular views of liposome distribution in *mpeg1:*GFP transgenic embryos, 2h after injection with Myocet liposomes ~100 nm (with and without 10 mol% DOPE-mPEG2000), 325 nm and 464 nm pores. Immobile liposome aggregates were observed to colocalize with *mpeg1:*GFP positive macrophages/monocytes within the caudal hematopoietic tissue (CHT). Fluorescence intensity was found to increase with increased liposome size, and phagocytosis could be prevented by PEGylation. **(b)** High-resolution imaging shows intracellular localization of 400 nm liposomes within macrophages/monocytes.

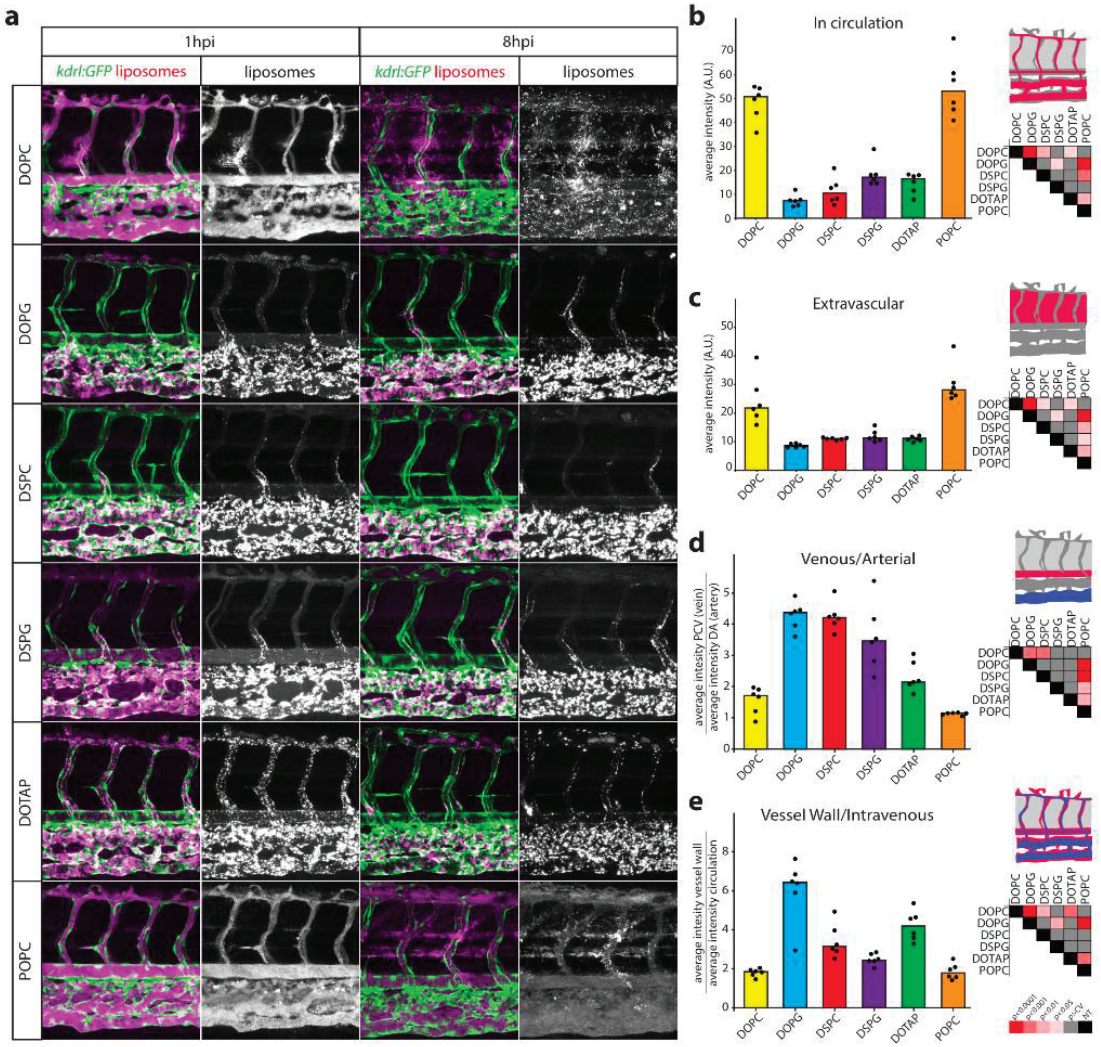

Supplementary Figure 4. Contribution of individual lipids to liposome biodistribution. **(a)** Cellular view of liposome distribution in Tg(*kdrl:*GFP) embryos, 1 h and 8 h after injection with liposomes generated from six different individual lipids. **(b)** Quantification of liposome levels in circulation based on rhodamine fluorescence intensity in the lumen of the dorsal aorta at 1 h after injection. **(c)** Quantification of extravascular liposome levels based on rhodamine fluorescence intensity outside of the vasculature between the DLAV and DA at 8 h after injection. **(d)** Quantification of liposome levels associated with venous vs. arterial endothelial cells based on rhodamine fluorescence intensity associated with caudal vein *vs.* DA at 8 h after injection. **(e)** Quantification of liposome levels associated with the vessel wall based on relative rhodamine fluorescence intensity associated with all endothelial cells *vs.* rhodamine fluorescence intensity in circulation at 1 h after injection**. (b-e)** Bar height represents median values, dots represent individual data points, significantly different pairs of values based on Kruskal-Wallis and Dunn's test with Bonferroni correction are indicated by colored boxes (representing significance levels; CV=critical value; NT=not tested). n=6 individually injected embryos per group (in 2 experiments).

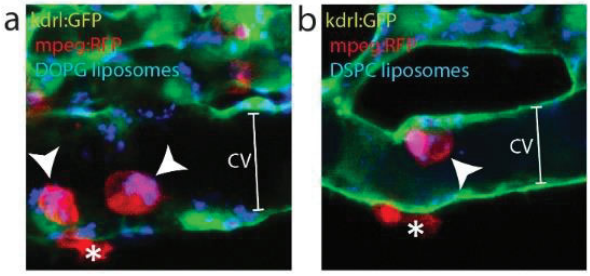

Supplementary Figure 5. Macrophage uptake of DOPG and DSPC liposomes. Confocal micrographs of *kdrl:*GFP (green)*; mpeg:*RFP (red) double transgenic embryos injected with DOPE-ATTO633 labeled DOPG **(a)** or DSPC **(b)** liposomes. Besides uptake of liposomes in caudal vein (CV, brackets) endothelial cells, uptake by plasma-exposed (arrowheads) but not extravascular (asterisks) macrophages/monocytes is also observed for both liposomes**.**

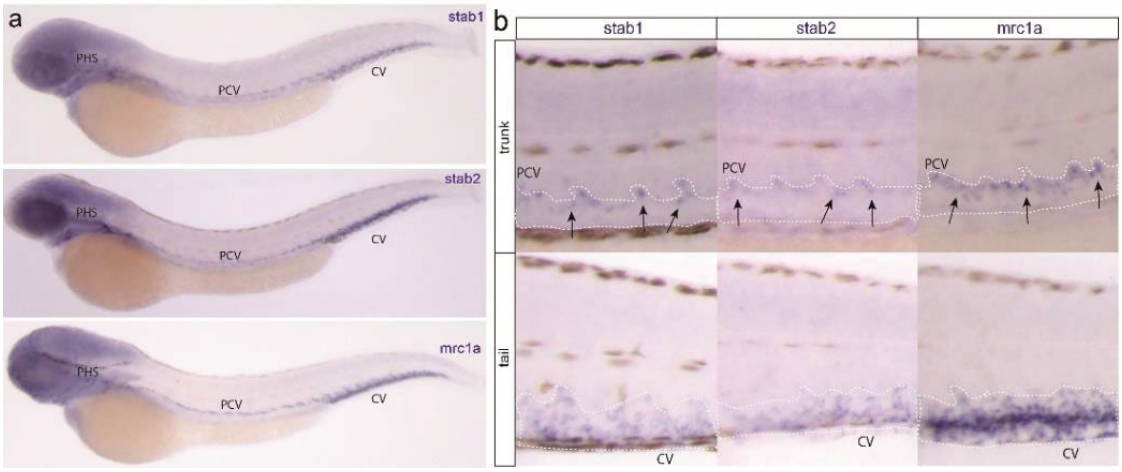

Supplementary Figure 6. Expression of LSEC marker genes in zebrafish embryos. (a-b) Whole-mount *in situ* hybridization of *stab1, stab2* and *mrc1a* mRNA. **(a)** Whole-embryo view showing expression of these genes in the PHS, CCV, PCV and CV **(b)** Higher-resolution image showing expression in the entire caudal vein, but only on the dorsal side of the PCV (arrows).

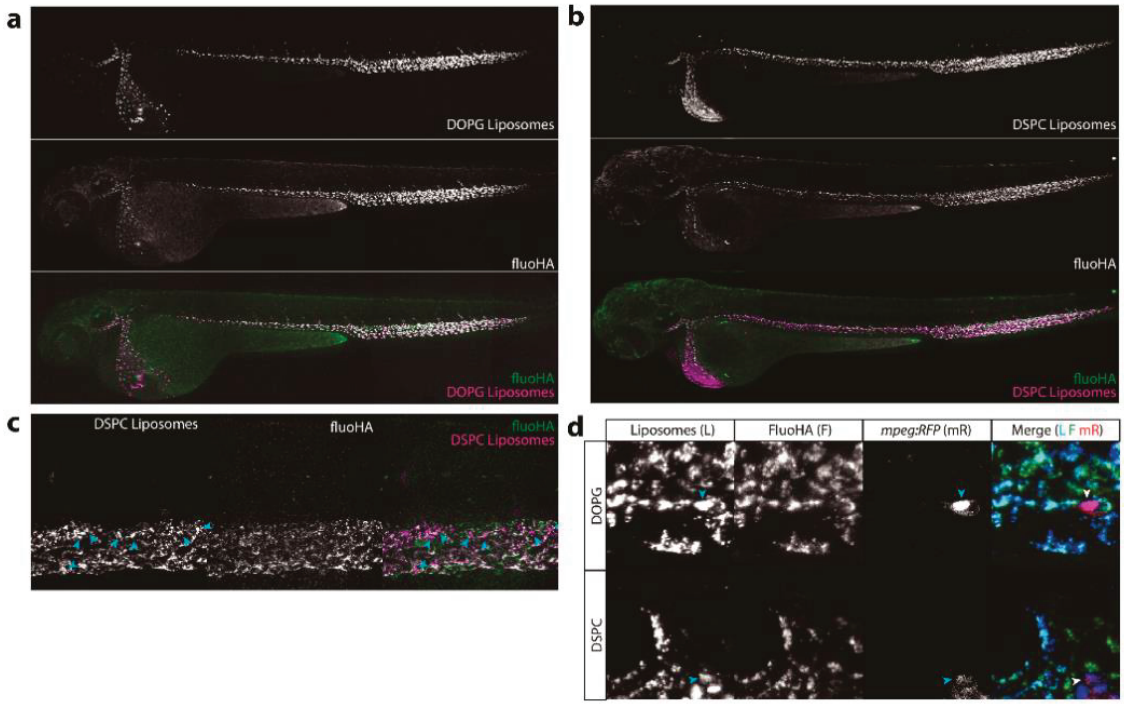

Supplementary Figure 7. FluoHA colocalization with liposomes. (a-b) Whole-embryo view of co-injected fluoHA (green) and **(a)** DOPG liposomes or **(b)** DSPC liposomes (red), 1 h after injection, reveals colocalization in PHS, CCV, PCV and CV scavenger endothelial cells. **(c)** Tissue level view of co-injected fluoHA and DOPG liposomes, 1 h after injection reveals colocalization in SECs. Monocytes/macrophages (arrowheads) take up DSPC but not fluoHA. **(d)** Cellular view of co-injected fluoHA (green) and DOPG or DSPC liposomes (blue) in *mpeg:*RFP (red) transgenic embryos. Colocalization of fluoHA with both liposomes is observed in all SECs, but not in macrophages/monocytes, which only take up liposomes, but not fluoHA.

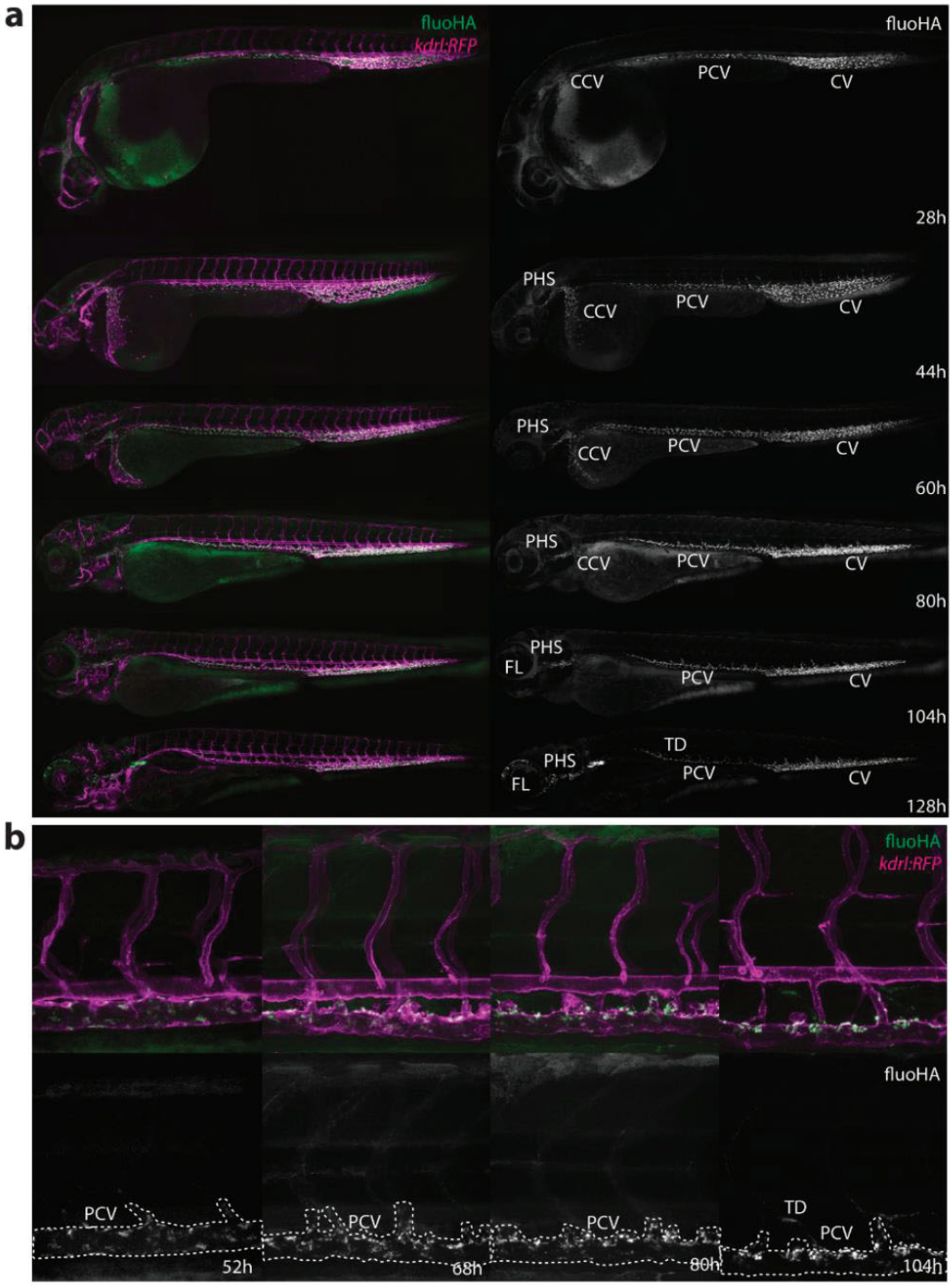

Supplementary Figure 8. FluoHA distribution through embryonic development. (a) Whole-embryo view of fluorescent hyaluronic acid (fluoHA) distribution in *kdrl:*RFP transgenic embryos, 1 h after injection. SECs, as identified through intracellular accumulation of fluoHA from 28 hpf to at least 128 hpf. From 104 hpf, fluoHA uptake is also observed in lymphatic vessels, such as the thoracic duct (TD) and facial lymphatics (FL). **(b)** Cellular view of fluoHA distribution in the trunk of *kdrl:*RFP transgenic embryos, 1 h after injection. A gradual restriction of fluoHA accumulation to the PCV is observed between 52 hpf and 104 hpf.

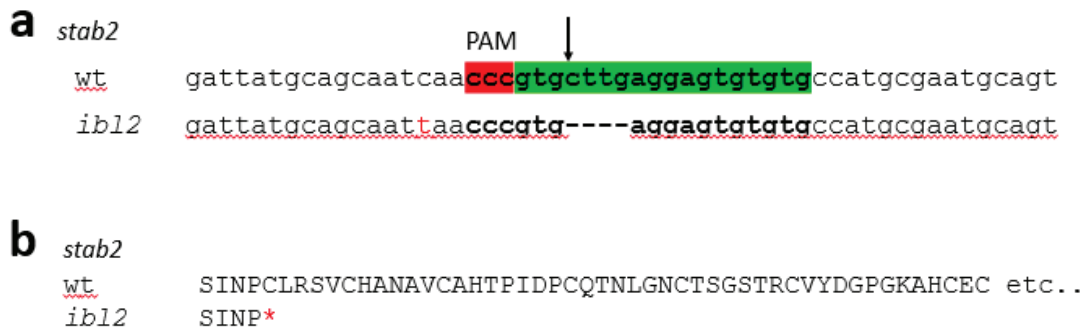

Supplementary Figure 9. CRISPR/Cas9 induced mutations. A. Nucleotide sequences surrounding the CRISPR/Cas9 targeting sites in the *stab2*^{ibl2} allele. Protospacer Adjacent Motif (PAM) sequences are indicated in red, sgRNA target sites are indicated in green, arrows indicate the predicted Cas9 cutting site. A silent single-nucleotide polymorphism (C->T, red) was also identified in the *stab2*^{ibl2} allele. B. Predicted amino acid sequences surrounding the CRISPR/Cas9 targeting sites in the *stab2*^{ibl2} allele. Frameshift-induced amino acids and stop codons are indicated in red.

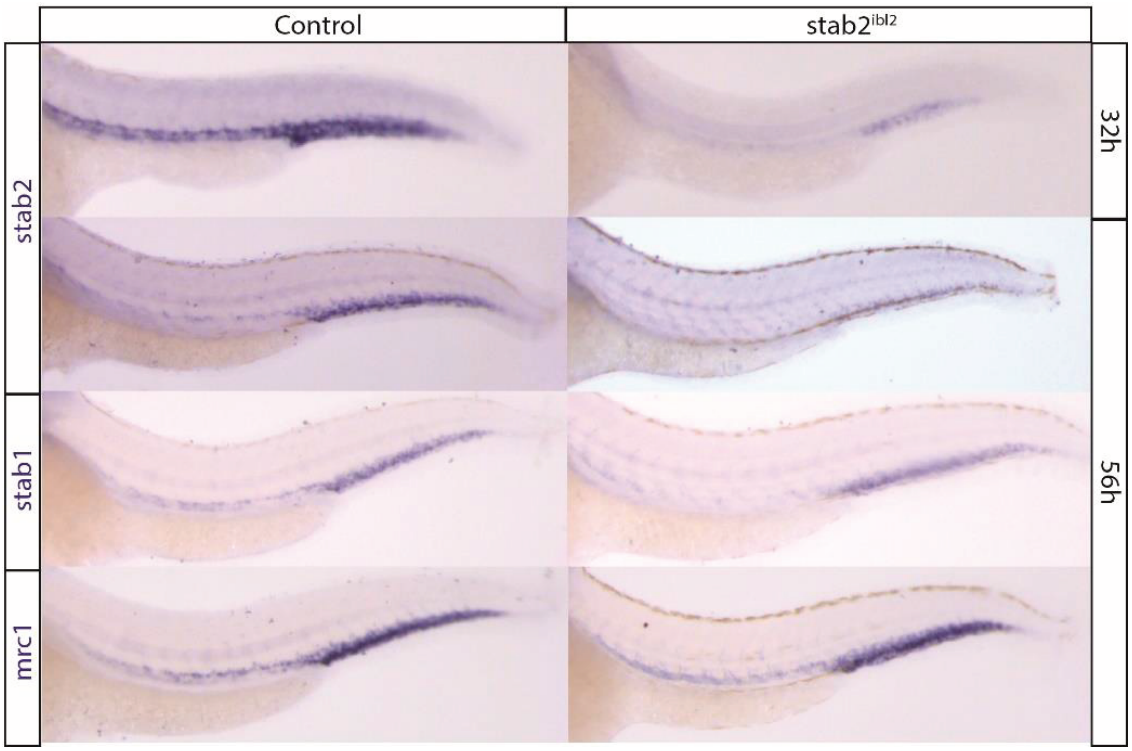

Supplementary Figure 10. Gene expression in *stab2*^{ibl2} homozygous mutant embryos. Whole-mount *in situ* hybridization of *stab1* and *mrc1* mRNA expression at 56 hpf and *stab2* mRNA expression at 32 hpf and 56 hpf in the trunk and tail of *stab2*^{ibl2} homozygous mutant and sibling control embryos. Reduction in *stab2* expression indicating nonsense-mediated decay of the *stab2*^{ibl2} mRNA is observed *stab2*^{ibl2} homozygous, but not sibling control embryos. Expression of *stab1* and *mrc1* is unchanged indicating normal SEC differentiation.

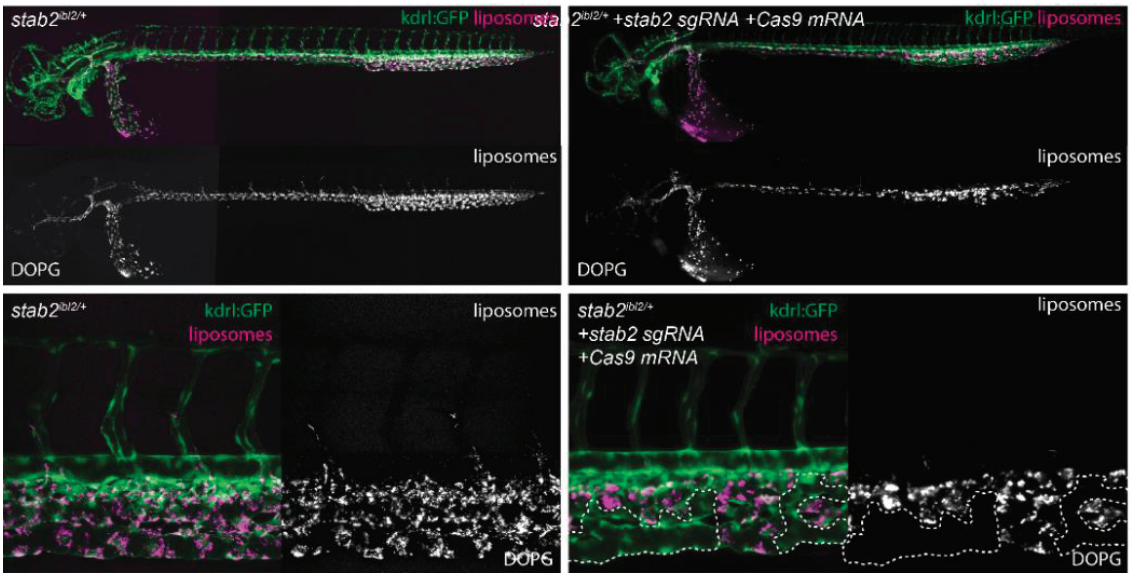

Supplementary Figure 11. Clonal *stab2* deletion. Whole-embryo and cellular views of DOPG liposome distribution in *stab2*$^{ibl2/+}$; *kdrl:*GFP embryos. CRISPR/Cas9 introduced mutations in the wildtype allele generated clones of cells without *stab2* function. In *stab2 sgRNA* and *Cas9* mRNA injected, but not control embryos, endothelial cell clones are observed in which DOPG accumulation is abrogated, indicating a requirement for *stab2* function within SECs.

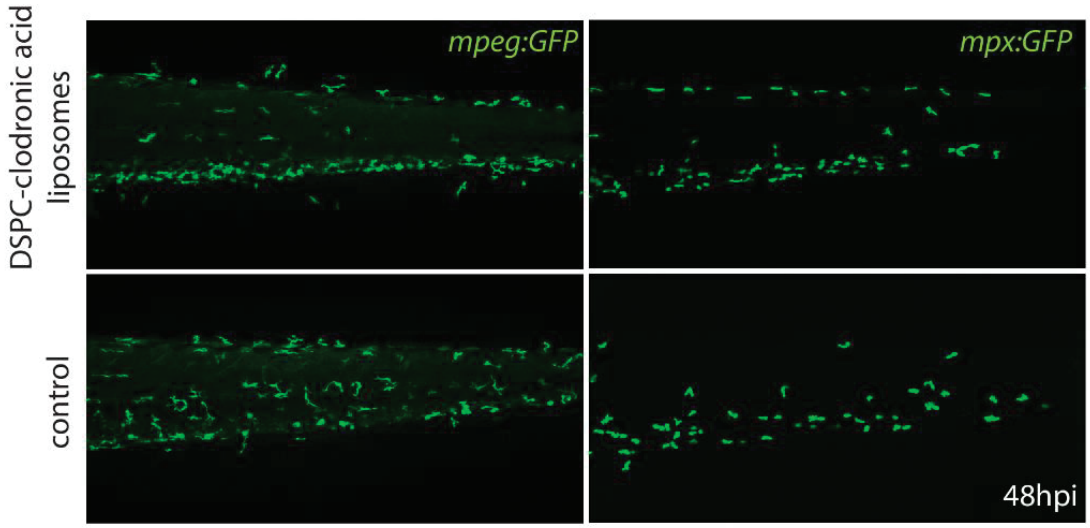

Supplementary Figure 12. Cell-type selectivity of DSPC-clodronic acid liposomes. Confocal imaging of *mpeg1:*GFP (macrophage/monocytes) and *mpx:*GFP (neutrophil) transgenic zebrafish embryos 48 h after injection with 1 nl of DSPC-clodronic acid liposomes (10 mM total lipids) showing normal development of these lineages in the tail of injected embryos compared to un-injected controls (UIC).

Reagents

1,2-dioleoyl-sn-glycero-3-phosphocholine (DOPC), 1,2-distearoyl-sn-glycero-3-phosphocholine (DSPC), 1,2-dioleoyl-sn-glycero-3-phospho-(1'-rac-glycerol) (DOPG), 1,2-distearoyl-sn-glycero-3-phospho-(1'-racglycerol) (DSPG), 1-palmitoyl-2-oleoyl-sn-glycero-3-phosphocholine (POPC), 1,2-dioleoyl-sn-glycero-3phospho-L-serine (sodium salt) (DOPS), 1,2-dioleoyl-3-trimethyl ammonium-propane (DOTAP),1,2dioleoyl-sn-glycero-3-phosphoethanolamine-N-[methoxy(polyethylene glycol)-2000] (DOPE-mPEG2000), 1,2-dioleoyl-sn-glycero-3-phosphoethanolamine -N-(lissamine rhodamine B sulfonyl) (Rhodamine-PE) were purchased from Avanti Polar Lipids (Alabaster, US). 1,2-Dioleoyl-sn-glycero-3-phosphoethanolamine-Atto 633 was purchased from ATTO-TEC GmbH (Germany). Additional DOPC and DSPC were purchased from Lipoid GmbH. Additional POPC and cholesterol was purchased from Sigma-Aldrich. All solvents were purchased from Biosolve Ltd. Dichloromethyl-enediphosphonic acid disodium salt (clodronic acid), carminic acid and dextran sulfate (40kDa) were purchased from Sigma-Aldrich. Hyaluronic acid (sodium salt, 100kDa) was purchased from Lifecore Biomedical Inc. Quantum dots (Qdot 605 ITK carboxyl) and oxidized low density lipoprotein (oxLDL from human plasma, DiI conjugate) were purchased from Thermo Fisher. 100 nm red fluorescent polystyrene, sulfate modified nanoparticles ('latex beads') were purchased from Sigma Aldrich.

Size and zeta potential measurements

Particle size and zeta potentials were measured using a Malvern Zetasizer Nano ZS. For DLS, measurements were carried out at room temperature in ddH_20 at a total lipid concentration of 100 μM. For zeta potential measurements, liposome solutions were first diluted in salt (NaCl) solution. Zeta potentials were measured at room temperature, at 500 μM total lipid concentration and 10 mM NaCl concentration. All reported DLS measurements and zeta potentials are the average of three measurements.

Imaging quantification

First, average intravascular fluorescence within the dorsal aorta (DA) was measured within an ~8 um*10 um rectangular area (~1*103 pixels) in a single confocal slice that captured the center of the DA. This measurement was repeated three times per embryo in independent sites within the DA. Second, total fluorescence and total vasculature associated fluorescence was quantified

using the following ImageJ macro:

ImageJ quantification macro

```
rename("stack");
run("Z Project...", "projection=[Max Intensity]");
run("Split Channels");
selectWindow("C2-MAX_stack");
close();
selectWindow("C1-MAX_stack");
run("Duplicate...", "title=vascular");
selectWindow("vascular");
setThreshold(5, 255);
run("Convert to Mask");
run("Invert LUT");
run("Subtract...", "value=254");
run("Duplicate...", "title=nonvascular");
run("Macro...", "code=v=abs(v-1)");
imageCalculator("Multiply create", "vascular","C3-MAX_stack");
imageCalculator("Multiply create", "nonvascular","C3-MAX_stack");
selectWindow("C3-MAX_stack");
run("Measure");
selectWindow("Result of vascular");
run("Measure");
run("Concatenate...", "  title=[Concatenated Stacks] keep image1=C1-MAX_stack
image2=[Result of nonvascular] image3=[Result of vascular] image4=[-- None --
]");
```

Finally, the angle of the dorsal aspect of the dorsal aorta (a straight line) was measured and the concatenated images were rotated to orient the dorsal aorta horizontally within the image. Images were subsequently cropped to a rectangle encompassing the caudal vein, DA or the area between the DA and the dorsal longitudinal anastomotic vessel (DLAV) to quantify the vasculature-associated fluorescence associated with veins (caudal vein) and arteries (DA), as well as the extravascular fluorescence around the intersegmental vessels. The latter area was used to quantify extravascular fluorescence since it does not contain pigment cells that are present on the dorsal and ventral side of the embryo and which are auto-fluorescent within the rhodamine-PE channel. Although the CHT endothelial cells appear to behave very similar to the CV endothelial cells, quantification was performed based on the CV alone for the following reasons. First, the CV is always perfused, whereas perfusion of the vessels within the CHT

is variable. Unperfused or weakly perfused vessels display absence of or reduced nanoparticle uptake. Secondly, variable numbers of hematopoietic cells - especially macrophages - are closely associated with CHT-ECs and much less with the CV. Macrophage uptake of nanoparticles could therefore lead to the false impression that CHT-ECs selectively take up nanoparticles.

From these data, the following measures were reported:
1. Average intravascular fluorescence (**Figure 1e**, **Supplementary Figure 4b**).
2. Venous/Arterial (**Figure 1f, 3a,b,f-k, 4a-j,m, Supplementary Figure 4d**): (Mean CV fluorescence/%GFP positive within CV area)/(Mean DA fluorescence/%GFP positive within DA area).
3. Extravascular (**Figure 1g, Supplementary Figure 4c**): Extravascular fluorescence/%GFP negative within ISV area.
4. Vessel wall/Intravenous (**Figure 1h, Supplementary Figure 4e**): (Total vascular fluorescence/%GFP positive within the total image)/Average intravascular fluorescence.

2.8 References

1. Blanco, E.; Shen, H.; Ferrari, M., Principles of nanoparticle design for overcoming biological barriers to drug delivery. *Nat Biotechnol* **2015,** *33* (9), 941-951.
2. Dawidczyk, C. M.; Kim, C.; Park, J. H.; Russell, L. M.; Lee, K. H.; Pomper, M. G.; Searson, P. C., State-of-the-art in design rules for drug delivery platforms: lessons learned from FDA-approved nanomedicines. *J Control Release* **2014,** *187*, 133-144.
3. Wang, A. Z.; Langer, R.; Farokhzad, O. C., Nanoparticle delivery of cancer drugs. *Annu Rev Med* **2012,** *63*, 185-198.
4. Wilhelm, S.; Tavares, A. J.; Dai, Q.; Ohta, S.; Audet, J.; Dvorak, H. F.; Chan, W. C. W., Analysis of nanoparticle delivery to tumours. *Nature Reviews Materials* **2016,** *1* (5), 16014.
5. Zhang, Y. N.; Poon, W.; Tavares, A. J.; McGilvray, I. D.; Chan, W. C. W., Nanoparticle-liver interactions: Cellular uptake and hepatobiliary elimination. *J Control Release* **2016,** *240*, 332-348.
6. Bertrand, N.; Leroux, J. C., The journey of a drug-carrier in the body: an anatomo-physiological perspective. *J Control Release* **2012,** *161* (2), 152-163.
7. Kamps, J. A.; Morselt, H. W.; Swart, P. J.; Meijer, D. K.; Scherphof, G. L., Massive targeting of liposomes, surface-modified with anionized albumins, to hepatic endothelial cells. *Proc Natl Acad Sci U S A* **1997,** *94* (21), 11681-11685.
8. Park, J. K.; Utsumi, T.; Seo, Y. E.; Deng, Y.; Satoh, A.; Saltzman, W. M.; Iwakiri, Y., Cellular distribution of injected PLGA-nanoparticles in the liver. *Nanomedicine* **2016,** *12* (5), 1365-1374.
9. Tsoi, K. M.; MacParland, S. A.; Ma, X. Z.; Spetzler, V. N.; Echeverri, J.; Ouyang, B.; Fadel, S. M.; Sykes, E. A.; Goldaracena, N.; Kaths, J. M.; Conneely, J. B.; Alman, B. A.; Selzner, M.; Ostrowski, M. A.; Adeyi, O. A.; Zilman, A.; McGilvray, I. D.; Chan, W. C., Mechanism of hard-nanomaterial clearance by the liver. *Nat Mater* **2016,** *15* (11), 1212-1221.
10. Rothkopf, C.; Fahr, A.; Fricker, G.; Scherphof, G. L.; Kamps, J. A., Uptake of phosphatidylserine-containing liposomes by liver sinusoidal endothelial cells in the serum-free perfused rat liver. *Biochim Biophys Acta* **2005,** *1668* (1), 10-16.
11. Sorensen, K. K.; Simon-Santamaria, J.; McCuskey, R. S.; Smedsrod, B., Liver Sinusoidal Endothelial Cells. *Compr Physiol* **2015,** *5* (4), 1751-1774.
12. MacPhee, P. J.; Schmidt, E. E.; Groom, A. C., Intermittence of blood flow in liver sinusoids, studied by high-resolution in vivo microscopy. *Am J Physiol* **1995,** *269* (5 Pt 1), G692-698.
13. Wisse, E., An electron microscopic study of the fenestrated endothelial lining of rat liver sinusoids. *Journal of ultrastructure research* **1970,** *31* (1-2), 125-150.
14. Aschoff, L., Das reticulo-endotheliale System. In *Ergebnisse der inneren Medizin und Kinderheilkunde*, Springer: 1924; pp 1-118.
15. Seternes, T.; Sorensen, K.; Smedsrod, B., Scavenger endothelial cells of vertebrates: a nonperipheral leukocyte system for high-capacity elimination of waste macromolecules. *Proc Natl Acad Sci U S A* **2002,** *99* (11), 7594-7597.
16. Breiner, K. M.; Schaller, H.; Knolle, P. A., Endothelial cell-mediated uptake of a hepatitis B virus: a new concept of liver targeting of hepatotropic microorganisms. *Hepatology* **2001,** *34* (4 Pt 1), 803-808.
17. Ganesan, L. P.; Mohanty, S.; Kim, J.; Clark, K. R.; Robinson, J. M.; Anderson, C. L., Rapid and efficient clearance of blood-borne virus by liver sinusoidal endothelium. *PLoS Pathog* **2011,** *7* (9), e1002281.
18. Mates, J. M.; Yao, Z.; Cheplowitz, A. M.; Suer, O.; Phillips, G. S.; Kwiek, J. J.; Rajaram, M. V.; Kim, J.; Robinson, J. M.; Ganesan, L. P.; Anderson, C. L., Mouse Liver Sinusoidal Endothelium Eliminates HIV-Like Particles from Blood at a Rate of 100 Million per Minute by a Second-Order Kinetic Process. *Front Immunol* **2017,** *8*, 35.
19. Knolle, P. A.; Wohlleber, D., Immunological functions of liver sinusoidal endothelial cells. *Cell Mol Immunol* **2016,** *13* (3), 347-353.
20. Sorensen, K. K.; McCourt, P.; Berg, T.; Crossley, C.; Le Couteur, D.; Wake, K.; Smedsrod, B., The scavenger endothelial cell: a new player in homeostasis and immunity. *Am J Physiol Regul Integr Comp Physiol* **2012,** *303* (12), R1217-1230.
21. Allen, T. M.; Cullis, P. R., Liposomal drug delivery systems: from concept to clinical applications. *Adv Drug Deliv Rev* **2013,** *65* (1), 36-48.
22. Sercombe, L.; Veerati, T.; Moheimani, F.; Wu, S. Y.; Sood, A. K.; Hua, S., Advances and Challenges of Liposome Assisted Drug Delivery. *Front Pharmacol* **2015,** *6*, 286.

23. Evensen, L.; Johansen, P. L.; Koster, G.; Zhu, K.; Herfindal, L.; Speth, M.; Fenaroli, F.; Hildahl, J.; Bagherifam, S.; Tulotta, C.; Prasmickaite, L.; Maelandsmo, G. M.; Snaar-Jagalska, E.; Griffiths, G., Zebrafish as a model system for characterization of nanoparticles against cancer. *Nanoscale* **2016,** *8* (2), 862-877.
24. Fenaroli, F.; Westmoreland, D.; Benjaminsen, J.; Kolstad, T.; Skjeldal, F. M.; Meijer, A. H.; van der Vaart, M.; Ulanova, L.; Roos, N.; Nystrom, B.; Hildahl, J.; Griffiths, G., Nanoparticles as drug delivery system against tuberculosis in zebrafish embryos: direct visualization and treatment. *ACS Nano* **2014,** *8* (7), 7014-7026.
25. Jiang, X. Y.; Sarsons, C. D.; Gomez-Garcia, M. J.; Cramb, D. T.; Rinker, K. D.; Childs, S. J., Quantum dot interactions and flow effects in angiogenic zebrafish (Danio rerio) vessels and human endothelial cells. *Nanomedicine* **2017,** *13* (3), 999-1010.
26. Sieber, S.; Grossen, P.; Detampel, P.; Siegfried, S.; Witzigmann, D.; Huwyler, J., Zebrafish as an early stage screening tool to study the systemic circulation of nanoparticulate drug delivery systems in vivo. *J Control Release* **2017,** *264*, 180-191.
27. Batist, G.; Barton, J.; Chaikin, P.; Swenson, C.; Welles, L., Myocet (liposome-encapsulated doxorubicin citrate): a new approach in breast cancer therapy. *Expert Opin Pharmacother* **2002,** *3* (12), 1739-1751.
28. Cornely, O. A.; Maertens, J.; Bresnik, M.; Ebrahimi, R.; Ullmann, A. J.; Bouza, E.; Heussel, C. P.; Lortholary, O.; Rieger, C.; Boehme, A., et al., Liposomal amphotericin B as initial therapy for invasive mold infection: a randomized trial comparing a high-loading dose regimen with standard dosing (AmBiLoad trial). *Clin Infect Dis* **2007,** *44* (10), 1289-1297.
29. Schmitt-Sody, M.; Strieth, S.; Krasnici, S.; Sauer, B.; Schulze, B.; Teifel, M.; Michaelis, U.; Naujoks, K.; Dellian, M., Neovascular targeting therapy: paclitaxel encapsulated in cationic liposomes improves antitumoral efficacy. *Clin Cancer Res* **2003,** *9* (6), 2335-2341.
30. Immordino, M. L.; Dosio, F.; Cattel, L., Stealth liposomes: review of the basic science, rationale, and clinical applications, existing and potential. *Int J Nanomedicine* **2006,** *1* (3), 297-315.
31. Murayama, E.; Kissa, K.; Zapata, A.; Mordelet, E.; Briolat, V.; Lin, H. F.; Handin, R. I.; Herbomel, P., Tracing hematopoietic precursor migration to successive hematopoietic organs during zebrafish development. *Immunity* **2006,** *25* (6), 963-975.
32. Isogai, S.; Horiguchi, M.; Weinstein, B. M., The vascular anatomy of the developing zebrafish: an atlas of embryonic and early larval development. *Dev Biol* **2001,** *230* (2), 278-301.
33. Cho, E. C.; Xie, J.; Wurm, P. A.; Xia, Y., Understanding the role of surface charges in cellular adsorption versus internalization by selectively removing gold nanoparticles on the cell surface with a I2/KI etchant. *Nano Lett* **2009,** *9* (3), 1080-1084.
34. Hen, G.; Nicenboim, J.; Mayseless, O.; Asaf, L.; Shin, M.; Busolin, G.; Hofi, R.; Almog, G.; Tiso, N.; Lawson, N. D.; Yaniv, K., Venous-derived angioblasts generate organ-specific vessels during zebrafish embryonic development. *Development* **2015,** *142* (24), 4266-4278.
35. Koltowska, K.; Paterson, S.; Bower, N. I.; Baillie, G. J.; Lagendijk, A. K.; Astin, J. W.; Chen, H.; Francois, M.; Crosier, P. S.; Taft, R. J.; Simons, C.; Smith, K. A.; Hogan, B. M., mafba is a downstream transcriptional effector of Vegfc signaling essential for embryonic lymphangiogenesis in zebrafish. *Genes Dev* **2015,** *29* (15), 1618-1630.
36. Stapelfeldt, H.; Jun, H.; Skibsted, L. H., Fluorescence properties of carminic acid in relation to aggregation, complex formation and oxygen activation in aqueous food models. *Food chemistry* **1993,** *48* (1), 1-11.
37. Schledzewski, K.; Geraud, C.; Arnold, B.; Wang, S.; Grone, H. J.; Kempf, T.; Wollert, K. C.; Straub, B. K.; Schirmacher, P.; Demory, A.; Schonhaber, H.; Gratchev, A.; Dietz, L.; Thierse, H. J.; Kzhyshkowska, J.; Goerdt, S., Deficiency of liver sinusoidal scavenger receptors stabilin-1 and -2 in mice causes glomerulofibrotic nephropathy via impaired hepatic clearance of noxious blood factors. *J Clin Invest* **2011,** *121* (2), 703-714.
38. Hogan, B. M.; Bos, F. L.; Bussmann, J.; Witte, M.; Chi, N. C.; Duckers, H. J.; Schulte-Merker, S., Ccbe1 is required for embryonic lymphangiogenesis and venous sprouting. *Nat Genet* **2009,** *41* (4), 396-398.
39. Wong, K. S.; Proulx, K.; Rost, M. S.; Sumanas, S., Identification of vasculature-specific genes by microarray analysis of Etsrp/Etv2 overexpressing zebrafish embryos. *Dev Dyn* **2009,** *238* (7), 1836-1850.
40. Zhou, B.; Weigel, J. A.; Fauss, L.; Weigel, P. H., Identification of the hyaluronan receptor for endocytosis (HARE). *J Biol Chem* **2000,** *275* (48), 37733-37741.

41. Simon-Santamaria, J.; Malovic, I.; Warren, A.; Oteiza, A.; Le Couteur, D.; Smedsrod, B.; McCourt, P.; Sorensen, K. K., Age-related changes in scavenger receptor-mediated endocytosis in rat liver sinusoidal endothelial cells. *J Gerontol A Biol Sci Med Sci* **2010,** *65* (9), 951-960.
42. Miller, C. M.; Donner, A. J.; Blank, E. E.; Egger, A. W.; Kellar, B. M.; Ostergaard, M. E.; Seth, P. P.; Harris, E. N., Stabilin-1 and Stabilin-2 are specific receptors for the cellular internalization of phosphorothioate-modified antisense oligonucleotides (ASOs) in the liver. *Nucleic Acids Res* **2016,** *44* (6), 2782-2794.
43. Park, S. Y.; Jung, M. Y.; Kim, H. J.; Lee, S. J.; Kim, S. Y.; Lee, B. H.; Kwon, T. H.; Park, R. W.; Kim, I. S., Rapid cell corpse clearance by stabilin-2, a membrane phosphatidylserine receptor. *Cell Death Differ* **2008,** *15* (1), 192-201.
44. Balogh, P.; Petz, A., Selective binding of biotinylated albumin to the lymphoid microvasculature. *Histochem Cell Biol* **2005,** *123* (4-5), 357-363.
45. Alidori, S.; Bowman, R. L.; Yarilin, D.; Romin, Y.; Barlas, A.; Mulvey, J. J.; Fujisawa, S.; Xu, K.; Ruggiero, A.; Riabov, V.; Thorek, D. L.; Ulmert, H. D.; Brea, E. J.; Behling, K.; Kzhyshkowska, J.; Manova-Todorova, K.; Scheinberg, D. A.; McDevitt, M. R., Deconvoluting hepatic processing of carbon nanotubes. *Nat Commun* **2016,** *7*, 12343.
46. Lee, S. J.; Park, S. Y.; Jung, M. Y.; Bae, S. M.; Kim, I. S., Mechanism for phosphatidylserine-dependent erythrophagocytosis in mouse liver. *Blood* **2011,** *117* (19), 5215-5223.
47. Harris, E. N.; Weigel, P. H., The ligand-binding profile of HARE: hyaluronan and chondroitin sulfates A, C, and D bind to overlapping sites distinct from the sites for heparin, acetylated low-density lipoprotein, dermatan sulfate, and CS-E. *Glycobiology* **2008,** *18* (8), 638-648.
48. Tamura, Y.; Adachi, H.; Osuga, J.; Ohashi, K.; Yahagi, N.; Sekiya, M.; Okazaki, H.; Tomita, S.; Iizuka, Y.; Shimano, H.; Nagai, R.; Kimura, S.; Tsujimoto, M.; Ishibashi, S., FEEL-1 and FEEL-2 are endocytic receptors for advanced glycation end products. *J Biol Chem* **2003,** *278* (15), 12613-12617.
49. Kawasaki, T.; Etoh, R.; Yamashina, I., Isolation and characterization of a mannan-binding protein from rabbit liver. *Biochem Biophys Res Commun* **1978,** *81* (3), 1018-1024.
50. Rost, M. S.; Sumanas, S., Hyaluronic acid receptor Stabilin-2 regulates Erk phosphorylation and arterial--venous differentiation in zebrafish. *PLoS One* **2014,** *9* (2), e88614.
51. Stoll, S. J.; Bartsch, S.; Kroll, J., HOXC9 regulates formation of parachordal lymphangioplasts and the thoracic duct in zebrafish via stabilin 2. *PLoS One* **2013,** *8* (3), e58311.
52. Hirose, Y.; Saijou, E.; Sugano, Y.; Takeshita, F.; Nishimura, S.; Nonaka, H.; Chen, Y. R.; Sekine, K.; Kido, T.; Nakamura, T.; Kato, S.; Kanke, T.; Nakamura, K.; Nagai, R.; Ochiya, T.; Miyajima, A., Inhibition of Stabilin-2 elevates circulating hyaluronic acid levels and prevents tumor metastasis. *Proc Natl Acad Sci U S A* **2012,** *109* (11), 4263-4268.
53. Verwegen, M.; Cornelissen, J. J., Clustered nanocarriers: the effect of size on the clustering of CCMV virus-like particles with soft macromolecules. *Macromol Biosci* **2015,** *15* (1), 98-110.
54. Askes, S. H.; Pomp, W.; Hopkins, S. L.; Kros, A.; Wu, S.; Schmidt, T.; Bonnet, S., Imaging Upconverting Polymersomes in Cancer Cells: Biocompatible Antioxidants Brighten Triplet-Triplet Annihilation Upconversion. *Small* **2016,** *12* (40), 5579-5590.
55. Plosker, G. L.; Goa, K. L., Clodronate. A review of its pharmacological properties and therapeutic efficacy in resorptive bone disease. *Drugs* **1994,** *47* (6), 945-982.
56. van Rooijen, N.; Hendrikx, E., Liposomes for specific depletion of macrophages from organs and tissues. *Methods Mol Biol* **2010,** *605*, 189-203.
57. Michen, B.; Graule, T., Isoelectric points of viruses. *J Appl Microbiol* **2010,** *109* (2), 388-397.
58. Elvevold, K.; Smedsrod, B.; Martinez, I., The liver sinusoidal endothelial cell: a cell type of controversial and confusing identity. *Am J Physiol Gastrointest Liver Physiol* **2008,** *294* (2), G391-400.
59. Patel, K. R.; Li, M. P.; Baldeschwieler, J. D., Suppression of liver uptake of liposomes by dextran sulfate 500. *Proc Natl Acad Sci U S A* **1983,** *80* (21), 6518-6522.
60. de Belder, A. N.; Wik, K. O., Preparation and properties of fluorescein-labelled hyaluronate. *Carbohydr Res* **1975,** *44* (2), 251-257.
61. Kawai, Y.; Smedsrod, B.; Elvevold, K.; Wake, K., Uptake of lithium carmine by sinusoidal endothelial and Kupffer cells of the rat liver: new insights into the classical vital staining and the reticulo-endothelial system. *Cell Tissue Res* **1998,** *292* (2), 395-410.
62. Voloshin, T.; Alishekevitz, D.; Kaneti, L.; Miller, V.; Isakov, E.; Kaplanov, I.; Voronov, E.; Fremder, E.; Benhar, M.; Machluf, M.; Apte, R. N.; Shaked, Y., Blocking IL1beta Pathway Following Paclitaxel Chemotherapy Slightly Inhibits Primary Tumor Growth but Promotes Spontaneous Metastasis. *Mol Cancer Ther* **2015,** *14* (6), 1385-1394.

63. Jin, S. W.; Beis, D.; Mitchell, T.; Chen, J. N.; Stainier, D. Y., Cellular and molecular analyses of vascular tube and lumen formation in zebrafish. *Development* **2005,** *132* (23), 5199-5209.
64. Ellett, F.; Pase, L.; Hayman, J. W.; Andrianopoulos, A.; Lieschke, G. J., mpeg1 promoter transgenes direct macrophage-lineage expression in zebrafish. *Blood* **2011,** *117* (4), e49-56.
65. Nguyen-Chi, M.; Phan, Q. T.; Gonzalez, C.; Dubremetz, J. F.; Levraud, J. P.; Lutfalla, G., Transient infection of the zebrafish notochord with E. coli induces chronic inflammation. *Dis Model Mech* **2014,** *7* (7), 871-882.
66. Bussmann, J.; Bos, F. L.; Urasaki, A.; Kawakami, K.; Duckers, H. J.; Schulte-Merker, S., Arteries provide essential guidance cues for lymphatic endothelial cells in the zebrafish trunk. *Development* **2010,** *137* (16), 2653-2657.
67. Hogan, B. M.; Herpers, R.; Witte, M.; Helotera, H.; Alitalo, K.; Duckers, H. J.; Schulte-Merker, S., Vegfc/Flt4 signalling is suppressed by Dll4 in developing zebrafish intersegmental arteries. *Development* **2009,** *136* (23), 4001-4009.
68. Mathias, J. R.; Perrin, B. J.; Liu, T. X.; Kanki, J.; Look, A. T.; Huttenlocher, A., Resolution of inflammation by retrograde chemotaxis of neutrophils in transgenic zebrafish. *J Leukoc Biol* **2006,** *80* (6), 1281-1288.
69. Thisse, C.; Thisse, B., High-resolution in situ hybridization to whole-mount zebrafish embryos. *Nat Protoc* **2008,** *3* (1), 59-69.
70. Varshney, G. K.; Pei, W.; LaFave, M. C.; Idol, J.; Xu, L.; Gallardo, V.; Carrington, B.; Bishop, K.; Jones, M.; Li, M.; Harper, U.; Huang, S. C.; Prakash, A.; Chen, W.; Sood, R.; Ledin, J.; Burgess, S. M., High-throughput gene targeting and phenotyping in zebrafish using CRISPR/Cas9. *Genome Res* **2015,** *25* (7), 1030-1042.
71. Carrington, B.; Varshney, G. K.; Burgess, S. M.; Sood, R., CRISPR-STAT: an easy and reliable PCR-based method to evaluate target-specific sgRNA activity. *Nucleic Acids Res* **2015,** *43* (22), e157.
72. Weinstein, B. M.; Stemple, D. L.; Driever, W.; Fishman, M. C., Gridlock, a localized heritable vascular patterning defect in the zebrafish. *Nat Med* **1995,** *1* (11), 1143-1147.
73. Schindelin, J.; Arganda-Carreras, I.; Frise, E.; Kaynig, V.; Longair, M.; Pietzsch, T.; Preibisch, S.; Rueden, C.; Saalfeld, S.; Schmid, B.; Tinevez, J. Y.; White, D. J.; Hartenstein, V.; Eliceiri, K.; Tomancak, P.; Cardona, A., Fiji: an open-source platform for biological-image analysis. *Nat Methods* **2012,** *9* (7), 676-682.
74. Schneider, C. A.; Rasband, W. S.; Eliceiri, K. W., NIH Image to ImageJ: 25 years of image analysis. *Nat Methods* **2012,** *9* (7), 671-675.
75. Pohlert, T., The pairwise multiple comparison of mean ranks package (PMCMR). *R package* **2014,** *27* (2020), 10.

Chapter 3

Stabilin-1 is required for the endothelial clearance of small anionic nanoparticles

Published:

Arias-Alpizar, G.; Koch, B.; Hamelmann, N. M.; Neustrup, M. A.; Paulusse, J. M. J.; Jiskoot, W.; Kros, A.; Bussmann, J., Stabilin-1 is required for the endothelial clearance of small anionic nanoparticles. Nanomedicine 2021, 34, 102395.

Image: A new Stabilin ligand, lipopolysaccharide (in green) removed from circulation by scavenging endothelial cells, macrophages in magenta

3.1 Abstract

Clearance of nanoparticles (NPs) after intravenous injection -mainly by the liver- is a critical barrier for the clinical translation of nanomaterials. Physicochemical properties of NPs are known to influence their distribution through cell-specific interactions; however, the molecular mechanisms responsible for liver cellular NP uptake are poorly understood. Liver sinusoidal endothelial cells and Kupffer cells are critical participants in this clearance process. Here we use a zebrafish model for liver-NP interaction to identify the endothelial scavenger receptor Stabilin-1 as a non-redundant receptor for the clearance of small anionic NPs. Furthermore, we show that physiologically, Stabilin-1 is required for the removal of bacterial lipopolysaccharide (LPS/endotoxin) from circulation and that Stabilin-1 cooperates with its homolog Stabilin-2 in the clearance of larger (~100 nm) anionic NPs. Our findings allow optimization of anionic nanomedicine biodistribution and targeting therapies that use Stabilin-1 and -2 for liver endothelium-specific delivery.

3.2 Introduction

Clinical application of nanoparticles (NPs) after intravenous (*i.v.*) administration and delivery of their cargo (*i.e.* drugs, DNA, RNA) are hampered by the rapid sequestration of NPs, mainly by cells in the liver.[1, 2] Consequently, removal of NPs with sizes above the renal filtration limit (~5.5 nm) from blood plasma,[3] leads to the accumulation of most NPs in the liver. Kupffer cells (KCs), the tissue-specific macrophages that are located on the luminal side of the liver capillary vasculature (*i.e.* sinusoids), recognize and internalize NPs and were long thought to be the only liver cell type responsible for NP clearance *in vivo*. However, recent studies on the cellular distribution of NPs within the liver have revealed important contributions of B-lymphocytes, hepatocytes, hepatic stellate cells and especially liver sinusoidal endothelial cells (LSECs).[4]

The relative contribution of KCs and LSECs to the clearance of circulating NPs depends mainly on size. Phagocytosis by KCs is responsible for clearance of particles with a size >500 nm.[5, 6] These NPs are captured by KCs either directly through endocytic receptors on their surface (such as scavenger and mannose receptors), or indirectly, after binding of serum proteins to the NP surface (*i.e.* opsonization) and subsequent recognition of the bound proteins by Fc- and complement receptors.[7] Compared to KCs, clearance by the more numerous LSECs (present in an approximately 1:2 ratio)[4] is largely dependent on clathrin-mediated endocytosis and is limited to particles with a size <500 nm.[8] Although for LSECs the molecular mechanisms leading to cellular NP uptake are less well understood, it is known that LSECs internalize biological colloids – such as viral particles,[9] bacterial lipopolysaccharide (LPS),[10, 11] oxidized lipoprotein particles[11, 12] and immune complexes[13] – at a similar rate to, or exceeding uptake by KCs.

Analysis and identification of the molecular mechanisms that mediate NP clearance will help in the challenging task of translation of nanomedicines. The analysis of LSEC function is complicated due to the rapid dedifferentiation of LSECs *in vitro*[14] and relies, consequently, on *in vivo* animal models. Recently, we have established an *in vivo* zebrafish model for NP clearance and have identified a cell type homologous to LSECs in the early zebrafish embryo.[15] These cells, which we named scavenging endothelial cells (SECs), in analogy with previously identified non-mammalian LSEC homologs[16] – are not located in the liver (as in mammals). Instead, they line the first embryonic veins and provide blood clearance before the liver vasculature becomes functional. Zebrafish is a

convenient model owing to their ease of genetic manipulation and optical transparency in embryonic stages that provides the opportunity to combine genome-editing techniques and non-invasive microscopy imaging in real-time. Furthermore, zebrafish embryos are used to screen and optimize formulations prior to clinical studies. Remarkably, the clearance function of SECs and their gene expression signature in the zebrafish are comparable to those of the mammalian LSECs, as demonstrated by the presence of several endocytic receptors including several scavenger receptors.[17]

LSEC-specific scavenger receptors are prominent candidates for mediating NP clearance in this cell type, since they have been reported to interact and endocytose a wide range of ligands including modified lipoprotein particles,[12] bacterial and viral pathogens,[18] and exosomes.[19] One of the LSEC-specific scavenger receptors – Stabilin-2 – has been found to bind and internalize apoptotic bodies[20] as well as exogenous ligands, such as antisense oligonucleotides[21] and NPs.[22] Indeed, by generating a zebrafish *stab2* knockout line, we showed that Stabilin-2 is an important receptor for SEC-mediated clearance of anionic NPs.[15] However, we also observed that some negatively charged NPs were not only dependent on this receptor for clearance, demonstrated by the uptake of NPs in the SECs even in the absence of a functional Stabilin-2.

In this study, we identify a requirement for the *stab2* homolog, Stabilin-1 (encoded by *stab1* gene), in the removal of small (~6-30 nm) NPs from circulation. These two scavenger receptors have highly similar domain structure, consistent with the binding of Stabilin-1 to most (but not all) Stabilin-2 ligands *in vitro*,[23] suggestive of functional redundancy.[24] In addition, we generated *stab1/stab2* double knockout zebrafish embryos to provide evidence that Stabilin receptors complement each other in NP clearance of larger NPs (~100 nm size), as well as in the removal of bacterial LPS from the circulation. Differential scavenging function between Stabilin-1 and Stabilin-2 suggests size as a determinant for receptor specificity.

3.3 Results

Generation and characterization of *stab1* and *stab2* double knockout zebrafish

Liver endothelium is characterized by the presence of scavenger receptors strongly expressed on the membrane cell surface. Given that the clearance of some anionic NPs are not exclusively dependent on the scavenging function of Stabilin-2,[15] we hypothesized that one or more other scavenger receptor(s) expressed in LSECs might be involved in the removal of NPs. To identify additional clearance receptors, we first analyzed the RNA expression of all scavenger receptors in LSECs from mice liver, based on published single-cell RNA sequencing datasets,[25-27] (**Supplementary Table 1**). Although this analysis revealed that *Stab2* is the most abundant scavenger receptor expressed in LSECs, the expression of seven other scavenger receptors (*Msr1, Scarb1, CD36, Scarf1, Mrc1, CXCl16* and *Stab1*) was consistently observed. Of these, the mannose receptor (*Mrc1*) and *Stab1* are the most abundant scavenger receptors expressed by LSECs besides *Stab2*. We previously reported that the zebrafish orthologues of these genes (*mrc1a* and *stab1*) are also highly expressed on SECs.[15] Since Stabilin-1 binds similar ligands as Stabilin-2,[23] we further analyzed the role of this receptor in NP clearance.

To this end, we generated a zebrafish *stab1* mutant line through CRISPR/Cas mutagenesis (guide RNA sequence in **Supplementary Table 2**). In this strain (*stab1*^{ibl3}), a deletion of one nucleotide causes a frame-shift, leading to a premature stop codon after amino acid number eighty-five. The predicted gene product is a truncated protein lacking most conserved domains, including the fasciclin, EGF-like and LINK domains (**Figure 1a**). This gene knockout approach allow us to study the biodistribution of NPs in zebrafish embryo and to compare the clearance by SECs in the presence and/or absence of functional Stabilin receptor(s). To study the combined contributions of Stabilin-1 and Stabilin-2, embryos with mutations in both *stab1* and *stab2 (stab*^{DKO}*)* were also generated intercrossing *stab1*^{ibl3} and *stab2*^{ibl2} carriers. Characterization of the generated mutants was performed by whole-mount *in situ* hybridization (ISH). Using antisense RNA probes we found a strong reduction of *stab1* expression in *stab1*^{ibl3} homozygous mutant embryos, consistent with nonsense-mediated decay (NMD) of the mutant RNA, whereas *stab2* and *mrc1a* expression were unaffected, indicating normal SEC differentiation (**Figure 1b**).

In *stab*^{DKO} embryos, expression of both *stab1* and *stab2* was also reduced through NMD. Of note, *stab2* expression was found to be slightly increased in *stab*^{DKO} compared to the signal in *stab2* mutant embryos. Importantly, *mrc1a* expression in *stab*^{DKO} embryos was maintained, indicating that SEC differentiation occurred even after the combined loss of *stab1* and *stab2.* Homozygous *stab1* zebrafish mutants develop a normal blood and lymphatic vascular system and we did not observe the previously described defects in lymphatic development induced by morpholino oligonucleotide-mediated after *stab1* knockdown[28] (**Figure 1c**). *Stab1* mutant embryos develop without obvious morphological defects into viable and fertile adults (**Figure 1d**) similar to *stab2* mutant zebrafish, as well as adult Stab1 knockout mice. Strikingly, although Stab1/2 double knockout mice display reduced viability due to kidney failure, adult *stab*^{DKO} zebrafish did not show increased mortality or pathology.

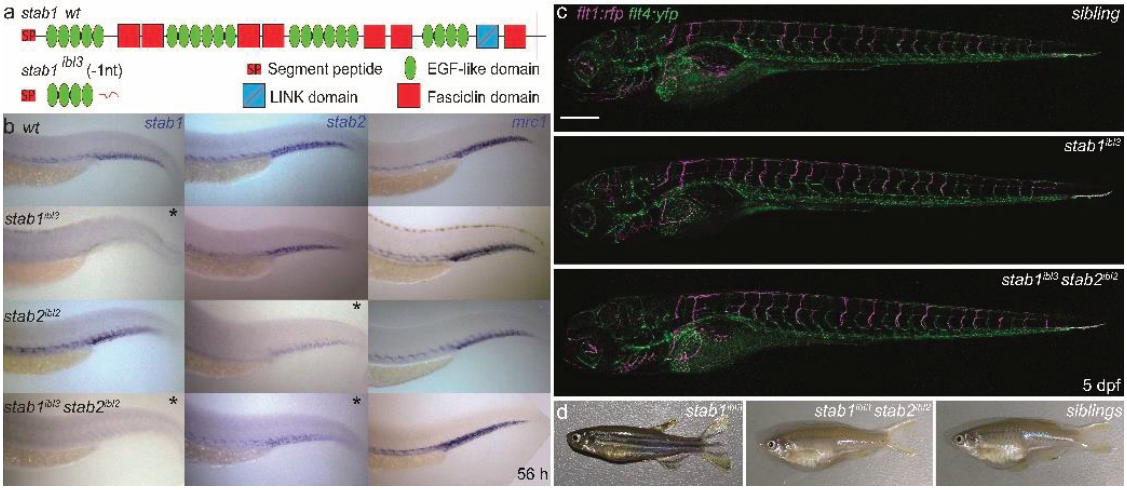

Figure 1. Generation and characterization of *stab1* and *stab1/stab2* mutants. (a) Schematic representation of a *stab1* domain structure predicted to be expressed from the wt Stabilin-1 and the *stab1*^{ibl3} allele. **(b)** *In situ* hybridization (ISH), mRNA expression of *stab1, stab2,* and *mrc1* in wt, *stab1*^{ibl3}, *stab2*^{ibl2} single mutants and s*tab1*^{ibl3}*stab2*^{ibl2} double mutant. *Reduced expression. **(c)** Tg(*fli1:*RFP *fli4:*YFP) *stab1*^{ibl3} mutant, s*tab1*^{ibl3}*stab2*^{ibl2} double mutant, and sibling at 5 dpf. Scale bar: 250 µm. **(d)** Representative fertile adult female *stab1*^{ibl3} single mutant, *stab1*^{ibl3}*stab2*^{ibl2} double mutant and sibling zebrafish.

Identification of Stabilin-1 function in the clearance of anionic NPs

Previously we found that two types of NPs were efficiently cleared by SECs even in the absence of *stab2* expression.[15] Specifically, these were quantum dots (Qdots) with a negatively charged surface coating and Cowpea Chlorotic Mottle

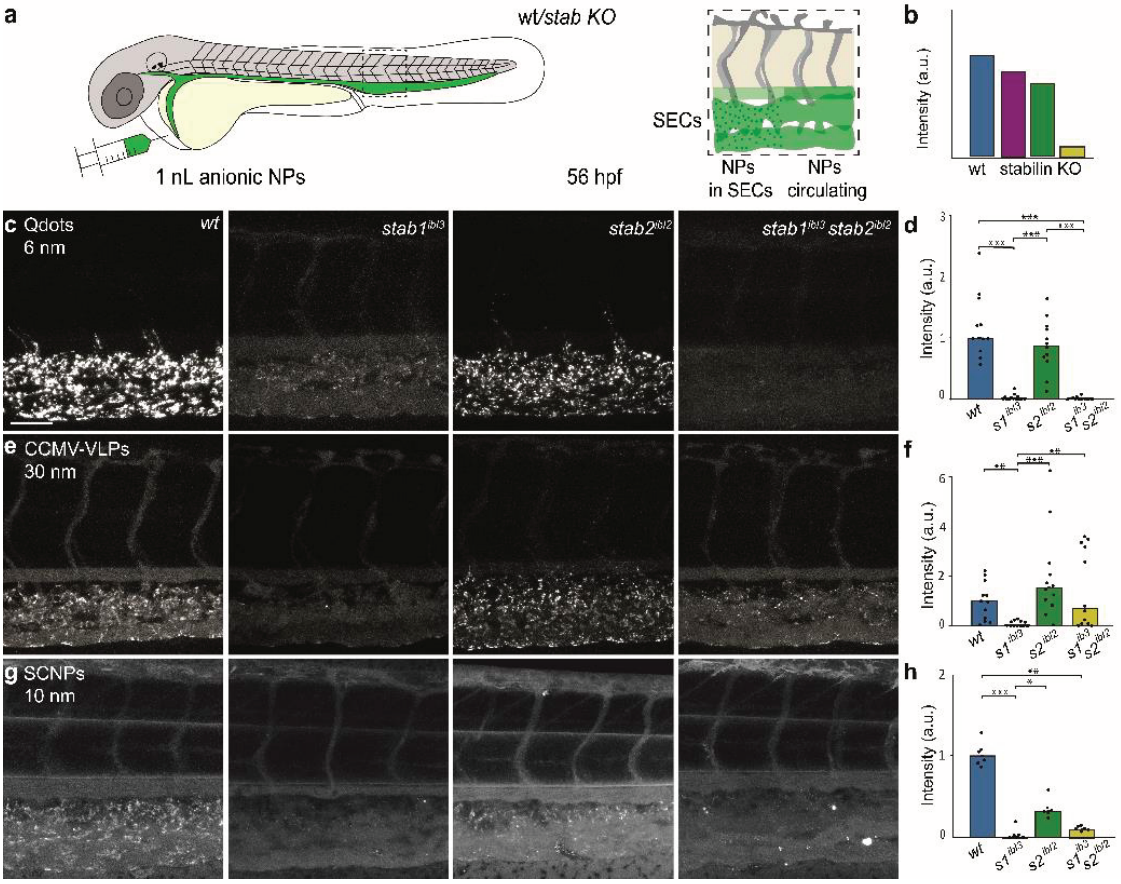

Figure 2. Clearance of small anionic NPs occurs mainly through Stabilin-1. (a) Schematics showing the site of injection within a 56 hours post fertilization (hpf) wt or *stab* knockout zebrafish. In a box, the caudal vein region, where SECs expressing Stabilins are located, a representation of NP circulating or cleared by SECs. **(b)** Representative graph comparing intensity of fluorescent NPs in wt and *stab* mutants. **(c-d)** Tissue level view and quantification of fluorescently labeled Qdots. **(e-f)** CCMV-VLP **(g-h)** SCNPs. After *i.v.* injection (1 nL) in wt *(AB/TL), stab1*^{ibl3}*, stab2*^{ibl2} single mutants and *stab1*^{ibl3}*stab2*^{ibl2} double mutants at 1-1.5 hpi. Scale bar: 50 µm. Bar height represents median values, dots represent individual data points, and brackets indicate significant values (*P< 0.05, **P<0.01, ***P<0,001) based on Kruskal-Wallis tests followed by two-tailed Dunn's tests with Bonferroni correction.

Virus derived virus-like particles (CCMV-VLPs), which are non-enveloped protein capsids with a hexagonal closed packed structure.[29] As most viruses, these VLPs have a negative surface charge. Biodistribution of the Qdots was unchanged in *stab2* mutants, while only a small reduction in the clearance of CCMV-VLPs was observed. The clearance of these two particle types, however, is apparently mediated through scavenger receptors, since it was completely inhibited by pre-injection with the general scavenger receptor inhibitor, dextran sulfate. Therefore, we injected fluorescently labeled Qdots and CCMV-VLP *i.v.*

into the duct of Cuvier of wildtype (wt), *stab1*^{ibl3}, *stab2*^{ibl2} and *stab*^{DKO} zebrafish embryos at 56 hours post fertilization (hpf) and subsequently imaged their biodistribution with confocal microscopy. The resulting accumulation of NP fluorescence representing SEC-mediated clearance was quantified (see **Methods** for details) on a cellular level in the caudal region of the zebrafish tail (**Figure 2a-b**). Importantly, this region also contains plasma-exposed macrophages, commonly known to remove NPs from circulation and analogous to the mammalian Kupffer cells (exemplified in **Supplementary Figure 1**). Strikingly, for both Qdots and CCMV-VLPs, we observed a strong reduction in NP clearance in both *stab1* ^{ibl3} mutants and *stab*^{DKO} embryos indicating a dominant role for Stabilin-1 in the clearance of these NP types (**Figure 2c-f** and **Supplementary Figure 2a-b**). NPs that were cleared mainly through Stabilin-1 differ in their composition (inorganic *vs.* viral capsids) and surface chemistry, and were also chemically distinct from the NPs cleared mainly through Stabilin-2 (which included lipid and polymeric particles).

The difference in surface chemistry of all NPs studied suggests a more general mechanism where particle size might be an important factor for receptor specificity. To further strengthen this hypothesis, we next injected chemically distinct (polymeric) small NPs. To this end, fluorescently labeled anionic single-chain polymeric NPs (SCNPs) were used. SCNPs are a polymeric NP type which consist of biodegradable polymer chains that are covalently cross-linked and folded to form a small particle.[30] The resulting NP size is defined by the length of the polymer chain and can be used to obtain small, uniform polymer NPs of 10-20 nm. Injection of ~10 nm SCNPs in the zebrafish embryo revealed that clearance of these particles occurred through SECs as expected. Importantly, SCNP clearance was strongly affected in *stab1* mutants, similar to Qdots and CCMV-VLPs (**Figure 2g-h** and **Supplementary Figure 2c**). This results indicates that - for negatively charged NPs – size, rather than chemical composition, is a predominant factor for receptor specificity.

Stabilin-1 and Stabilin-2 are complementary receptors in the clearance of anionic NPs by SECs

Previous studies on the biodistribution of polymer- and lipid-based NPs including polymersomes,[15, 31] fibrillar supramolecular polymers,[32] solid polystyrene (PS) NPs and liposomes[15] in zebrafish *stab2* mutants revealed a residual uptake of NPs in SECs in the absence of *stab2* expression. Common characteristics of these NPs were a negative surface, but these NPs differed in size, shape, composition and rigidity. To investigate a complementary role of

Stabilin-1 to Stabilin-2 in the clearance of NPs ~100 nm, we injected negatively charged DOPG-liposomes and polymersomes in *stab*^{DKO} embryos. Interestingly, the clearance of both NPs in *stab*^{DKO} embryos was strongly affected, more than that observed in *stab2* single mutants. The loss of a functional Stabilin-1 did not affect the biodistribution of these particles compared to wt embryos (**Figure 3a-d** and **Supplementary Figure 3a-b**), in striking contrast to the biodistribution of the smaller NPs. This indicates a cooperative role of Stabilin-1 and Stabilin-2 in NP clearance, consistent with their highly similar ligand profile.[23]

We next analyze the behavior of more rigid solid NPs. Therefore, we used anionic poly(D,L-lactide-co-glycolide) (PLGA) NPs and spherical silica NPs (siNPs) due to their relevant importance in drug delivery or biomedical imaging agents applications.[33, 34] Similar to polymersomes and DOPG-liposomes, anionic PLGA NPs and siNPs are cleared through SECs in wt zebrafish. Their biodistribution remained unchanged in *stab1* mutants, but clearance was strongly affected in *stab2* mutants, and even more in *stab*^{DKO} mutants (**Figure 3e-h** and **Supplementary Figure 3c-d**). Interestingly, for the PLGA NPs, the absence of SEC clearance resulted in increased macrophage uptake (indicated by white arrows in **Figure 3e,g** and **Supplementary Figure 1**). The absence of molecular interactions between NPs for most of the ~100 nm NPs and SECs in the *stab*^{DKO} embryos is evidence of a combined contribution of Stabilin-1 and Stabilin-2, where Stabilin-2 is the predominant receptor involved in the clearance in this size range. However, this contribution seems to be a more complex process that depends not only on size but also on the particle composition. We observed this behavior for anionic NP type (polystyrene NPs) of different sizes (**Supplementary Figure 4a**). In this case, we first qualitatively confirmed SEC-uptake of these particles through co-injection with fluorescently labeled hyaluronic acid (fluoHA), a Stabilin-2 ligand and a marker for SEC endocytosis (**Supplementary Figure 4b-c**). SEC clearance is only partly affected in *stab*^{DKO} mutants, indicating the presence of at least one additional clearance receptor besides Stabilin-1 and Stabilin-2 (**Supplementary Figure 4d-g**).

Identification of an endogenous Stabilin ligand: bacterial LPS

Clearance of synthetic nanoparticles can only be reflective of physiological mechanisms that are required for the removal of naturally occurring particles in the 10 nm to 200 nm size range. We therefore sought to identify naturally occurring circulating particles of this dimension as a probable physiologic Stabilin ligands. One such ligand is LPS, which is the main component of the outer membrane of Gram-negative bacteria with the lipid A portion, an anchor in the

bacterial cell wall, that provides toxicity and activates immune responses in mammals.[35] We rationally hypothesized that bacterial endotoxin LPS would be one of this natural ligands for three reasons. First, LPS is highly toxic and must be rapidly eliminated from host circulation, which is performed mainly by LSECs scavenger receptors of unknown identity.[10, 18] Second, due to its amphiphilic nature, LPS self-assembles into small anionic NPs with a diameter of ~50 nm, resembling synthetic NPs.[36, 37] Third, Stabilin-2 has been shown to bind to Gram-negative

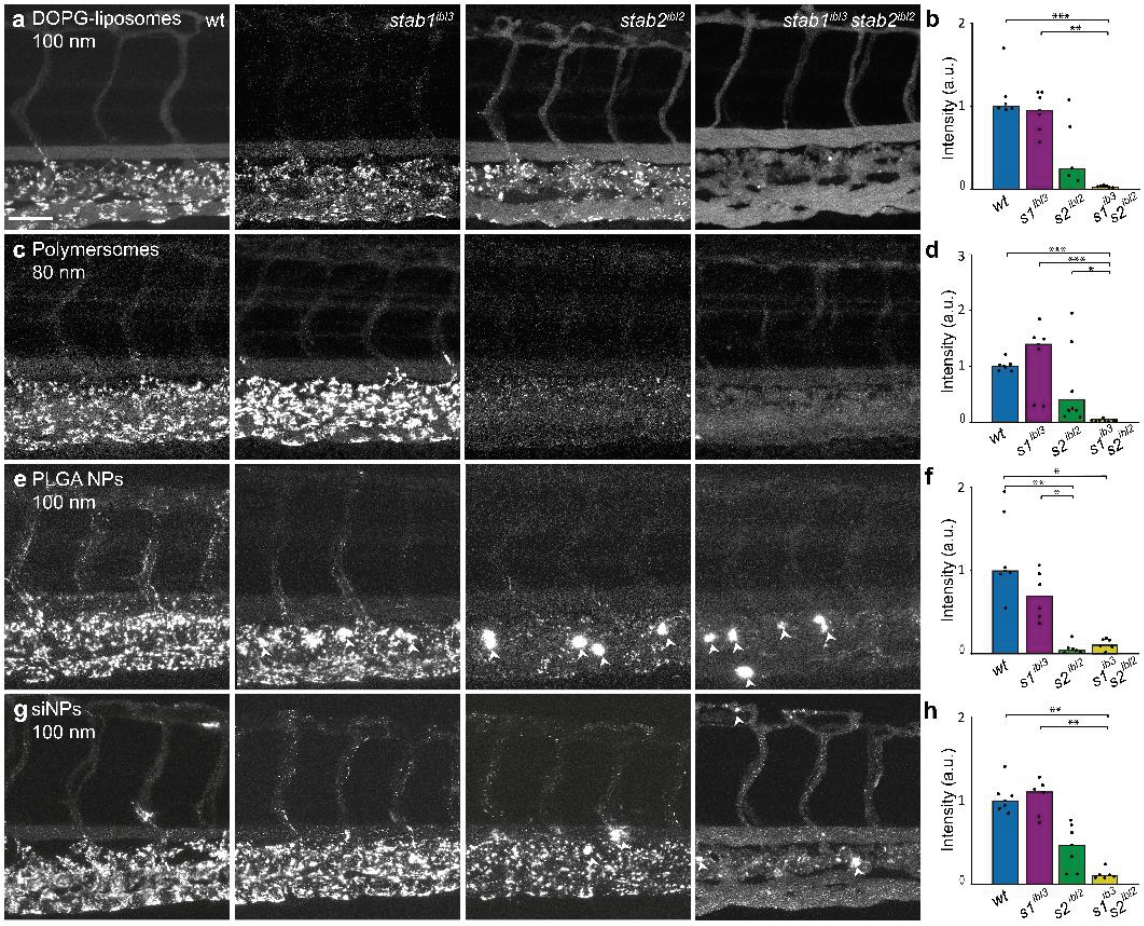

Figure 3. Combined contribution of Stabilin-1 and Stabilin-2 in the clearance of anionic NPs. (a-b) Tissue level view (40x) and quantification of fluorescently labeled DOPG-liposomes, **(c-d)** polymersomes, **(e-f)** PLGA NPs, **(g-h)** siNPs after *i.v.* injection (1 nL) in wt (AB/TL), *stab1*^{ibl3}, *stab2*^{ibl2} single and *stab1*^{ibl3}*stab2*^{ibl2} double mutants at 1-1.5 hours post injection (hpi). White arrows indicate apparent NP uptake within plasma-exposed macrophages. Scale bar: 50 µm. Graphs represent intensity of fluorescent NPs in wt and *stab* mutants. Bar height represents median values, dots are individual data points, and brackets indicate significant values (*P< 0.05, **P<0.01, ***P<0,001) based on Kruskal-Wallis tests followed by two-tailed Dunn's tests with Bonferroni correction.

bacteria - which contain LPS - *in vitro*.[38] To investigate whether circulating LPS is indeed cleared by SECs through Stabilin receptors, fluorescently labeled LPS (Alexa488-LPS) from the Gram-negative bacterium *Salmonella minnesota*[39] was *i.v.* administered. LPS diluted into a salt suspension is proposed to aggregate into micelles at concentrations above the critical micelle concentration (CMC).[36, 37, 40] The LPS concentration injected (500 µg/ml) is above the CMC (~10 µg/ml)[40] even after dilution into the blood of a zebrafish embryo (estimated 30-fold dilution factor, excluding red blood cells, at 2 dpf).[41] Distribution of fluorescent LPS in Tg(*mpeg1:*mCherry) zebrafish, shows no extensive co-localization with labeled macrophages (**Supplementary Figure 5**). This result indicates that phagocytosis by plasma-exposed macrophages does not represent the main clearance route of LPS in the zebrafish embryo, at 56 hpf. Instead, LPS was associated mainly with SECs located in the caudal vein region of wt zebrafish (**Figure 4a,e**), confirming their functional homology to mammalian LSECs.[10]

Next, we injected LPS in *stab2, stab1* and double mutant zebrafish embryos (**Figure 4b-d, f-h**). Association of LPS with SECs was maintained in *stab2* mutants (**Figure 4b, g**). In this case, although a slight decrease in the LPS clearance was observed compared to wt embryos, SEC-uptake was not significantly changed between these two groups (**Figure 4i**). Importantly, LPS uptake by SECs was reduced in *stab1* knockout and completely abrogated in $stab^{DKO}$ mutants, leading to a strong increased level of LPS in circulation (**Figure 4d,h**). This result revealed a cooperative function of Stabilin-1 and Stabilin-2 in LPS uptake and clearance. The loss of LPS uptake in the double knockouts was very similar to that observed after pre-administration of a competitive inhibitor dextran sulfate (**Supplementary Figure 6**), indicating LPS is a common ligand for Stabilin-1 and Stabilin-2, and both receptors are redundantly required for the removal of LPS from the circulation.

3.4 Discussion and Conclusion

The understanding of *in vivo* behavior of NPs and their molecular and cellular interactions after *i.v.* administrations is essential to improve efficacy and pharmacokinetics of nanomaterials. Here, we identify Stabilin-1, a scavenger receptor expressed in LSECs in mammals, is involved in the clearance of small anionic NPs. Interestingly, while mice lacking both *Stab1* and *Stab2* revealed a glomerulofibrotic nephropathy secondary to impaired liver clearance of noxious blood factors[42, 43] leading to strongly reduced viability, we observed that $stab^{DKO}$ adult zebrafish were obtained in mendelian ratios and were phenotypically

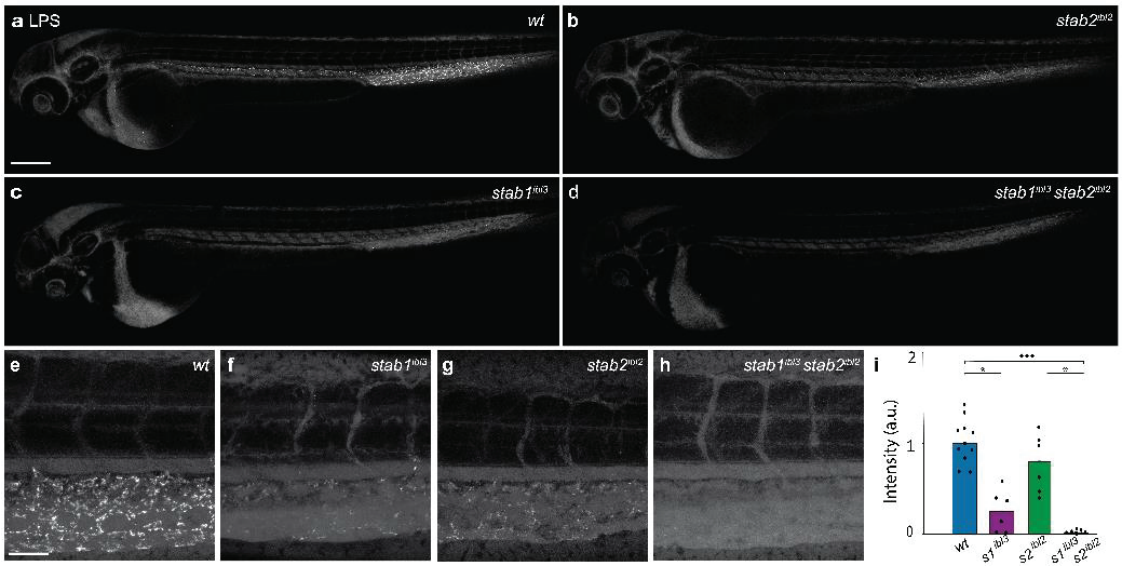

Figure 4. LPS clearance is mediated by Stabilin-1 and Stabilin-2. (a) Biodistribution of Alexa488 LPS (1 nL of 500 µm/mL) in wt (*AB/TL*), **(b)** *stab2*^{ibl2} mutant, **(c)** *stab1*^{ibl3} mutant, **(d)** *stab1*^{ibl3}*stab2*^{ibl2} double mutant at 56 hpf, 1.5 hpi, whole body view (10x). Scale bar: 200 µm. **(e-h)** Tissue level views, caudal region (40x). Scale bar: 50 µm. **(i)** Graph represents intensity of fluorescent LPS in wt and *stab* mutants. Bar height represents median values, dots represent individual data points, and brackets indicate significant values (*P< 0.05, ***P<0,001) based on Kruskal-Wallis tests followed by two-tailed Dunn's tests with Bonferroni correction.

indistinguishable from single mutant and wt zebrafish. Since the reduced viability observed in *Stab1/Stab2* double knockout mice is due mainly to kidney failure, the viability of *stab*^{DKO} fish potentially reflects the high regenerative capacity of the zebrafish kidney.[44]

Through comparison of NP biodistribution in wt and single/double Stabilin mutants we could quantify the relative contribution of Stabilin receptors to the clearance of specific NPs in zebrafish embryos. The analysis of physicochemical properties (**Supplementary Table 3**) and *in vivo* biodistribution of NPs involved in differential uptake for both Stabilin receptors revealed a dependency on size of the particle. Particle size is a critical parameter affecting cellular uptake of nanotherapeutics.[45] Depending on the intended application (*e.g.* drug targeting, vaccine delivery or nucleic acid delivery) an optimal size range is desired.[46, 47] In addition, improved internalization associated with small nanoparticles (~25-50 nm) has been previously shown.[48, 49] Gold nanoparticles in this size range coated with antibodies, for example, display improved endocytosis and regulation of cellular functions.[48] Similarly, ~25-50 nm range has been suggested as an optimal size to reach the maximum cellular uptake.[49] For *in vivo* activity of small

particles, NP clearance by the liver is an important factor influencing biodistribution, but so far has not been linked to a specific receptor. The preference between Stabilin-1 and Stabilin-2 could be attributed indirectly to biological factors or to differences in the structural domains. Biologically, although NP protein corona formation *in vivo* is known to affect the fate of NPs, the different chemistries of the various NPs involved in this study strongly suggest that charge and size are predominant requirements in the interactions between NPs and Stabilin receptors. Structurally, both receptors are initially expressed as a 310 kDa protein, have a very similar domain structure, and are known to share a very common ligand binding profile.[23] So far, it is unknown which structural differences could explain the differential requirement for both receptors to NP clearance.

Besides NPs, the identification of a endogenous ligand of Stabilins, LPS provides important information in the mechanism of clearance of endotoxins. Mechanistically, LPS is known to be detected through toll-like receptor factor 4 and myeloid differentiation factor 2 (TLR4/Md-2) complex in mammals.[50] Inflammatory responses to LPS have been previously observed in the zebrafish,[5] but the signaling involved in LPS-sensing is not well understood. Since SECs in the zebrafish are functionally homologous to LSECs[15] and LPS is known to be recognized by LSECs in mammals,[10, 18] we believe our results contribute to the mechanistic understanding of recognition and clearance of endotoxin LPS – especially at high concentrations above the CMC - important not only in the identification and study of host-pathogen interactions but also in inflammation and immunity responses.

In conclusion, by using the zebrafish as model that allows genetic analysis and imaging of NP clearance *in vivo*, we demonstrate that Stabilin-1 is required independently of Stabilin-2, for endothelial clearance of small anionic Qdots, CCMV-VLP, SCNPs (6-30 nm) from the circulation. Since NPs with very different chemistries are cleared by Stabilin-1, this strongly suggests negative surface charge and size as the predominant factors that determine a requirement for Stabilin-1 in NP clearance. We also show a combined contribution between Stabilin-1 and Stabilin-2 in the clearance of anionic liposomes, polymeric PS and siNPs (~100 nm) and in the removal of LPS. These results reveal a partial redundancy between *stab1* and *stab2*, both important for NPs clearance, and suggest a differential uptake where size is one of the key parameters determining the selective uptake by each receptor. Given size is particularly important in vaccine development, biomedical imaging applications and delivery technologies, improved mechanistic insights into the interactions between size-

selected NPs and the liver at the molecular level contributes to the optimization of small nanomaterials and avenues for receptor-specific targeting.

3.5 Materials and Methods

Nanoparticles

Fluorescent Alexa488-LPS from *Salmonella minnessota,* PS NPs, and Qdots layered with an organic CdSeS/ZnS and a carboxylic acid as a reactive group (consisting of a monolayer of octylamine-modified poly acrylic acid and a monolayer of poly acrylic acid -PnOAm-co-PAA- copolymer cap), were purchased from Life Technologies (Eugene, US) by Thermo Fisher Scientific and Sigma-Aldrich (The Netherlands). SiNPs were purchased from HiQ-Nano SRL (Arnesano, Italy). FluoHA was prepared through conjugation of hyaluronic acid (100 kDa) with fluorescein isothiocyanate (Isomer I, Sigma-Aldrich The Netherlands) as previously described.[51] PLGA NPs were formulated in house with a microfluidic system. DOPG-liposomes containing 1 mol% DOPE-lissamine rhodamine were formulated with a extrusion system as described previously.[15] Negatively charged SCNPs were synthesized, characterized and provided by our collaborators N. Hamelmann and J. Paulusse. (University of Twente, The Netherlands). Rhodamine-loaded polymersomes[31] on PIB/PEG block copolymers were a kind gift from S. Askes & S. Bonnet (Leiden University, The Netherlands). Atto-647 labeled CCMV-VLPs[29] were a kind gift from R. van der Hee & J. Cornelissen (University of Twente, The Netherlands).

Zebrafish handling and strains

Zebrafish (*Danio rerio*) were maintained and handled according to the guidelines from the Zebrafish Model Organism Database (http://zfin.org) and in compliance with the directives of the local animal welfare committee of Leiden University. Housing and husbandry recommendations were followed as recommended by Alestrom *et al*.[52] Fertilization was performed by natural spawning at the beginning of the light period and eggs were raised at 28.5°C in egg water (60 µg/ml Instant Ocean sea salts). The following established zebrafish strains were used in this study: Tg(*mpeg1:*mCherry),[53] Tg(*flt1*^{enh}*:*RFP)^{hu5333},[54] Tg(*flt4*^{BAC}*:*YFP)^{hu7135},[55] *stab2*^{ibl2},[15] *stab1*^{ibl3} (described in this work).

CRISPR/Cas9 mutagenesis

Cloning-free sgRNAs for CRISPR/Cas9 mutagenesis were designed and synthesized as described.[56, 57] 125 pg of sgRNA (**Supplementary Table 2**) and 300 pg cas9 mRNA were co-injected into a single-cell wt embryo fish. Primers nucleotide sequences, sgRNA sequence and predicted *stab1* and *stab2* amino acid sequences in the *stab1*^{ibl3} and *stab2*^{ibl2} were used as reported.[15] Double *stab1*^{ibl3} and *stab2*^{ibl2} mutants were generated by crossing adult homozygous zebrafish *stab2*^{ibl2} and *stab* ^{ibl3} mutants.

In situ hybridization

Whole-mount ISH was performed as described previously.[58] The sequences for probes generation (*stab1*, *stab*2, *mrc1)* were used as reported.[15]

Zebrafish i.v. microinjections and imaging

NPs formulation were injected into 2-day old zebrafish embryos (52-56 hpf) using a modified microangraphy protocol.[59] One nl volume of NP formulation were calibrated and injected into the duct of Cuvier after embryos were embedded in 0.4% agarose containing 0.01% tricaine as described.[15] We created a small injection space by penetrating the skin with the injection microneedle and gently pulling the needle back, thereby creating a small pyramidal space in which the NPs were injected. Representative embryos were randomly selected according to successful injections and imaged by confocal microscopy after one hour post injection. Confocal z-stacks were captured on a Leica TCS SPE or LEICA TCS SP8 confocal microscope, using a 10x air objective (HCX PL FLUOTAR), a 40x water-immersion objective (HCX APO L), or a 63x oil-immersion objective (HC PL APO CS). In order to compare images between strains, microscopy settings (laser intensity, gain and offset) were identical between stacks and sessions. Whole-embryo images were a compilation of 3-4 overlapping z-stacks. Fiji distribution of ImageJ[60, 61] was used to process and quantify images. At least 6 images were used for quantification.

Imaging quantification

Quantification was performed in the caudal region of the zebrafish, a region known to contain Stabilin endothelium, and that includes the dorsal aorta, the caudal vein and the caudal hematopoietic tissue (could include macrophages associated with SECs). First, an average intravascular within the dorsal aorta was

measured within a rectangular area in a single confocal slice that captured the center of the dorsal aorta. This measurement was repeated three times per embryo in independent sites within the dorsal aorta. Next, the maximum intensity value obtained per image was used to adjust the threshold according to the max value measure in the aorta (in circulation), generating a binary image. The strong fluorescence signal observed by accumulated phagocytosed NPs could lead to a misinterpretation of a SEC signal. For that reason and since the aim of this quantification is to compare the contribution of stabilins in the clearance of NPs and not directly the phagocytosis of macrophages, we attempt to remove the signal potentially associated with macrophages by means of size filtering (0,25-20 um) and to use a qualitative approach to refer to macrophages uptake. From the resulting image, a value of 254 was subtracted in order to get values of 0 (no signal) or 1 (fluorescence). The image of interest was multiplied (max x mask) and to obtain the mean intensity and the area (%) of the analyzed image. Having these values, the total area with signal (% area x and total signal /100) and the total signal (mean signal x total area) were calculated. The median intensity value of the total signal obtained from the mutants was normalized against the wt counterpart. The angle of the dorsal aspect of the dorsal aorta (a straight line) was measured and then concatenated. Images were rotated to orient the DA horizontally within the image and were subsequently cropped.

Statistical analysis

For comparisons between multiple groups, we used Kruskal-Wallis tests followed by two-tailed Dunn's tests with Bonferroni correction using the PMCMR package in R or GraphPad Prism. No statistical methods were used to predetermine sample size, but group sizes were greater than 5 in order for the null distribution of the Kruskal-Wallis statistic to approximate the X^2 distribution (with k-1 degrees of freedom). Graphs show all individual data points and the median. Confocal image stacks (raw data) are available upon request.

3.6 Abbreviations

CCMV-VLP	cowpea chlorotic mottle virus derived virus-like particles
dpf	day(s) post fertilization
DOPG	1,2-dioleoyl-*sn*-glycero-3-phospho-(1'-*rac*-glycerol)
ECs	endothelial cells
fluoHA	fluorescently labeled hyaluronic acid
hpi	hour(s) post injection
ISH	*in situ* hybridization
KCs	kupffer cells
LPS	lipopolysaccharide
LSECs	liver sinusoidal endothelial cells
NP	nanoparticle(s)
PIB-PEG	polyisobutylene-polyethylene glycol
PLGA	poly(D,L-lactide-co-glycolide
PS	polystyrene
Qdots	quantum dots
SCNPs	single chain nanoparticles
SECs	scavenging endothelial cells
siNPs	silica nanoparticles
wt	wildtype

3.7 Supporting Information

Supplementary Table 1. Scavenger receptors RNA expression in mouse liver. Comparison of gene expression according to 3 published single-cell RNA sequencing datasets. Values are calculated through dividing the average RNA count over all LSECs for the respective scavenger receptor gene by the average RNA count over all LSECs of all scavenger receptors. The colors indicate the most abundant scavenger receptors expressed in LSECs, consistent in the 3 datasets, from light yellow to red (higher relative expression of one scavenger receptor over all others).

SR family	Gene	Halpern et al.[25]	Tabula Muris[27]	Sabbagh et al.[26]
SR-A1	*Msr1*	1.01	0.71	0.69
SR-A3	*Scara3*	0.00	0.00	0.00
SR-A4	*Colec12*	0.13	0.03	0.05
SR-A5	*Scara5*	0.00	0.00	0.00
SR-A6	*Marco*	0.09	0.00	0.00
SR-B1	*Scarb1*	0.38	0.41	0.24
SR-B2	*Cd36*	0.74	1.91	2.54
SR-D1	*Cd68*	0.09	0.02	0.01
SR-E1	*Olr1*	0.00	0.00	0.01
SR-E2	*Clec7a*	0.13	0.01	0.00
SR-E3	*Mrc1*	9.68	8.14	3.93
SR-E4	*Asgr1*	0.33	0.01	0.00
SR-F1	*Scarf1*	0.50	0.56	0.10
SR-F2	*Scarf2*	0.00	0.00	0.00
SR-F3	*Megf10*	0.00	0.00	0.00
SR-G1	*Cxcl16*	1.08	1.18	0.12
SR-H1	*Stab1*	3.62	3.71	4.10
SR-H2	*Stab2*	5.58	7.27	12.18
SR-I1	*Cd163*	0.12	0.01	0.00
SR-I2	*Cd163l*	0.00	0.00	0.00
SR-J1	*Ager*	0.00	0.00	0.01
SR-K1	*Cd44*	0.26	0.00	0.00
SR-L1	*Lrp1*	0.27	0.02	0.02
SR-L2	*Lrp2*	0.00	0.00	0.00

Supplementary Table 2. Guide RNA sequence for CRISPR/Cas and forward and reverse primers of *stab1* mutant (-1nt).[15] Target sequence in green.

Stab1	Sequence
sgRNA	TAATACGACTCACTATAGGTAG**AAATTGGCGGTCGCC**GTTTTAGAGCTAGAAATAGC
Primer Forward	TGTAAAACGACGGCCAGTAGACTTTGGGTGCTGTAACCAT
Primer Reverse	GTGTCTTCCTAACGTACATTTGAACCCGT

Supplementary Table 3. Physicochemical properties of NPs used.

NPs	Concentration Injected	Size (nm) ^	PDI	ζ-potential (mV) ^	Reference
Carboxylated QDots	0.25 mg/mL	6 *	ND	-70.8	*
Polymersomes PIB:PEG(1:0.75 mol/ratio)	1 mg/mL	73.34	0.181	-24.0	[62]
DOPG-liposomes	1 mM (total lipids) + 1 mol% DOPE-LR	112.1	0.042	-37.0	[15]
CCMV-VLP T=3 capsids	ND	28	ND	-15.0	[29]**
SCNPs	5 mg/mL	10.0	0.016	-33.0	[30]#
PLGA NPs	0,25 mg/mL	108.0	0.086	-37.1	NA
siNPs 90 nm	10 mg/mL	130.4	0.172	-22.0	*
PS 40 nm 5% solid	0.1 mg/mL	57.3	0.176	-30.7	*
PS 100 nm 2% solid	0.1 mg/mL	107.3	0.022	-51.5	*
PS 200 nm 2 % solid	0.2 mg/mL	246.3	0.090	-51.0	*
PS 500 nm 2 % solid	0.4 mg/mL	553.8	0.339	-46.8	*
PS 1000 nm 2% solid	2 mg/mL	1191.8	0.628	-74.7	*
PS 2000 nm 2% solid	10 mg/mL	1474.0	0.128	-40.1	*

^Measurements were performed in technical triplicates.
PDI: polydispersity index. ND: Not determined. NA: Not applicable. LR: Lissamine rhodamine.
*Commercially available.
** Unmodified (no conjugated dye).
# Anionic SCNPs (DTAF labeled, not included in ref [9]).

Size and zeta potentials measurements

The formulations were analyzed at room temperature in ddH_2Oon a Malvern Zetasizer Nano ZS (Malvern Panalytical B.V., Almelo, the Netherlands) to determine the hydrodynamic particles sizes and polydispersity indexes (PDIs)

with dynamic light scattering (measured at a detection angle of 174.7°), and the zeta potentials with laser Doppler electrophoresis. Before the measurements, the formulations were diluted. The measurements were performed in technical triplicates and the average was reported.

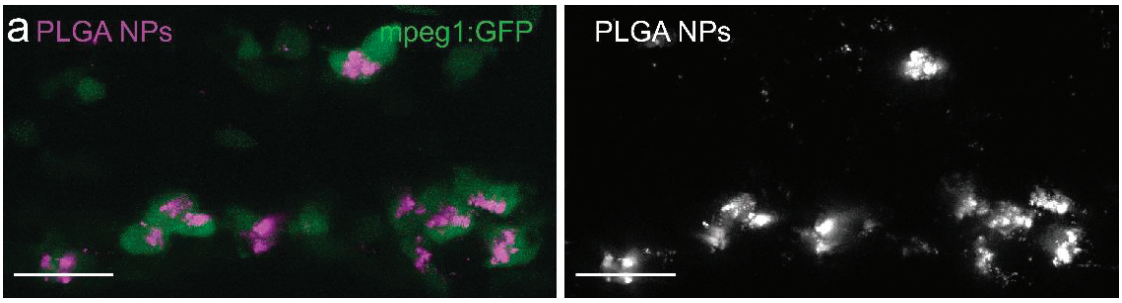

Supplementary Figure 1. Nanoparticles phagocytosed by plasma-exposed macrophages. (a) Colocalization of PLGA NPs (magenta) in *stab*^{DKO} zebrafish Tg(*mpeg1*:mCherry) stably expressing GFP in macrophages at 1.5 hpi. Scale bars: 25 μm.

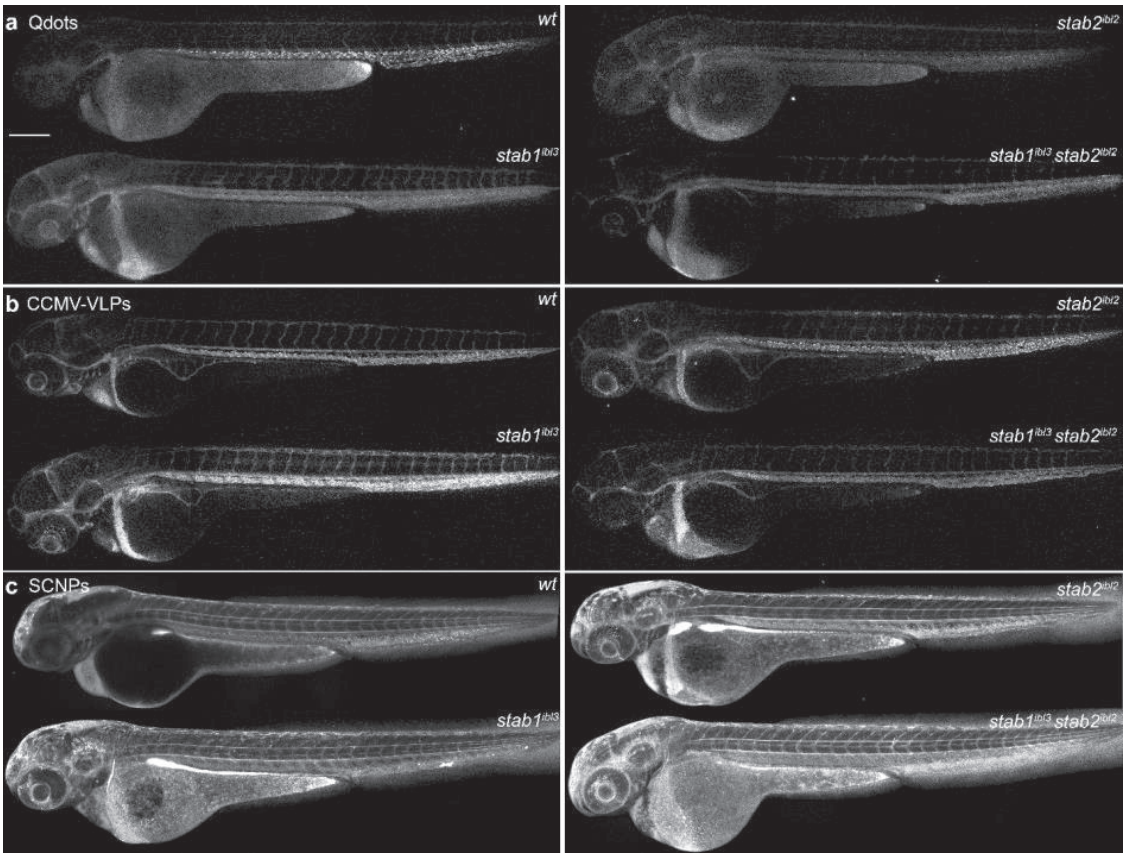

Supplementary Figure 2. Anionic NPs cleared mainly by Stabilin-1 receptor. (a) Biodistribution and uptake of Qdots, **(b)** CCMV-VLPs, and **(c)** SCNPs in whole zebrafish view of wildtype (*AB/TL*), *stab1*^{ibl3}, *stab2*^{ibl2} single mutants and *stab1*^{ibl3} *stab2*^{ibl2} double mutants at 56 hpf,1-1.5 hpi. Scale bar 200 μm.

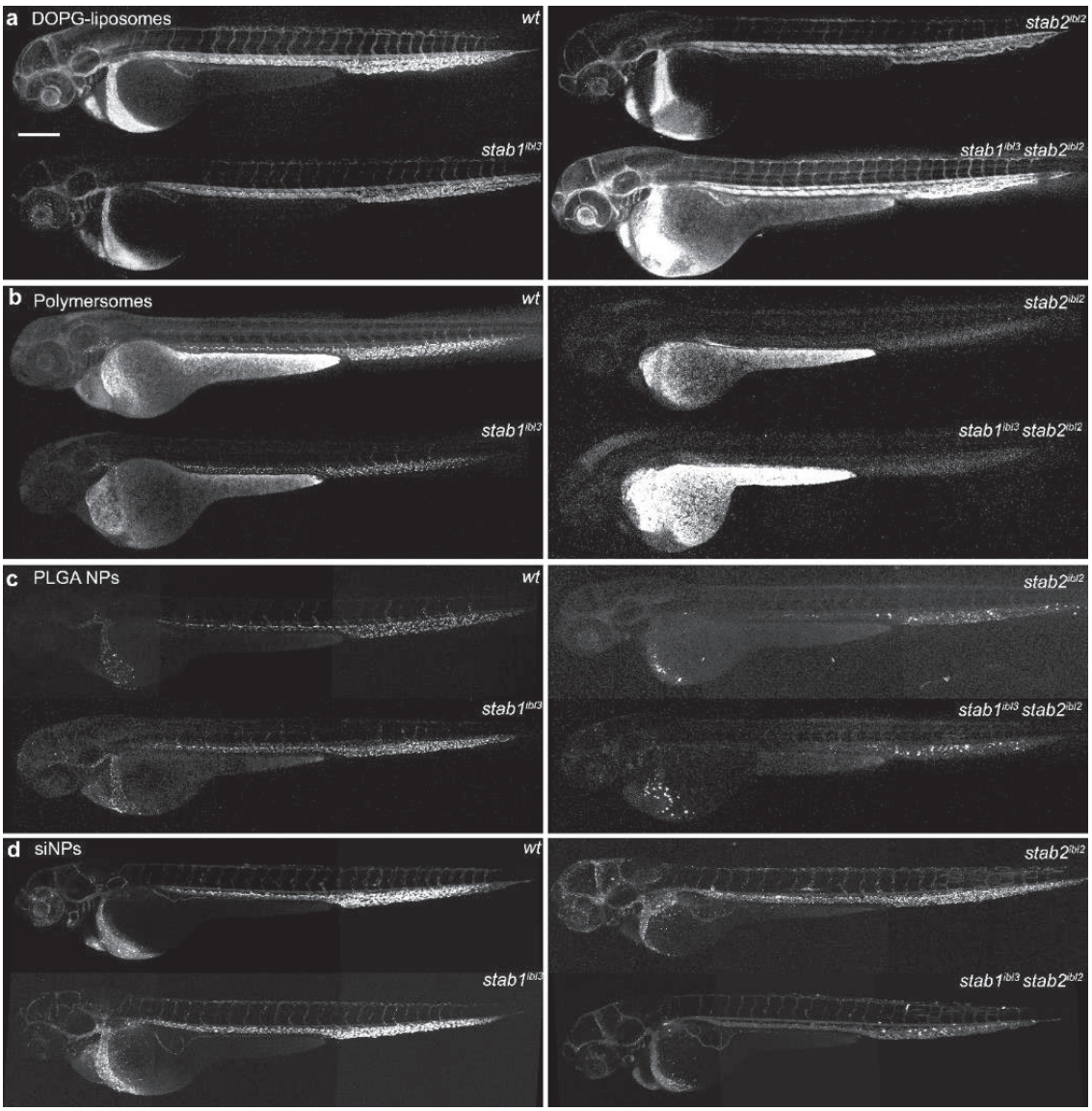

Supplementary Figure 3. Anionic NPs cleared by Stabilin-1 and/or Stabilin-2 receptors. (a) Biodistribution and uptake of DOPG-liposomes, **(b)** Polymersomes **(c)** PLGA NPs, **(d)** siNPs in wildtype (*AB/TL*), *stab1*^{ibl3}, *stab2*^{ibl2} single mutants and *stab1*^{ibl3} *stab2*^{ibl2} double mutants at 56 hpf,1-1.5 hpi. Scale bar 200 μm.

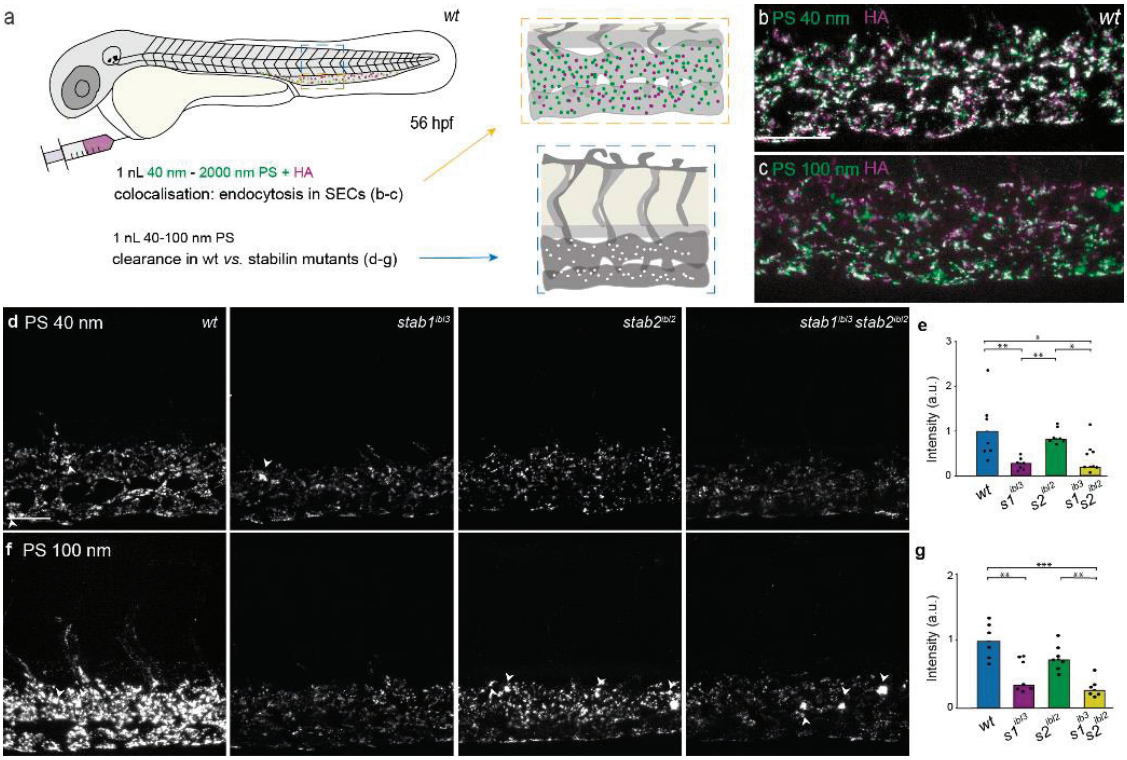

Supplementary Figure 4. Uptake of PS particles by SECs through Stabilin-1 and/or Stabilin-2. (a) Schematic representation of a zebrafish embryo and the injection site at 2 days old (54-56 hpf). Boxes shows the region imaged. **(b-c)** Distribution and endocytosis of PS, in green, with a size of 40, and 100 respectively, co-injected with fluoHA (20 mg/mL) (in magenta) in wt zebrafish at 1-1.5 hpi. FluoHA was used as an *in vivo* marker for SECs, colocalization of fluoHA with PS indicates endocytosis. **(d-g)** Uptake and images quantification of 40 nm and 100 nm PS particles (1 nL of 100 µg/mL) in wt, and *stabilin* mutants at 1-1.5 hpi. White arrows indicate apparent PS uptake in blood resident macrophages. Scale bars: 50 µm. Bar height represents median values, dots represent individual data points, and brackets indicate significant values (*P< 0.05, **P<0.01, ***P<0,001) based on Kruskal-Wallis tests followed by two-tailed Dunn's tests with Bonferroni correction.

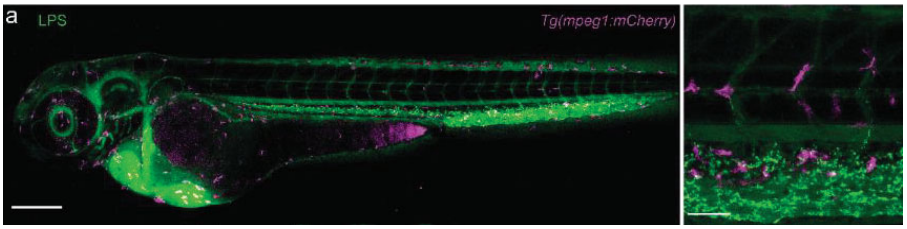

Supplementary Figure 5. Distribution of fluorescently labeled LPS. (a) Alexa488-LPS in Tg(*mpeg1*:mCherry) zebrafish stably expressing mCherry in macrophages at 1.5 hpi. Scale bars: 200 µm (whole body view) and 50 µm (tissue level view).

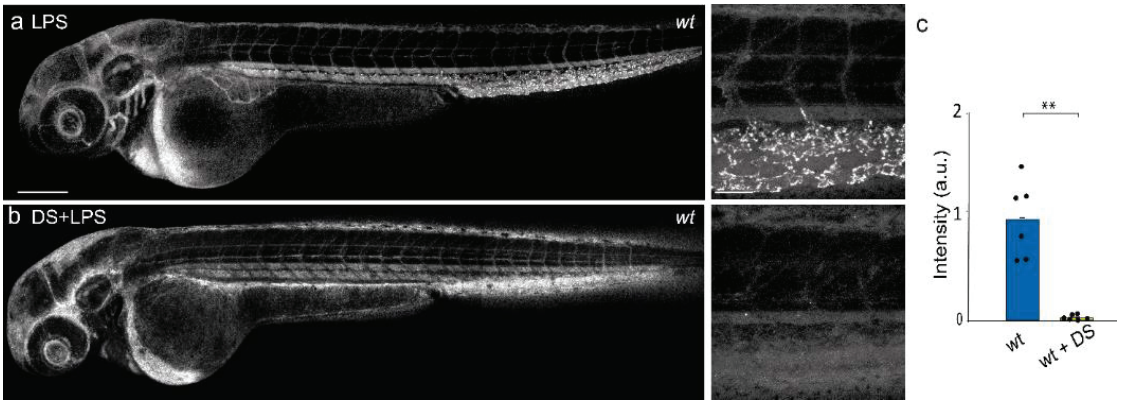

Supplementary Figure 6. Dextran sulfate (DS) inhibits uptake of LPS by SECs. (a) Biodistribution of Alexa488 LPS in wildtype (*AB/TL*) **(b)** LPS biodistribution after 30 min of dextran sulfate (20 mg/mL) at 56 hpf, 1.5 hpi, whole body view and respective tissue level view (caudal region). Scale bar: 200 µm (whole view) and 50 µm (tissue level). **(c)** Graph represents intensity of fluorescent LPS in wt and after administration of dextran sulfate, DS. Bar height represents median values, dots represent individual data points, and brackets indicate significant value (**P<0.01) based on Kruskal-Wallis tests followed by two-tailed Dunn's tests with Bonferroni correction using the PMCMR package in R.

3.9 References

1. Zhang, Y. N.; Poon, W.; Tavares, A. J.; McGilvray, I. D.; Chan, W. C. W., Nanoparticle-liver interactions: Cellular uptake and hepatobiliary elimination. *J Control Release* **2016,** *240*, 332-348.
2. Polo, E.; Collado, M.; Pelaz, B.; Del Pino, P., Advances toward More Efficient Targeted Delivery of Nanoparticles in Vivo: Understanding Interactions between Nanoparticles and Cells. *ACS Nano* **2017,** *11* (3), 2397-2402.
3. Choi, H. S.; Liu, W.; Misra, P.; Tanaka, E.; Zimmer, J. P.; Itty Ipe, B.; Bawendi, M. G.; Frangioni, J. V., Renal clearance of quantum dots. *Nat Biotechnol* **2007,** *25* (10), 1165-1170.
4. Tsoi, K. M.; MacParland, S. A.; Ma, X. Z.; Spetzler, V. N.; Echeverri, J.; Ouyang, B.; Fadel, S. M.; Sykes, E. A.; Goldaracena, N.; Kaths, J. M.; Conneely, J. B.; Alman, B. A.; Selzner, M.; Ostrowski, M. A.; Adeyi, O. A.; Zilman, A.; McGilvray, I. D.; Chan, W. C., Mechanism of hard-nanomaterial clearance by the liver. *Nat Mater* **2016,** *15* (11), 1212-1221.
5. Hayashi, Y.; Takamiya, M.; Jensen, P. B.; Ojea-Jimenez, I.; Claude, H.; Antony, C.; Kjaer-Sorensen, K.; Grabher, C.; Boesen, T.; Gilliland, D.; Oxvig, C.; Strahle, U.; Weiss, C., Differential Nanoparticle Sequestration by Macrophages and Scavenger Endothelial Cells Visualized in Vivo in Real-Time and at Ultrastructural Resolution. *ACS Nano* **2020,** *14* (2), 1665-1681.
6. Shiratori, Y.; Tananka, M.; Kawase, T.; Shiina, S.; Komatsu, Y.; Omata, M., Quantification of sinusoidal cell function in vivo. *Semin Liver Dis* **1993,** *13* (1), 39-49.
7. Tenzer, S.; Docter, D.; Kuharev, J.; Musyanovych, A.; Fetz, V.; Hecht, R.; Schlenk, F.; Fischer, D.; Kiouptsi, K.; Reinhardt, C.; Landfester, K.; Schild, H.; Maskos, M.; Knauer, S. K.; Stauber, R. H., Rapid formation of plasma protein corona critically affects nanoparticle pathophysiology. *Nat Nanotechnol* **2013,** *8* (10), 772-781.
8. Rejman, J.; Oberle, V.; Zuhorn, I. S.; Hoekstra, D., Size-dependent internalization of particles via the pathways of clathrin- and caveolae-mediated endocytosis. *Biochem J* **2004,** *377* (Pt 1), 159-169.
9. Breiner, K. M.; Schaller, H.; Knolle, P. A., Endothelial cell-mediated uptake of a hepatitis B virus: a new concept of liver targeting of hepatotropic microorganisms. *Hepatology* **2001,** *34* (4 Pt 1), 803-808.
10. Yao, Z.; Mates, J. M.; Cheplowitz, A. M.; Hammer, L. P.; Maiseyeu, A.; Phillips, G. S.; Wewers, M. D.; Rajaram, M. V.; Robinson, J. M.; Anderson, C. L.; Ganesan, L. P., Blood-Borne Lipopolysaccharide Is Rapidly Eliminated by Liver Sinusoidal Endothelial Cells via High-Density Lipoprotein. *J Immunol* **2016,** *197* (6), 2390-2399.
11. van Oosten, M.; van de Bilt, E.; van Berkel, T. J.; Kuiper, J., New scavenger receptor-like receptors for the binding of lipopolysaccharide to liver endothelial and Kupffer cells. *Infect Immun* **1998,** *66* (11), 5107-5112.
12. Li, R.; Oteiza, A.; Sorensen, K. K.; McCourt, P.; Olsen, R.; Smedsrod, B.; Svistounov, D., Role of liver sinusoidal endothelial cells and stabilins in elimination of oxidized low-density lipoproteins. *Am J Physiol Gastrointest Liver Physiol* **2011,** *300* (1), G71-81.
13. Wohlleber, D.; Knolle, P. A., The role of liver sinusoidal cells in local hepatic immune surveillance. *Clin Transl Immunology* **2016,** *5* (12), e117.
14. Sellaro, T. L.; Ravindra, A. K.; Stolz, D. B.; Badylak, S. F., Maintenance of hepatic sinusoidal endothelial cell phenotype in vitro using organ-specific extracellular matrix scaffolds. *Tissue Eng* **2007,** *13* (9), 2301-2310.
15. Campbell, F.; Bos, F. L.; Sieber, S.; Arias-Alpizar, G.; Koch, B. E.; Huwyler, J.; Kros, A.; Bussmann, J., Directing Nanoparticle Biodistribution through Evasion and Exploitation of Stab2-Dependent Nanoparticle Uptake. *ACS Nano* **2018,** *12* (3), 2138-2150.
16. Seternes, T.; Sorensen, K.; Smedsrod, B., Scavenger endothelial cells of vertebrates: a nonperipheral leukocyte system for high-capacity elimination of waste macromolecules. *Proc Natl Acad Sci U S A* **2002,** *99* (11), 7594-7597.
17. Wong, K. S.; Proulx, K.; Rost, M. S.; Sumanas, S., Identification of vasculature-specific genes by microarray analysis of Etsrp/Etv2 overexpressing zebrafish embryos. *Dev Dyn* **2009,** *238* (7), 1836-1850.
18. Hampton, R. Y.; Golenbock, D. T.; Penman, M.; Krieger, M.; Raetz, C. R., Recognition and plasma clearance of endotoxin by scavenger receptors. *Nature* **1991,** *352* (6333), 342-344.

19. Verweij, F. J.; Revenu, C.; Arras, G.; Dingli, F.; Loew, D.; Pegtel, D. M.; Follain, G.; Allio, G.; Goetz, J. G.; Zimmermann, P.; Herbomel, P.; Del Bene, F.; Raposo, G.; van Niel, G., Live Tracking of Inter-organ Communication by Endogenous Exosomes In Vivo. *Dev Cell* **2019,** *48* (4), 573-589 e574.
20. Park, S. Y.; Jung, M. Y.; Kim, H. J.; Lee, S. J.; Kim, S. Y.; Lee, B. H.; Kwon, T. H.; Park, R. W.; Kim, I. S., Rapid cell corpse clearance by stabilin-2, a membrane phosphatidylserine receptor. *Cell Death Differ* **2008,** *15* (1), 192-201.
21. Miller, C. M.; Donner, A. J.; Blank, E. E.; Egger, A. W.; Kellar, B. M.; Ostergaard, M. E.; Seth, P. P.; Harris, E. N., Stabilin-1 and Stabilin-2 are specific receptors for the cellular internalization of phosphorothioate-modified antisense oligonucleotides (ASOs) in the liver. *Nucleic Acids Res* **2016,** *44* (6), 2782-2794.
22. Alidori, S.; Bowman, R. L.; Yarilin, D.; Romin, Y.; Barlas, A.; Mulvey, J. J.; Fujisawa, S.; Xu, K.; Ruggiero, A.; Riabov, V.; Thorek, D. L.; Ulmert, H. D.; Brea, E. J.; Behling, K.; Kzhyshkowska, J.; Manova-Todorova, K.; Scheinberg, D. A.; McDevitt, M. R., Deconvoluting hepatic processing of carbon nanotubes. *Nat Commun* **2016,** *7*, 12343.
23. Harris, E. N.; Cabral, F., Ligand Binding and Signaling of HARE/Stabilin-2. *Biomolecules* **2019,** *9* (7), 273.
24. Nowak, M. A.; Boerlijst, M. C.; Cooke, J.; Smith, J. M., Evolution of genetic redundancy. *Nature* **1997,** *388* (6638), 167-171.
25. Halpern, K. B.; Shenhav, R.; Massalha, H.; Toth, B.; Egozi, A.; Massasa, E. E.; Medgalia, C.; David, E.; Giladi, A.; Moor, A. E.; Porat, Z.; Amit, I.; Itzkovitz, S., Paired-cell sequencing enables spatial gene expression mapping of liver endothelial cells. *Nat Biotechnol* **2018,** *36* (10), 962-970.
26. Sabbagh, M. F.; Heng, J. S.; Luo, C.; Castanon, R. G.; Nery, J. R.; Rattner, A.; Goff, L. A.; Ecker, J. R.; Nathans, J., Transcriptional and epigenomic landscapes of CNS and non-CNS vascular endothelial cells. *Elife* **2018,** *7*.
27. Schaum, N.; Karkanias, J.; Neff, N. F.; May, A. P.; Quake, S. R.; Wyss-Coray, T.; Darmanis, S.; Batson, J.; Botvinnik, O.; Chen, M. B., et al., Single-cell transcriptomics of 20 mouse organs creates a Tabula Muris. *Nature* **2018,** *562* (7727), 367-372.
28. Stoll, S. J.; Bartsch, S.; Kroll, J., HOXC9 regulates formation of parachordal lymphangioplasts and the thoracic duct in zebrafish via stabilin 2. *PLoS One* **2013,** *8* (3), e58311.
29. Verwegen, M.; Cornelissen, J. J., Clustered nanocarriers: the effect of size on the clustering of CCMV virus-like particles with soft macromolecules. *Macromol Biosci* **2015,** *15* (1), 98-110.
30. Kroger, A. P. P.; Hamelmann, N. M.; Juan, A.; Lindhoud, S.; Paulusse, J. M. J., Biocompatible Single-Chain Polymer Nanoparticles for Drug Delivery-A Dual Approach. *ACS Appl Mater Interfaces* **2018,** *10* (37), 30946-30951.
31. Askes, S. H.; Pomp, W.; Hopkins, S. L.; Kros, A.; Wu, S.; Schmidt, T.; Bonnet, S., Imaging Upconverting Polymersomes in Cancer Cells: Biocompatible Antioxidants Brighten Triplet-Triplet Annihilation Upconversion. *Small* **2016,** *12* (40), 5579-5590.
32. Saez Talens, V.; Arias-Alpizar, G.; Makurat, D. M. M.; Davis, J.; Bussmann, J.; Kros, A.; Kieltyka, R. E., Stab2-Mediated Clearance of Supramolecular Polymer Nanoparticles in Zebrafish Embryos. *Biomacromolecules* **2020,** *21* (3), 1060-1068.
33. Davis, M. E.; Chen, Z. G.; Shin, D. M., Nanoparticle therapeutics: an emerging treatment modality for cancer. *Nat Rev Drug Discov* **2008,** *7* (9), 771-782.
34. Rezvantalab, S.; Drude, N. I.; Moraveji, M. K.; Güvener, N.; Koons, E. K.; Shi, Y.; Lammers, T.; Kiessling, F., PLGA-Based Nanoparticles in Cancer Treatment. *Frontiers in Pharmacology* **2018,** *9* (1260).
35. Raetz, C. R.; Whitfield, C., Lipopolysaccharide endotoxins. *Annu Rev Biochem* **2002,** *71*, 635-700.
36. Sasaki, H.; White, S. H., Aggregation behavior of an ultra-pure lipopolysaccharide that stimulates TLR-4 receptors. *Biophys J* **2008,** *95* (2), 986-993.
37. Wang, C.; Nelson, T.; Chen, D.; Ellis, J. C.; Abbott, N. L., Understanding lipopolysaccharide aggregation and its influence on activation of Factor C. *J Colloid Interface Sci* **2019,** *552*, 540-553.
38. Adachi, H.; Tsujimoto, M., FEEL-1, a novel scavenger receptor with in vitro bacteria-binding and angiogenesis-modulating activities. *J Biol Chem* **2002,** *277* (37), 34264-34270.
39. Triantafilou, K.; Triantafilou, M.; Fernandez, N., Lipopolysaccharide (LPS) labeled with Alexa 488 hydrazide as a novel probe for LPS binding studies. *Cytometry* **2000,** *41* (4), 316-320.
40. Aurell, C. A.; Wistrom, A. O., Critical aggregation concentrations of gram-negative bacterial lipopolysaccharides (LPS). *Biochem Biophys Res Commun* **1998,** *253* (1), 119-123.

41. Craig, M. P.; Gilday, S. D.; Dabiri, D.; Hove, J. R., An optimized method for delivering flow tracer particles to intravital fluid environments in the developing zebrafish. *Zebrafish* **2012,** *9* (3), 108-119.
42. Palani, S.; Elima, K.; Ekholm, E.; Jalkanen, S.; Salmi, M., Monocyte Stabilin-1 Suppresses the Activation of Th1 Lymphocytes. *J Immunol* **2016,** *196* (1), 115-123.
43. Schledzewski, K.; Geraud, C.; Arnold, B.; Wang, S.; Grone, H. J.; Kempf, T.; Wollert, K. C.; Straub, B. K.; Schirmacher, P.; Demory, A.; Schonhaber, H.; Gratchev, A.; Dietz, L.; Thierse, H. J.; Kzhyshkowska, J.; Goerdt, S., Deficiency of liver sinusoidal scavenger receptors stabilin-1 and -2 in mice causes glomerulofibrotic nephropathy via impaired hepatic clearance of noxious blood factors. *J Clin Invest* **2011,** *121* (2), 703-714.
44. Diep, C. Q.; Ma, D.; Deo, R. C.; Holm, T. M.; Naylor, R. W.; Arora, N.; Wingert, R. A.; Bollig, F.; Djordjevic, G.; Lichman, B.; Zhu, H.; Ikenaga, T.; Ono, F.; Englert, C.; Cowan, C. A.; Hukriede, N. A.; Handin, R. I.; Davidson, A. J., Identification of adult nephron progenitors capable of kidney regeneration in zebrafish. *Nature* **2011,** *470* (7332), 95-100.
45. Hoshyar, N.; Gray, S.; Han, H.; Bao, G., The effect of nanoparticle size on in vivo pharmacokinetics and cellular interaction. *Nanomedicine (Lond)* **2016,** *11* (6), 673-692.
46. Hassett, K. J.; Benenato, K. E.; Jacquinet, E.; Lee, A.; Woods, A.; Yuzhakov, O.; Himansu, S.; Deterling, J.; Geilich, B. M.; Ketova, T.; Mihai, C.; Lynn, A.; McFadyen, I.; Moore, M. J.; Senn, J. J.; Stanton, M. G.; Almarsson, O.; Ciaramella, G.; Brito, L. A., Optimization of Lipid Nanoparticles for Intramuscular Administration of mRNA Vaccines. *Mol Ther Nucleic Acids* **2019,** *15*, 1-11.
47. Sykes, E. A.; Chen, J.; Zheng, G.; Chan, W. C., Investigating the impact of nanoparticle size on active and passive tumor targeting efficiency. *ACS Nano* **2014,** *8* (6), 5696-5706.
48. Jiang, W.; Kim, B. Y.; Rutka, J. T.; Chan, W. C., Nanoparticle-mediated cellular response is size-dependent. *Nat Nanotechnol* **2008,** *3* (3), 145-150.
49. Zhang, S.; Li, J.; Lykotrafitis, G.; Bao, G.; Suresh, S., Size-Dependent Endocytosis of Nanoparticles. *Adv Mater* **2009,** *21*, 419-424.
50. Nagai, Y.; Akashi, S.; Nagafuku, M.; Ogata, M.; Iwakura, Y.; Akira, S.; Kitamura, T.; Kosugi, A.; Kimoto, M.; Miyake, K., Essential role of MD-2 in LPS responsiveness and TLR4 distribution. *Nat Immunol* **2002,** *3* (7), 667-672.
51. de Belder, A. N.; Wik, K. O., Preparation and properties of fluorescein-labelled hyaluronate. *Carbohydr Res* **1975,** *44* (2), 251-257.
52. Alestrom, P.; D'Angelo, L.; Midtlyng, P. J.; Schorderet, D. F.; Schulte-Merker, S.; Sohm, F.; Warner, S., Zebrafish: Housing and husbandry recommendations. *Lab Anim* **2019**, 23677219869037.
53. Ellett, F.; Pase, L.; Hayman, J. W.; Andrianopoulos, A.; Lieschke, G. J., mpeg1 promoter transgenes direct macrophage-lineage expression in zebrafish. *Blood* **2011,** *117* (4), e49-56.
54. Bussmann, J.; Bos, F. L.; Urasaki, A.; Kawakami, K.; Duckers, H. J.; Schulte-Merker, S., Arteries provide essential guidance cues for lymphatic endothelial cells in the zebrafish trunk. *Development* **2010,** *137* (16), 2653-2657.
55. Hogan, B. M.; Herpers, R.; Witte, M.; Helotera, H.; Alitalo, K.; Duckers, H. J.; Schulte-Merker, S., Vegfc/Flt4 signalling is suppressed by Dll4 in developing zebrafish intersegmental arteries. *Development* **2009,** *136* (23), 4001-4009.
56. Varshney, G. K.; Pei, W.; LaFave, M. C.; Idol, J.; Xu, L.; Gallardo, V.; Carrington, B.; Bishop, K.; Jones, M.; Li, M.; Harper, U.; Huang, S. C.; Prakash, A.; Chen, W.; Sood, R.; Ledin, J.; Burgess, S. M., High-throughput gene targeting and phenotyping in zebrafish using CRISPR/Cas9. *Genome Res* **2015,** *25* (7), 1030-1042.
57. Carrington, B.; Varshney, G. K.; Burgess, S. M.; Sood, R., CRISPR-STAT: an easy and reliable PCR-based method to evaluate target-specific sgRNA activity. *Nucleic Acids Res* **2015,** *43* (22), e157.
58. Thisse, C.; Thisse, B., High-resolution in situ hybridization to whole-mount zebrafish embryos. *Nat Protoc* **2008,** *3* (1), 59-69.
59. Weinstein, B. M.; Stemple, D. L.; Driever, W.; Fishman, M. C., Gridlock, a localized heritable vascular patterning defect in the zebrafish. *Nat Med* **1995,** *1* (11), 1143-1147.
60. Schindelin, J.; Arganda-Carreras, I.; Frise, E.; Kaynig, V.; Longair, M.; Pietzsch, T.; Preibisch, S.; Rueden, C.; Saalfeld, S.; Schmid, B.; Tinevez, J. Y.; White, D. J.; Hartenstein, V.; Eliceiri, K.; Tomancak, P.; Cardona, A., Fiji: an open-source platform for biological-image analysis. *Nat Methods* **2012,** *9* (7), 676-682.
61. Schneider, C. A.; Rasband, W. S.; Eliceiri, K. W., NIH Image to ImageJ: 25 years of image analysis. *Nat Methods* **2012,** *9* (7), 671-675.

62. Askes, S. H. C.; Bossert, N.; Bussmann, J.; Talens, V. S.; Meijer, M. S.; Kieltyka, R. E.; Kros, A.; Bonnet, S.; Heinrich, D., Dynamics of dual-fluorescent polymersomes with durable integrity in living cancer cells and zebrafish embryos. *Biomaterials* **2018,** *168*, 54-63.

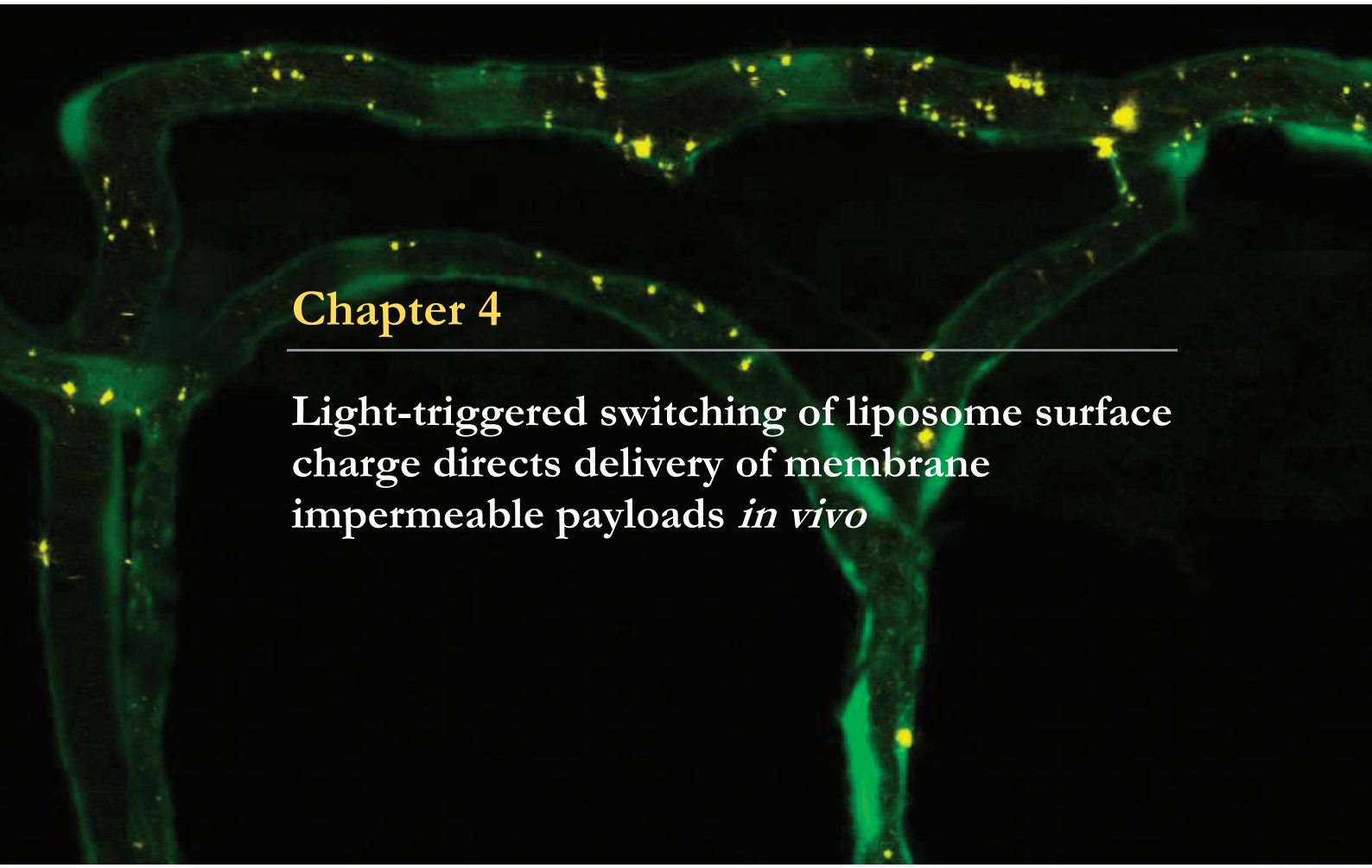

Chapter 4

Light-triggered switching of liposome surface charge directs delivery of membrane impermeable payloads *in vivo*

Published:

Arias-Alpizar, G*.; Kong, L.*; Vlieg, R. C.; Rabe, A.; Papadopoulou, P.; Meijer, M. S.; Bonnet, S.; Vogel, S.; van Noort, J.; Kros, A.; Campbell, F., Light-triggered switching of liposome surface charge directs delivery of membrane impermeable payloads in vivo. Nat Communications 2020, 11 (1), 3638

These authors contributed equally*

Image: Cationic liposomes, after UV-light exposure, in a zebrafish blood vessel

4.1 Abstract

Surface charge plays a fundamental role in determining the fate of a nanoparticle, and any encapsulated contents, *in vivo*. Herein, we describe, and visualise in real time, light-triggered switching of liposome surface charge, from neutral to cationic, *in situ* and *in vivo* (embryonic zebrafish). Prior to light activation, intravenously administered liposomes, composed of just two lipid reagents, freely circulate and successfully evade innate immune cells present in the fish. Upon *in situ* irradiation and surface charge switching, however, liposomes rapidly adsorb to, and are taken up by, endothelial cells and/or are phagocytosed by blood resident macrophages. Coupling complete external control of nanoparticle targeting together with the intracellular delivery of encapsulated (and membrane impermeable) cargos, these compositionally simple liposomes are proof that advanced nanoparticle function *in vivo* does not require increased design complexity but rather a thorough understanding of the fundamental nano-bio interactions involved.

4.2 Introduction

Surface charge is a key determinant of nanoparticle fate *in vivo*.[1] Following intravenous (*i.v.*) injection, nanoparticles with high surface charge density, either anionic or cationic, are rapidly cleared from circulation by specialised cells of the reticuloendothelial system (RES).[2-4] In mammals, RES cell types are primarily located in the liver (key hepatic RES cell types: Kupffer cells, KCs, and liver sinusoidal endothelial cells, LSECs) and spleen. These cells are responsible for clearing up to 99% of *i.v.* administered nanoparticles from circulation.[5] High nanoparticle surface charge density has a qualitative and quantitative impact on serum protein binding,[6-11] driving the opsonisation of circulating nanoparticles and subsequent recognition and clearance by the RES.[12-14] In addition, cationic nanoparticles tend to adsorb to the anionic surface of cells and are subsequently internalised,[15-19] often leading to acute cytotoxicity.[20-22] Given the adverse pharmacokinetics of charged nanoparticles in the body, most clinically approved, nanoparticle-drug formulations (nanomedicines) possess a (near) neutral surface charge to prolong circulation lifetimes and maximise drug exposure within target (vascularized) tissues in the body.[23]

We have previously shown that *i.v.* administered liposomes with (near) neutral surface charge, and optimally 100 nm in size, tend to freely circulate in embryonic zebrafish (*Danio rerio*).[24] Anionic nanoparticles (in our experience, <20 mV measured zeta (ζ) potential) interact strongly with RES cell types, namely scavenging endothelial cells (SECs, *via* a *stabilin*-mediated clearance pathway) and blood resident macrophages.[24, 25] Whereas, cationic liposomes (>20 mV measured ζ-potential) are rapidly removed from circulation through a combination of non-specific cellular interactions (*i.e.* adsorption to the anionic surface of the blood vessel walls), and/or clearance *via* the RES.[23] While usually considered detrimental to *in vivo* performance, the non-specific, cellular interactions of cationic nanoparticles/complexes (*e.g.* Lipofectamine™) have been widely exploited to deliver membrane impermeable, (genetic) material across cell membranes *in vitro*.[26-29] In these cases, a net cationic surface charge not only promotes non-specific adsorption and uptake within cultured cells but also facilitates endosomal escape and cytosolic payload release. In contrast, anionic and neutral nanoparticles are generally taken up sparingly by non-RES cell types, while those that are internalised tend to localise within lysosomes,[20, 30] a chemically hostile environment in which encapsulated payloads are rapidly degraded.

The contrasting fates of differently charged nanoparticles have all the ingredients of an ideal targeted drug delivery system. On the one hand, *i.v.* administered, (near) neutral nanoparticles freely circulate, maximising exposure within any (vascularized) tissue of the body. On the other, cationic nanoparticles are non-specifically taken up by virtually all cells, delivering high intracellular concentrations of encapsulated (and membrane impermeable) payloads. Herein,

we describe the rapid switching of liposome surface charge, from neutral to cationic, *in situ* and *in vivo* using light as exclusive trigger (**Figure 1**). Light is chosen as trigger given the rapid and quantitative photolysis of common chemical photocages,[31] its proven clinical relevance[32] and the prospect of emerging technologies to apply light deep within patients.

These include fiber-optic[33, 34] and injectable microLED hardware,[35] as well as photocleavable chemical functionality sensitive to visible or near infrared (NIR) light.[36-38] Light wavelengths between 600 and 950 nm can penetrate various human tissues (skin, fat and blood) up to a depth of 2 cm.[39] As model organism, we select the small and transparent zebrafish embryo. This organism is increasingly being used as a versatile preclinical screening platform for nanoparticles[40] and offers unprecedented opportunities to image nanoparticles across whole live organisms (*i.e.* visualising total injected nanoparticle doses), at cellular resolution and in real time.[41] Moreover, the zebrafish embryo can *qualitatively* predict nanoparticle interactions with scavenging cell types of the reticuloendothelial system in mammalian models.[24, 42]

In this study, following *i.v.* administration within a zebrafish embryo, photoactive liposomes, composed of just two lipids and prior to light activation, freely circulate and do not significantly interact with RES and/or other cell types of the embryo. Following *in situ* light activation, however, rapid surface charge switching results in non-specific adsorption and uptake of liposomes across the entire endothelium of the fish, as well as phagocytic uptake in blood resident macrophages. Importantly, light triggered surface charge switching does not disrupt liposome integrity and encapsulated, membrane impermeable payloads are successfully transported across cell membranes following surface charge switching.

4.3 Results

Design of photoactive liposomes

Photoswitching the surface charge of a liposome – from neutral to cationic – requires photoactive lipids embedded within a liposome membrane (**Figure 1**). In the absence of light and at physiological pH, photocaged lipids should carry no net charge to maintain a (near) neutral liposome surface charge (*i.e.* freely circulating). To ensure sufficient cationic surface charge density following photoactivation (in our experience, liposomes with a measured ζ-potential >20 mV), photocaged lipids should make up a significant proportion, if not all, of the overall lipid membrane composition. And, for optimal performance, photolysis and subsequent charge switching should be rapid. Finally, to achieve intracellular delivery of (membrane impermeable) drugs, encapsulated payloads should remain entrapped within liposomes, before, during and after light activation. Surface charge switching should not, therefore, involve any large-

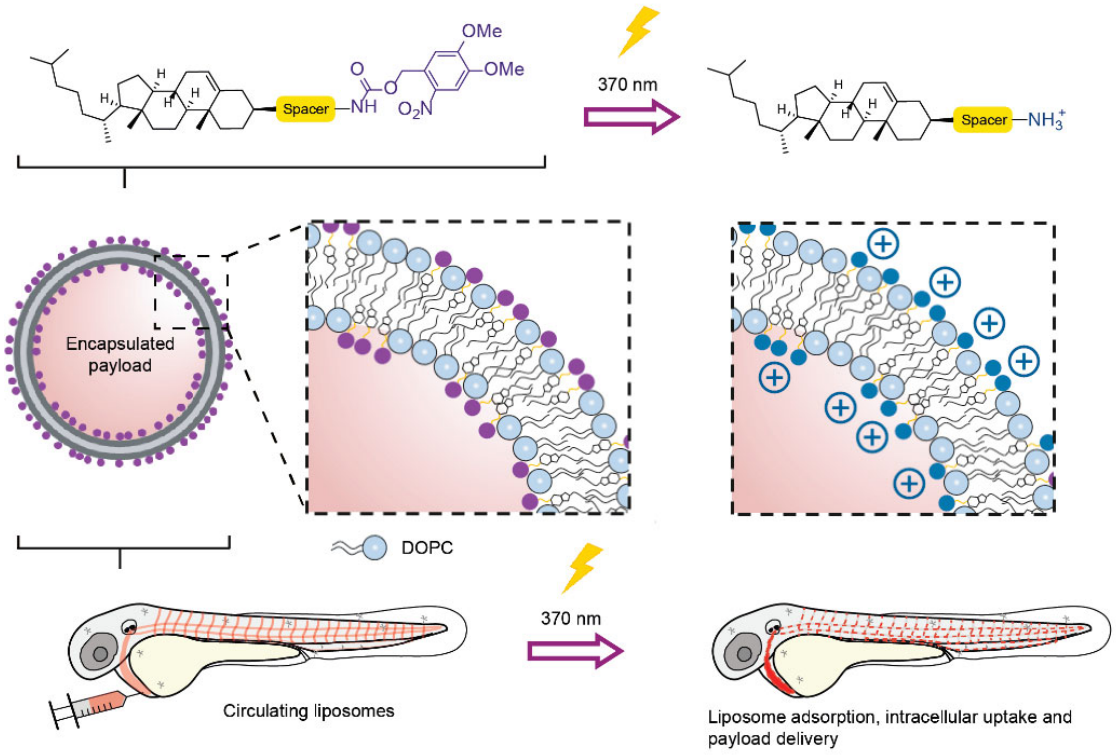

Figure 1. Photoswitching the surface charge of a liposome – from neutral to cationic– requires photoactive lipids embedded within a liposome membrane. Prior to light activation, charge neutral, photoactive liposomes freely circulate throughout the vasculature of a zebrafish embryo and do not interact with RES cell types, or any other cell type, of the embryonic fish. Upon light irradiation and photolysis of photocaged, cholesterylamine lipids, rapid surface charge switching, from neutral to cationic, leads to non-specific adsorption of liposomes across the endothelium of the embryo, liposome uptake and intracellular delivery of liposome-encapsulated, membrane impermeable payloads. DOPC=1,2-dioleoyl-sn-glycero-3-phosphocholine.

scale reorganisation of the liposome membrane and with it the potential for leakage of encapsulated drugs.

To ensure the non-specific adsorption of cationic liposomes to blood vessel walls following light triggered surface charge switching, we first assessed the physicochemical properties and *in vivo* behaviour of liposomes containing cationic, cholesterylamine compounds, **1-3** (**Figure 2a,** see reference 43 for synthesis and characterisation). Cholesterol can be incorporated into a reconstituted (phospho)lipid bilayer up to approximately 50 mol%,[44] and is often included in liposomal formulations to modulate drug retention and release profiles.[45] Knowing the hydroxyl head group of cholesterol sits deeper within a lipid bilayer than neighbouring phospholipid head groups,[46] a series of cholesterylamine compounds, **1-3**, were assessed, in which the spacer length between the hydrophobic cholesteryl anchor and primary amine head group was varied. In all cases, linkers were connected to cholesterol via an ester bond. While

spacers were primarily included to ensure effective charge presentation at the lipid-water interface, our choice of spacer chemistry was also influenced knowing the final photocaged cholesteryl compounds would be charge neutral, hydrophobic and potentially form lipid droplets within a phospholipid membrane.[47] In this scenario and upon light activation, we envisaged extensive membrane remodelling to reposition the newly revealed primary amine at the water-lipid interface and with it the potential for contents leakage. To minimise this risk and to increase the amphipathicity of the final photocaged cholesteryl compound, we focused on short glycine and polyethylene glycol (PEG) linkers as hydrophilic and/or uncharged spacers.

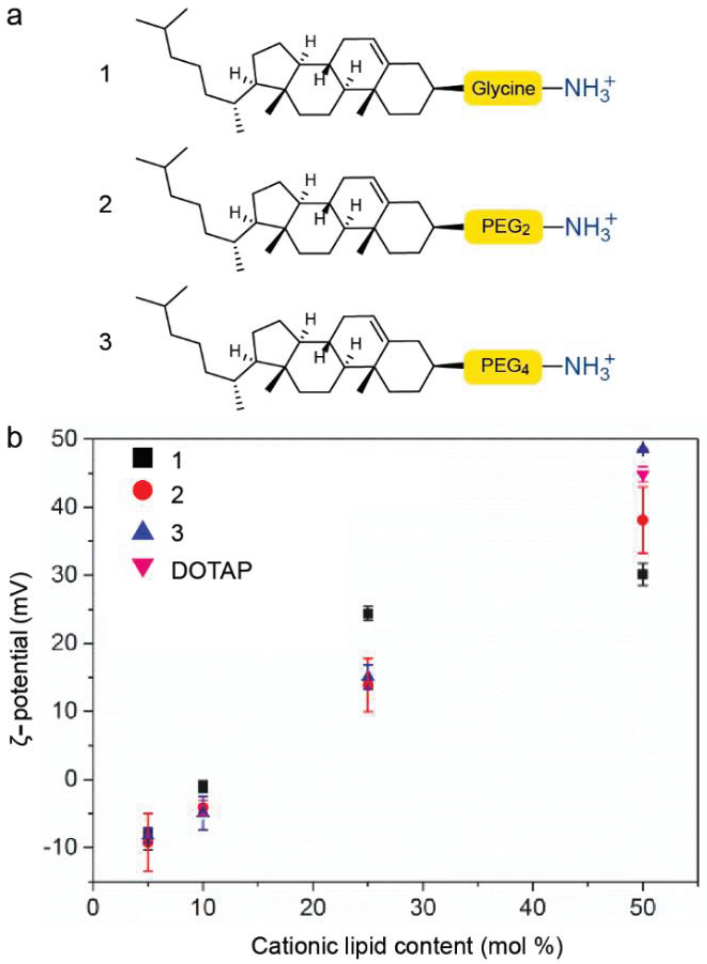

Figure 2. Varying cholesterylamine content within DOPC liposomes. (a) Cationic cholesterylamine analogues, **1-3. (b)** Measured surface charges (ζ-potential) of DOPC liposomes containing varying mol% **1-3**. DOPC:DOTAP (1:1) liposomes are included as a representative (commercially available) cationic liposome formulation. Measure of centre: mean; Error bars: standard deviation.

Liposomes, containing varying amounts of **1-3**, up to 50 mol%, were co-formulated with zwitterionic, 1,2-dioleoyl-*sn*-glycero-3-phosphocholine (DOPC) phospholipids. All formulated liposomes were prepared by standard extrusion techniques and were approximately 100 nm in size, with polydispersity indices (PDI) <0.2 as measured by dynamic light scattering (DLS, **Supplementary Table 1**). DOPC was chosen as co-formulant phospholipid as we have previously shown liposomes composed of 100% DOPC,[24] as well as 1:1 mixtures of DOPC and cholesterol (**Supplementary Figure 1**), freely circulate throughout the vasculature of an embryonic zebrafish beyond 1 hour post-injection (hpi). As expected, increasing the amount of cholesterylamine, **1-3**, within the DOPC liposome membrane resulted in greater cationic surface charge (**Figure 2b** and **Supplementary Table 1**). However, at high mol% of cationic lipids, a trend emerged whereby longer spacers resulted in an increasingly cationic surface charge. Satisfyingly, the measured surface charge of DOPC:**3** (1:1) liposomes was comparable to liposomes formulated with commercially available, cationic 1,2-dioleoyl-3-trimethylammonium-propane (DOTAP) lipids (**Figure 2b**). We have previously shown that *i.v.* administered DOTAP liposomes (*e.g.* EndoTAG-1® - DOPC:DOTAP (45:55) and 100% DOTAP liposomes) non-specifically adsorb to blood vessel walls throughout the vasculature of an embryonic zebrafish.[24]

Following *i.v.* microinjection in a two day old zebrafish embryo (2 days post-fertilisation, dpf), all three cationic liposome formulations – *i.e.* DOPC co-formulated with 50 mol% **1**, **2** or **3** – showed comparable biodistributions to cationic DOPC:DOTAP (1:1) liposomes (**Supplementary Figure 2a**). In all cases, liposomes were mainly visible as immobile punctae bound to all blood vessel walls (both arterial and venous) and largely removed from circulation at 1 hpi (**Figures 3a-c** and **Supplementary Figures 2b,c**). In contrast, DOPC liposomes co-formulated with lower mol% of cholesterylamine **3** showed variable biodistributions dependent on the surface charge density of the liposome (**Figure 3d,i**). In particular, (near) neutral DOPC liposomes, containing 10 mol% **3**, were extensively taken up by blood-resident macrophages within the caudal haematopoietic tissue (CHT) of the embryonic fish (**Figures 3j,k** and **Supplementary Figure 3** for whole embryo images).

Light-triggered switching of liposome surface charge *in vitro* and *in vivo*

As DOPC:**3** (1:1) liposomes possessed the highest measured cationic surface charge, we proceeded to photocage **3**, forming the uncharged, photoactive cholesteryl compound, **4** (**Figure 4a**). Upon UV irradiation (370 ± 7 nm, 202 mW cm^{-2}), in H_2O/MeCN/^{t}BuOH (1:1:1), complete photolysis of **4** was achieved in less than two minutes, with clean photolysis confirmed by the appearance of two isosbestic points in the UV spectra (**Supplementary Figure 4a**). Irradiation of DOPC:**4** (1:1) liposomes, formulated in 10 mM HEPES buffer (pH 7.4), resulted in comprehensive surface charge reversal – from ζ-potential -8 to +26 mV – within this same short timeframe (**Figure 4b**).

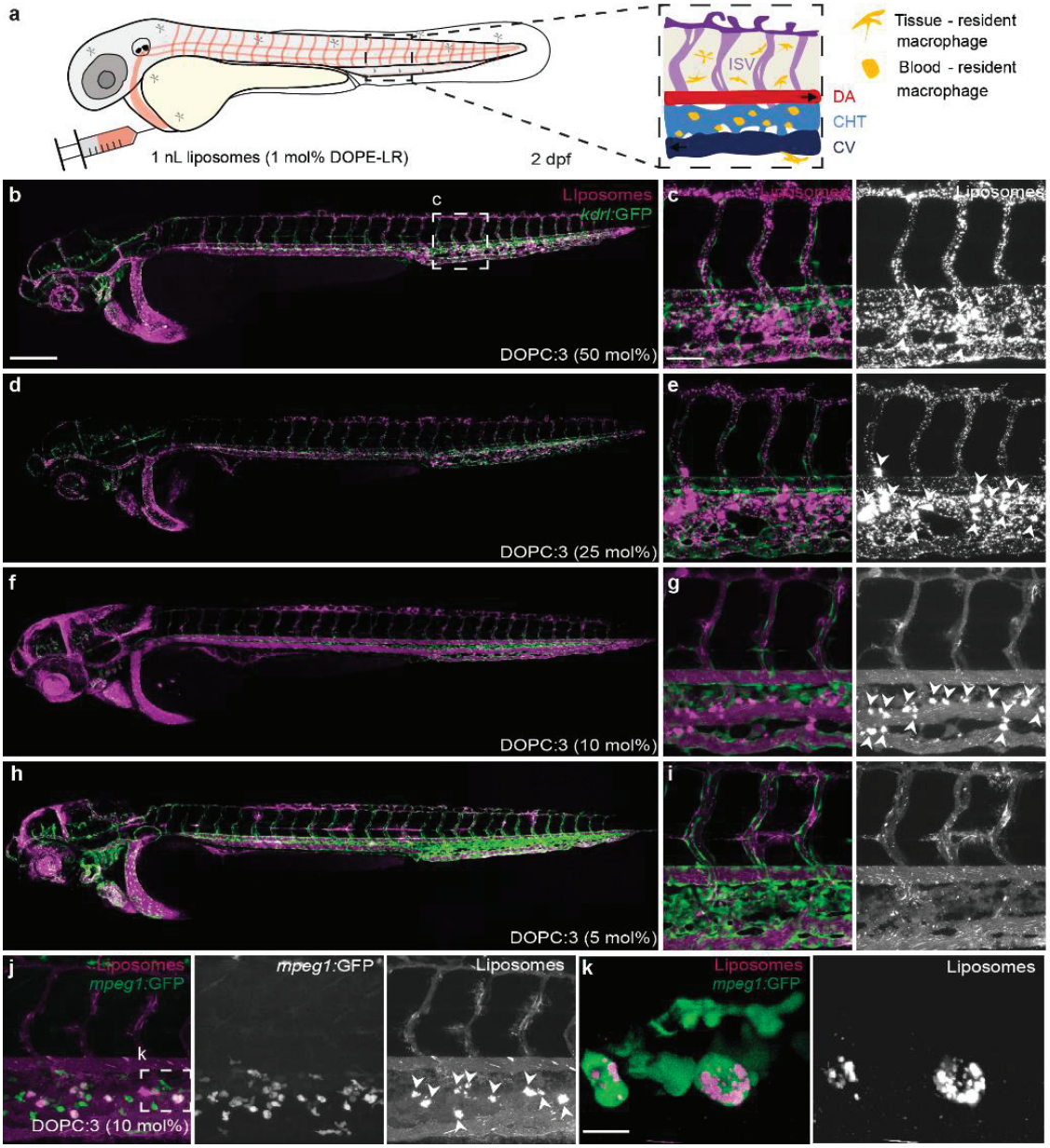

Figure 3. Biodistribution of cationic, DOPC:3 liposomes in embryonic zebrafish. (a) Schematic showing the site of microinjection within a zebrafish embryo, two days post-fertilisation (dpf). Boxed region showing the organisation of blood vessels/macrophages within the tail of the embryo. DA: dorsal aorta; CHT: caudal hematopoietic tissue; CV: caudal vein; ISV: intersegmental vessel. Black arrows indicate direction of blood flow. **(b-i)** Biodistribution of DOPC liposomes containing cholesterylamine, **3**, at varying mol%. Whole embryo (10x magnification) and tissue level (40x magnification) views of liposome distribution in *kdrl:*GFP transgenic embryos, stably expressing GFP in all endothelial cells, at 1 hpi. White arrowheads indicate apparent liposome uptake within blood resident macrophages, based on location and cell morphology. **(j, k)** Tissue and cellular (63x magnification) level views of DOPC:**3** (10mol% **3**) liposome distribution in *mpeg1:*GFP transgenic embryos, stably expressing GFP in all macrophages, at 1 hpi. Extensive fluorescence co-localization of liposomes and transgenic GFP confirmed the uptake of DOPC:**3** (10mol% **3**) liposomes in blood resident macrophages of the zebrafish embryo.

Slight variations in the positions of macrophages (between **j** and **k**) are due to macrophage migration during the time taken to change magnification settings on the confocal microscope. All liposomes (**b-k**) contained 1 mol% fluorescent lipid probe, DOPE-LR, for visualisation. Scale bars: 200 μm (whole embryo); 50 μm (tissue level); 10 μm (cellular level).

Despite batch-to-batch variation (resulting in measured zeta potentials ranging from +20 to +35 mV ζ-potential), the cationic surface charge of irradiated DOPC:**4→3** (1:1) liposomes was consistently lower than that of parent DOPC:**3** (1:1) liposomes (ζ-potential +48 mV). Both formulations should, in theory, be compositionally identical and, at this point, we do not have a reasonable explanation for this discrepancy. The measured size (approx. 100 nm) and PDI (<0.1) of DOPC:**4** (1:1) liposomes was unchanged before and after irradiation (**Supplementary Figure 4b** and **Supplementary Table 1**). Likewise, their spherical, unilamellar morphology, as imaged by cryo-transmission electron microcopy (CryoTEM), generally remained unchanged before and after UV irradiation (**Figure 4c**, see **Supplementary Figure 5** for larger populations), although a small fraction (<10%) of irradiated DOPC:**4→3** liposomes did appear non-spherical (oblong) (**Supplementary Figures 5b,e**). Whether this morphological change is the result of membrane reorganization upon light triggered photolysis of membrane embedded **4** is hard to conclude given we persistently observed only very small populations of DOPC:**4** liposomes (prior to light activation) by CryoTEM. Importantly, however, any potential membrane reorganization did not lead to disruption of liposome integrity and liposome encapsulated and membrane impermeable contents remained within the aqueous core of the liposome before, during and after light activation (**Supplementary Figure 6**).

Following microinjection in the embryonic zebrafish (54-56 hours post fertilization, hpf) and prior to light activation, DOPC:**4** liposomes (formulated at 1:1 molar ratio in all subsequent experiments) were freely circulating and did not significantly interact with RES cell types of the embryonic fish, namely blood resident macrophages and scavenging endothelial cells, at 1 hpi (**Figures 4d-f,h-j**). Indeed, the exponential circulation lifetime decay of DOPC:**4** liposomes in the embryonic fish was very similar to that previously observed for 100 nm liposomes based on the lipid composition of Myocet®.[24] Myocet® (lipid composition: POPC:cholesterol; 55:45) is a clinically approved liposomal-doxorubicin formulation designed to evade the RES, circulate freely and passively target solid tumors *via* the enhanced permeability and retention (EPR) effect.[48] In humans, the circulation half-life of Myocet® is 2.5 h.[49] In this case, like Myocet®, a significant fraction of photoactive DOPC:**4** liposomes remained in circulation >4 hpi (**Figure 4g** and **Supplementary Figures 7** and **8** for individual images used for quantification). Upon *in situ* irradiation (15 min, 370 ± 7 nm, ~90 mW cm^{-2}, ~2.4 J per embryo, 1 hpi) of the entire zebrafish embryo, however, a dramatic change in liposome fate was observed, whereby DOPC:**4→3** liposomes

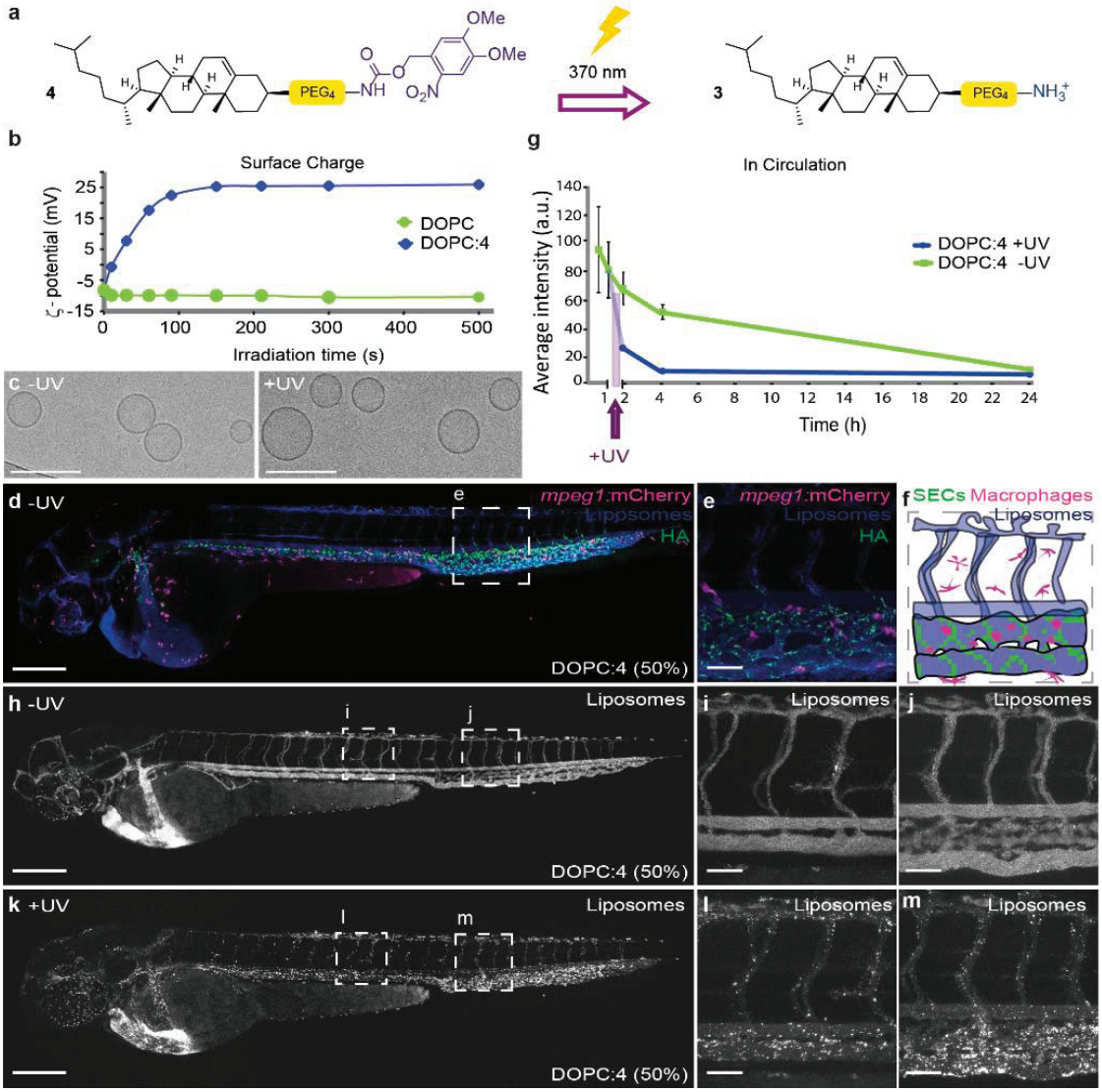

Figure 4. Photoswitching liposome surface charge *in vitro* and *in vivo*. (a) Chemical structure of **4** and its photolysis to **3**. **(b)** Evolution of measured surface charge of DOPC:**4** liposomes (1:1) as a function of UV (370 ± 7 nm, 202 mW cm^{-2}) irradiation time. Note: batch-to-batch variation resulted in measured zeta potentials of DOPC:**4**→**3** liposomes ranging from +20 to +35 mV. 100% DOPC control liposomes demonstrate surface charge of liposomes without photoactive lipids is unaffected by UV irradiation. **(c)** CryoTEM images of DOPC:**4** before and after *in situ* irradiation (15 min, 370 ± 7 nm, 202 mW cm^{-2}). Scale bar: 200 nm. See Supplementary Information Figure 5 for low magnification CryoTEM images. **(d,e)** Whole embryo and tissue level views of DOPC:**4** liposome biodistribution following co-injection with fluoHA in *mpeg1:*mCherry transgenic embryos (2 dpf). FluoHA is a specific *in vivo* marker of SECs and does not compete with liposome binding.[25] Liposomes (**d,e**) contained 1 mol% fluorescent lipid probe, DOPE-Atto633, for visualization. **(f)** Tissue level organization of macrophages and fluoHA-labelled SECs within the tail region of an *mpeg1:*mCherry embryo (2 dpf). **(g)** Quantification of DOPC:**4** liposome levels in circulation based on mean liposome fluorescence intensity in the lumen of the DA at 0.5, 1, 2, 4, and 24 hpi (measure of centre: median; error bars: standard deviation); n = 6 (0.5 and 1 hpi) and n = 3 (2, 4 and 24 hpi) individually injected embryos

per formulation per time point (see **Supplementary Figure 7** for individual images). (**h-j**) Whole embryo and tissue level views of DOPC:**4** liposome biodistribution in *kdrl:*GFP embryos, prior to UV irradiation, 1 hpi. (**k-m**) Whole embryo and tissue level views of DOPC: **4→3** liposome biodistribution in *kdrl:*GFP embryos, directly after *in situ* irradiation (15 min, 370 ± 7 nm, ~90 mW cm^{-2}, ~2.4 J per embryo), approx. 1.5 hpi. Liposomes (**h-m**) contained 1 mol% fluorescent lipid probe, DOPE-LR, for visualization. Scale bars (**d-m**): 200 µm (whole embryo); 50 µm (tissue level)

were now visible as immobile punctae associated with all blood vessel walls (**Figures 4k-m**) and largely removed from the circulating blood flow (**Figure 4g**). The biodistribution of DOPC:**4→3** liposomes matched that of cationic DOPC:**3** (1:1) liposomes (**Figures 3b,c**), confirming successful photoswitching of DOPC:**4** liposome surface charge – from (near) neutral to cationic – *in situ* and *in vivo*. In contrast, the biodistribution of freely circulating DOPC liposomes (100% DOPC content) was unaffected following identical irradiation procedures, confirming that the observed changes in biodistribution require the combination of both circulating DOPC:**4** liposomes as well as applied UV light (**Supplementary Figure 9**). All UV irradiated embryos used in this study continued to develop normally without observable phenotypic abnormalities up to 6 dpf, confirming the suitability of this animal model for photoactivation studies.[50] Furthermore, any small potential increase in the temperature of the embryo as a result of UV irradiation will likely be counteracted by the remarkable resilience of the zebrafish embryo (from 1 dpf) to heat stress.[51]

Having shown photoswitching of liposome surface charge occurs within seconds (**Figure 4b**), we next investigated the tissue level fate of *i.v.* administered DOPC:**4** liposomes, within the embryonic zebrafish, in real time (imaging rate: 1 frame per second, fps), before and during light-triggered surface charge switching. For this, a custom built, two-photon microscope was equipped with a 370 ± 7 nm LED, enabling alternating UV irradiation (95% UV duty cycle, **Figure 5a**) and two-photon fluorescence imaging (see **Supporting Information** for setup, **Supplementary Figure 10**). For these experiments, we focused on a single plane (200 µm x 200 µm) of view which included both the dorsal aorta (DA) and posterior cardinal vein (PCV) to ensure potential liposome selectivity (venous *vs.* arterial endothelium) could be observed (**Figure 5b**). From the acquired movie, two fundamental and competing interactions of cationic nanoparticles could be simultaneously observed, namely non-specific adsorption of liposomes to endothelial cells (ECs) and liposome aggregation in circulation (**Supplementary Movie 1** and **Figure 5d** for selected individual frames). Non-specific adsorption of liposomes to ECs was observed less than a minute after light activation, evident as emerging punctae of immobile fluorescence adhered to all blood vessel walls within the plane of view. The number of immobile punctae increased over time, and while there was no apparent selectivity for arterial or venous blood vessels, the largest number of liposomes were associated with the walls of the intersegmental vessel (ISV) connected to, and extending dorsally from, the

PCV (**Figure 5d**). ISVs are narrower blood vessels than both DA or caudal vein (CV) and the blood flow or CV blood vessels, under reduced shear stress.[52, 53] This, in turn, presumably increases the propensity of cationic liposomes to adhere to the anionic, heparan sulfated endothelium of the ISV through direct electrostatic interactions.

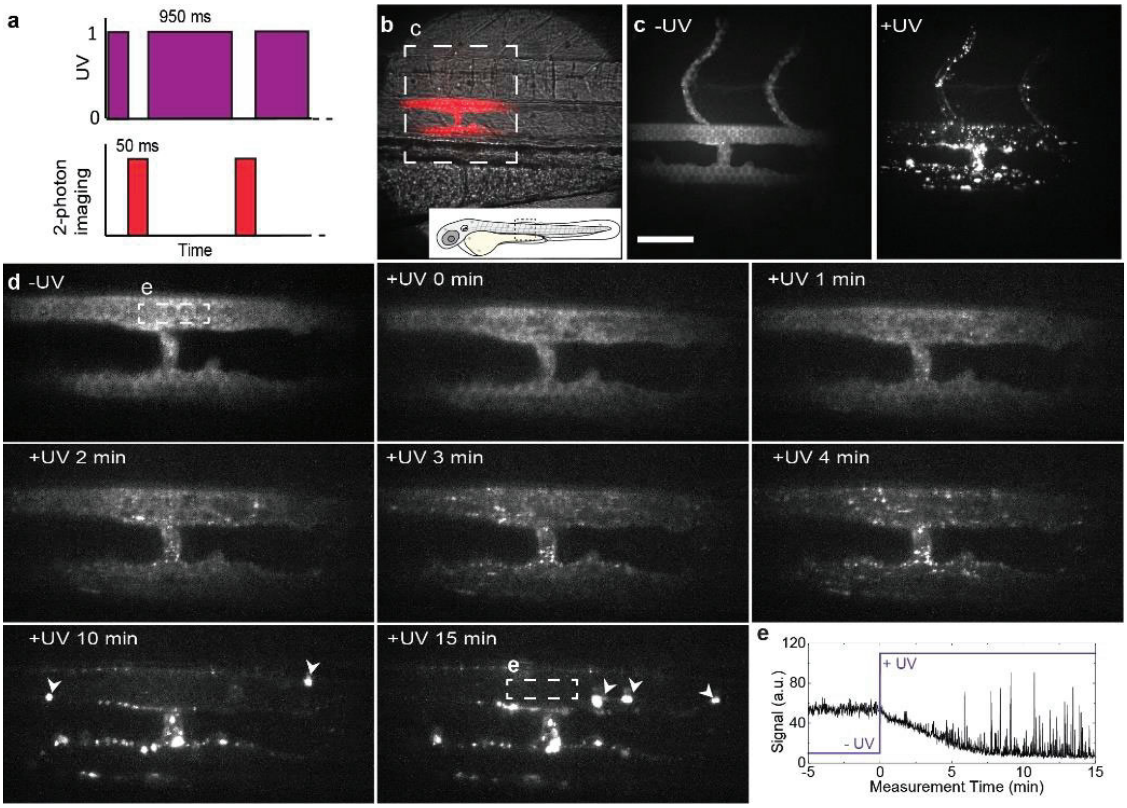

Figure 5. Real time multi-photon imaging of liposome surface charge switching *in situ* and *in vivo*. (a) The zebrafish embryo was exposed to UV light between the acquisitions of the camera, resulting in a 95% duty cycle of UV illumination per frame. **(b)** Transmission image of the imaging location, emission image overlaid in red. **(c)** Maximum intensity projections of two-photon z-stacks (spanning the full width of the embryo) showing DOPC:**4** liposome distribution, before and after UV exposure. These images confirm the vessel connected to, and extending dorsally from the PCV, is an ISV. **(d)** Time-lapse images of DOPC:**4(→3)** liposome distribution before and during UV irradiation. In later timeframes, large clusters of liposomes (indicated with white arrowheads) were observed passing through the plane of view in circulation. **(e)** Mean fluorescence intensity within the ROI (lumen of the DA, white square in **(c**, 15 min). Liposome fluorescence intensity immediately decreased upon UV irradiation. High intensity spikes of fluorescence, due to large circulating liposome aggregates passing through the ROI, registered from 5 minutes after UV irradiation start. Liposomes contained 1 mol% fluorescent lipid probe, DOPE-LR, for visualisation. Scale bars: 50 µm.

Competing with the non-specific adsorption to the blood vessel walls, cationic liposome aggregation in circulation was also observed following light activation. This could be directly visualized as increasingly large and bright fluorescent particles passing through the plane of view in circulation (**Supplementary Movie 1,** see link for movies and **Figures 5d,e**). Aggregation of cationic liposomes is caused by the adsorption of anionic serum proteins/ macromolecules to the newly revealed cationic nanoparticle surface,[54, 55] and we have recently shown cationic liposomes adsorb significantly more serum proteins than anionic or neutral liposomes *in vitro*.[56] Adsorption of this protein corona will not only mask underlying cationic surface charge (preventing direct electrostatic interaction with blood vessel walls) but will induce liposome aggregation and concomitant uptake in blood resident macrophages. Indeed, over the course of this research and in the absence of light activation, we have observed variable, low level uptake of DOPC:**4** liposomes within blood resident macrophages, predominantly within the CHT of the embryo. This may be due to incidental light exposure during experimental and microscopy procedures, partial photolysis and subsequent aggregation of liposomes in circulation, followed by irreversible recognition and clearance *via* the RES. These simultaneous and competing interactions of cationic liposomes *in vivo* can be explained by the contrasting fates of DOPC:**4→3** liposomes as they transition through various intermediate charged states, from (near) neutral to cationic surface charge.

In particular, during the light triggered transition of DOPC:**4** liposome surface charge, an intermediate physicochemical state, highly prone to blood-resident macrophage uptake (*i.e.* compositionally similar to DOPC liposomes containing 10 mol% **3**), is, at least momentarily, inevitable (**Figure 6a**). The extent of macrophage uptake versus non-specific adsorption to ECs, should, therefore, be dependent on the residence time of partially activated DOPC:**4→3** liposomes in circulation. To test this hypothesis, we systematically reduced the applied UV light dose (from 75% to 10% UV duty cycle; 1.8 to 0.24 J per embryo respectively) to extend the time taken for DOPC:**4** liposomes to transition from a (near) neutral to cationic surface charge *in situ* and *in vivo* (**Figures 6b-i**). In this way, the biodistribution of DOPC:**3** liposomes, containing varying mol% **3** (**Figures 3b-i**), could be replicated. Most striking, at 25% applied light (0.6 J per embryo), DOPC:**4→3** liposomes were predominantly taken up by blood resident macrophages within the CHT of the embryonic zebrafish, analogous to (near) neutral DOPC:**3** liposomes (10 mol% **3**) (**Figures 6d, e, j-l**). This result confirmed that an extended residence time of only partially activated DOPC:**4→3** liposomes leads to irreversible clearance of liposomes by the RES.

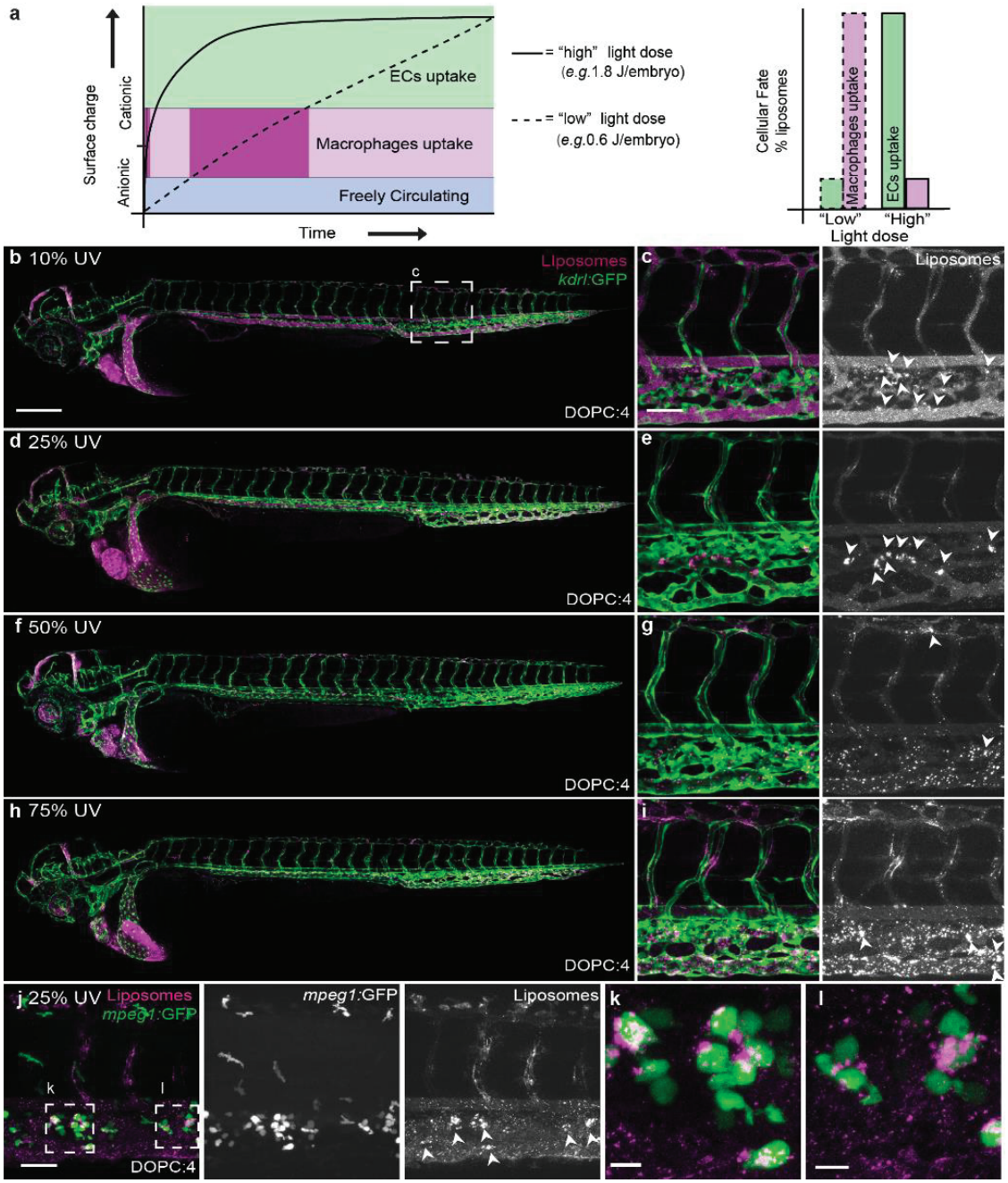

Figure 6. Effect of light dose on the *in vivo* fate of DOPC:4 liposomes. (a) Reducing the UV light dose applied to the embryo increases the time taken for DOPC:**4** liposomes to transition to DOPC:**3** liposomes. This, in turn, increases the resident time spent by DOPC:**4→3** liposomes at an intermediate cationic surface charge density leading to irreversible clearance of liposomes by blood resident macrophages. **(b-i)** Whole embryo and tissue level views of DOPC:**4** liposome biodistribution in *kdrl:*GFP embryos following embryo irradiation with variable light doses (15 min, 370 ± 7 nm, ~90 mW cm^{-2}, UV duty cycle stated for each image). Apparent liposome uptake in blood resident macrophages highlighted with white arrowheads. **(j-l)** Tissue level and zoomed views of DOPC:**4→3** liposome biodistribution in *mpeg1:*GFP embryos following embryo irradiation at 25% UV

duty cycle (15 min, 370 ± 7 nm, 0.6 J per embryo). Liposomes contained 1 mol% fluorescent lipid probe, DOPE-LR, for visualisation. Scale bars: 200 µm (whole embryo); 50 µm (tissue level), 10 µm (zoomed).

Light-triggered liposomal cell uptake and payload delivery

Next, we investigated the intracellular fate of DOPC:**4** liposomes following *in situ* and *in vivo* surface charge switching. To verify endocytosis of DOPC:**4→3** liposomes, a pH-sensitive fluorescent lipid probe (DOPE-pHrodo, 1 mol%) was incorporated within the DOPC:**4** liposome membrane. The fluorescence intensity of pHrodo increases >100-fold in mildly acidic environments (*e.g.* late endosomes/lysosomes, pH <6). To accurately assess evolving pHrodo fluorescence, wild type (*AB/TL*) embryos were used to avoid potential fluorescence bleed through from transgenic fluorescent markers. Following *i.v.* injection and in the absence of light, pHrodo-associated fluorescence was observed in a small number of cells within the CHT of the embryonic fish (**Figures 7a, b**). While the absence of cell specific (transgenic) fluorescent markers does not allow for definitive identification of this cell type, its location within the CHT and rounded morphology (delineated by pHrodo fluorescence), is characteristic of low-level phagocytic uptake of DOPC:**4(→3)** liposomes within blood resident macrophages, as previously mentioned. Following *in situ* light irradiation, however, increasing pHrodo fluorescence, primarily associated with SECs, was observed over time (up to 5 hpi) (**Figure 7c**).

This timeframe suggests a significant fraction of DOPC:**4→3** liposomes are not only endocytosed by SECs but remain within endosomes during trafficking and maturation to late endosomes/lysosomes. This would be consistent with the very high lysosomal activity of SECs, whose primary physiological role in the body is to recognize, clear and breakdown endogenous and pathogenic waste from the blood.[57] It is also possible that a fraction of endocytosed, cationic DOPC:**4→3** liposomes, within SECs, macrophages or other ECs, manage to successfully escape endosomes prior to the first imaging time point. Within the cytosol and beyond the acidic endosome microenvironment, potential intracellular fluorescence associated with pHrodo probes would not be visible.

Having confirmed endocytosis of light-activated DOPC:**4→3** liposomes *in vivo*, we finally investigated the *in vivo* fate of liposome encapsulated and membrane impermeable payloads, following light triggered surface charge switching. For this, self-quenching concentrations of water soluble, sulforhodamine B (SR-B, 10 mM) were passively encapsulated within DOPC:**4** liposomes. As for empty liposomes, the morphology and size of the SR-B filled DOPC:**4** liposomes did not significantly change following irradiation (**Figure 7d**). To monitor the fate of liposome encapsulated SR-B *in vivo*, we again performed alternating UV irradiation and two-photon fluorescence imaging (1fps) within live embryos

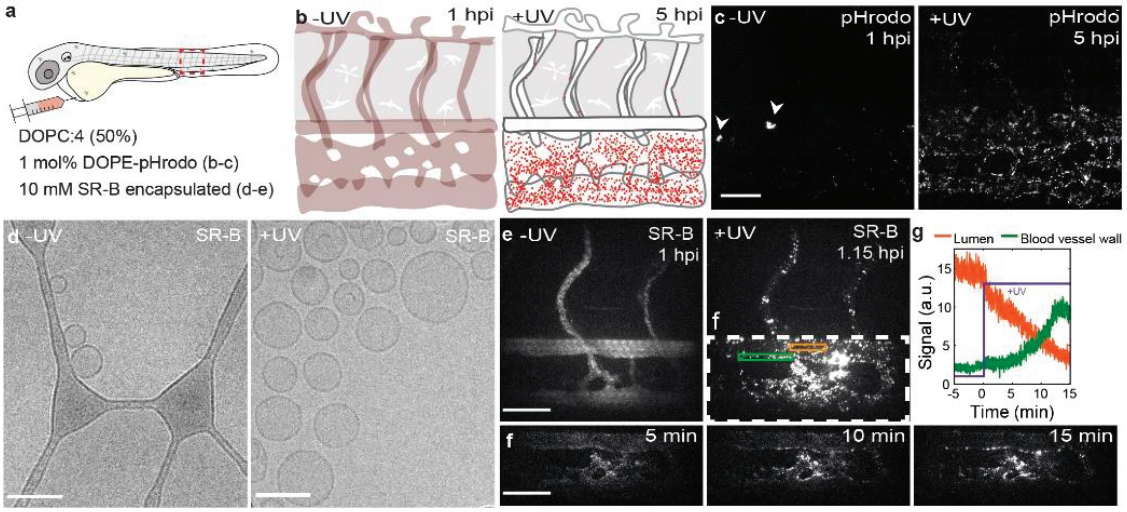

Figure 7. Cellular fate of DOPC:4→3 liposomes and their encapsulated payloads. **(a,b)** Schematics showing the site of microinjection within a 2 dpf embryo and the evolving fluorescence of pHrodo-containing DOPC:**4→3** liposomes within the tail region of a wildtype (*AB/TL*) embryonic zebrafish, over time. The fluorescence intensity of pHrodo increases >100-fold in mildly acidic environments (*e.g.* late endosomes/lysosomes, pH <6) and is, therefore, particularly apparent within SECs – cells with exceptionally high lysosomal activity. **(c)** Tissue level views of evolving pHrodo-associated fluorescence over time either in the absence of UV irradiation and following *in situ* UV irradiation (15 min, 370 ± 7 nm, 2.4 Jcm^{-2}). In the absence of UV irradiation, pHrodo-associated fluorescence is observed within a small number of cells within the CHT of the embryo (white arrowheads). Liposomes contained 1 mol% DOPE-pHrodo for visualisation. Scale bar: 50 µm. **(d)** CryoTEM images of SR-B filled, DOPC:**4** liposomes before and after *in situ* irradiation (15 min, 370 ± 7 nm, 202 mW cm^{-2}). Scale bars: 100 nm. **(e)** Maximum intensity projections of two-photon z-stacks (spanning the full width of the embryo) showing SR-B filled DOPC:**4** liposome distribution, before and after UV irradiation. Scale bar: 50 µm. **(f)** Time-lapse images of SR-B filled DOPC: **4→3** liposome distribution during UV irradiation. Scale bar: 50 µm. **(g)** Mean SR-B fluorescence intensity within ROIs (lumen of the DA, orange line; DA vessel wall, green line, shown in **(e)**), before and during UV irradiation. SR-B fluorescence intensity in circulation decreases upon UV irradiation with a concomitant increase in SR-B fluorescence intensity associated with the DA blood vessel wall. Liposomes **(e-g)** containing encapsulated SR-B (10 mM) and otherwise unlabelled.

(**Figures 7e-g** and **Supplementary Movie 2,** see link for movies). In this case, we focused on a single plane (200 µm x 200 µm) of view to include the DA, CHT and CV. This region of the embryo includes a significant population of SECs, as well as blood resident macrophages, within which DOPC:**4→3** liposomes extensively accumulate. From the acquired movies, SR-B filled DOPC:**4** liposomes, prior to light activation, appeared freely circulating, evident as homogenous, low level (quenched) SR-B fluorescence, confined within the zebrafish vasculature. Upon light triggered activation (95% UV duty cycle, 2.3 J per embryo) and surface charge switching, however, localized and de-quenched

SR-B could be seen as increasingly bright, fluorescent punctae, associated with all blood vessel walls but most prevalent throughout the sinusoid-like network of CHT blood vessels. Again, it is likely that DOPC: **4→3** liposome association and uptake within the CHT is enhanced due to the reduced blood flow velocities and sheer stresses experienced by liposomes within this sinusoidal-like tissue. Likewise, the co-existence of immobile (arrows, **Supplementary Movie,** see link for movies, as well as highly mobile (arrowheads, **Supplementary Movie 2**) SR-B fluorescent punctae is again indicative of intracellular SR-B delivery to both ECs (immobile) and blood resident macrophages (mobile). As a representative membrane impermeable, small molecule cargo, the successful intracellular delivery of liposome-encapsulated SR-B serves as promising evidence that this proof-of-concept technology will likely be transferable to other, therapeutically relevant (and membrane impermeable) payloads.

4.4 Discussion and Conclusion

The discovery of simple and effective targeted drug delivery systems should be preceded by a thorough understanding of the nano-bio interactions involved.[58] Here, we exploit the well characterised and contrasting fates of differently charged nanoparticles *in vivo*, however, our ability to rationally design a system that is both simple and effective has relied on comprehensive *in vivo* interrogation of all aspects of this technology (*i.e.* different light dosages, surface charge densities, interactions with the RES).

To this end, the embryonic zebrafish has provided an invaluable pre-clinical *in vivo* screening platform, offering unprecedented opportunities to assess, analyse and optimise nanoparticle behaviour over an entire live organism (*i.e.* visualising total injected doses), at cellular resolution and in real time.[42, 59, 60] Furthermore, the presence and conserved function of key RES cell types enables predictive assessment of fundamentally important *in vivo* clearance mechanisms of nanoparticles.[24, 41] It is important to stress here, however, that these predictions are strictly qualitative. Given the significant differences in relative numbers of RES cells (*i.e.* SECs *vs.* blood resident macrophages), RES tissue size and organization, quantitative predictions (based on observations in the embryonic zebrafish) of nanoparticle clearance by the mammalian RES are not yet possible. As such, the embryonic zebrafish should not replace experiments in larger (mammalian) models but, instead, should be used to guide and optimize nanoparticle design prior to first injections in higher vertebrates.

At a fundamental level, the ability to visualise the formation of a cationic nanoparticle *in situ* has revealed, for the first time, the co-existence of two competing interactions of cationic nanoparticles occurring simultaneously *in vivo*, namely non-specific adsorption to blood vessel walls and opsonisation in circulation. This observation not only highlights the importance of considering the fate of all intermediate physicochemical states of stimuli-responsive

nanoparticles as they transition from A to B, but, more generally, suggests that the fate of any given cationic nanoparticle is dependent on its surface charge density. Our data indicates that above a certain cationic surface charge threshold, *i.v.* administered nanoparticles will predominantly stick to (and be internalised by) endothelial cells, particularly in blood vessels with reduced blood flow velocity, while below this charge threshold, nanoparticles will tend to aggregate in circulation and be subsequently cleared by the RES. In our experience, *i.v.* administered liposomes with a measured surface charge >20 mV will tend to stick to endothelial cells, whereas those with a surface charge between +5 to +20 mV will tend to aggregate in circulation. Importantly, while we believe a threshold value will apply to all nanoparticle classes, this will likely vary depending on the surface chemistry and self-assembly of any individual nanoparticle and should be determined on a case-by-case basis.

In terms of targeting, the exclusive use of light as trigger forgoes any requirement for exploitable differences between target and non-target tissues (*e.g.* passive targeting of solid tumours *via* the EPR effect). As such, this liposome technology has the potential to be transferable to any light accessible tissue. Given the poor tissue penetration and significant potential cytotoxicity of using short wavelength UV-A light,[61, 62] however, we would aim future efforts at replacing *o*-nitrobenzyl chemistries with photocages sensitive to longer wavelength light or two-photon activation. In this vein, a family of zwitterionic BODIPY-derived photocages have recently been reported that can be efficiently cleaved using single photon visible or NIR light.[37] In theory, these photocages, connected to a cholesterylamine lipid anchor and incorporated within DOPC liposomes should not affect the surface charge and, therefore, the biodistribution of photoactive liposomes. In addition, light can be focused with precise spatial resolution. This has been exemplified by the clinical application of Visudyne® - a liposome-photosensitizer (verteporfin) formulation, administered intravenously and indicated for the photodynamic therapy of age-related macular degeneration (AMD).[63] In this case, non-thermal, red light (689 nm) is applied to the eye of a patient to trigger localised therapy. Unfortunately, given the small size (2-3 mm in length) of the zebrafish embryo and the practical difficulties in ensuring no incident or scattered UV-A light reached the dark side of the agar embedded embryo, we have been unable to demonstrate localised liposome surface charge switching and intracellular uptake within the embryonic fish in this study.

In conclusion, we describe a liposome technology that successfully couples complete external control of *in vivo* liposome targeting together with the transport of encapsulated and membrane impermeable cargos across cell membranes. While these combined features are unique in the context of stimuli-responsive drug delivery systems (reviewed in refs [64, 65]), including those for which charge switching is central to function (reviewed in ref [66]), the stand out feature of these liposomes is undoubtedly their compositional simplicity. The last decades have seen the empirical design of increasingly more complex

nanomedicine designs, but it is now generally acknowledged that this approach has impeded rather than promoted the clinical translation of new nanomedicines.[58, 67-69] In contrast, clinically approved and targeted nanomedicines tend to be compositionally simple,[49] with designs based on robust physicochemical principles (*e.g.* PEGylation to improve circulation lifetimes)[70] and well characterised and exploitable, albeit now clinically questionable,[71, 72] biological phenomena (*e.g.* the EPR effect of select solid tumours).[73] Following these principles, we have designed a simple and effective proof-of-concept liposome technology, composed of just two lipids, based on, and preceded by, a thorough understanding of both the physicochemical and *in vivo* nano-bio interactions involved. As such, it is our hope that this study, and in particular the tools and methods employed, will expedite a transition from the empirical design of increasingly complex nanomedicines to the rational design of new, simple and effective nanomedicines.[74]

4.5 Materials and Methods

Materials and Reagents

1,2-dioleoyl-*sn*-glycero-3-phosphocholine (DOPC), 1,2-dioleoyl-3-trimethyl ammonium-propane (DOTAP), 1,2-dioleoyl-*sn*-glycero-3 phosphoethanolamine-N-(lissamine rhodamine B sulfonyl) (Rhodamine-PE) were purchased from Avanti Polar Lipids (Alabaster, AL, US). 1,2-Dioleoyl-*sn*-glycero-3-phospho-ethanolamine-Atto 633 was purchased from ATTO-TEC GmbH (Germany). Additional DOPC was purchased from Lipoid GmbH. Cholesterol and sulforhodamine B (SR-B, sodium salt) were purchased from Sigma Aldrich. pHrodo™ Red, succinimidyl ester (pHrodo™ Red, SE) was purchased from Thermo Fisher Scientific. DOPE-pHrodo was prepared through conjugation of DOPE with pHrodo succinimidyl ester under basic conditions, followed by column chromatography.[75] Fluorescein-labeled hyaluronic acid (fluoHA) was prepared through conjugation of hyaluronic acid (100 kDa) with fluorescein isothiocyanate (Isomer I, Sigma-Aldrich) under mildly basic conditions, followed by ethanol precipitation.[76] All other chemical reagents were purchased at the highest grade available from Sigma Aldrich and used without further purification. All solvents were purchased from Biosolve Ltd. For anhydrous reactions, solvents were dried over activated molecular sieves (3 Å, 4–8 mesh). *HEPES buffer*: HEPES (10 mM) adjusted to pH 7.4 with 1 m aqueous NaOH. Ultrapure MilliQ® water, purified by a MilliQ Advantage A10 water purification system from MilliPore, was used throughout.

Chemical synthesis and characterization

Described in reference [43].

Light source and actinometry

A commercially available 375-nm LED (Maximum measured wavelength = 370 nm, FWHM = 13.4 nm; H2A1-H375-S, Roithner Lasertechnik, Vienna, Austria), driven by a custom-built LED driver (I = 350 mA), was used as UV light source in all cases. The optical power density of the LED light source was determined using an integrating sphere setup. For this, the LED was positioned precisely 5 cm above the 6.0 mm aperture of an integrating sphere (AvaSphere-30-IRRAD, Avantes, Apeldoorn, The Netherlands). This sphere was connected by an optical fiber (FC-UV600-2, Avantes) to a UV-Vis spectrometer (AvaSpec-ULS2048L StarLine CCD spectrometer, Avantes). The setup was calibrated using a NIST-traceable calibration light source (Avalight-HAL-CAL-ISP30, Avantes). The LED was switched on, and allowed to warm up for 1 min, before a spectrum was recorded (see **Supplementary Figure 11** for measured UV-Vis spectrum). The obtained spectrum was integrated to obtain the total incident optical power density (in mW cm^{-2}). Light dosages (J per embryo) were obtained by multiplying the optical power density by the irradiation time. Average embryo surface area used was 0.03 cm^2 (0.1 x 0.3 cm). Precise irradiation setups are detailed within experimental descriptions.

Liposome preparation

All liposomes (without encapsulated payloads) were formulated in either (deionized) H_2O or 10 mM HEPES buffer at a total lipid concentration of 4 mM. Individual lipids, as stock solutions (1-10 mM) in chloroform, were combined to the desired molar ratios and dried to a film, first under a stream of N_2 then >1 h under vacuum. Large unilamellar vesicles were formed through extrusion above the T_m of all lipids (room temperature, Mini-extruder, Avanti Polar Lipids, Alabaster, US). Hydrated lipids were passed 11 times through 2 x 400 nm polycarbonate (PC) membranes (Nucleopore Track-Etch membranes, Whatman), followed by 11 times through 2 x 100 nm PC pores. All liposome dispersions were stored at 4°C. All liposomes were stable for at least 1 month (in the dark).

Size and zeta potential measurements

Particle size and zeta potentials were measured using a Malvern Zetasizer Nano ZS (software version 7.13, Malvern Panalytical). For DLS (operating wavelength = 633 nm), measurements were carried out at room temperature in water or HEPES (10 mM) buffer at a total lipid concentration of approx. 100 µM. Zeta potentials were measured at 500 µM total lipid concentration, using a dip-cell electrode (Malvern), at room temperature. For liposomes formulated in water, aq. NaCl was added to the liposome solution to a final concentration of 10 mM NaCl before zeta potential measurement. All reported DLS measurements and zeta potentials are the average of three measurements. For DLS and zeta

potential experiments monitoring changes following light activation, liposomes were irradiated (370 ± 7 nm, 202 mW cm^{-2}) in quartz cuvettes with the LED mounted at a distance of 1 cm from the sample. The same liposome sample was used for time course DLS and zeta potential measurements.

CryoTEM

Liposomes (3-6 µL, 4 mM total lipid concentration) were applied to a freshly glow-discharged carbon 200 mesh Cu grid (Lacey carbon film, Electron Microscopy Sciences, Aurion, Wageningen, The Netherlands). Grids were blotted for 1, 2 or 3 s at 99% humidity in a Vitrobot plunge-freezer (FEI VitrobotTM Mark III, Thermo Fisher Scientific). CryoTEM images were collected on a Talos L120C (NeCEN, Leiden University) operating at 120 kV. Images were recorded manually at a nominal magnification of 17500x or 36000x yielding a pixel size at the specimen of 5.88 or 2.90 ångström (Å), respectively. For CryoTEM images monitoring changes following light activation, liposomes were irradiated (15 mins, 370 ± 7 nm, 202 mW cm^{-2}) in quartz cuvettes with the LED mounted at a distance of 1 cm from the sample. The same liposome sample was used for before and after UV.

Sulforhodamine-B (SR-B) encapsulation and characterization

DOPC:**4** (1:1) lipid films (10 mM total lipids) were hydrated with HEPES buffer (1 mL) containing SR-B (10 mM) and formulated by extrusion, as described for empty liposomes. Un-encapsulated SR-B was removed by size exclusion chromatography (Illustra™ NAP™ Sephadex™ G-25 DNA grade pre-made columns (GE Healthcare)) following the supplier's instructions. Eluted liposomes with encapsulated SR-B were diluted 2.5x during SEC (to approximately 4 mM [total lipid]) and injected without further dilution.

Contents leakage assay: SR-B leakage from DOPC:**4** (1:1) liposomes, before and after light activation, was monitored using a TECAN Infinite M1000 Fluorescence Plate Reader and were performed in 96-well plates (PP Microplate, solid F-bottom (flat), chimney well) at room temperature. Final experimental volume in each well was 200 µL. To monitor SR-B leakage (and dye de-quenching) during photoactivation, fluorescence emission (excitation: 520 nm; emission: 580 nm) was measured every 20 s for 600 s, the sample was then irradiated (20 mins, 370 ± 7 nm, 202 mW cm^{-2}) in a quartz cuvette, with the LED mounted at a distance of 1 cm from the sample, returned to the 96-well plate and fluorescence emission measured for a further 10 mins. After this, Triton X-100 (10 µL, 1% w/v) was added to the sample well (10 s agitation) to solubilize liposomes and release any remaining encapsulated SR-B.

Zebrafish husbandry, injections and irradiation setup

Zebrafish (*Danio rerio*, strain *AB/TL*) were maintained and handled in accordance with guidelines from the European Convention on the protection of vertebrate animals used for experimental and other scientific purposes,[77] and in compliance with the directives of the local animal welfare committee of Leiden University. Fertilization was performed by natural spawning at the beginning of the light period, and eggs were raised at 28.5 °C in egg water (60 μg mL^{-1} Instant Ocean sea salts). The following previously established zebrafish lines were used: Tg*(kdrl:*eGFP*)*^{s843},[78] Tg*(mpeg1*:GFP*)*^{gl22},[79] Tg*(mpeg1:*mCherry*)*^{gl23}.[79] Liposomes were injected into 2-day old zebrafish embryos (52-56 hpf) using a modified microangraphy protocol.[80] Embryos were anesthetized in 0.01% tricaine and embedded in 0.4% agarose containing tricaine before injection. To improve reproducibility of microangiography experiments, 1 nL sample volumes were calibrated and injected into the sinus venous/duct of Cuvier. A small injection space was created by penetrating the skin with the injection needle and gently pulling the needle back, thereby creating a small pyramidal space in which the liposomes were injected. Successfully injected embryos were identified through the backward translocation of venous erythrocytes and the absence of damage to the yolk ball. For embryo irradiation, the UV source (370 ± 7 nm) was positioned approximately 1.5 cm above the agar-embedded embryo (~90 mW cm^{-2}). 15 min total irradiation time (~2.4 J per embryo light dose) was used in all cases of embryo irradiation followed by confocal imaging. For experiments monitoring changes in liposome biodistribution following light triggered surface charge switching, the same embryo was imaged before and after UV irradiation.

Confocal image acquisition and quantification

Zebrafish embryos were selected according to successful injections and randomly picked from a dish of 20-60 successfully injected embryos. At least four zebrafish were visualized and the most representative zebrafish was imaged by a Leica TCS SPE or SP8 confocal microscope (Leica Application Suite X software, version 3.5.5.19976, Leica Microsystems). Confocal z-stacks were captured using a 10x air objective (HCX PL FLUOTAR), a 40x water-immersion objective (HCX APO L) or 63x water-immersion objective (HC PL APO CS). For whole-embryo views, 3 overlapping z-stacks were captured to cover the complete embryo. Laser intensity, gain and offset settings were identical between stacks and experiments. Images were processed and quantified using the Fiji distribution of ImageJ.[81, 82] For quantification of liposome circulation lifetime decay, at least three individual embryos (biological replicates) were imaged using confocal microscopy at each time point. Quantification (not blinded) was performed on 40x confocal z-stacks (optical thickness of 2-3 μm per slice) using methods and ImageJ macros previously described.[24] Median values are reported.

Two-Photon Setup and Image Acquisition

A custom-built two-photon multifocal microscope was used for simultaneous UV irradiation and two-photon fluorescent imaging (see **Supplementary Figure 10** for schematic of the multiphoton microscope setup). A femtosecond pulsed Ti:Sa laser set at 830 nm (Coherent, Chameleon Ultra) was used as excitation source. Multifocal illumination of the sample was achieved by a diffractive optical element (DOE, custom made by Holoeye) which splits the laser beam into an array of 25 x 25 foci. A virtual light sheet was created by spiral scanning the foci within the 50 ms exposure time of the camera using a fast-scanning mirror (Newport, FSM-300-1).[83] The virtual light sheet was focused and emission photons collected by a 25X, high-NA water-dipping objective (Nikon, CFI75 Apochromat 25XC W). The objective was positioned onto a piezo stage (P-726 PIFOC, PI) for z-stack measurements. Emission light was separated from the excitation path by a dichroic mirror (700 dcxr, Chroma). After passing through a 700 nm short pass filter, emission photons were detected with a 2048 x 2048 pixel sCMOS camera (Hamamatsu, Orca Flash 4.0 V2). Emission images were taken at the start of the experiment with a white LED. After the emission images, the UV-LED was installed at the location of the white LED. The UV LED was positioned approximately 1.5 cm (~90 mW cm^{-2}) above the sample and on/off-times were timed by the same data acquisition card (USB-6226, National Instruments) which triggered the camera. Simultaneous UV irradiation and two-photon fluorescent imaging was performed one hour post injection. To ensure stability, embryos were imaged for 15 minutes before the measurement. Once embryos were stable, images were taken every 1 second for 5 minutes. After 5 minutes the UV lamp was turned on and switched off only during camera exposure. Two-photon microscopy data was processed using custom-built LabVIEW software (version 2018 SP2, National Instruments).

Statistics and Reproducibility

All experiments presented in the main manuscript were repeated at least twice with the exception of **Figures 6b,c**. All replicate experiments were performed using freshly prepared liposomes. Unless clearly stated in the manuscript text (*e.g.* varying macrophage uptake prior to UV activation), all replicate experiments were successful and confirm the presented data. All experiments presented in Supplementary Information were repeated at least twice, with the exception of **Supplementary Figures 1** and **9**. All replicate experiments were performed using freshly prepared liposomes. For all experiments performed in embryonic zebrafish, at least four embryos were randomly selected (from a pool of >20 successfully injected embryos) and imaged (low resolution microscopy). Unless clearly stated in the manuscript text (*e.g.* varying macrophage uptake prior to UV activation), all imaged embryos showed consistent results and confirmed the presented data. From these four embryos, one was selected for

high resolution, confocal microscopy. No statistical analysis is performed in this work.

Data Availability

Source data (raw confocal z-stacks and collated data as single Excel sheet) underpinning the data presented in **Figure 4g** have been deposited within the public image database, fighare.com (DOI: 10.6084/m9.figshare.12387629).

Link for the movies:
https://www.nature.com/articles/s41467-020-17360-9#Sec21

4.6 Abbreviations

AMD	age-related macular degeneration
CHT	caudal hematopoietic tissue
CryoTEM	Cryo transmission electron microscopy
CV	caudal vein
DA	dorsal aorta
DLS	dynamic light scattering
DOPC	1,2-dioleoyl-*sn*-glycero-3-phosphocholine
DOTAP	1,2-dioleoyl-3-trimethylammonium-propane
dpf	day(s) post fertilization
ECs	endothelial cells
EPR	enhanced permeability and retention
fluoHA	fluorescently labeled hyaluronic acid
hpi	hour(s) post injection
ISV	intersegmental vessel
i.v.	intravenous
KCs	Kupffer cells
LSECs	liver sinusoidal endothelial cells
NIR	near infrared light
PCV	posterior cardinal vein
PDI	polydispersity indices
PEG	polyethylene glycol
RES	reticuloendothelial system
SECs	scavenging endothelial cells
SR-B	sulforhodamine B

4.7 Supporting Information

Supplementary Table 1. Composition, size and measured zeta potentials of liposomes. All reported DLS measurements and zeta potentials are the average of three measurements. For measurements monitoring changes following light activation, liposomes were irradiated (20 mins, 370 nm, 202 $mWcm^{-2}$) in quartz cuvettes, with the LED mounted at a distance of 1 cm from the sample. Reported sizes and zeta potentials are for individual liposome samples but representative over multiple sample preparations. The number of individual liposome preparations varied depending on liposome formulation. In the case of DOPC:4 liposomes (prior to UV irradiation), sizes and zeta potentials did not significantly deviate across >10 independent formulations. This included variations in DOPC supplier, $CHCl_3$ lipid stock solutions and synthesized batches of 4. In contrast, batch-to-batch variation in the measured zeta potential of DOPC:4→3 liposomes (*i.e.* after UV irradiation) resulted in a liposome surface charges ranging from +20 to +35 mV ζ-potential. The same liposome sample was measured before and after UV irradiation.

Composition	mol%	Buffer	Size		Zeta potential (mV)
			D_h (nm)	PDI	
DOPC:1	95:5	water	116.9	0.108	-7.70
	90:10	water	117.7	0.082	-1.05
	75:25	water	109.5	0.139	24.40
	50:50	water	119.7	0.068	30.13
DOPC:2	95:5	water	113.4	0.098	-9.25
	90:10	water	114.4	0.085	-4.15
	75:25	water	117.8	0.100	13.84
	50:50	water	117.4	0.101	38.10
DOPC:3	95:5	water	112.5	0.058	-8.25
	90:10	water	102.8	0.074	-4.94
	75:25	water	110.8	0.134	15.07
	50:50	water	122.7	0.156	48.53
DOPC:DOTAP	50:50	water	123.9	0.050	44.83
DOPC:4 (before UV)	50:50	HEPES	105.2	0.085	-8.07
DOPC:4 (after UV)	50:50	HEPES	115.2	0.101	25.93

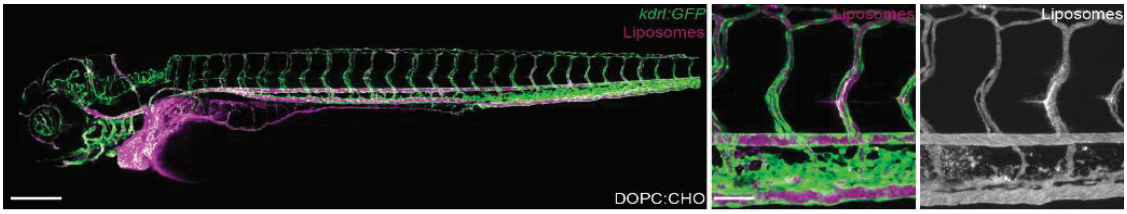

Supplementary Figure 1. Biodistribution of DOPC:cholesterol liposomes. Whole embryo and tissue level views of DOPC:cholesterol (1:1) liposome distribution in *kdrl:*GFP transgenic embryos (2 dpf), 1 hpi. DOPC:cholesterol liposomes freely circulate throughout the vasculature of the embryonic zebrafish and do not appreciably interact with blood-resident macrophages, SECs, or any other endothelial cell types of the embryo. Liposomes contained 1 mol% fluorescent lipid probe, DOPE-LR, for visualization. Scale bars: 200 μm (whole embryo); 50 μm (tissue level).

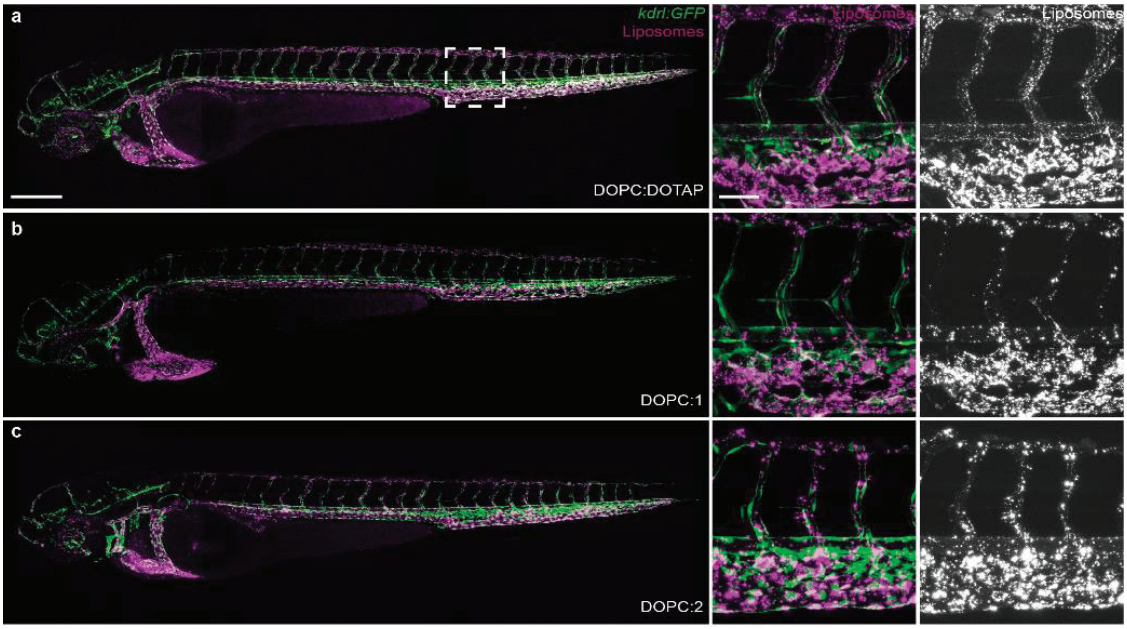

Supplementary Figure 2. Biodistribution of cationic liposomes. Whole embryo and tissue level views of liposome distribution in *kdrl*:GFP transgenic embryos (2 dpf), 1 hpi of **(a)** DOPC:DOTAP (1:1), **(b)** DOPC:1 (1:1) and **(c)** DOPC:2 (1:1) liposomes. All three cationic liposome formulations are visible as immobile fluorescent punctae associated with blood vessel walls throughout the vasculature of the zebrafish embryo and are largely removed from circulation. Liposomes contained 1 mol% fluorescent lipid probe, DOPE-LR, for visualization. Scale bars: 200 μm (whole embryo); 50 μm (tissue level).

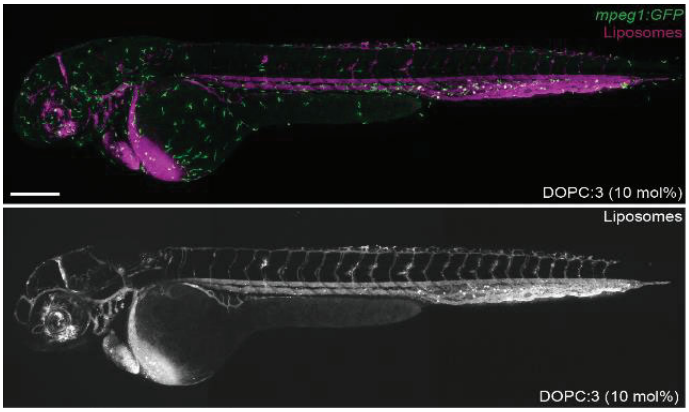

Supplementary Figure 3. Uptake of DOPC:3 (9:1) liposomes within blood resident macrophages. Whole embryo views of DOPC:**3** (9:1) liposome distribution in *mpeg1:*GFP transgenic embryos (2 dpf), 1 hpi. Extensive fluorescence colocalization of liposomes and blood resident macrophages can be observed primarily within the CHT of the embryonic fish. In addition, a significant fraction of liposomes remains in circulation. Liposomes contained 1 mol% fluorescent lipid probe, DOPE-LR, for visualization. Scale bar: 200 µm (whole embryo).

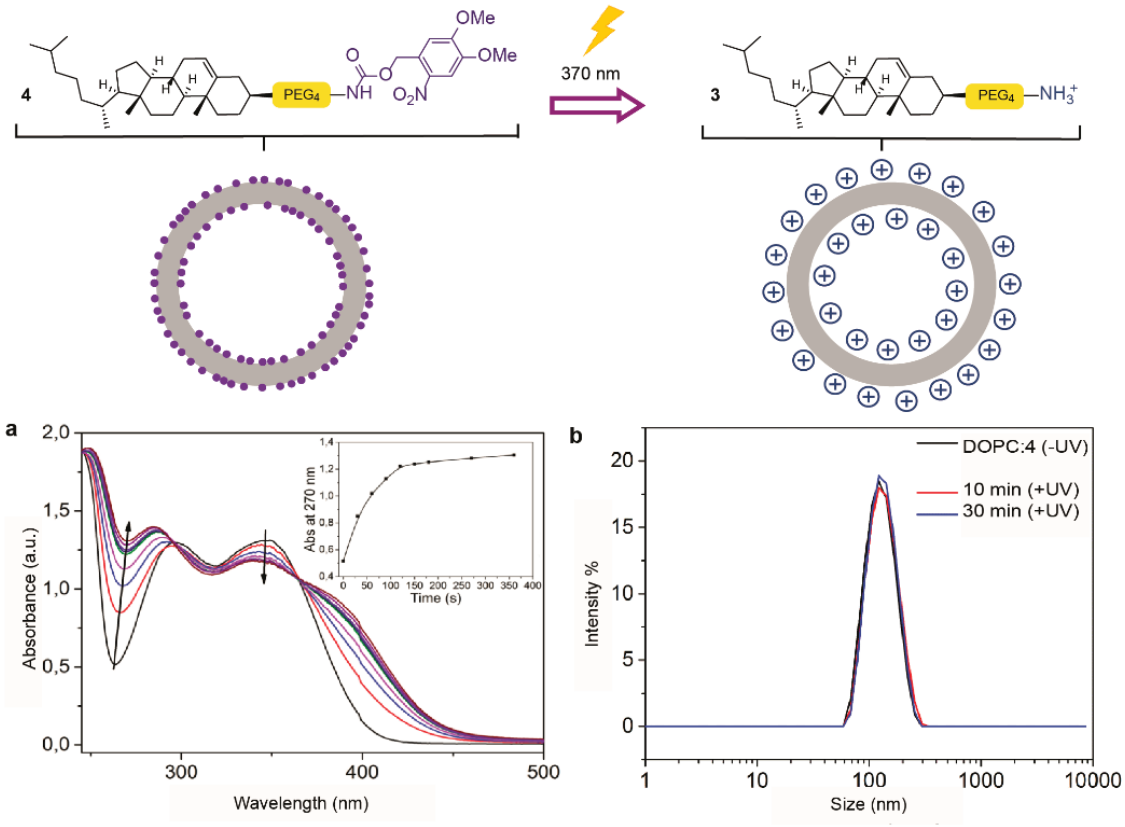

Supplementary Figure 4. Photolysis of 4. (a) Time evolution of the UV/Vis spectra of a solution of 4 (200 µM; H2O/MeCN/tBuOH, 1:1:1) during UV irradiation (370 ± 7 nm, 202 mW cm-2). Inset: Time evolution of the UV absorbance at 270 nm. **(b)** DLS spectra of DOPC:4 (1:1) liposomes before and after light activation (10 and 30 min, 370 ± 7 nm, 202 mW cm-2) and surface charge switching.

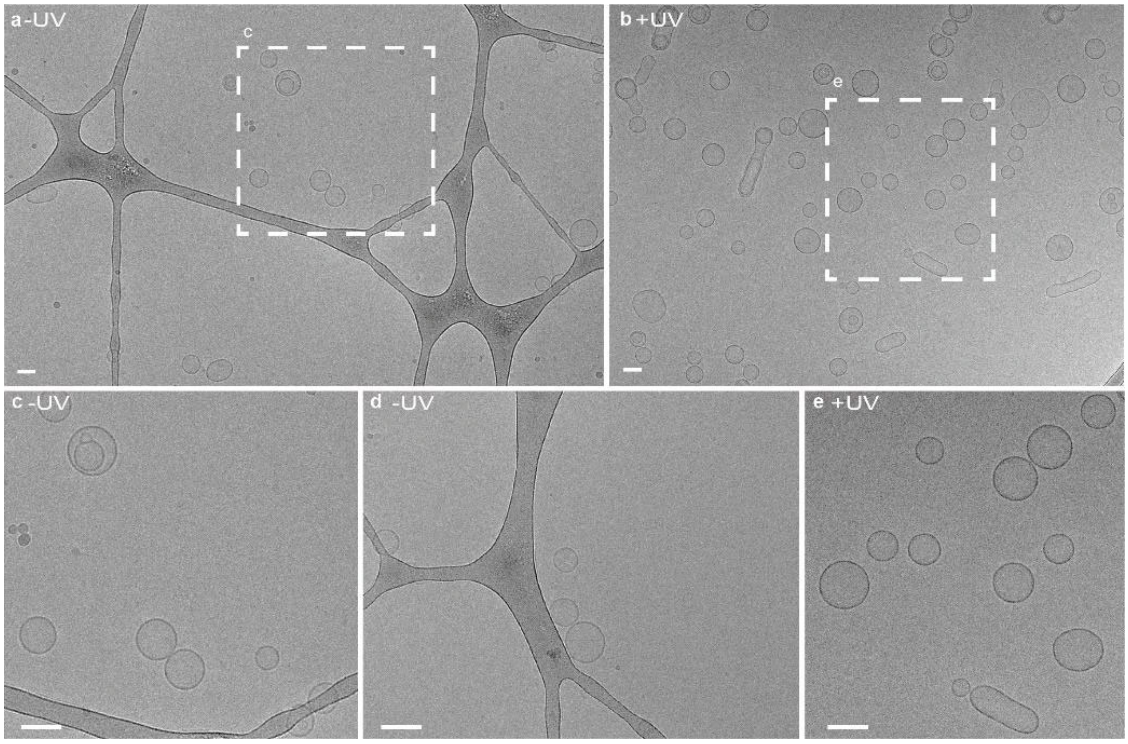

Supplementary Figure 5. Low magnification CryoTEM images of DOPC:4 liposomes before and after UV. CryoTEM images of (empty) DOPC:4 liposomes **(a,c,d)** before and **(b,e)** after in situ irradiation (15 min, 370 ± 7 nm, 202 mW cm-2). Note: Two individual CryoTEM panels of the same liposome sample are shown for the -UV sample as observed populations of DOPC:4 liposomes, prior to UV irradiation, were consistently less than those after UV irradiation despite identical liposome concentrations. Scale bars: 100 nm.

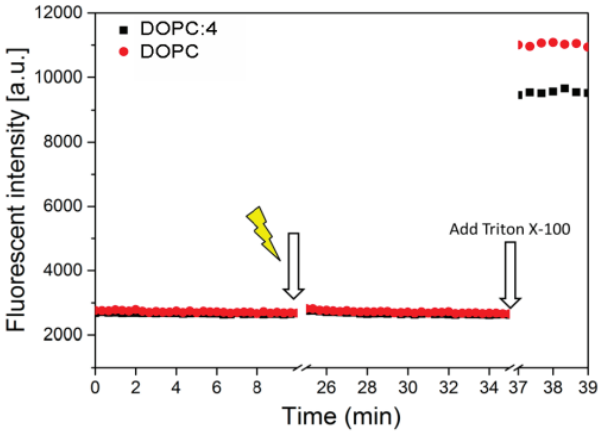

Supplementary Figure 6. Contents (SR-B) leakage. SR-B leakage (and dye de-quenching) from DOPC:**4** liposomes before and after UV irradiation. Fluorescence emission (excitation: 520 nm; emission: 580 nm) was measured every 20 s for 600 s, the sample was then irradiated (20 mins, 370 ± 7 nm, 202 mW cm-2) in a quartz cuvette and fluorescence re-measured for a further 600 s. Triton X-100 (10 µL, 1% w/v) was added to solubilize liposomes and release encapsulated SR-B. DOPC (100% DOPC content) was

used as a control to demonstrate contents leakage was not dependent on UV irradiation.

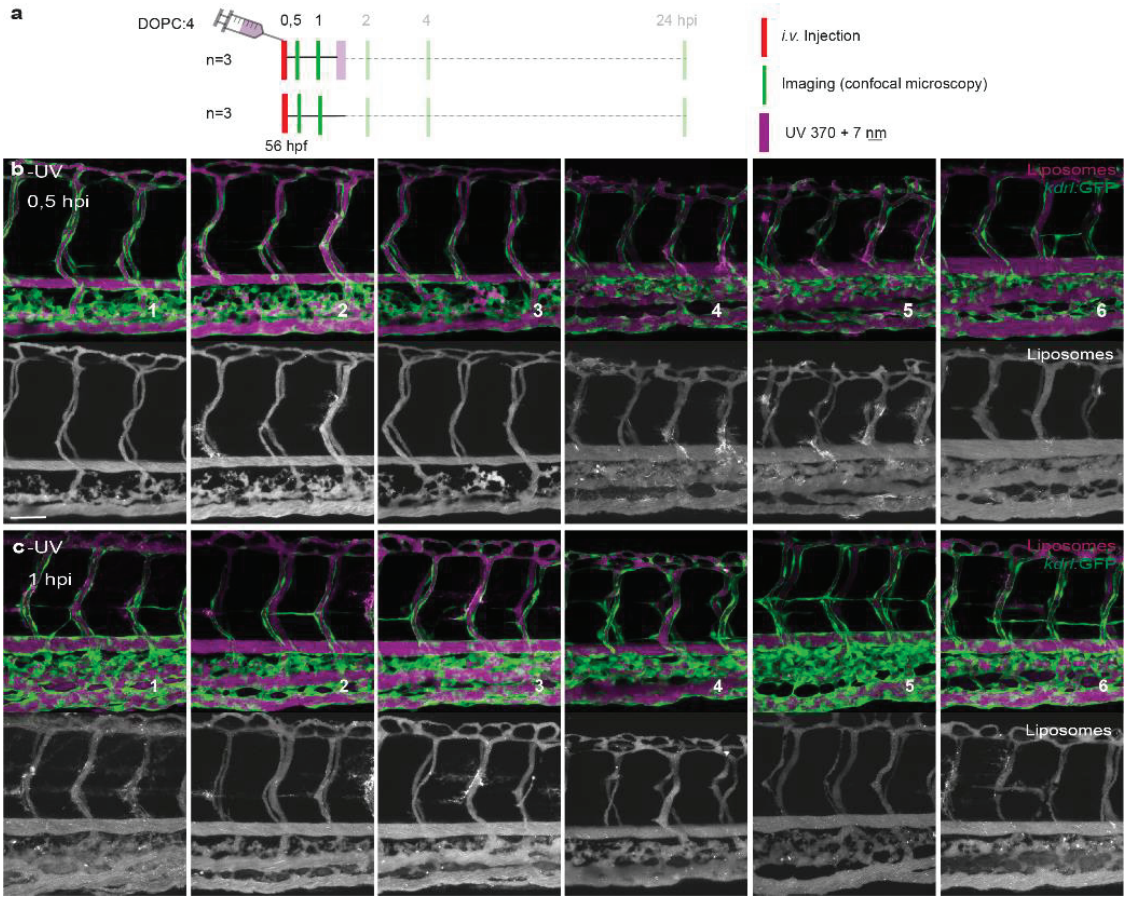

Supplementary Figure 7. Individual tissue level images used for quantification of circulation lifetime decays. (a) Time schedule of injections, time course imaging and UV irradiation used to quantify liposome circulation lifetime decay. Tissue level views of DOPC:**4 l**iposome distribution in *kdrl:*GFP transgenic zebrafish embryos at **(b)** 0.5 hpi (n=6), **(c)** 1 hpi (n=6). Quantification of circulation lifetime decays performed as previously described.8 Liposomes contained 1 mol% fluorescent lipid probe, DOPE-LR, for visualization. Scale bar: 50 μm (tissue level).

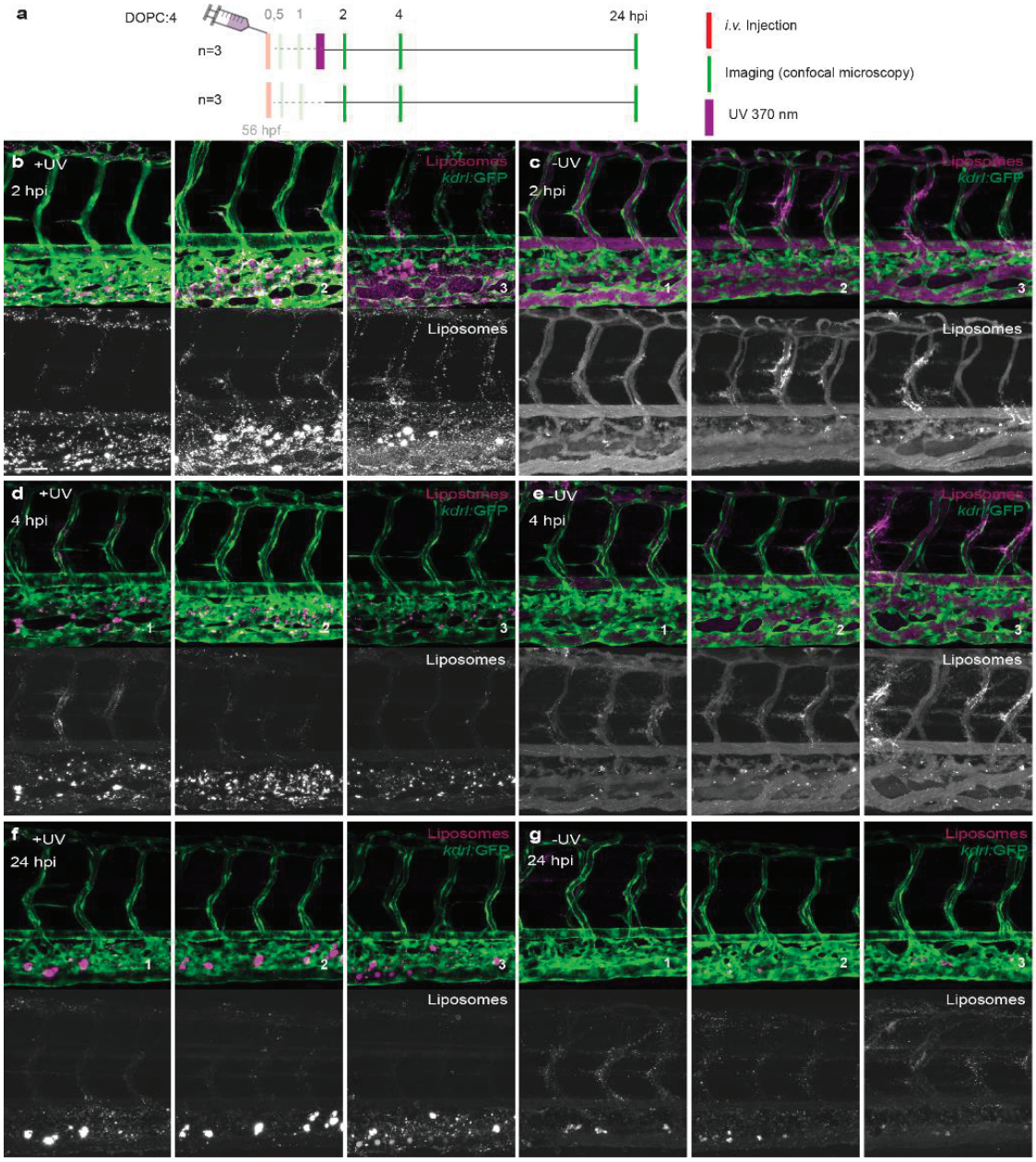

Supplementary Figure 8. Individual tissue level images used for quantification of circulation lifetime decays. (a) Time schedule of injections, time course imaging and UV irradiation used to quantify liposome circulation lifetime decay. Tissue level views of DOPC:4 liposome distribution in *kdrl:*GFP transgenic zebrafish embryos at **(c)** 2 hpi (n=3), **(e)** 4 hpi (n=3), **(g)** 24 hpi (n=3) in the absence of UV irradiation, and of DOPC:**4→3** liposomes at **(b)** 2 hpi (n=3), **(d)** 4 hpi (n=3), **(f)** 24 hpi (n=3) following UV irradiation at 1.1 hpi. Quantification of circulation lifetime decays performed as previously described.8 Liposomes contained 1 mol% fluorescent lipid probe, DOPE-LR, for visualization. Scale bar: 50 μm (tissue level).

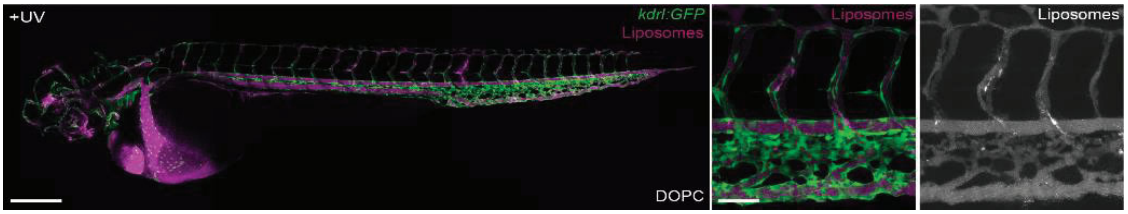

Supplementary Figure 9. Biodistribution of freely circulating DOPC liposomes following UV irradiation. Whole embryo and tissue level views of DOPC (100% DOPC content) liposome distribution in *kdrl:GFP* transgenic embryos (2 dpf), 1 hpi. following UV in situ irradiation (15 min, 370 ± 7 nm, ~90 mW cm-2, ~2.4 J per embryo). The biodistribution of DOPC liposomes was unaffected by UV irradiation and liposomes remained in circulation. Liposomes contained 1 mol% fluorescent lipid probe, DOPE-LR, for visualization. Scale bars: 200 μm (whole embryo); 50 μm (tissue level).

4.9 References

1. Zhao, Z.; Ukidve, A.; Krishnan, V.; Mitragotri, S., Effect of physicochemical and surface properties on in vivo fate of drug nanocarriers. *Adv Drug Deliv Rev* **2019,** *143*, 3-21.
2. Elci, S. G.; Jiang, Y.; Yan, B.; Kim, S. T.; Saha, K.; Moyano, D. F.; Yesilbag Tonga, G.; Jackson, L. C.; Rotello, V. M.; Vachet, R. W., Surface Charge Controls the Suborgan Biodistributions of Gold Nanoparticles. *ACS Nano* **2016,** *10* (5), 5536-5542.
3. Xiao, K.; Li, Y.; Luo, J.; Lee, J. S.; Xiao, W.; Gonik, A. M.; Agarwal, R. G.; Lam, K. S., The effect of surface charge on in vivo biodistribution of PEG-oligocholic acid based micellar nanoparticles. *Biomaterials* **2011,** *32* (13), 3435-3446.
4. He, C.; Hu, Y.; Yin, L.; Tang, C.; Yin, C., Effects of particle size and surface charge on cellular uptake and biodistribution of polymeric nanoparticles. *Biomaterials* **2010,** *31* (13), 3657-3666.
5. Zhang, Y. N.; Poon, W.; Tavares, A. J.; McGilvray, I. D.; Chan, W. C. W., Nanoparticle-liver interactions: Cellular uptake and hepatobiliary elimination. *J Control Release* **2016,** *240*, 332-348.
6. Devine, D. V.; Wong, K.; Serrano, K.; Chonn, A.; Cullis, P. R., Liposome-complement interactions in rat serum: implications for liposome survival studies. *Biochim Biophys Acta* **1994,** *1191* (1), 43-51.
7. Gessner, A.; Lieske, A.; Paulke, B.; Muller, R., Influence of surface charge density on protein adsorption on polymeric nanoparticles: analysis by two-dimensional electrophoresis. *Eur J Pharm Biopharm* **2002,** *54* (2), 165-170.
8. Gessner, A.; Lieske, A.; Paulke, B. R.; Muller, R. H., Functional groups on polystyrene model nanoparticles: influence on protein adsorption. *J Biomed Mater Res A* **2003,** *65* (3), 319-326.
9. Lundqvist, M.; Stigler, J.; Elia, G.; Lynch, I.; Cedervall, T.; Dawson, K. A., Nanoparticle size and surface properties determine the protein corona with possible implications for biological impacts. *Proc Natl Acad Sci U S A* **2008,** *105* (38), 14265-14270.
10. Walkey, C. D.; Chan, W. C., Understanding and controlling the interaction of nanomaterials with proteins in a physiological environment. *Chem Soc Rev* **2012,** *41* (7), 2780-2799.
11. Lazarovits, J.; Chen, Y. Y.; Sykes, E. A.; Chan, W. C., Nanoparticle-blood interactions: the implications on solid tumour targeting. *Chem Commun (Camb)* **2015,** *51* (14), 2756-2767.
12. Aggarwal, P.; Hall, J. B.; McLeland, C. B.; Dobrovolskaia, M. A.; McNeil, S. E., Nanoparticle interaction with plasma proteins as it relates to particle biodistribution, biocompatibility and therapeutic efficacy. *Adv Drug Deliv Rev* **2009,** *61* (6), 428-437.
13. Alexis, F.; Pridgen, E.; Molnar, L. K.; Farokhzad, O. C., Factors affecting the clearance and biodistribution of polymeric nanoparticles. *Mol Pharm* **2008,** *5* (4), 505-515.
14. Cullis, P. R.; Chonn, A.; Semple, S. C., Interactions of liposomes and lipid-based carrier systems with blood proteins: Relation to clearance behaviour in vivo. *Adv Drug Deliv Rev* **1998,** *32* (1-2), 3-17.
15. Arvizo, R. R.; Miranda, O. R.; Thompson, M. A.; Pabelick, C. M.; Bhattacharya, R.; Robertson, J. D.; Rotello, V. M.; Prakash, Y. S.; Mukherjee, P., Effect of nanoparticle surface charge at the plasma membrane and beyond. *Nano Lett* **2010,** *10* (7), 2543-2548.
16. Cho, E. C.; Xie, J.; Wurm, P. A.; Xia, Y., Understanding the role of surface charges in cellular adsorption versus internalization by selectively removing gold nanoparticles on the cell surface with a I2/KI etchant. *Nano Lett* **2009,** *9* (3), 1080-1084.
17. Nazarenus, M.; Zhang, Q.; Soliman, M. G.; Del Pino, P.; Pelaz, B.; Carregal-Romero, S.; Rejman, J.; Rothen-Rutishauser, B.; Clift, M. J.; Zellner, R.; Nienhaus, G. U.; Delehanty, J. B.; Medintz, I. L.; Parak, W. J., In vitro interaction of colloidal nanoparticles with mammalian cells: What have we learned thus far? *Beilstein J Nanotechnol* **2014,** *5*, 1477-1490.
18. Verma, A.; Stellacci, F., Effect of surface properties on nanoparticle-cell interactions. *Small* **2010,** *6* (1), 12-21.
19. Yue, Z. G.; Wei, W.; Lv, P. P.; Yue, H.; Wang, L. Y.; Su, Z. G.; Ma, G. H., Surface charge affects cellular uptake and intracellular trafficking of chitosan-based nanoparticles. *Biomacromolecules* **2011,** *12* (7), 2440-2446.
20. Frohlich, E., The role of surface charge in cellular uptake and cytotoxicity of medical nanoparticles. *Int J Nanomedicine* **2012,** *7*, 5577-5591.
21. Goodman, C. M.; McCusker, C. D.; Yilmaz, T.; Rotello, V. M., Toxicity of gold nanoparticles functionalized with cationic and anionic side chains. *Bioconjug Chem* **2004,** *15* (4), 897-900.
22. Kim, S. T.; Saha, K.; Kim, C.; Rotello, V. M., The role of surface functionality in determining nanoparticle cytotoxicity. *Acc Chem Res* **2013,** *46* (3), 681-691.

23. Bobo, D.; Robinson, K. J.; Islam, J.; Thurecht, K. J.; Corrie, S. R., Nanoparticle-Based Medicines: A Review of FDA-Approved Materials and Clinical Trials to Date. *Pharm Res* **2016,** *33* (10), 2373-2387.
24. Campbell, F.; Bos, F. L.; Sieber, S.; Arias-Alpizar, G.; Koch, B. E.; Huwyler, J.; Kros, A.; Bussmann, J., Directing Nanoparticle Biodistribution through Evasion and Exploitation of Stab2-Dependent Nanoparticle Uptake. *ACS Nano* **2018,** *12* (3), 2138-2150.
25. Hayashi, Y.; Takamiya, M.; Jensen, P. B.; Ojea-Jimenez, I.; Claude, H.; Antony, C.; Kjaer-Sorensen, K.; Grabher, C.; Boesen, T.; Gilliland, D.; Oxvig, C.; Strahle, U.; Weiss, C., Differential Nanoparticle Sequestration by Macrophages and Scavenger Endothelial Cells Visualized in Vivo in Real-Time and at Ultrastructural Resolution. *ACS Nano* **2020,** *14* (2), 1665-1681.
26. Friend, D. S.; Papahadjopoulos, D.; Debs, R. J., Endocytosis and intracellular processing accompanying transfection mediated by cationic liposomes. *Biochim Biophys Acta* **1996,** *1278* (1), 41-50.
27. Gao, X.; Huang, L., A novel cationic liposome reagent for efficient transfection of mammalian cells. *Biochem Biophys Res Commun* **1991,** *179* (1), 280-285.
28. Yin, H.; Kanasty, R. L.; Eltoukhy, A. A.; Vegas, A. J.; Dorkin, J. R.; Anderson, D. G., Non-viral vectors for gene-based therapy. *Nat Rev Genet* **2014,** *15* (8), 541-555.
29. Zhao, Y.; Huang, L., Lipid nanoparticles for gene delivery. *Adv Genet* **2014,** *88*, 13-36.
30. Song, W.; Popp, L.; Yang, J.; Kumar, A.; Gangoli, V. S.; Segatori, L., The autophagic response to polystyrene nanoparticles is mediated by transcription factor EB and depends on surface charge. *J Nanobiotechnology* **2015,** *13*, 87.
31. Klan, P.; Solomek, T.; Bochet, C. G.; Blanc, A.; Givens, R.; Rubina, M.; Popik, V.; Kostikov, A.; Wirz, J., Photoremovable protecting groups in chemistry and biology: reaction mechanisms and efficacy. *Chem Rev* **2013,** *113* (1), 119-191.
32. Yun, S. H.; Kwok, S. J. J., Light in diagnosis, therapy and surgery. *Nat Biomed Eng* **2017,** *1*.
33. Ibsen, S.; Zahavy, E.; Wrasidlo, W.; Hayashi, T.; Norton, J.; Su, Y.; Adams, S.; Esener, S., Localized in vivo activation of a photoactivatable doxorubicin prodrug in deep tumor tissue. *Photochem Photobiol* **2013,** *89* (3), 698-708.
34. Moore, C. M.; Pendse, D.; Emberton, M., Photodynamic therapy for prostate cancer--a review of current status and future promise. *Nat Clin Pract Urol* **2009,** *6* (1), 18-30.
35. Kim, T. I.; McCall, J. G.; Jung, Y. H.; Huang, X.; Siuda, E. R.; Li, Y.; Song, J.; Song, Y. M.; Pao, H. A.; Kim, R. H., et al., Injectable, cellular-scale optoelectronics with applications for wireless optogenetics. *Science* **2013,** *340* (6129), 211-216.
36. Goswami, P. P.; Syed, A.; Beck, C. L.; Albright, T. R.; Mahoney, K. M.; Unash, R.; Smith, E. A.; Winter, A. H., BODIPY-derived photoremovable protecting groups unmasked with green light. *J Am Chem Soc* **2015,** *137* (11), 3783-3786.
37. Peterson, J. A.; Wijesooriya, C.; Gehrmann, E. J.; Mahoney, K. M.; Goswami, P. P.; Albright, T. R.; Syed, A.; Dutton, A. S.; Smith, E. A.; Winter, A. H., Family of BODIPY Photocages Cleaved by Single Photons of Visible/Near-Infrared Light. *J Am Chem Soc* **2018,** *140* (23), 7343-7346.
38. Rubinstein, N.; Liu, P.; Miller, E. W.; Weinstain, R., meso-Methylhydroxy BODIPY: a scaffold for photo-labile protecting groups. *Chem Commun (Camb)* **2015,** *51* (29), 6369-6372.
39. Smith, A. M.; Mancini, M. C.; Nie, S., Bioimaging: second window for in vivo imaging. *Nat Nanotechnol* **2009,** *4* (11), 710-711.
40. Brittijn, S. A.; Duivesteijn, S. J.; Belmamoune, M.; Bertens, L. F.; Bitter, W.; de Bruijn, J. D.; Champagne, D. L.; Cuppen, E.; Flik, G.; Vandenbroucke-Grauls, C. M., et al., Zebrafish development and regeneration: new tools for biomedical research. *Int J Dev Biol* **2009,** *53* (5-6), 835-850.
41. Sieber, S.; Grossen, P.; Uhl, P.; Detampel, P.; Mier, W.; Witzigmann, D.; Huwyler, J., Zebrafish as a predictive screening model to assess macrophage clearance of liposomes in vivo. *Nanomedicine* **2019,** *17*, 82-93.
42. Sieber, S.; Grossen, P.; Detampel, P.; Siegfried, S.; Witzigmann, D.; Huwyler, J., Zebrafish as an early stage screening tool to study the systemic circulation of nanoparticulate drug delivery systems in vivo. *J Control Release* **2017,** *264*, 180-191.
43. Arias-Alpizar, G.; Kong, L.; Vlieg, R. C.; Rabe, A.; Papadopoulou, P.; Meijer, M. S.; Bonnet, S.; Vogel, S.; van Noort, J.; Kros, A.; Campbell, F., Light-triggered switching of liposome surface charge directs delivery of membrane impermeable payloads in vivo. *Nat Commun* **2020,** *11* (1), 3638.
44. Kirby, C.; Clarke, J.; Gregoriadis, G., Effect of the cholesterol content of small unilamellar liposomes on their stability in vivo and in vitro. *Biochem J* **1980,** *186* (2), 591-598.

45. Briuglia, M. L.; Rotella, C.; McFarlane, A.; Lamprou, D. A., Influence of cholesterol on liposome stability and on in vitro drug release. *Drug Deliv Transl Res* **2015,** *5* (3), 231-242.
46. Fantini, J.; Barrantes, F. J., How cholesterol interacts with membrane proteins: an exploration of cholesterol-binding sites including CRAC, CARC, and tilted domains. *Front Physiol* **2013,** *4*, 31.
47. Olzmann, J. A.; Carvalho, P., Dynamics and functions of lipid droplets. *Nat Rev Mol Cell Biol* **2019,** *20* (3), 137-155.
48. Batist, G.; Barton, J.; Chaikin, P.; Swenson, C.; Welles, L., Myocet (liposome-encapsulated doxorubicin citrate): a new approach in breast cancer therapy. *Expert Opin Pharmacother* **2002,** *3* (12), 1739-1751.
49. Chang, H. I.; Yeh, M. K., Clinical development of liposome-based drugs: formulation, characterization, and therapeutic efficacy. *Int J Nanomedicine* **2012,** *7*, 49-60.
50. Dong, Q.; Svoboda, K.; Tiersch, T. R.; Monroe, W. T., Photobiological effects of UVA and UVB light in zebrafish embryos: evidence for a competent photorepair system. *J Photochem Photobiol B* **2007,** *88* (2-3), 137-146.
51. Wang, R.; Zhang, H.; Du, J.; Xu, J., Heat resilience in embryonic zebrafish revealed using an in vivo stress granule reporter. *J Cell Sci* **2019,** *132* (20).
52. Gomez-Garcia, M. J.; Doiron, A. L.; Steele, R. R. M.; Labouta, H. I.; Vafadar, B.; Shepherd, R. D.; Gates, I. D.; Cramb, D. T.; Childs, S. J.; Rinker, K. D., Nanoparticle localization in blood vessels: dependence on fluid shear stress, flow disturbances, and flow-induced changes in endothelial physiology. *Nanoscale* **2018,** *10* (32), 15249-15261.
53. Jiang, X. Y.; Sarsons, C. D.; Gomez-Garcia, M. J.; Cramb, D. T.; Rinker, K. D.; Childs, S. J., Quantum dot interactions and flow effects in angiogenic zebrafish (Danio rerio) vessels and human endothelial cells. *Nanomedicine* **2017,** *13* (3), 999-1010.
54. Rausch, K.; Reuter, A.; Fischer, K.; Schmidt, M., Evaluation of nanoparticle aggregation in human blood serum. *Biomacromolecules* **2010,** *11* (11), 2836-2839.
55. Zhao, W.; Zhuang, S.; Qi, X. R., Comparative study of the in vitro and in vivo characteristics of cationic and neutral liposomes. *Int J Nanomedicine* **2011,** *6*, 3087-3098.
56. Pattipeiluhu, R.; Crielaard, S.; Klein-Schiphorst, I.; Florea, B. I.; Kros, A.; Campbell, F., Unbiased Identification of the Liposome Protein Corona using Photoaffinity-based Chemoproteomics. *ACS Cent Sci* **2020,** *6* (4), 535-545.
57. Smedsrod, B., Clearance function of scavenger endothelial cells. *Comp Hepatol* **2004,** *3 Suppl 1*, S22.
58. Witzigmann, D.; Hak, S.; van der Meel, R., Translating nanomedicines: Thinking beyond materials? A young investigator's reply to 'The Novelty Bubble'. *J Control Release* **2018,** *290*, 138-140.
59. Sieber, S.; Grossen, P.; Bussmann, J.; Campbell, F.; Kros, A.; Witzigmann, D.; Huwyler, J., Zebrafish as a preclinical in vivo screening model for nanomedicines. *Adv Drug Deliv Rev* **2019,** *151-152*, 152-168.
60. Witzigmann, D.; Uhl, P.; Sieber, S.; Kaufman, C.; Einfalt, T.; Schoneweis, K.; Grossen, P.; Buck, J.; Ni, Y.; Schenk, S. H.; Hussner, J.; Meyer Zu Schwabedissen, H. E.; Quebatte, G.; Mier, W.; Urban, S.; Huwyler, J., Optimization-by-design of hepatotropic lipid nanoparticles targeting the sodium-taurocholate cotransporting polypeptide. *Elife* **2019,** *8*.
61. McMillan, T. J.; Leatherman, E.; Ridley, A.; Shorrocks, J.; Tobi, S. E.; Whiteside, J. R., Cellular effects of long wavelength UV light (UVA) in mammalian cells. *J Pharm Pharmacol* **2008,** *60* (8), 969-976.
62. Narayanan, D. L.; Saladi, R. N.; Fox, J. L., Ultraviolet radiation and skin cancer. *Int J Dermatol* **2010,** *49* (9), 978-986.
63. Fenton, C.; Perry, C. M., Verteporfin: a review of its use in the management of subfoveal choroidal neovascularisation. *Drugs Aging* **2006,** *23* (5), 421-445.
64. Blum, A. P.; Kammeyer, J. K.; Rush, A. M.; Callmann, C. E.; Hahn, M. E.; Gianneschi, N. C., Stimuli-responsive nanomaterials for biomedical applications. *J Am Chem Soc* **2015,** *137* (6), 2140-2154.
65. Mura, S.; Nicolas, J.; Couvreur, P., Stimuli-responsive nanocarriers for drug delivery. *Nat Mater* **2013,** *12* (11), 991-1003.
66. Chen, X.; Liu, L.; Jiang, C., Charge-reversal nanoparticles: novel targeted drug delivery carriers. *Acta Pharm Sin B* **2016,** *6* (4), 261-267.
67. Time to deliver. *Nat Biotechnol* **2014,** *32* (10), 961.
68. Venditto, V. J.; Szoka, F. C., Jr., Cancer nanomedicines: so many papers and so few drugs! *Adv Drug Deliv Rev* **2013,** *65* (1), 80-88.

69. Wicki, A.; Witzigmann, D.; Balasubramanian, V.; Huwyler, J., Nanomedicine in cancer therapy: challenges, opportunities, and clinical applications. *J Control Release* **2015,** *200*, 138-157.
70. Immordino, M. L.; Dosio, F.; Cattel, L., Stealth liposomes: review of the basic science, rationale, and clinical applications, existing and potential. *Int J Nanomedicine* **2006,** *1* (3), 297-315.
71. Sindhwani, S.; Syed, A. M.; Ngai, J.; Kingston, B. R.; Maiorino, L.; Rothschild, J.; MacMillan, P.; Zhang, Y.; Rajesh, N. U.; Hoang, T., et al., The entry of nanoparticles into solid tumours. *Nat Mater* **2020,** *19* (5), 566-575.
72. Wilhelm, S.; Tavares, A. J.; Dai, Q.; Ohta, S.; Audet, J.; Dvorak, H. F.; Chan, W. C. W., Analysis of nanoparticle delivery to tumours. *Nature Reviews Materials* **2016,** *1* (5), 16014.
73. Maeda, H.; Nakamura, H.; Fang, J., The EPR effect for macromolecular drug delivery to solid tumors: Improvement of tumor uptake, lowering of systemic toxicity, and distinct tumor imaging in vivo. *Adv Drug Deliv Rev* **2013,** *65* (1), 71-79.
74. Hua, S.; de Matos, M. B. C.; Metselaar, J. M.; Storm, G., Current Trends and Challenges in the Clinical Translation of Nanoparticulate Nanomedicines: Pathways for Translational Development and Commercialization. *Front Pharmacol* **2018,** *9*, 790.
75. Kemmer, G. C.; Bogh, S. A.; Urban, M.; Palmgren, M. G.; Vosch, T.; Schiller, J.; Gunther Pomorski, T., Lipid-conjugated fluorescent pH sensors for monitoring pH changes in reconstituted membrane systems. *Analyst* **2015,** *140* (18), 6313-6320.
76. de Belder, A. N.; Wik, K. O., Preparation and properties of fluorescein-labelled hyaluronate. *Carbohydr Res* **1975,** *44* (2), 251-257.
77. Alestrom, P.; D'Angelo, L.; Midtlyng, P. J.; Schorderet, D. F.; Schulte-Merker, S.; Sohm, F.; Warner, S., Zebrafish: Housing and husbandry recommendations. *Lab Anim* **2020,** *54* (3), 213-224.
78. Jin, S. W.; Beis, D.; Mitchell, T.; Chen, J. N.; Stainier, D. Y., Cellular and molecular analyses of vascular tube and lumen formation in zebrafish. *Development* **2005,** *132* (23), 5199-5209.
79. Ellett, F.; Pase, L.; Hayman, J. W.; Andrianopoulos, A.; Lieschke, G. J., mpeg1 promoter transgenes direct macrophage-lineage expression in zebrafish. *Blood* **2011,** *117* (4), e49-56.
80. Weinstein, B. M.; Stemple, D. L.; Driever, W.; Fishman, M. C., Gridlock, a localized heritable vascular patterning defect in the zebrafish. *Nat Med* **1995,** *1* (11), 1143-1147.
81. Schindelin, J.; Arganda-Carreras, I.; Frise, E.; Kaynig, V.; Longair, M.; Pietzsch, T.; Preibisch, S.; Rueden, C.; Saalfeld, S.; Schmid, B.; Tinevez, J. Y.; White, D. J.; Hartenstein, V.; Eliceiri, K.; Tomancak, P.; Cardona, A., Fiji: an open-source platform for biological-image analysis. *Nat Methods* **2012,** *9* (7), 676-682.
82. Schneider, C. A.; Rasband, W. S.; Eliceiri, K. W., NIH Image to ImageJ: 25 years of image analysis. *Nat Methods* **2012,** *9* (7), 671-675.
83. van den Broek, B.; Ashcroft, B.; Oosterkamp, T. H.; van Noort, J., Parallel nanometric 3D tracking of intracellular gold nanorods using multifocal two-photon microscopy. *Nano Lett* **2013,** *13* (3), 980-986.

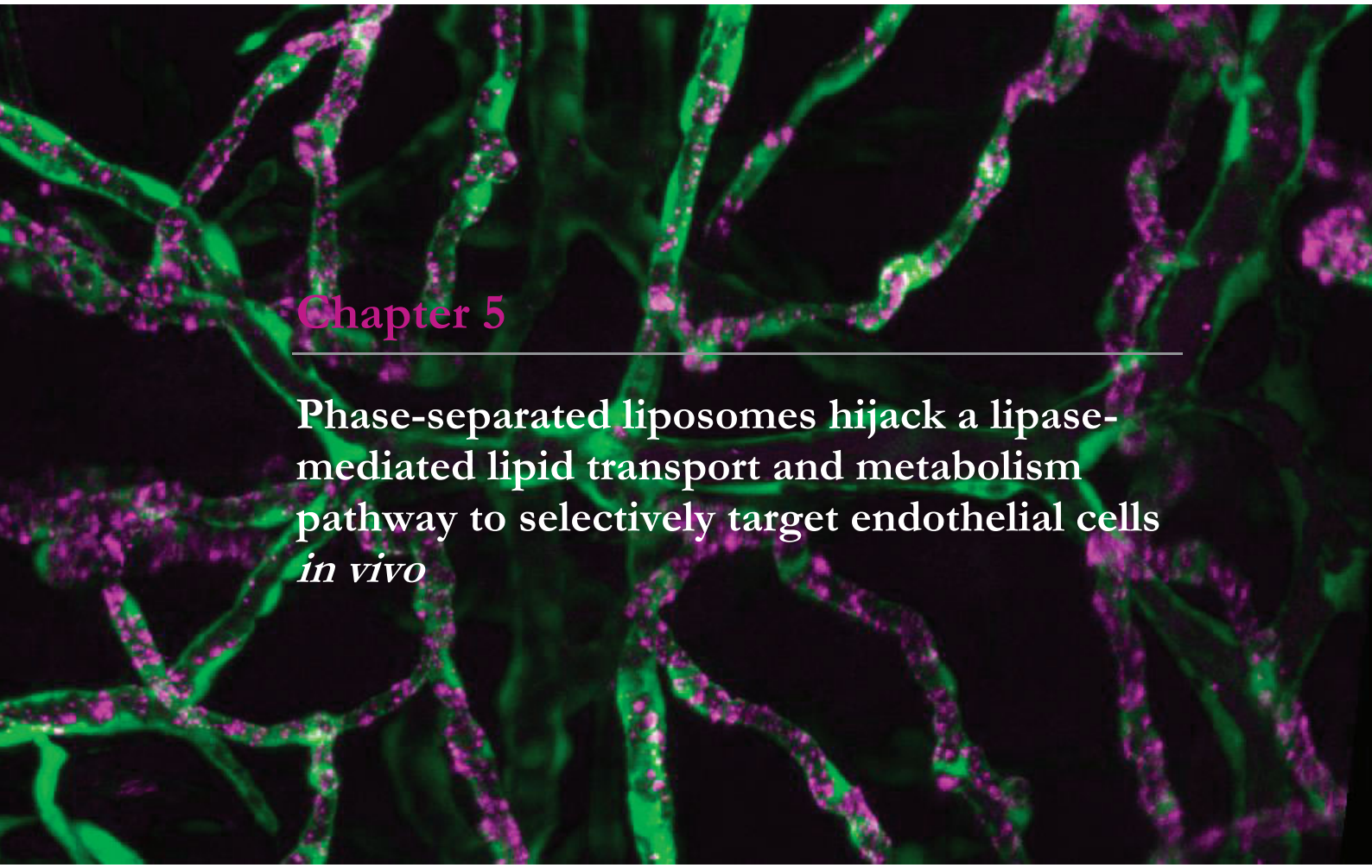

Chapter 5

Phase-separated liposomes hijack a lipase-mediated lipid transport and metabolism pathway to selectively target endothelial cells *in vivo*

Manuscript in preparation:

Arias-Alpizar, G.*; Papadopoulou, P.*; Rios, X.; Moradi, M.A.; Pattipeiluhu, R.; Bussmann, J.; Sommerdijk, N.; Llop, J.; , J.; Kros, A.; Campbell, F. Phase-Separated, "Parachute" Liposomes Hijack a Triglyceride Lipase-Mediated Lipid Transport and Metabolism Pathway to Selectively Target Endothelial Cells *in vivo*.

These authors contributed equally*

Image: Brain vasculature of a zebrafish larvae showing accumulation of PAP3 liposomes.

5.1 Abstract

Plasma lipid transport and metabolism are fundamental to ensure correct cellular function(s) throughout the body. Dynamically regulated in both time and space, the well characterized mechanisms underpinning lipid transport and metabolism offer an enticing rationale towards designing nanoparticles capable of cell selective targeting. Here, we describe a liposome formulation, composed of just two lipids, that hijacks an endogenous triglyceride lipase-mediated pathway of plasma lipid transport and metabolism to selectively target, and be taken up by, endothelial cells *in vivo*. Discovered, screened and mechanistically probed in embryonic zebrafish, liposome targeting of endothelial cells is mediated exclusively through a unique, phase-separated 'parachute' morphology. This morphology drives preferential liposome recognition and binding to endothelium-bound (endothelial) lipase. Once bound, liposomes are subsequently taken up by endothelial cells. Within the zebrafish larvae, endothelial lipase selectivity leads to liposome accumulation and intracellular uptake at the brain endothelium. In young mice, extensive liposome accumulation within the liver and spleen matches the high expression of endothelial lipase within these metabolic organs. Overall, these compositionally simplistic liposomes offer new avenues towards the discovery of lipid-based nanoparticles capable of cell selective targeting *in vivo*.

5.2 Introduction

All cells rely on plasma lipid transport to maintain the correct intracellular balance of essential and non-essential fatty acids. This requires dynamic regulation of the secretion, transport, and metabolism of water-insoluble fats throughout the body. Often packaged as nanometer-sized, solid lipid particles (*i.e.* lipoproteins), many of the biological mechanisms regulating plasma lipid transport and metabolism are well understood[1] and provide an enticing rationale to design lipid-based nanomedicines capable of preferential cellular targeting. To date however, Onpattro® - a lipid nanoparticle (LNP)-based RNAi therapy - remains the only example of a lipid-based nanomedicine explicitly functioning through hijacking of an endogenous plasma lipid transport and metabolism pathway (*i.e.* apolipoprotein E-mediated targeting of the low density lipoprotein receptor (LDLR)) to preferentially target specific cells (*i.e.* hepatocytes) of the body.[2, 3]

The three main plasma lipid transport forms are free fatty acids (FAs), triglycerides (TGs) and cholesteryl esters (CEs).[1] Free FAs are generally transported as a complex with serum albumin, whereas TGs and CEs are transported within the core of plasma lipoproteins – solid lipid particles surrounded by a lipid monolayer rich in phospholipids and stabilized by apolipoprotein(s). The five major classes of lipoproteins are chylomicrons, very low density lipoproteins (VLDLs), intermediate density lipoproteins (IDLs), low density lipoproteins (LDLs) and high density lipoproteins (HDLs). Dietary fats (*i.e.* essential fatty acids) are processed within the intestine and secreted into blood as chylomicrons (*guide size*: 100 – 1000 nm); endogenous fatty acids are primarily processed within the liver and secreted as VLDLs (*size*: 50 - 200 nm); IDLs and LDLs (*size*: 20 - 50 nm) are lipoprotein metabolites enriched in cholesterol and, at high levels, are associated with atherogenic disorders;[4, 5] and HDL (*size:* 8-12 nm) is primarily involved in cholesterol reverse transport, sequestering excess cholesterol from lipoproteins and/or cells and transporting it back to the liver.[6] With the exception of HDL, a single, surface-bound apolipoprotein B (apoB100 or apoB48 for VLDL and chylomicrons respectively) stabilizes each secreted lipoprotein. HDLs, in contrast, are stabilized by apolipoprotein A-I (apoAI).[7, 8]

Once secreted into the bloodstream, soluble and exchangeable apolipoproteins (*e.g.* apoA, C, D and E) recognize and bind to the surface of a circulating lipoprotein. Binding preference is modulated by lipoprotein size (*i.e.* curvature),

composition and local/systemic apolipoprotein concentrations. Once bound, apolipoproteins guide lipoproteins to specific targets within the body. For example, apoE is a ligand for LDLr, promoting uptake primarily in hepatocytes;[9] apoA1 is a cofactor of lecithin cholesterol acyltransferase (LCAT),[10] promoting the conversion of cholesterol to cholesteryl esters; and lipoprotein-bound apoC2 functions as an obligatory cofactor of lipoprotein lipase (LPL).[11, 12]

Following transport, lipoproteins are typically metabolized to release extracellular free fatty acids at the target site that are subsequently taken up by cells locally. For this, triglyceride lipases are key hydrolytic enzymes that regulate lipid metabolism throughout the body. The three principle members of the triglyceride lipase family are LPL,[13] hepatic lipase (HL),[14] and endothelial lipase (EL)[15, 16] (encoded by the human genes *LPL*, *LIPC,* and *LIPG* respectively). All three share significant structural homology, including a conserved catalytic triad of amino acids (serine, aspartate and histidine), as well as conserved heparin and lipoprotein binding domains.[15, 16] LPL is mainly synthesized in adipose tissue, heart and skeletal muscle, HL in hepatocytes, and EL in vascular endothelial cells.[15] Once expressed, triglyceride lipases are secreted and actively transported (in the case of LPL and HL) to the local endothelium where they anchor to heparan sulfate proteoglycans (HSPG) *via* electrostatic interactions.[17] As hydrolytic enzymes, LPL primarily hydrolyzes triglycerides,[18] HL – triglycerides and phospholipids,[14, 19] and EL – phospholipids.[15] Substrate specificity is determined by sequence variation in the lid region of each enzyme.[15, 20, 21] However, whereas LPL and HL metabolize fats primarily derived from VLDL and chylomicrons, the principle function of EL is the regulation of HDL metabolism *via* interactions with apoA-1. [15, 22-25] In addition, all three triglyceride lipase family members are capable of internalizing lipoproteins *via* proteoglycan- or receptor-mediated pathways in a non-enzymatic fashion.[17, 26]

Herein, we describe an intravenously (*i.v.*) administered liposome formulation, composed of just two lipids, that selectively targets endothelial cells *via* an endogenous triglyceride lipase-mediated mechanism of recognition, binding, and intracellular uptake. With no additional functionality, liposome targeting selectivity is exclusively mediated through a phase-separated, “parachute” morphology. Our data strongly suggests a targeting preference for EL over other triglyceride lipases, however, given their promiscuous function and close structural homology, contributions from other lipases cannot be excluded. Within embryonic zebrafish, liposomes selectively target, and are taken up by, brain endothelial cells (bECs). Within 6-8 week old mice, liposomes predominantly accumulate within the liver and spleen. Specific targeting

strategies of triglyceride lipase-mediated mechanisms become attractive due to the importance of EL in cardiovascular disease and its overexpression in different tumors. This work contributes to the preferential targeting of triglycerides lipase mediated mechanisms and shed the light on the design of new nanotechnology platforms based on endogenous mechanisms of plasma lipid transport and metabolism.

5.3 Results

PAP3 liposomes accumulate at the brain endothelium of embryonic zebrafish

Zebrafish embryos are convenient, accurate and cost effective animals to study the behavior and pharmacokinetics of nanoparticles *in vivo*,[27, 28] to assess and predict key nanoparticle-liver interactions within higher vertebrates[29, 30] and to identify the biological mechanisms underpinning nanoparticle fate *in vivo*.[29-31] From a preliminary screen of *i.v.* administered liposomes, we unexpectedly observed selective accumulation of a liposomal formulation, PAP3, within the head region of a three-day old (~78 hpf) zebrafish embryo (**Figure 1a,b**). PAP3 liposomes (size: ~120 nm) were composed of an equimolar mixture of just two lipids, a novel synthetic lipid, 2-hydroxy-3-oleamidopropyl oleate (DOaG), and naturally occurring, 1,2-distearyl-*sn*-glycero-3-phosphocholine (DSPC) (**Figure 1c**). These liposomes contained no additional targeting functionality. Looking closely within the head region of the zebrafish embryo, PAP3 liposomes clearly accumulated within some (*e.g.* mesencephalic vein (MsV), mesencephalic artery (MsA), middle mesencephalic central artery (MMCtA), middle cerebral vein (MCeV), primordial hindbrain channels (PHBC) and cerebral arteries (CtAs)), but not all (*e.g.* dorsal longitudinal vein (DLV), primordial midbrain channel (PMBC)) blood vessels and capillaries (**Figure 1d**). These specific blood vessels and capillaries in which PAP3 liposomes selectively accumulated have been previously characterized as the brain endothelium (*i.e.* bECs), constituting the blood-brain-barrier (BBB) of the developing embryo.[32-34]

In terms of a neurovascular unit, anatomical features that regulate mammalian brain homeostasis and permeability are conserved in zebrafish. These features include endothelial tight junctions, maintained by specialized tight junction proteins (*e.g.* Claudin-5);[33, 35, 36] pericytes and glia cells surrounding the brain vasculature;[37, 38] and the expression of substrate specific transporters (*e.g.* GLUT1).[39] All these features are present and functional (as assessed by

permeability assay) within the embryonic zebrafish by 3 days post-fertilization (dpf).[40] Importantly, angiogenesis within the brain of the embryonic zebrafish is temporally coupled to barriergenesis.[39] This means nascent bECs immediately express genes associated with BBB function. As such, the dynamic expression of the tight junction protein Claudin-5, encoded by *claudin5a*, has been used to dynamically map the developing brain endothelium of the embryonic zebrafish over time.[33, 35, 36, 39] This simple and clear delineation of brain versus systemic endothelial cells within the head region of the embryonic zebrafish provides an ideal *in vivo* screening platform to assess potential bEC targeting specificity of nanoparticles using standard fluorescence microscopy setups (**Figure 2a** and **Supplementary Figure 1a**).[33,35, 36]

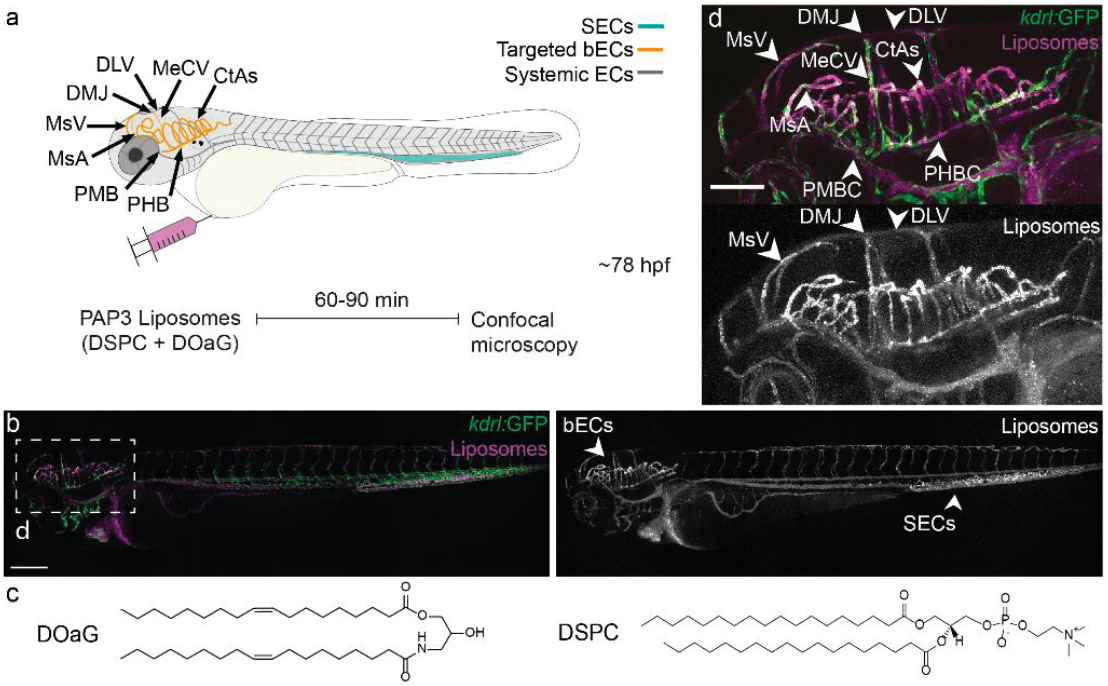

Figure 1. Biodistribution of PAP3 liposomes in zebrafish larvae. (a) Schematic zebrafish larvae in lateral (whole body) view, showing the site of microinjection and key cranial vessels. Fluorescently labeled liposomes are imaged with confocal microscope after 60-90 min. The vasculature as follows, liposomes targeted bECs in yellow and systemic endothelium in dark gray, scavenging endothelial cells (SECs) in cyan, at ~72 hours post fertilization (hpf). **(b)** Biodistribution of PAP3 liposomes (magenta/grey) in Tg(*kdrl*:GPF), expressing GFP in all endothelial cells, lateral view (10x magnification) at 78 hpf, 1.5 hours post injection (hpi). **(c)** Chemical structure of lipids used in equimolar mixture for the formulation of PAP3 liposomes, DOaG and DSPC lipids. **(d)** Zoom of the cranial region in lateral view. bECs, brain endothelial cells; CtAs, central arteries; DLV, dorsal longitudinal vein; DMJ, dorsal midline junction; MCeV, middle cerebral vein; MsA, mesencephalic artery; MsV, mesencephalic vein; PMBC, primordial midbrain channel; PHBC, primordial hindbrain channel; SECs, scavenging endothelial cells. Liposomes prepared by extrusion, concentration 5 mM containing 0.2 mol% DOPE-LR. Scale bars: 200 µm (lateral view) and 100 µm (zoom).

To verify selective accumulation with bECs, PAP3 liposomes were administered (*i.v.*) within embryonic zebrafish at different developmental stages (2, 3 and 4 dpf) (**Figure 2b-d**). This two-day timeframe spans the late-stage development of the embryonic BBB, most prominently within the mid- and forebrain, following complete hindbrain vascular invasion by 48 hpf (characterized by CtA capillary loops connecting both PHBCs with the central basilar artery (BA)).[32] Accordingly, at 2 dpf, PAP3 liposomes mainly targeted functional bECs within blood vessels and capillaries of the hindbrain, namely CtAs, BA and PHBCs (**Figure 2b**). At 3 dpf, as blood vessels irrigate rostrally throughout the brain,[41] PAP3 liposomes accumulated within newly formed capillaries of the mid- and forebrain (**Figure 2e**), as well as within the continually expanding BBB vasculature of the hindbrain (**Figure 2f-h** and **Supplementary Figure 1a-b** for a Z-stack depth color-coded of the vasculature in dorsal view). At 4 dpf, PAP3 liposomes extensively accumulated throughout the now developed brain endothelium of the embryonic zebrafish (**Figure 2d**)**.** Notably at all developmental stages, liposomes remained freely circulating within systemic blood vessels (*e.g.* PMBC and DLV) (**Figure 2i**)**,** confirming a targeting preference of PAP3 liposomes for bECs. Indeed, colocalization of PAP3 liposome accumulation and Claudin-5 expression, notably within the CtAs, MMCtA (**Figure 2h-i**) and MsA, was confirmed in Tg*(cldn5a:*eGFP*)*[33] embryos stably expressing an integrated eGFP-Claudin5a fusion protein (**Figure 2j-k** and **Supplementary Figure 1c**)**.**

In addition to bEC targeting, PAP3 liposomes also accumulated within the caudal hematopoietic tissue (CHT) and caudal vein (CV) of the embryo (**Fig. 1a,b**)**.** We have previously shown that these blood vessels are composed of scavenger endothelial cells (SECs) that are genetically and functionally equivalent to liver sinusoidal endothelial cells (LSECs) in mammals.[29] These cells proficiently clear anionic (as well as 100% DSPC liposomes) nanoparticles from circulation, predominantly mediated by the scavenger receptors, Stabilin-1 and -2. Administration of PAP3 liposomes in zebrafish mutants lacking scavenger receptors Stabilin-1 and Stabilin-2 (*stabilin-1*^{ibl3} *stabilin-2*^{ibl1})[30] (**Supplementary Figure 2**) resulted in significantly reduced liposome accumulation within the CHT and CV of the embryo whilst maintaining bEC targeting. This confirmed that (off-)targeting of PAP3 liposomes to SECs but not bECs was Stabilin-dependent.

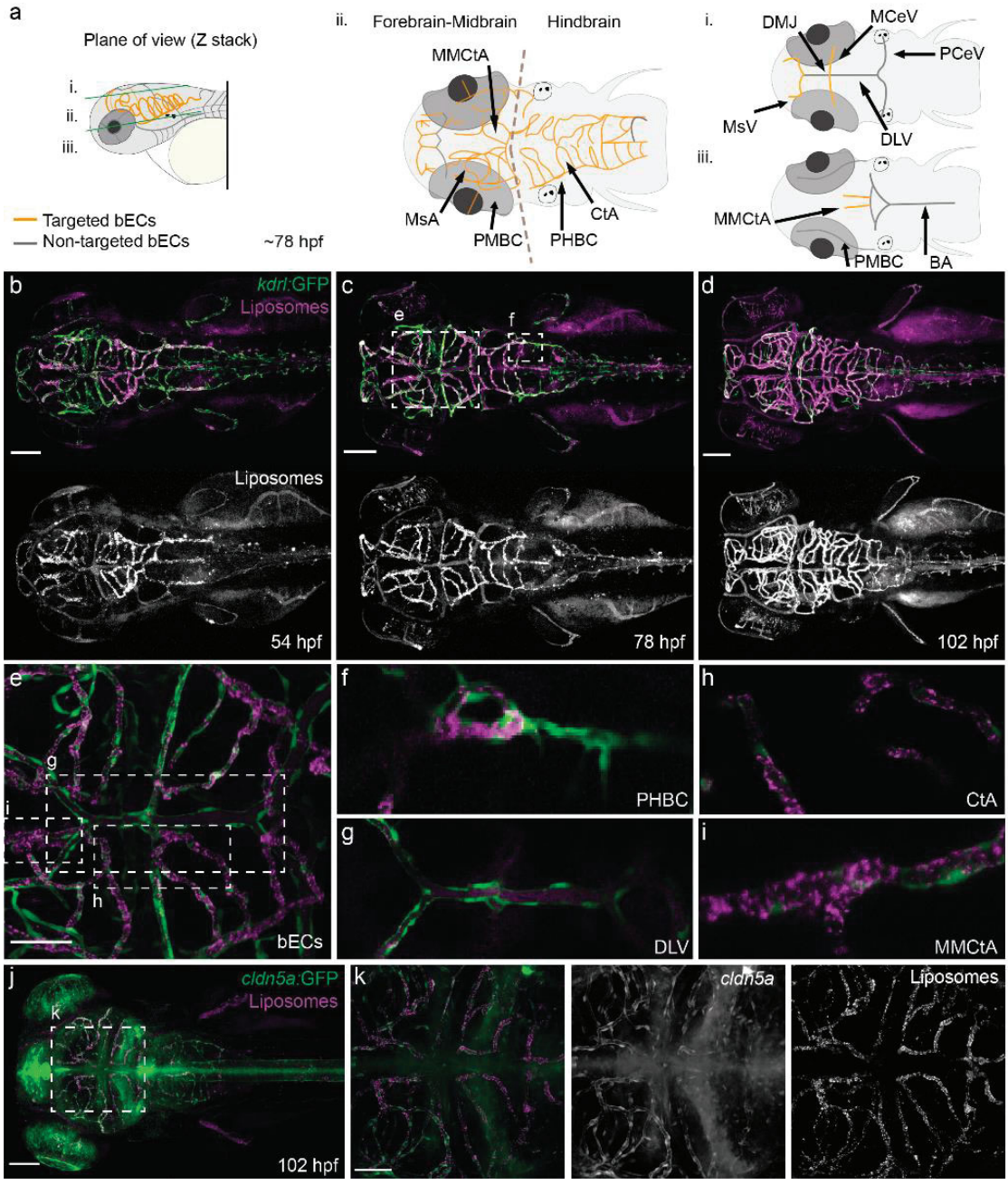

Figure 2. PAP3 liposomes accumulate in the bECs of zebrafish. (a) Schematic zebrafish larvae with key blood vessels in different planes of view. See **Supplementary Figure 1a-b** for a Z-stacks depth color-coded zebrafish vasculature. Dorsal view, showing the **i.** top, **ii.** middle and **iii.** bottom layer diagram. The vasculature as follows, targeted brain endothelial cells (bECs) in yellow and non-targeted systemic endothelium in dark gray, at ~78 hours post fertilization (hpf). PHBC, primordial hindbrain channel; CtA, central artery; DLV, dorsal longitudinal vein; MsA, mesencephalic artery; MsV, mesencephalic vein; MMCtA, middle mesencephalic central artery. (**b**) Biodistribution of PAP3 liposomes (magenta/grey) in dorsal view (10x magnification) 1.5 hpi at 54 hpf, **(c)** 78 hpf, **(d)** 102 hpf. Inset of **(e)** shows the biodistribution of PAP3 liposomes in bECS. **(f)** Posterior part of the PHBC, **(g)** DLV, **(h)** CtA, **(i)** MMCtA in Tg(*kdrl:*GFP). **(j-k)**

Biodistribution of PAP3 liposomes (magenta/grey) in Tg*(cldn5a:*GFP*)* transgenic line with GFP-labeling blood and choroid plexus brain barrier showing colocalization of *cldn5a* with fluorescent liposomes. Zoom in of the region that includes the hindbrain vasculature and colocalization with *cldn5a* expression is shown in **Supplementary Figure 1c**. Liposomes prepared by extrusion, concentration 5mM containing 0.2 mol% DOPE-LR. Scale bars: 100 µm (dorsal view), 50 µm (tissue level).

CryoTEM revealed a novel 'parachute' liposome morphology that is essential for BBB targeting in embryonic zebrafish

To rationalize bEC targeting specificity, and in the absence of any additional targeting functionality (*e.g.* targeting ligands), cryogenic transmission electron was used. Unexpectedly, these images revealed a highly unusual, phase-separated "parachute" morphology, characterized by a single electron rich protrusion within each liposomal membrane (**Figure 3a-c** and **Supplementary Figure 3**)**.** Such parachute-like structures have been previously reported for vesicle-polymer hybrid nanoparticles[42, 43] but not purely lipidic nanoparticles. Given the flat, bilayer preference of amphipathic DSPC, we assume that the observed phase-separated protrusion is rich in PAP3 lipid. Indeed, at a molecular level, DOaG is structurally very similar to a diacylglycerol (DAG) whose hydrophobicity and geometry are known to decrease the spontaneous curvature of PC lipid membranes and perturb lamellar membrane structures resulting in the formation of non-bilayer phases.[44-48]

To correlate phase separation and bEC targeting, PAP3 liposomes were formulated at varying molar ratios (10-50 mol% DOaG; >50 mol% DOaG resulted in severe liposome aggregation) and both liposome morphology and *in vivo* (zebrafish larvae) biodistribution were compared (**Figure 3d-i**). As reference, pure DSPC liposomes were characteristically non-spherical, bi-layered particles and were proficiently cleared by SECs (within the CHT and CV) of a three day old zebrafish embryo (**Supplementary Figure 4**). This biodistribution mirrored that of DSPC liposomes in a two day old zebrafish embryo whose uptake within SECs was shown to be Stabilin mediated.[29] CryoTEM images of PAP3 liposomes (10 mol% DOaG) revealed a mixture of non-spherical, bi-layered or multilamellar particles with no evident phase separation (**Figure 3d, Supplementary Figure 5a**). As for DSPC liposomes, these liposomes mostly accumulated with SECs within the CV and CHT of the larvae (**Supplementary Figure 6a**) and did not target bECs (**Figure 3e**). Likewise, PAP3 liposomes (20 mol% DOaG) were predominantly non-spherical (**Figure 3f, Supplementary Figure 5b**), mainly accumulated within SECs (**Supplementary Figure 6b**) and

did not target bECs (**Figure 3g**). However, in this case, small electron-rich protrusions within the liposome membrane suggested a liposome formulation approaching its miscibility threshold (**Figure 3f –** white arrows). This was confirmed by the phase separation of PAP3 (30 mol%) liposomes whereby a single lipid protrusion was now clearly associated with each discreet liposome (**Figure 3h, Supplementary Figure 5c**).

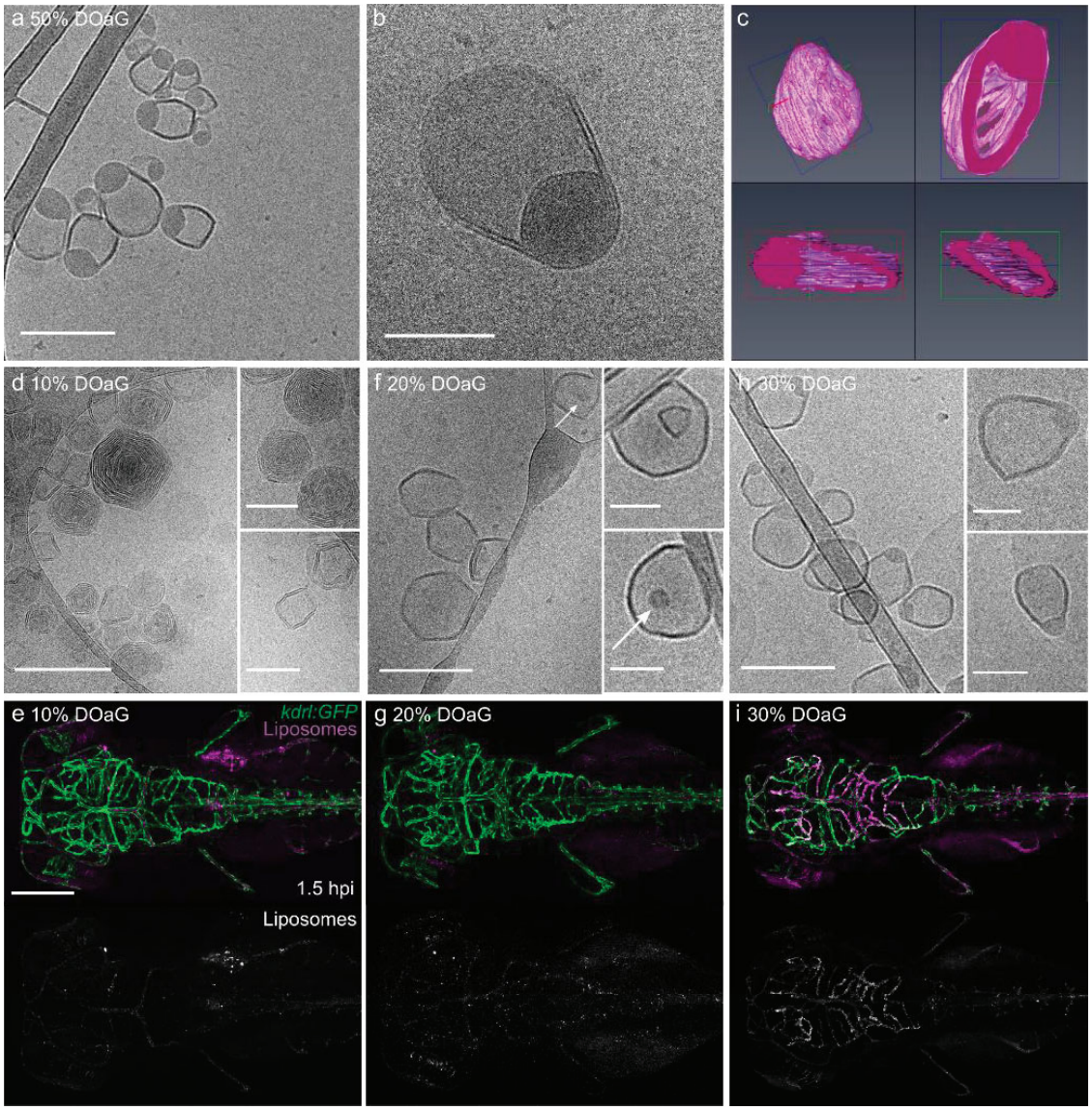

Figure 3. CryoTEM of PAP3 liposomes characterized by phase separation correlates with the bECs targeting in zebrafish larvae. (a-b) CryoTEM of PAP3 (50 mol% DOaG) liposomes and **(c)** Tomography of a representative PAP3 (50 mol% DOaG) liposome from different angles**.** Cryo-TEM and biodistribution (magenta/grey) of **(d-e**) DOaG 10 mol%, **(f-g)** 20 mol%, and **(h-i)** 30 mol%. Biodistribution in Tg*(kdrl:*GFP*)* at ~78 hpf, 1.5 hpi, liposomes concentration 5 mM containing 0.2 mol% DOPE-LR. Liposomes described in all panels made by ethanol injection except panel **b** and **c**, made by extrusion. Scale bars: 200 nm and 100 nm for higher magnification insets for CryoTEM and 200 µm for dorsal view.

PAP3 (30 mol% DOaG) liposomes, as for PAP3 liposomes (*i.e.* 50 mol% DOaG), proficiently targeted bECs of the zebrafish larvae (**Figure 3i** and **Supplementary Figure 6c**). The miscibility threshold of approximately 30 mol% DOaG (within a DSPC bilayer) closely mirrored the value previously reported for structurally similar DAG (25 mol% miscibility threshold) within a PC bilayer.[49] Accordingly, replacing PAP3 with its diacylglycerol analogue 1,3-dioleyolglycerol (DOG) (**Supplementary Figure 7a**), also resulted in phase-separated liposomes and bEC targeting (**Supplementary Figure 7b-d**). Phase separation is also dependent on the gel phase state of a lipid bilayer. Consequently, switching co-formulant phospholipid from saturated DSPC (phase transition temperature (T*m*) 55°C) to unsaturated DOPC (T*m* -17°C) resulted in liposomes (at room temperature) with no apparent phase separation and severely ablated bEC targeting (**Supplementary Figure 8**). Altogether, these experiments confirmed the critical requirement of phase-separated lipid protrusions for bEC selective liposome accumulation within the embryonic zebrafish.

PAP3 liposome targeting and uptake by bECs in zebrafish larvae is mediated by (endothelial) lipase

In the absence of any additional targeting functionality (*i.e.* targeting ligands), we next investigated whether PAP3 liposomes could be hijacking endogenous plasma lipid transport mechanisms to selectively target bECs of the embryonic zebrafish. Importantly, all major elements of mammalian plasma lipid transport and metabolism, including the expression of apolipoproteins, lipoprotein receptors (*e.g.* low density lipoprotein receptor, LDLR) and enzymes (*e.g.* lipases), are present and functional in a three day old zebrafish embryo.[50-52] These conserved features have led to the zebrafish being widely used as *in vivo* model to investigate various lipid disorders,[53-55] including hypertriglyceridemia, a disease caused by a malfunction in lipase-mediated plasma lipid transport and metabolism.[56]

Following secretion into blood, the typical first step of lipoprotein-mediated plasma lipid transport is the binding of soluble apolipoproteins.[1] To identify serum proteins preferentially adsorbed to PAP3 liposomes, we therefore first performed a photoaffinity-based capture of the liposome protein corona.[57] Importantly, given the practical difficulties in obtaining sufficient embryonic zebrafish serum, these experiments were performed in human serum and do not necessarily reflect the exact composition and abundance of serum proteins in the developing zebrafish embryo. For this method, it was necessary to incorporate

the photoaffinity probe, IKS02 (5 mol%),[57] within the PAP3 liposome formulation. Incorporation of this probe did not significantly alter the physicochemical properties or *in vivo* behavior of PAP3 liposomes (**Supplementary Table 1**). Following protein corona capture, isolation, and subsequent proteomic analysis, we identified soluble apolipoproteins as the major protein corona components of both PAP3 and control DSPC liposomes (**Supplementary Figure 9**). However, no obvious differences in protein corona composition could easily explain the very different *in vivo* fates of these two liposome formulations. In contrast, when compared to the characterized protein corona of near-neutral liposomes based on the lipid composition of Myocet®,[57] the significant enrichment of apoA1 and A4, as well as the presence of apoC2 and C3, on the surface of PAP3 liposomes, at least conformed to a lipoprotein-like transport and metabolism targeting rationale.

Given the presence of apolipoproteins on the surface of PAP3 liposomes, we next investigated the potential role of lipases in the selective recognition and binding of PAP3 liposomes within the embryonic fish. Lipases are heparin-releasable[14, 58] and following heparin pre-injection (*i.v.*; 30 minutes prior to PAP3 liposome administration), PAP3 liposomes predominantly remained in circulation with no apparent bEC targeting (**Figure 4a-f**). While this strongly suggested lipase involvement, heparin is also known to bind a wide range of other proteins that could (in)directly disrupt liposome targeting of bECs.[59] To confirm lipase-mediated recognition, we therefore inhibited lipase activity within the embryonic fish using the selective lipase inhibitor, XEN445.[60, 61] This resulted in a significant decrease in bEC targeting of PAP3 liposomes and confirmed triglyceride lipases play a fundamental role in PAP3 liposome targeting selectivity within the embryonic fish (**Figure 4g-i**). Furthermore, XEN445 has demonstrated high selectivity for EL (IC_{50} = 237 nM) over LPL (IC_{50} = 20 μM) and HL (IC_{50} = 9.5 μM).[60] Taken together with the high expression of EL within the head region of zebrafish embryos[62] (from 2 to 4 dpf) and the observed dominance of apoA1 on the PAP3 liposome surface, it is plausible that PAP3 liposomes preferentially target EL by hijacking endogenous mechanisms of HDL recognition and metabolism.[15, 23] Given the promiscuous and overlapping functions of the triglyceride lipase family members, however, it is not possible to exclude contributions of other triglyceride lipase family members.

Completing its journey within the embryonic zebrafish, we finally assessed the fate of PAP3 liposomes following (endothelial) lipase-mediated recognition and binding at the luminal surface of bECs. Surprisingly, we observed that liposomes already associated with bECs were no longer heparin-releasable (**Figure 5a-c**).

This suggested PAP3 liposomes, following initial lipase-mediated attachment, were processed by bECs and internalized *via* non-enzymatic mechanisms of lipase-mediated lipoprotein. As stated previously, lipase-mediated lipoprotein internalization is particular proficient in the case of EL-mediated uptake of HDL particles.[17, 26] To investigate potential intracellular uptake of PAP3 liposomes, the endosomal pH-sensitive dye, pHrodo™, was incorporated within the PAP3 liposome membrane *via* a phospholipid anchor (as in reference [28]) (**see Supporting Information** for characterization and **Supplementary Figure 10** for pH-dependent emission). Incorporation of this fluorescent probe did not significantly alter the size or bEC targeting proficiency of PAP3 liposomes (**Supplementary Table 1**).

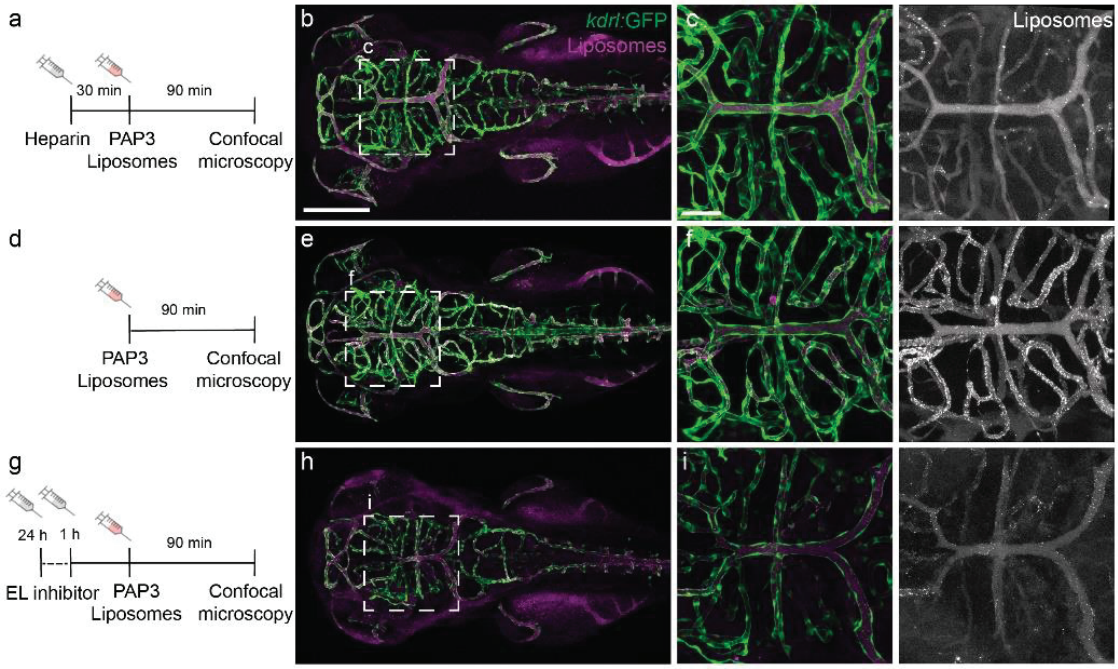

Figure 4. bECs targeting by PAP3 liposomes is inhibited by heparin and an EL lipase inhibitor. (a) Timeline of injection and imaging. **(b-c)** Biodistribution of PAP3 liposomes (in magenta or grey) (10 and 40x magnification) after heparin administration, **(d)** Timeline (injection and imaging). **(e-f)** Biodistribution of PAP3 liposomes at 1.5 hpi. **(g)** Timeline. **(h-i)** Biodistribution of liposomes (1.5 hpi) after a double (24 h and 1 h prior liposomes) administration of an EL inhibitor (XEN 445,1 nl of 50 mM). All zebrafish larvae, Tg*(kdrl:*GFP*)* at ~78 hpi. Liposomes made by extrusion, concentration 5 mM containing 0.2 mol% DOPE-LR. Scale bars: 200 µm (whole embryo) and 50 µm (tissue level).

Following liposome administration, pHrodo™-associated fluorescence was clearly observed within the brain endothelium, *e.g.* CtAs and MMCtA, but not systemic blood vessels, *e.g.* DLV or PMBC (**Figure 5e-f**).This mirrored the observed biodistribution of PAP3 liposomes and suggests PAP3 liposomes are endocytosed by bECs following initial lipase-mediated recognition and attachment.

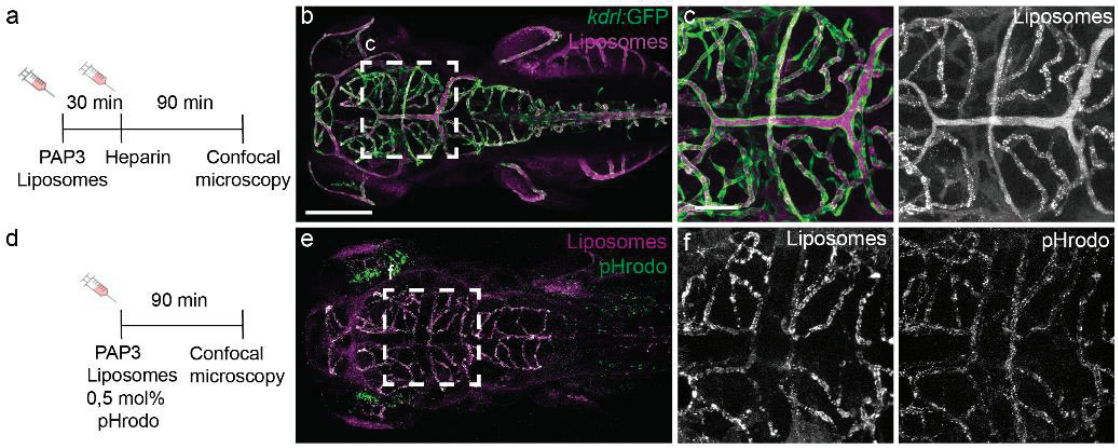

Figure 5. Internalization of PAP3 by zebrafish bECs. (a) Timeline of injection and imaging. **(b-c)** Biodistribution of PAP3 liposomes (5 mM containing 0.2 mol% LR-DOPE, in magenta of grey) (10 and 40x magnification) after post-administration of heparin. **(d)** Timeline of injection and imaging. **(e-f)** Biodistribution of PAP3 liposomes (10 mM) containing 0.5 mol% of pH sensitive DOPE-pHrodo (green/grey) to indicate endocytosis and 0.5 mol% of non-sensitive pH dye NBD (magenta/grey) to label liposomes. All zebrafish larvae at ~78 hpi. Liposomes made by extrusion. Scale bars: 200 µm (whole embryo) and 50 µm (tissue level).

PAP3 liposomes target the liver and spleen in mice

To correlate our findings in mammals, we quantified the dynamic biodistribution of PAP3 liposomes following *i.v.* administration in 6-8 week old female mice (**Figure 6a**). For these experiments, a non-exchangeable ^{64}Cu ($T_{1/2}$= 12,7 h) radionuclide was incorporated as positron emission tomography (PET) tracer. To chelate ^{64}Cu to the liposome membrane, the lipid-NOTA conjugate, NOTA-Bz-SCN-C18 (0.2 % mol), was incorporated within the PAP3 formulation. Based on 'cold' experiments using stable Cu isotopes, the incorporation of this lipid and/or Cu chelation protocol did not affect the physicochemical properties, morphology and/or bEC targeting proficiency of PAP3 liposomes in embryonic zebrafish (**Supplementary Figure 11** and **Table 1**). Following tail vein injection (930±50 kBq/100 µL; n=3), PET scans were obtained, from 1 min to 24 hours post-injection, to visualize and quantify (% injected dose per cm^3; %ID/cm^3) *in vivo*

liposome biodistribution (**Figure 6b**). Calculated *in vivo* values were subsequently validated through *ex vivo* radioanalysis (%ID/g) of major organs (heart, brain, liver, spleen, kidney, lung, and stomach) and blood, following cardiac perfusion and organ collection at selected time points (10 min, 2 h and 24 hpi) (**Figures 6c-e**). These analyses revealed rapid and extensive accumulation of PAP3 liposomes within the murine liver and spleen, with values of *ca.* 70% ID/cm^3 and 25% ID/cm^3 of the liposome injected dose accumulated in liver and spleen, respectively, at 10 min post-injection. This strongly suggested active clearance of PAP3 liposomes within these two organs. In contrast, low accumulation was observed in any other major organ analyzed and, unlike the zebrafish larvae, murine brain accumulation of PAP3 liposomes was negligible. Equivalent values were obtained in *ex vivo* experiments using gamma counting (**Figures 3d** and **3e**).

The extensive and rapid accumulation of PAP3 liposomes within the murine liver and spleen correlates with the high expression of EL within both these metabolic organs.[15, 16] However, EL is also known to be highly expressed in other organs with high metabolic rates and vascularization, notably the lungs. The absence of any significant PAP3 liposome accumulation within the lungs may, therefore, indicate a significant proportion of PAP3 liposomes are scavenged by LSECs within the liver and spleen, presumably in a Stabilin-1 and -2 dependent manner, as was observed in the zebrafish larvae (**Figure 1b**), and/or phagocytosed by Kupffer cells (*i.e.* liver resident macrophages) and splenic macrophages.

5.4 Discussion and Conclusion

Described is a liposome formulation, consisting of just two lipid reagents, that proficiently targets endothelial cells *via* an endogenous (endothelial) lipase-mediated mechanism of recognition and cellular uptake. While lipases, in particular small secretory phospholipase A_2 (sPLA2), have been previously exploited to achieve localized, stimuli-responsive drug release within target tissues (*e.g.* solid tumors),[63, 64] nanoparticle targeting HSPG-anchored triglyceride lipases, functioning as both attachment and bridging biomolecule, has not before been described.

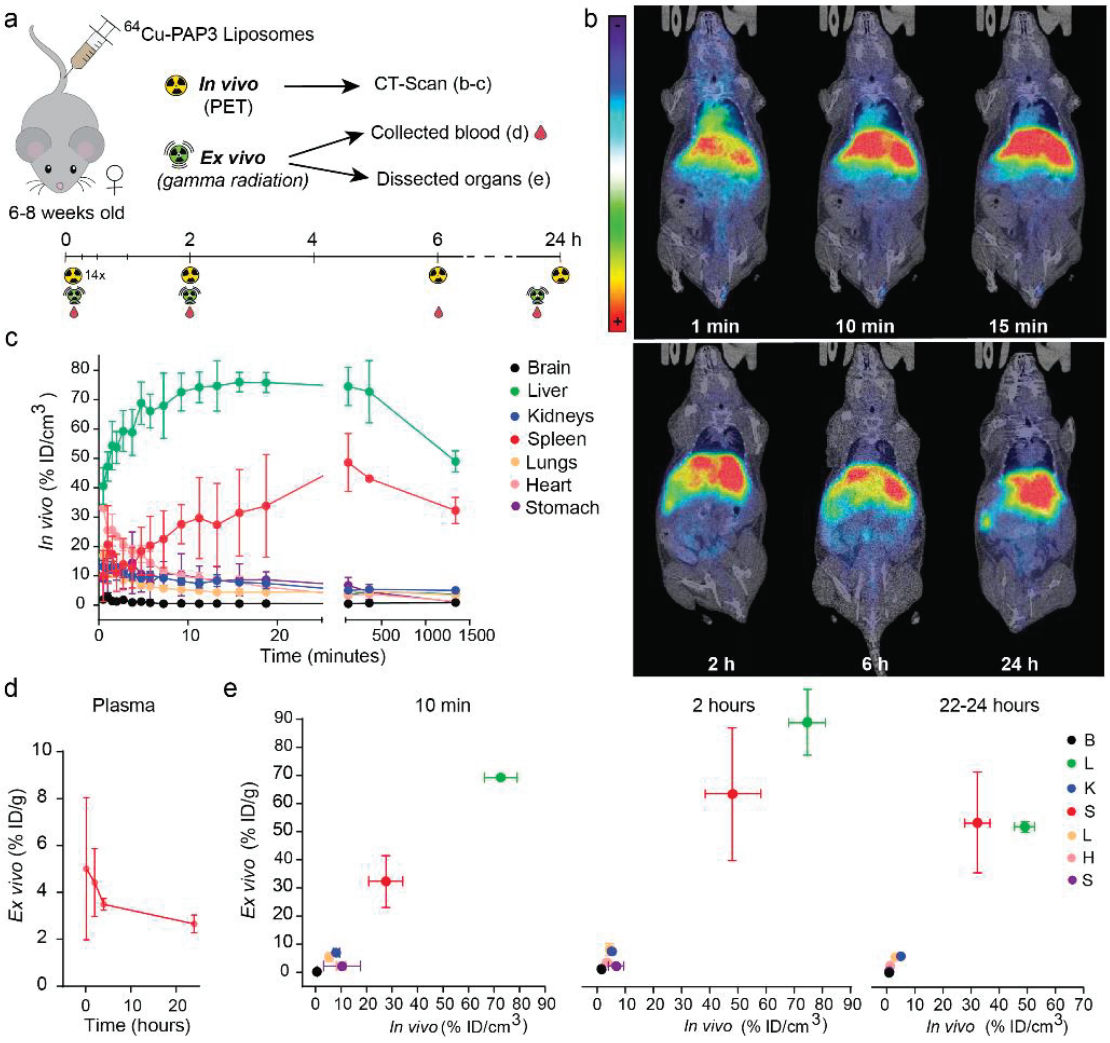

Figure 6. Biodistribution of radiolabeled PAP3 liposomes in mice. (a) Scheme of injection, PAP3 radiolabeled liposomes containing 0.2 mol% of ^{64}Cu-NOTA-Bz-SCN-C18 were injected in 6-8 weeks female mice (n=3). I*n vivo* and *ex vivo* experiments using positron emission tomography (PET) and gamma radiation counter, including blood samples, were performed at different time points (up to 24 h). **(b)** Representative PET images (coronal projections) obtained at 1, 10, 15 min and 2-6-24 h after injection of PAP3 liposomes. PET images have been co-registered with representative CT slices for anatomical localization of the radioactive signal. **(c)** *In vivo* quantitative tracer uptake values in brain, liver, kidneys, spleen, lungs, heart and stomach, at 0.5, 1, 1.5, 2.75, 3.75, 4.75, 5.75, 7.25, 9.25, 11.25, 13.25, 15.75, 18.75, 120, 360, 1340 minutes after injection. Measurements are decay-corrected and presented as %ID/cm^3. **(d)** Concentration of radioactivity in plasma at 10 min, 2, 6 and 24 h after *i.v.* administration of ^{64}Cu-labelled PAP3 liposomes. **(e)** Correlation between concentration of radioactivity in different organs (brain, liver, kidneys, spleen, lungs, heart and stomach) as determined by PET imaging (*in vivo*) and dissection/gamma counting (*ex vivo*) at 10min, 2 and 22-24 h after administration.

Lacking any additional targeting functionality, lipase recognition of PAP3 liposomes is exclusively mediated through a unique 'parachute' morphology, characterized by a single, phase-separated lipid protrusion. This protrusion resembles, in both structure and size, a solid lipid nanoparticle (*i.e* lipoprotein), and, as for analogous DAG/PC lipid mixtures, is likely characterized by increased stress on a bended membrane and increased surface hydrophobicity.[65, 66] Importantly, however, although stable in ddH_2O, PAP3 liposomes formulated in physiological salt solution (and in the absence of serum proteins) were highly unstable. As for endogenous lipoproteins (requiring apoB-48, apoB-100 or apoA-I for chylomicrons, VLDL and HDL, respectively),[1] PAP3 liposome serum stability therefore appears to be dependent on the adsorption of soluble apolipoproteins (*e,g.* apoA1) to the liposome surface. While greater molecular understanding of how these phase-separated protrusions are incorporated within the PAP3 liposome membrane is undoubtedly needed, the compositional simplicity of these liposomes, their unique morphology and their unprecedented *in vivo* behavior provide new opportunities and design guidelines to develop nanomedicines capable of exploiting endogenous plasma lipid transport and metabolism pathways.

While the demonstrated targeting of any (or all) triglyceride lipase family member(s) represents a significant advance in the development of targeted nanoparticles, our results point to a specific targeting preference for EL over LPL and HL. In mice, EL expression is dynamically restricted in both time and space. This is most evident during embryonic stages when high EL expression is observed, particularly in the brain, between embryonic days E8.5 and E11.5 but not at later developmental stages.[67] In healthy adult mice, EL expression is mainly restricted to the lungs, liver, spleen, testes and ovaries (during pregnancy) and is particularly high in the placenta of pregnant mice.[15, 16, 67, 68] A similar restricted pattern of EL expression has been reported in humans.[15] In the diseased state, and beyond its determinant role in regulating plasma HDL-cholesterol levels,[69, 70] EL plays an important role in the initiation and proliferation of various cancers, including breast, gastric and testicular cancers.[71-73] In these cases, aberrant EL overexpression within the tumor environment may be triggered by severe oxidative stress, which in turn leads to endothelial cell migration and angiogenesis through activation of sphigosine-1-phosphate (S1P).[74] Overall, EL plays a crucial angiogenic role in both the healthy and diseased states and, given its restricted expression, notably within the reproductive organs and tumor microenvironment, could be a highly lucrative target for new nanoparticle-based cell-specific therapies.

In conclusion, cell specific targeting is a central tenet to the realization of the widespread use of nanomedicines in the clinic. However, it remains a largely unmet goal. To realize this goal, it is becoming increasingly clear that a thorough understanding of the fundamental nano-bio interactions involved is an absolute requirement. To this end, this work once again highlights the unique opportunities the zebrafish embryo can offer within nanomedicine discovery and development pipelines. Beyond the already reviewed benefits of size, transparency, fecundity and ease of genetic manipulation,[75] in this case, the very discovery of ('irrational') PAP3 liposomes was only possible due to our ability to visualize large numbers of liposome formulations *in vivo* at high resolution and across an entire living organism. Arising from an unexpected molecular rearrangement of a proposed cationic lipid (**Supplementary Figure 12**), the discovery of PAP3 liposomes was ultimately pure serendipity.

5.5 Materials and Methods

General reagents

1,2-dioleoyl-*sn*-glycero-3-phosphocholine(DOPC),1,2-distearoyl-*sn*-glycero-3phosphocholine (DSPC), 1,2-dioleoyl-*sn*-glycero-3-phosphoethanolamine-N-(lissamine rhodamine B sulfonyl) (DOPE-LR) and NOTA-Bz-SCN-C18 (custom made), were purchased from Avanti Polar Lipids (Alabaster, AL, US). Additional DSPC was purchased from Lipoid GmbH. pHrodo™ Red, succinimidyl ester (pHrodo™ Red, SE) was purchased from Thermo Fisher Scientific. DOPE-pHrodo was synthesized as previously reported.[76] All other chemical reagents were purchased at the highest grade available from Sigma Aldrich and used without further purification. All solvents were purchased from Biosolve Ltd. Ultrapure MilliQ® water, purified by a MilliQ Advantage A10 water purification system from MilliPore, was used throughout. DOaG & DOG lipid lipids were synthesized and characterised in house.

Liposome formulation

Liposomes were formulated by extrusion or by ethanol injection method in ddH_2O at a total lipid concentration of 5mM, unless otherwise stated. In the case of extrusion, individual lipids as stock solutions (1-10 mM) in chloroform, were combined to the desired molar ratios and dried to a thin film, first under N_2 stream, then >1 h under vacuum. Lipid films were hydrated in 1mL ddH2O above the T_m of all lipids (65-70 ^oC), with gentle vortexing if necessary, to form a

suspension. Large unilamellar vesicles were formed through extrusion (mini extruder, Avanti Polar Lipids) above the T_m of all lipids (*i.e.* 65-70 °C). Hydrated lipids were passed 11 times through 2 x 400 nm polycarbonate (PC) membranes (Nucleopore Track-Etch membranes, Whatman), followed by 11 times through 2 x 100 nm PC membranes. All liposomes were stored at 4 °C and used within 1 week. In the case of ethanol injection, lipid films were re-dissolved in ethanol to a total lipid concentration of 50 mM. Using a glass micro-syringe (Hamilton, syringe series 700, volume 50 or 500ul) the ethanolic solution was rapidly injected in a glass vial containing 0.5mL or 1mL ddH_2O (1:10 v:v; EtOH:H_2O) at 70°C, under constant vigorous stirring (650rpm), to form large unilamellar vesicles. Liposomes were then transferred to a dialysis tube (Spectrum labs, 3.5k MWCO) or a dialysis cassette (slide-A-Lyzer™ 3.5k MWCO, Thermo Fisher Scientific) and dialyzed against ddH_2O overnight at 4°C, to ensure complete ethanol removal. All liposomes were stored at 4°C and used within 1 week.

Size and zeta potential measurements

Particle size and zeta potentials were measured using a Malvern Zetasizer Nano ZS. For DLS (operating wavelength = 633 nm), measurements were carried out at room temperature in water at a total lipid concentration of approx. 100 µM. Zeta potentials were measured at 500 µM total lipid concentration, using a dip-cell electrode (Malvern), at room temperature. For liposomes formulated in water, aq. NaCl was added to the liposome solution to a final concentration of 10 mM NaCl before zeta potential measurement. All reported DLS measurements and zeta potentials are the average of three measurements.

CryoTEM and 3D tomography

Liposomes (3 µL, 5 mM total lipid concentration) were applied to a freshly glow-discharged carbon 200 mesh Cu grid (Lacey carbon film, Electron Microscopy Sciences, Aurion, Wageningen, The Netherlands). Grids were blotted for 3 s at 99% humidity in a Vitrobot plunge-freezer (FEI VitrobotTM Mark III, Thermo Fisher Scientific). Cryo-EM images were collected on a Talos L120C or a KRIOS (NeCEN, Leiden University) operating at 120 kV or 300kV, respectively. In the case of Talos, images were recorded manually at a nominal magnification of 17500x or 28000x yielding a pixel size at the specimen of 5.83 or 3.56 ångström (Å), respectively. In the case of KRIOS, images were recorded manually at a nominal magnification of 33000x yielding a pixel size at the specimen of 3.48 Å. Alternatively, imaging and cryo-ET was performed on a Titan Krios operating at 300kV (TU Eindhoven). Images were recorded manually at a nominal

magnification of 6500x or 24000x yielding a pixel size at the specimen of 13.87 or 3.86 Å, respectively. Tomographic tilt series acquisition was performed with Inspect3D software (Thermo Fisher Scientific) with a total electron dose of less than 100 e/nm^2. Alignment and reconstruction of the series were performed using IMOD[77] and 3D analysis software Avizo 9 (Thermo Fisher Scientific).

Zebrafish husbandry and injections

Zebrafish (*Danio rerio*, strain AB/TL) were maintained and handled according to the guidelines from the Zebrafish Model Organism Database (http://zfin.org) and in compliance with the directives of the local animal welfare committee of Leiden University. Fertilization was performed by natural spawning at the beginning of the light period, and eggs were raised at 28.5 °C in egg water (60 ug/ mL Instant Ocean sea salts). The following previously established zebrafish lines were used: Tg*(cldn5b:*eGFP*),*[33] Tg*(kdrl:*eGFP*)*^{s843},[78] Tg*(mpeg1:*GFP*)*^{gl22},[79] Tg*(mpeg1:*mCherry*)*^{gl23}.[79] Liposomes were injected into 54-120 hours post fertilization zebrafish embryos using a modified microangiography protocol.[5] Embryos were anesthetized in 0.01% tricaine and embedded in 0.4% agarose containing tricaine before injection. To improve reproducibility of microangiography experiments, 1 nl volume were calibrated and injected into the sinus venosus/Duct of Cuvier or the primary head sinus. A small injection space was created by penetrating the skin with the injection needle and gently pulling the needle back, thereby creating a small pyramidal space in which the liposomes and polymers were injected. Successfully injected embryos were identified through the backward translocation of venous erythrocytes and the absence of damage to the yolk ball.

Confocal imaging acquisition and editing

Zebrafish embryos were randomly picked from a dish of 20-60 successfully injected embryos. Confocal z-stacks were captured on a Leica TCS SPE or SP8 confocal microscope, using a 10x air objective (HCX PL FLUOTAR), a 40x water-immersion objective (HCX APO L) or 63x water-immersion objective (HC PL APO CS). For whole-embryo views, 3 overlapping z-stacks were captured to cover the complete embryo. Laser intensity, gain and offset settings were identical between stacks and experiments. Images were processed and quantified using the Fiji distribution of ImageJ.[80, 81] Confocal image stacks (raw data) are available upon request.

Protein corona analysis

Protein corona was analyzed as described in reference.[57] Briefly, PAP3 liposomes were formulated incorporating 5 mol% of the IKS02 photoaffinity lipid probe and incubated in human serum. Protein adsorbed to the surface of the liposomes were identified *in situ* by cross linking proteins to the diazirine group of the IK probe with light irradiation. Afterwards, the captured proteins were isolated and quantified with LC-MS/MS.

Studies in mice

General

Female mice weighting *ca.* 18-20 g (BALB/cJRj, 6-8 weeks, Janvier; see below for number of animals) were used. The animals were maintained and handled in accordance with the Guidelines for Accommodation and Care of Animals (European Convention for the Protection of Vertebrate Animals Used for Experimental and Other Scientific Purposes) and internal guidelines. All experimental procedures were approved by the Ethical Committee of CIC biomaGUNE and by local authorities (Diputación Foral de Guipúzcoa) before conducting experimental work.

Radiolabeling of liposomes

PAP3 liposomes with 12.5 mM total lipid concentration were made by ethanol injection as described above with only difference that 0.2 mol% of NOTA-Bz-SCN-C18 (custom made, Avanti Polar Lipids) was added to the lipid film. Additionally, the required total volume of liposomes was made in two batches of 500 µl to ensure avoidance of aggregation. After formation of particles and removal of ethanol, $^{64}CuCl_2$ in 0.1 M aq. ammonium acetate pH=5.5 was added to the liposome solution and the mixture was incubated at room temperature (20 mins) (1:4 v/v ammonium acetate/liposomes). Subsequently, the free $^{64}CuCl_2$ was removed by size exclusion chromatography (NAP™-25 columns Sephadex™, GE Healthcare) equilibrated with 10 mM Tris buffer pH=7.4. Elution fractions of 500 µl containing the radiolabeled liposomes were collected from the SEC column and their radioactivity was checked using a dose calibrator (CPCRC-25R, Capintec Inc., NJ, USA). The fraction containing the higher concentration of radioactivity was used for subsequent *in vivo* imaging and *ex vivo* studies.

PET imaging studies

For PET imaging studies, anesthesia was induced by inhalation of 3% isoflurane in pure O_2 and maintained by 1.5-2% isofluorane in 100% O_2. With the animal under anesthesia, the labelled liposomes were injected *via* one of the lateral tail veins (930±50 kBq/100 µL; n=3). Dynamic whole-body images (20 min duration) were acquired list-mode in one bed position in a 511 keV ± 30% energetic window immediately after administration of the labelled liposomes using a MOLECUBES β-CUBE scanner. Static 10 min images were also acquired at 2h, 6h and 24f after administration. After each PET scan, whole body high resolution computed tomography (CT) acquisitions were performed on the MOLECUBES X-CUBE scanner, to provide anatomical information as well as the attenuation map for the later reconstruction of the PET images. Dynamic PET images were reconstructed with OSEM-3D iterative algorithm, using the following frames: 4 × 30 s, 4 × 60 s, 4 × 120 s, 2 × 180 s. Static images were reconstructed as a single frame using the same method. Images were analyzed using π-MOD image analysis software (π-MOD Technologies Ltd, Zurich, Switzerland). With that aim, volumes of interest (VOIs) were manually drawn in major organs, namely brain, lungs, kidneys, spleen, stomach, liver, bladder and heart, using the CT images for anatomical reference, and decay–corrected time–activity curves were obtained. Values were normalized to VOI volume and injected activity and values were expressed as percentage of injected dose per cubic centimeter of tissue (%ID/cm^3).

Ex vivo biodistribution studies

Animals (n=3 per compound and time point) were anesthetized with isoflurane 3% isoflurane in pure O_2 and maintained by 1.5-2% isoflurane in 100% O_2. A solution containing the labelled liposomes (730 ± 140 kBq/100 µl) was injected through one of the lateral tail veins. Animals were recovered from anesthesia and at pre-determined time points (t=10 min, and 2, 6 and 24 h), animals were anesthetized again and sacrificed by perfusion using saline solution and brain, liver, kidneys, spleen, lungs, heart, and stomach were quickly removed and rinsed with water. The amount of radioactivity in each organ was measured in an automatic gamma counter (2470 Wizard, PerkinElmer). Blood samples were obtained just before perfusion. Part of the blood was processed to separate the plasma, which was also counted in the gamma counter. Results were normalized to injected dose and organ weight to express the results as percentage of injected dose per gram of tissue (%ID/g).

5.6 Abbreviations

Å	Ångström
ApoA	apolipoprotein A
BA	basilar artery
BBB	blood brain barrier
bECs	brain endothelial cells
CE	cholesteryl esters
CHT	caudal hematopoietic tissue
CryoTEM	Cryo-transmission electron microscopy
CV	caudal vein
DLV	dorsal longitudinal vein
DOPE-LR	1,2-dioleoyl-*sn*-glycero-3-phosphoethanolamine-N-(lissamine rhodamine B sulfonyl)
DSPC	1,2-distearyl-*sn*-glycero-3-phosphocholine
DOaG	2-hydroxy-3-oleamidopropyl oleate
dpf	days post fertilization
EL	endothelial lipase
FAs	fatty acids
HDL	high density lipoproteins
HL	hepatic lipase
HSPG	heparan sulfate proteoglycan
hpi	hour(s) post injection
i.v.	Intravenously
LCAT	lecithin cholesterol acyltransferase
LDL(R)	low density lipoproteins (receptor)
LNP	lipid nanoparticle
LPL	lipoprotein lipase
LSECs	liver sinusoidal endothelial cells
Ms(A/V)	mesencephalic artery/vein
MCeV	middle cerebral vein
MMCtA	middle mesencephalic central artery
PMBC	primordial midbrain channel
PHBC	primordial hindbrain channel
SECs	scavenging endothelial cells
TG	triglycerides
VLDL	very low density lipoproteins
wt	wildtype

5.7 Supporting Information

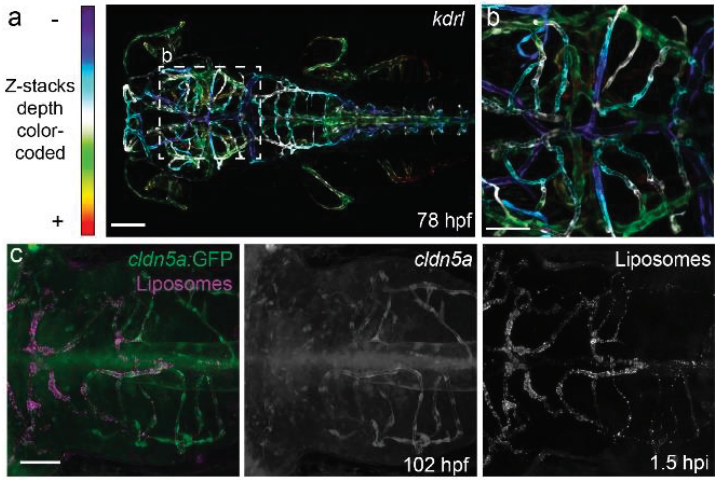

Supplementary Figure 1. Zebrafish embryo ECs in dorsal view and biodistribution of PAP3 liposomes in Tg*(cldn5a:*eGFP). (a-b) Z-stacks depth color-coded of a Tg(*kdrl*:GFP), dorsal view, at 78 hours post injection (hpi). Thermal colored scale, blue (dorsal) up to red (ventral). **(c)** Biodistribution of PAP3 liposomes (5 mM containing 0.2 mol% DOPE-LR, in magenta or gray) after 1.5 hpi in dorsal view. bECs, zoom in (magnification 40x) the hindbrain region showing correlation of PAP3 liposomes (magenta/gray) with expression of *cldn5a* at ~102 hpf. (Whole embryo, 10x in **Figure 2j**). Scale bars: 100 µm (a) and 50 µm (b-c).

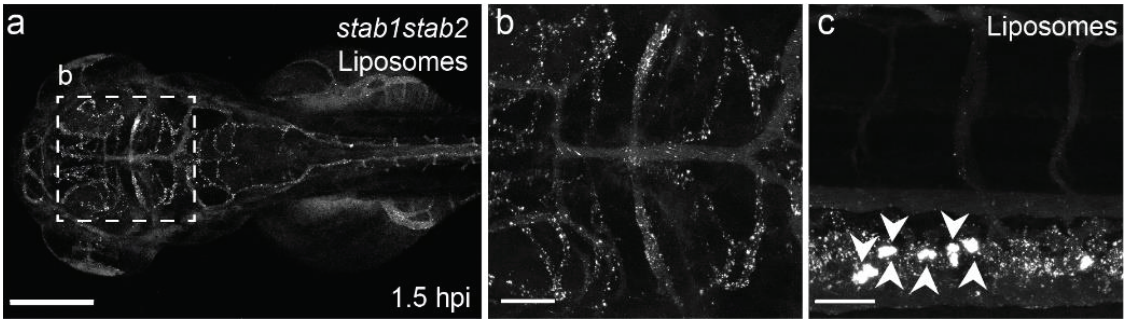

Supplementary Figure 2. Biodistribution of PAP3 liposomes in *stab1stab2* double knockout zebrafish embryo. (a) PAP3 liposomes (5 mM containing 0.2 mol% DOPE-LR, in gray) biodistribution in dorsal view (magnification 10x) *i.v.* injected in zebrafish line stab1^{ibl3}stab2^{ibl1},[30] 1.5 hpi at ~76 hpf. **(b)** Zoom in (magnification 40x) of bECs **(c)** Caudal region in lateral view (magnification 40x) showing accumulation of PAP3 liposomes in scavenging endothelial cells (SECs), expressing Stabilin-1 and Stabilin-2, analogous to liver sinusoidal endothelial cells in mice[29] and in apparent blood-exposed macrophages (white arrows). Scale bar: 200 µm (a) and 50 µm (b-c).

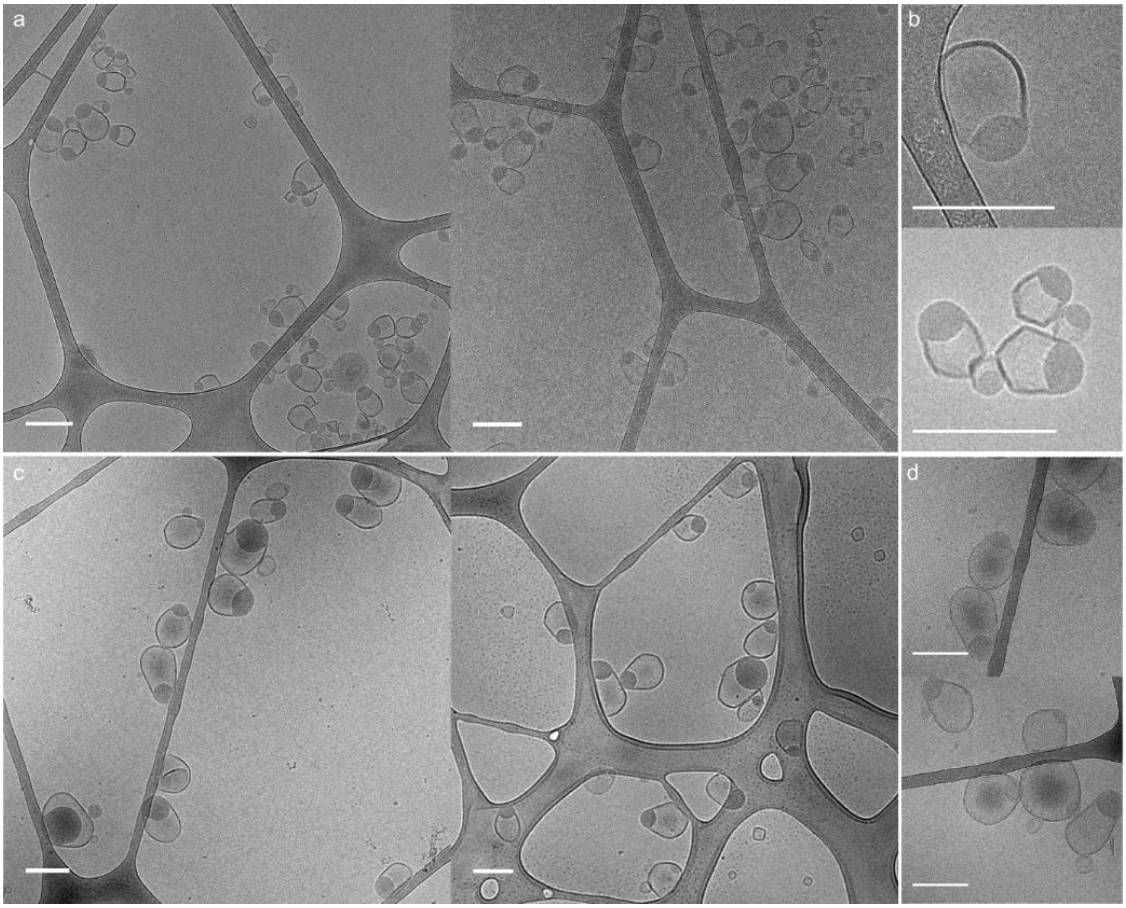

Figure Supplementary 3. CryoTEM images of 'parachute' PAP3 liposomes formulated by two methods. (a-b) PAP3 liposomes formulated by ethanol injection method. **(c-d)** PAP3 liposomes formulated by extrusion method. Scales bars: 200 nm.

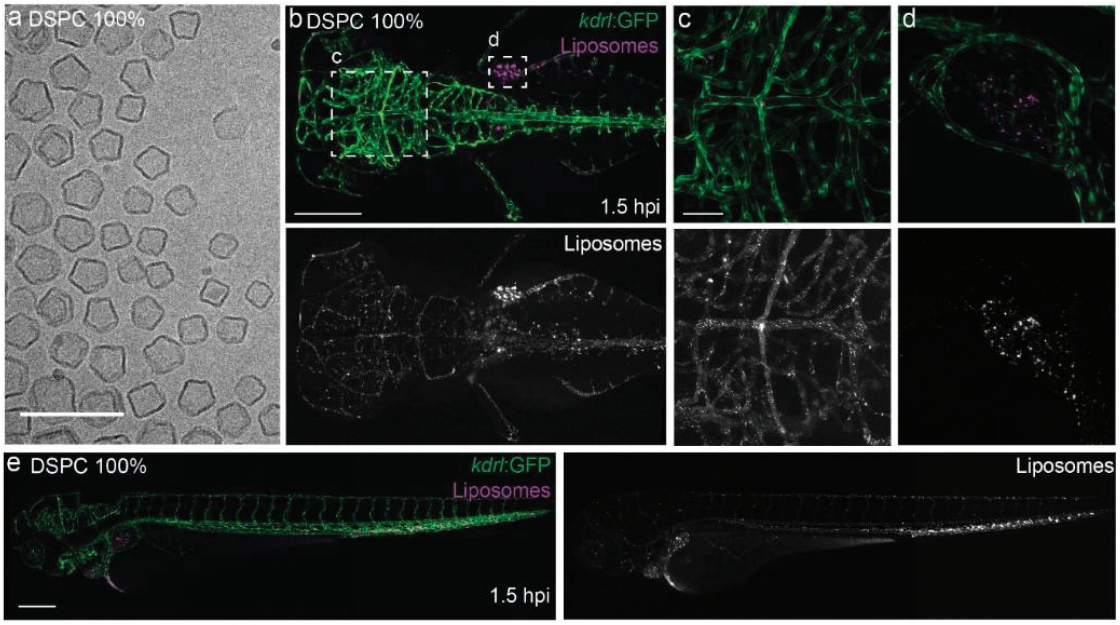

Supplementary Figure 4. CryoTEM and biodistribution of DSPC liposomes in zebrafish embryo. (a) CryoTEM images of DSPC liposomes. **(b)** Biodistribution of DSPC liposomes (5 mM containing 0.2 mol% DOPE-LR, in magenta or gray) in Tg(*kdrl:*GFP) transgenic line, at 3 dpf, 1.5 hpi in dorsal view (magnification 10x). **(c)** Brain endothelial cells (bECs) at tissue level (magnification 40x) in dorsal view. **(d)** Liver endothelium (magnification 40x), in lateral view. **(e)** Whole body lateral view (same fish, magnification 10x). Liposomes prepared by extrusion. Scale bars: 200 nm (cryoTEM), 200 μm (dorsal and lateral views) and 50 μm (tissue level).

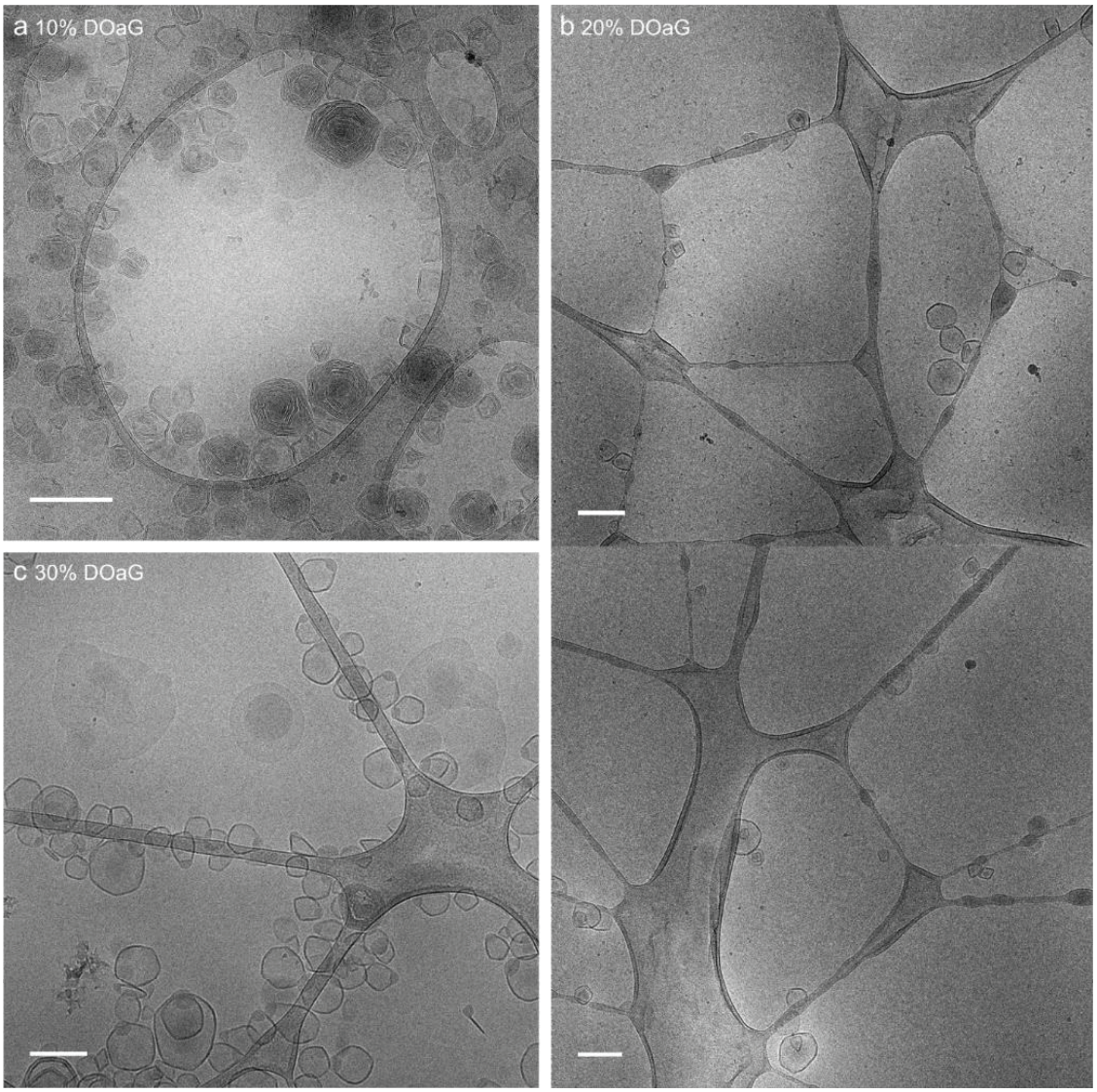

Supplementary Figure 5. CryoTEM images of PAP3 liposomes formulated at varying molar ratios. (a) Liposomes composed of DSPC and 10 mol%, **(b)** 20 mol% (2 images included because of low population of particles in an individual image), and **(c)** 30 mol% DOaG. Scales bars: 200 nm.

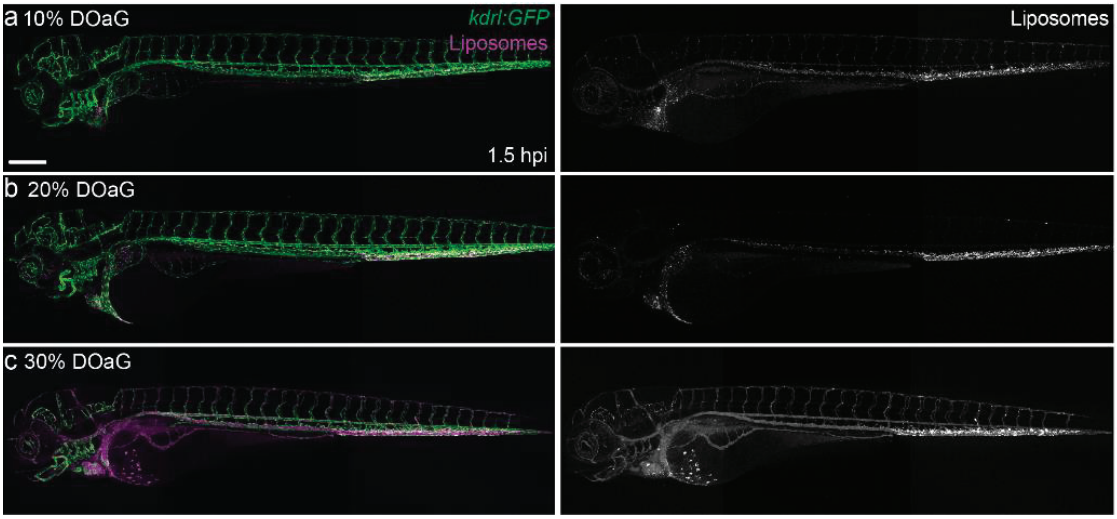

Supplementary Figure 6. Biodistribution of PAP3 liposomes formulated at varying molar ratios. a) Liposomes (5 mM containing 0.2 mol% DOPE-LR, magenta or gray) composed of DSPC and 10 mol%, **b)** 20 mol%, or **c)** 30 mol% DOaG in a Tg(*kdrl:*GFP) embryo at 78 hpf, 1.5 hpi (10x magnification). Scale bar 200 μm.

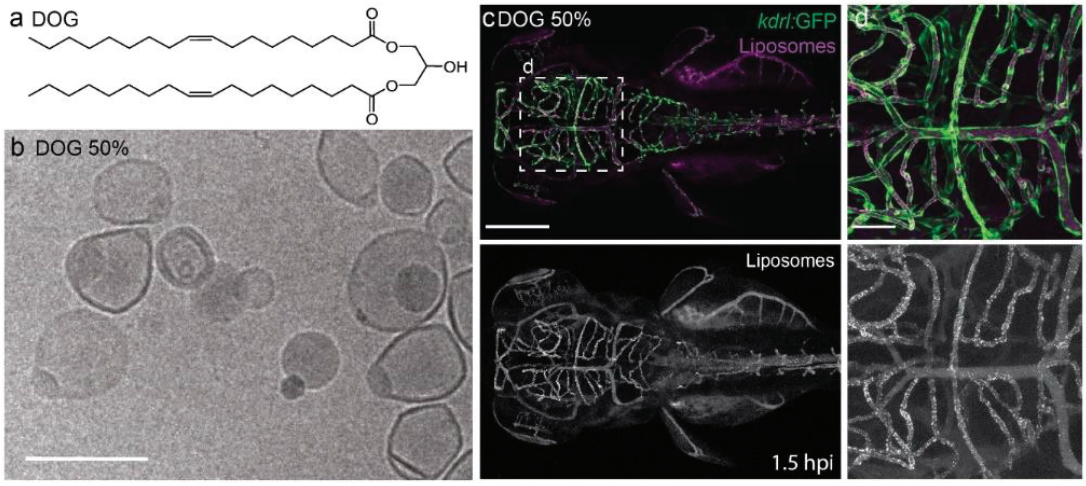

Supplementary Figure 7. CryoTEM and biodistribution of DSPC and DOG containing liposomes. (a) Chemical structure of 1,3-DiOleoyl Glycerol (DG(18:1/0:0/18:1) **(b)** CryoTEM of liposomes containing DSPC and DOG in equal ratios. **(c)** Biodistribution of DSPC-DOG (5 mM containing 0.2 mol% DOPE-LR, in magenta or gray) in zebrafish at 78 hpf, 1.5 hpi in dorsal view. **(d)** bECs (40x magnification). Scale bars: 200 nm (cryoTEM), 200 μm (dorsal view) and 50 μm (tissue level).

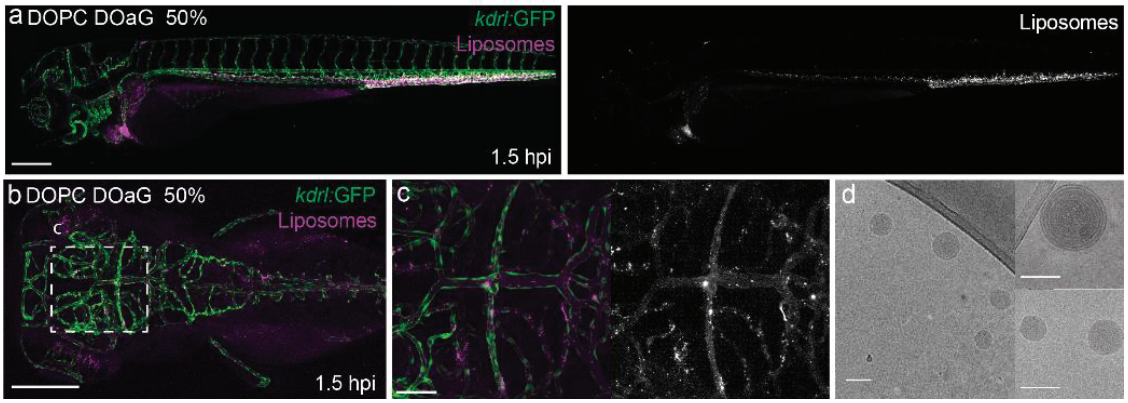

Supplementary Figure 8. DOPC-DOaG liposomes in zebrafish embryo. (a) Biodistribution of liposomes composed of DOPC and DOaG in equal ratios (magenta or gray) in Tg(*kdrl*:GFP) transgenic line, at 78 hpf, 1.5 hpi in lateral view. **(b)** Dorsal view (10x magnification.) **(c)** bECs, at tissue level (40x magnification). **(d)** CryoTEM images of DOPC:DOaG liposomes showing multilamellar or solid lipid-like morphology. Liposomes formulated by ethanol injection, concentration 5 mM containing 0.2 mol% DOPE-LR. Extrusion was not possible with this formulation. Scale bars: 200 µm (dorsal and lateral views), 50 µm (tissue level) and 100 nm for CryoTEM.

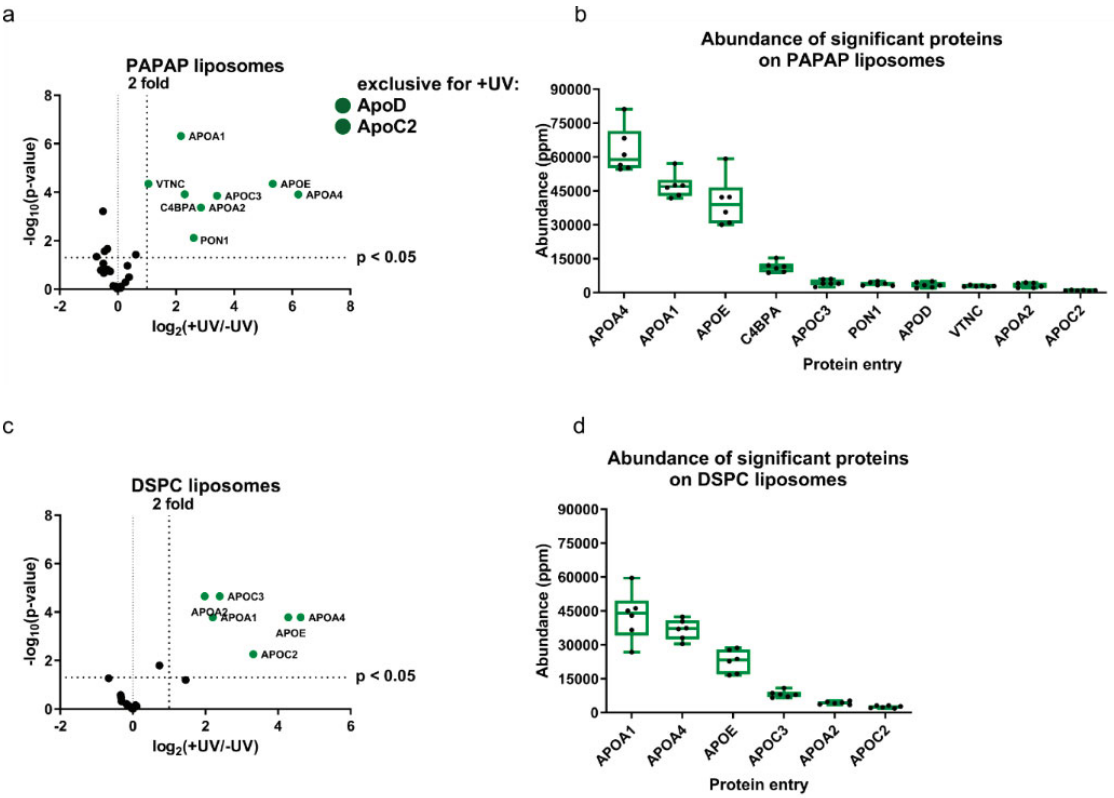

Supplementary Figure 9. Identification of the PAP3 liposome protein corona, isolated via photoaffinity method. (a, c) Volcano plots of enrichment over background (log_2(+UV/-UV) plotted against the statistical significance of this comparison (-log_{10}(*p*-

value)) of PAP3 and DSPC liposomes respectively. Proteins meeting all selection criteria labeled in green. Proteins without background labeling are listed as exclusive for +UV. **(b, d)** Abundance plots of proteins (replicate abundancies of the top10 proteins (ppm) withing the +UV samples) identified in PAP3 and DSPC liposomes respectively. Liposomes with affinity probe (IKS02 5mol%) incorporated into the liposome membrane made by extrusion.

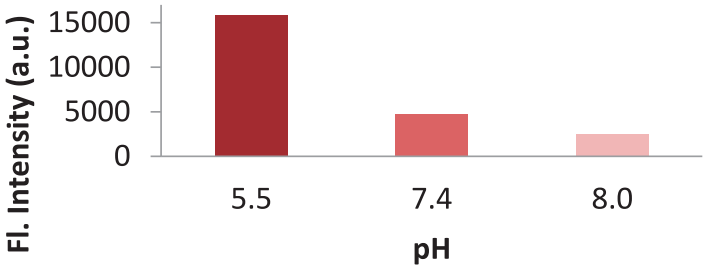

Supplementary Figure 10. Fluorescence intensity of PAP3 liposomes containing 0.5 %mol DOPE-pHrodo™ at different pH (5.5, 7.4 and 8).

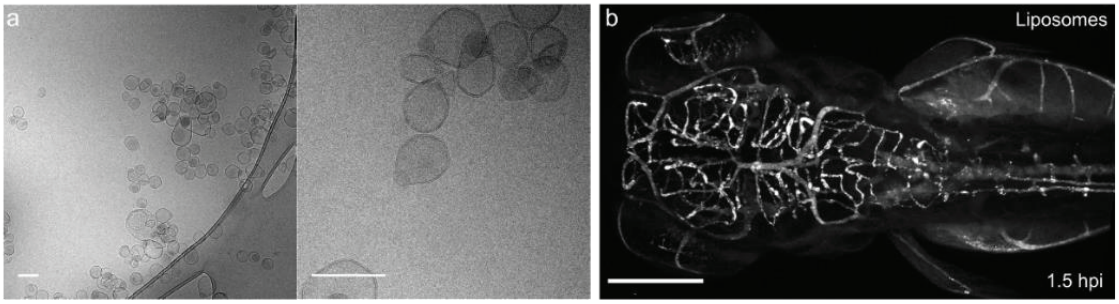

Supplementary Figure 11. CryoTEM and biodistribution of ^{64}Cu - PAP3 liposomes containing NOTA-Bz-SCN-C18. (a) CryoTEM images of PAP3 liposomes containing 0.2%mol NOTA-Bz-SCN-C18 after Cu chelation (stable Cu isotope). **(b)** Biodistribution of PAP3 liposomes containing 0.2%mol NOTA-Bz-SCN-C18 after ^{64}Cu chelation in zebrafish. Sample administered in mice was later injected in zebrafish to ensure bEC targeting was retained. Sample was injected in zebrafish two weeks later to ensure radioactivity decay. Scale bars : 200 nm (cryoTEM), 200 µm (dorsal view).

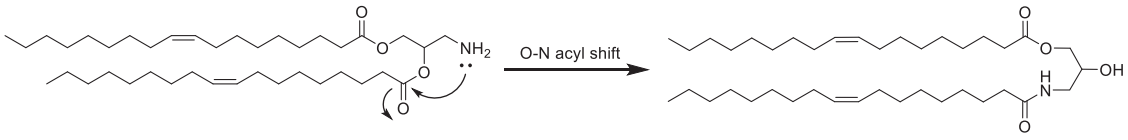

Supplementary Figure 12. O-N intramolecular acyl migration. Cationic lipid originally used for another project underwent rearrangement resulting in DOaG lipid.

Supplementary Table 1. Physicochemical properties of liposomes

Liposomes	Preparation method	Size (nm)	PDI	Stability*
DSPC	Extrusion	± 110.9	0.062	> month
PAP3 liposomes (10%DOaG)	Ethanol injection	± 137.5	0.179	n/a
PAP3 liposomes (20%DOaG)	Ethanol injection	± 107.5	0.181	n/a
PAP3 liposomes (30%DOaG)	Ethanol injection	± 136.5	0.281	n/a
PAP3 liposomes (50%DOaG)	Ethanol injection	± 123.0	0.218	~7 days
	Extrusion	± 153.1	0.114	~7 days
DSPC:DOaG:IKS02 (45:50:5)	Extrusion	± 129.4	0.163	n/a
DSPC:DOG (50:50)	Extrusion	± 161.7	0.318	~7days
DOPC:DOaG (50:50)	Ethanol Injection	± 200.2	0.141	~2 days
DSPC:DOaG:NOTA (49.9:49.9:0.2)	Ethanol Injection	± 174.0	0.159	~5 days
DSPC:DOaG:NOTA (49.9:49.9:0.2) *labelled with Cu^{2+} (cold)*	Ethanol Injection	± 260.8	0.231	~1day
DSPC:DOaG:DOPE-pHrodo:NBD (49.5 :49.5 :0.5 :0.5)	Extrusion	± 126.2	0.227	n/a

*Determined by dynamic light scattering (DLS) measurements for each formulation, over the period of 2,3,7,14 and 30 days.

5.8 References

1. Feingold, K. R., Introduction to Lipids and Lipoproteins. In *Endotext*, Feingold, K. R.; Anawalt, B.; Boyce, A.; Chrousos, G.; de Herder, W. W.; Dhatariya, K.; Dungan, K.; Grossman, A.; Hershman, J. M.; Hofland, J.; Kalra, S.; Kaltsas, G.; Koch, C.; Kopp, P.; Korbonits, M.; Kovacs, C. S.; Kuohung, W.; Laferrere, B.; McGee, E. A.; McLachlan, R.; Morley, J. E.; New, M.; Purnell, J.; Sahay, R.; Singer, F.; Stratakis, C. A.; Trence, D. L.; Wilson, D. P., Eds. South Dartmouth (MA), 2000.
2. Akinc, A.; Maier, M. A.; Manoharan, M.; Fitzgerald, K.; Jayaraman, M.; Barros, S.; Ansell, S.; Du, X.; Hope, M. J.; Madden, T. D.; Mui, B. L.; Semple, S. C.; Tam, Y. K.; Ciufolini, M.; Witzigmann, D.; Kulkarni, J. A.; van der Meel, R.; Cullis, P. R., The Onpattro story and the clinical translation of nanomedicines containing nucleic acid-based drugs. *Nat Nanotechnol* **2019,** *14* (12), 1084-1087.
3. Akinc, A.; Querbes, W.; De, S.; Qin, J.; Frank-Kamenetsky, M.; Jayaprakash, K. N.; Jayaraman, M.; Rajeev, K. G.; Cantley, W. L.; Dorkin, J. R., et al., Targeted delivery of RNAi therapeutics with endogenous and exogenous ligand-based mechanisms. *Mol Ther* **2010,** *18* (7), 1357-1364.
4. Ference, B. A.; Ginsberg, H. N.; Graham, I.; Ray, K. K.; Packard, C. J.; Bruckert, E.; Hegele, R. A.; Krauss, R. M.; Raal, F. J.; Schunkert, H., et al., Low-density lipoproteins cause atherosclerotic cardiovascular disease. 1. Evidence from genetic, epidemiologic, and clinical studies. A consensus statement from the European Atherosclerosis Society Consensus Panel. *Eur Heart J* **2017,** *38* (32), 2459-2472.
5. Goldstein, J. L.; Brown, M. S., A century of cholesterol and coronaries: from plaques to genes to statins. *Cell* **2015,** *161* (1), 161-172.
6. Fielding, C. J.; Fielding, P. E., Molecular physiology of reverse cholesterol transport. *J Lipid Res* **1995,** *36* (2), 211-228.
7. Allan, C. M.; Fidge, N. H.; Morrison, J. R.; Kanellos, J., Monoclonal antibodies to human apolipoprotein AI: probing the putative receptor binding domain of apolipoprotein AI. *Biochem J* **1993,** *290 (Pt 2)*, 449-455.
8. Vadiveloo, P. K.; Allan, C. M.; Murray, B. J.; Fidge, N. H., Interaction of apolipoprotein AII with the putative high-density lipoprotein receptor. *Biochemistry* **1993,** *32* (36), 9480-9485.
9. Hussain, M. M.; Strickland, D. K.; Bakillah, A., The mammalian low-density lipoprotein receptor family. *Annu Rev Nutr* **1999,** *19*, 141-172.
10. Subbaiah, P. V.; Albers, J. J.; Chen, C. H.; Bagdade, J. D., Low density lipoprotein-activated lysolecithin acylation by human plasma lecithin-cholesterol acyltransferase. Identity of lysolecithin acyltransferase and lecithin-cholesterol acyltransferase. *J Biol Chem* **1980,** *255* (19), 9275-9280.
11. Shen, Y.; Lookene, A.; Zhang, L.; Olivecrona, G., Site-directed mutagenesis of apolipoprotein CII to probe the role of its secondary structure for activation of lipoprotein lipase. *J Biol Chem* **2010,** *285* (10), 7484-7492.
12. Amar, M. J.; Sakurai, T.; Sakurai-Ikuta, A.; Sviridov, D.; Freeman, L.; Ahsan, L.; Remaley, A. T., A novel apolipoprotein C-II mimetic peptide that activates lipoprotein lipase and decreases serum triglycerides in apolipoprotein E-knockout mice. *J Pharmacol Exp Ther* **2015,** *352* (2), 227-235.
13. Mead, J. R.; Irvine, S. A.; Ramji, D. P., Lipoprotein lipase: structure, function, regulation, and role in disease. *J Mol Med (Berl)* **2002,** *80* (12), 753-769.
14. Connelly, P. W., The role of hepatic lipase in lipoprotein metabolism. *Clin Chim Acta* **1999,** *286* (1-2), 243-255.
15. Jaye, M.; Lynch, K. J.; Krawiec, J.; Marchadier, D.; Maugeais, C.; Doan, K.; South, V.; Amin, D.; Perrone, M.; Rader, D. J., A novel endothelial-derived lipase that modulates HDL metabolism. *Nat Genet* **1999,** *21* (4), 424-428.
16. Hirata, K.; Dichek, H. L.; Cioffi, J. A.; Choi, S. Y.; Leeper, N. J.; Quintana, L.; Kronmal, G. S.; Cooper, A. D.; Quertermous, T., Cloning of a unique lipase from endothelial cells extends the lipase gene family. *J Biol Chem* **1999,** *274* (20), 14170-14175.
17. Fuki, I. V.; Blanchard, N.; Jin, W.; Marchadier, D. H.; Millar, J. S.; Glick, J. M.; Rader, D. J., Endogenously produced endothelial lipase enhances binding and cellular processing of plasma lipoproteins via heparan sulfate proteoglycan-mediated pathway. *J Biol Chem* **2003,** *278* (36), 34331-34338.
18. Santamarina-Fojo, S.; Dugi, K. A., Structure, function and role of lipoprotein lipase in lipoprotein metabolism. *Curr Opin Lipidol* **1994,** *5* (2), 117-125.
19. Landin, B.; Nilsson, A.; Twu, J. S.; Schotz, M. C., A role for hepatic lipase in chylomicron and high density lipoprotein phospholipid metabolism. *J Lipid Res* **1984,** *25* (6), 559-563.

20. Dugi, K. A.; Dichek, H. L.; Santamarina-Fojo, S., Human hepatic and lipoprotein lipase: the loop covering the catalytic site mediates lipase substrate specificity. *J Biol Chem* **1995,** *270* (43), 25396-25401.
21. McCoy, M. G.; Sun, G. S.; Marchadier, D.; Maugeais, C.; Glick, J. M.; Rader, D. J., Characterization of the lipolytic activity of endothelial lipase. *J Lipid Res* **2002,** *43* (6), 921-929.
22. Yu, J. E.; Han, S. Y.; Wolfson, B.; Zhou, Q., The role of endothelial lipase in lipid metabolism, inflammation, and cancer. *Histol Histopathol* **2018,** *33* (1), 1-10.
23. Ishida, T.; Choi, S.; Kundu, R. K.; Hirata, K.; Rubin, E. M.; Cooper, A. D.; Quertermous, T., Endothelial lipase is a major determinant of HDL level. *J Clin Invest* **2003,** *111* (3), 347-355.
24. Paradis, M. E.; Lamarche, B., Endothelial lipase: its role in cardiovascular disease. *Can J Cardiol* **2006,** *22 Suppl B*, 31B-34B.
25. Jin, W.; Millar, J. S.; Broedl, U.; Glick, J. M.; Rader, D. J., Inhibition of endothelial lipase causes increased HDL cholesterol levels in vivo. *J Clin Invest* **2003,** *111* (3), 357-362.
26. Strauss, J. G.; Zimmermann, R.; Hrzenjak, A.; Zhou, Y.; Kratky, D.; Levak-Frank, S.; Kostner, G. M.; Zechner, R.; Frank, S., Endothelial cell-derived lipase mediates uptake and binding of high-density lipoprotein (HDL) particles and the selective uptake of HDL-associated cholesterol esters independent of its enzymic activity. *Biochem J* **2002,** *368* (Pt 1), 69-79.
27. Sieber, S.; Grossen, P.; Detampel, P.; Siegfried, S.; Witzigmann, D.; Huwyler, J., Zebrafish as an early stage screening tool to study the systemic circulation of nanoparticulate drug delivery systems in vivo. *J Control Release* **2017,** *264*, 180-191.
28. Arias-Alpizar, G.; Kong, L.; Vlieg, R. C.; Rabe, A.; Papadopoulou, P.; Meijer, M. S.; Bonnet, S.; Vogel, S.; van Noort, J.; Kros, A.; Campbell, F., Light-triggered switching of liposome surface charge directs delivery of membrane impermeable payloads in vivo. *Nat Commun* **2020,** *11* (1), 3638.
29. Campbell, F.; Bos, F. L.; Sieber, S.; Arias-Alpizar, G.; Koch, B. E.; Huwyler, J.; Kros, A.; Bussmann, J., Directing Nanoparticle Biodistribution through Evasion and Exploitation of Stab2-Dependent Nanoparticle Uptake. *ACS Nano* **2018,** *12* (3), 2138-2150.
30. Arias-Alpizar, G.; Koch, B.; Hamelmann, N. M.; Neustrup, M. A.; Paulusse, J. M. J.; Jiskoot, W.; Kros, A.; Bussmann, J., Stabilin-1 is required for the endothelial clearance of small anionic nanoparticles. *Nanomedicine: Nanotechnology, Biology and Medicine* **2021**, 102395.
31. Hayashi, Y.; Takamiya, M.; Jensen, P. B.; Ojea-Jiménez, I.; Claude, H.; Antony, C.; Kjaer-Sorensen, K.; Grabher, C.; Boesen, T.; Gilliland, D.; Oxvig, C.; Strähle, U.; Weiss, C., Differential Nanoparticle Sequestration by Macrophages and Scavenger Endothelial Cells Visualized in Vivo in Real-Time and at Ultrastructural Resolution. *ACS Nano* **2020,** *14* (2), 1665-1681.
32. Quinonez-Silvero, C.; Hubner, K.; Herzog, W., Development of the brain vasculature and the blood-brain barrier in zebrafish. *Dev Biol* **2020,** *457* (2), 181-190.
33. van Leeuwen, L. M.; Evans, R. J.; Jim, K. K.; Verboom, T.; Fang, X.; Bojarczuk, A.; Malicki, J.; Johnston, S. A.; van der Sar, A. M., A transgenic zebrafish model for the in vivo study of the blood and choroid plexus brain barriers using claudin 5. *Biol Open* **2018,** *7* (2).
34. Ulrich, F.; Ma, L. H.; Baker, R. G.; Torres-Vazquez, J., Neurovascular development in the embryonic zebrafish hindbrain. *Dev Biol* **2011,** *357* (1), 134-151.
35. Zhang, J.; Liss, M.; Wolburg, H.; Blasig, I. E.; Abdelilah-Seyfried, S., Involvement of claudins in zebrafish brain ventricle morphogenesis. *Ann N Y Acad Sci* **2012,** *1257*, 193-198.
36. Zhang, J.; Piontek, J.; Wolburg, H.; Piehl, C.; Liss, M.; Otten, C.; Christ, A.; Willnow, T. E.; Blasig, I. E.; Abdelilah-Seyfried, S., Establishment of a neuroepithelial barrier by Claudin5a is essential for zebrafish brain ventricular lumen expansion. *Proc Natl Acad Sci U S A* **2010,** *107* (4), 1425-1430.
37. Ando, K.; Fukuhara, S.; Izumi, N.; Nakajima, H.; Fukui, H.; Kelsh, R. N.; Mochizuki, N., Clarification of mural cell coverage of vascular endothelial cells by live imaging of zebrafish. *Development* **2016,** *143* (8), 1328-1339.
38. Lyons, D. A.; Talbot, W. S., Glial cell development and function in zebrafish. *Cold Spring Harb Perspect Biol* **2014,** *7* (2), a020586.
39. Umans, R. A.; Henson, H. E.; Mu, F.; Parupalli, C.; Ju, B.; Peters, J. L.; Lanham, K. A.; Plavicki, J. S.; Taylor, M. R., CNS angiogenesis and barriergenesis occur simultaneously. *Dev Biol* **2017,** *425* (2), 101-108.
40. O'Brown, N. M.; Megason, S. G.; Gu, C., Suppression of transcytosis regulates zebrafish blood-brain barrier function. *Elife* **2019,** *8*.
41. Isogai, S.; Horiguchi, M.; Weinstein, B. M., The vascular anatomy of the developing zebrafish: an atlas of embryonic and early larval development. *Dev Biol* **2001,** *230* (2), 278-301.

42. Moradi, M.-A.; Bomans, P. H. H.; Jackson, A. W.; van Herk, A. M.; Heuts, J. P. A., A quantitative cryoTEM study on crosslinked nanocapsule morphology in RAFT-based vesicle polymerization. *European Polymer Journal* **2018,** *108*, 329-336.
43. Moradi, M. A.; Tempelaar, S.; van Herk, A. M.; Heuts, J. P. A., Morphology Control of Liposome - RAFT Oligomer Precursors to Complex Polymer Nanostructures. *Macromolecules* **2019,** *52* (24), 9476-9483.
44. De Boeck, H.; Zidovetzki, R., Effects of diacylglycerols on the structure of phosphatidylcholine bilayers: a 2H and 31P NMR study. *Biochemistry* **1989,** *28* (18), 7439-7446.
45. Goldberg, E. M.; Lester, D. S.; Borchardt, D. B.; Zidovetzki, R., Effects of diacylglycerols and Ca2+ on structure of phosphatidylcholine/phosphatidylserine bilayers. *Biophys J* **1994,** *66* (2 Pt 1), 382-393.
46. Jimenez-Monreal, A. M.; Villalain, J.; Aranda, F. J.; Gomez-Fernandez, J. C., The phase behavior of aqueous dispersions of unsaturated mixtures of diacylglycerols and phospholipids. *Biochim Biophys Acta* **1998,** *1373* (1), 209-219.
47. Goni, F. M.; Alonso, A., Structure and functional properties of diacylglycerols in membranes. *Prog Lipid Res* **1999,** *38* (1), 1-48.
48. Szule, J. A.; Fuller, N. L.; Rand, R. P., The effects of acyl chain length and saturation of diacylglycerols and phosphatidylcholines on membrane monolayer curvature. *Biophys J* **2002,** *83* (2), 977-984.
49. Campomanes, P.; Zoni, V.; Vanni, S., Local accumulation of diacylglycerol alters membrane properties nonlinearly due to its transbilayer activity. *Communications Chemistry* **2019,** *2* (1), 72.
50. Otis, J. P.; Zeituni, E. M.; Thierer, J. H.; Anderson, J. L.; Brown, A. C.; Boehm, E. D.; Cerchione, D. M.; Ceasrine, A. M.; Avraham-Davidi, I.; Tempelhof, H.; Yaniv, K.; Farber, S. A., Zebrafish as a model for apolipoprotein biology: comprehensive expression analysis and a role for ApoA-IV in regulating food intake. *Dis Model Mech* **2015,** *8* (3), 295-309.
51. Miyares, R. L.; de Rezende, V. B.; Farber, S. A., Zebrafish yolk lipid processing: a tractable tool for the study of vertebrate lipid transport and metabolism. *Dis Model Mech* **2014,** *7* (7), 915-927.
52. Kim, J. Y.; Seo, J.; Cho, K. H., Aspartame-fed zebrafish exhibit acute deaths with swimming defects and saccharin-fed zebrafish have elevation of cholesteryl ester transfer protein activity in hypercholesterolemia. *Food Chem Toxicol* **2011,** *49* (11), 2899-2905.
53. Song, Y.; Cone, R. D., Creation of a genetic model of obesity in a teleost. *FASEB J* **2007,** *21* (9), 2042-2049.
54. Nishio, S.; Gibert, Y.; Bernard, L.; Brunet, F.; Triqueneaux, G.; Laudet, V., Adiponectin and adiponectin receptor genes are coexpressed during zebrafish embryogenesis and regulated by food deprivation. *Dev Dyn* **2008,** *237* (6), 1682-1690.
55. Anderson, J. L.; Carten, J. D.; Farber, S. A., Zebrafish lipid metabolism: from mediating early patterning to the metabolism of dietary fat and cholesterol. *Methods Cell Biol* **2011,** *101*, 111-141.
56. Liu, C.; Gates, K. P.; Fang, L.; Amar, M. J.; Schneider, D. A.; Geng, H.; Huang, W.; Kim, J.; Pattison, J.; Zhang, J.; Witztum, J. L.; Remaley, A. T.; Dong, P. D.; Miller, Y. I., Apoc2 loss-of-function zebrafish mutant as a genetic model of hyperlipidemia. *Dis Model Mech* **2015,** *8* (8), 989-998.
57. Pattipeiluhu, R.; Crielaard, S.; Klein-Schiphorst, I.; Florea, B. I.; Kros, A.; Campbell, F., Unbiased Identification of the Liposome Protein Corona using Photoaffinity-based Chemoproteomics. *ACS Central Science* **2020,** *6* (4), 535-545.
58. Muller, D. P.; Gamlen, T. R., The activity of hepatic lipase and lipoprotein lipase in glycogen storage disease: evidence for a circulating inhibitor of postheparin lipolytic activity. *Pediatr Res* **1984,** *18* (9), 881-885.
59. Ori, A.; Wilkinson, M. C.; Fernig, D. G., A systems biology approach for the investigation of the heparin/heparan sulfate interactome. *J Biol Chem* **2011,** *286* (22), 19892-19904.
60. Sun, S.; Dean, R.; Jia, Q.; Zenova, A.; Zhong, J.; Grayson, C.; Xie, C.; Lindgren, A.; Samra, P.; Sojo, L.; van Heek, M.; Lin, L.; Percival, D.; Fu, J. M.; Winther, M. D.; Zhang, Z., Discovery of XEN445: a potent and selective endothelial lipase inhibitor raises plasma HDL-cholesterol concentration in mice. *Bioorg Med Chem* **2013,** *21* (24), 7724-7734.
61. Lo, P. K.; Yao, Y.; Zhou, Q., Inhibition of LIPG phospholipase activity suppresses tumor formation of human basal-like triple-negative breast cancer. *Sci Rep* **2020,** *10* (1), 8911.
62. Thisse, B., Thisse, C. , Fast release clones: A high throughput expression analysis. Submission, Z. D. D., Ed. http://zfin.org, 2004.

63. Zhu, G.; Mock, J. N.; Aljuffali, I.; Cummings, B. S.; Arnold, R. D., Secretory phospholipase A(2) responsive liposomes. *J Pharm Sci* **2011,** *100* (8), 3146-3159.
64. Sharipov, M.; Tawfik, S. M.; Gerelkhuu, Z.; Huy, B. T.; Lee, Y. I., Phospholipase A2-Responsive Phosphate Micelle-Loaded UCNPs for Bioimaging of Prostate Cancer Cells. *Sci Rep* **2017,** *7* (1), 16073.
65. Gomez-Fernandez, J. C.; Corbalan-Garcia, S., Diacylglycerols, multivalent membrane modulators. *Chem Phys Lipids* **2007,** *148* (1), 1-25.
66. Alwarawrah, M.; Dai, J.; Huang, J., Modification of Lipid Bilayer Structure by Diacylglycerol: A Comparative Study of Diacylglycerol and Cholesterol. *J Chem Theory Comput* **2012,** *8* (2), 749-758.
67. Lindegaard, M. L.; Nielsen, J. E.; Hannibal, J.; Nielsen, L. B., Expression of the endothelial lipase gene in murine embryos and reproductive organs. *J Lipid Res* **2005,** *46* (3), 439-444.
68. Lindegaard, M. L.; Olivecrona, G.; Christoffersen, C.; Kratky, D.; Hannibal, J.; Petersen, B. L.; Zechner, R.; Damm, P.; Nielsen, L. B., Endothelial and lipoprotein lipases in human and mouse placenta. *J Lipid Res* **2005,** *46* (11), 2339-2346.
69. Ishida, T.; Choi, S. Y.; Kundu, R. K.; Spin, J.; Yamashita, T.; Hirata, K.; Kojima, Y.; Yokoyama, M.; Cooper, A. D.; Quertermous, T., Endothelial lipase modulates susceptibility to atherosclerosis in apolipoprotein-E-deficient mice. *J Biol Chem* **2004,** *279* (43), 45085-45092.
70. Badellino, K. O.; Wolfe, M. L.; Reilly, M. P.; Rader, D. J., Endothelial lipase is increased in vivo by inflammation in humans. *Circulation* **2008,** *117* (5), 678-685.
71. Lo, P. K.; Yao, Y.; Lee, J. S.; Zhang, Y.; Huang, W.; Kane, M. A.; Zhou, Q., LIPG signaling promotes tumor initiation and metastasis of human basal-like triple-negative breast cancer. *Elife* **2018,** *7*.
72. Dong, X.; Wang, G.; Zhang, G.; Ni, Z.; Suo, J.; Cui, J.; Cui, A.; Yang, Q.; Xu, Y.; Li, F., The endothelial lipase protein is promising urinary biomarker for diagnosis of gastric cancer. *Diagn Pathol* **2013,** *8*, 45.
73. Nielsen, J. E.; Lindegaard, M. L.; Friis-Hansen, L.; Almstrup, K.; Leffers, H.; Nielsen, L. B.; Rajpert-De Meyts, E., Lipoprotein lipase and endothelial lipase in human testis and in germ cell neoplasms. *Int J Androl* **2010,** *33* (1), e207-215.
74. Tatematsu, S.; Francis, S. A.; Natarajan, P.; Rader, D. J.; Saghatelian, A.; Brown, J. D.; Michel, T.; Plutzky, J., Endothelial lipase is a critical determinant of high-density lipoprotein-stimulated sphingosine 1-phosphate-dependent signaling in vascular endothelium. *Arterioscler Thromb Vasc Biol* **2013,** *33* (8), 1788-1794.
75. Sieber, S.; Grossen, P.; Bussmann, J.; Campbell, F.; Kros, A.; Witzigmann, D.; Huwyler, J., Zebrafish as a preclinical in vivo screening model for nanomedicines. *Adv Drug Deliv Rev* **2019,** *151-152*, 152-168.
76. Kemmer, G. C.; Bogh, S. A.; Urban, M.; Palmgren, M. G.; Vosch, T.; Schiller, J.; Gunther Pomorski, T., Lipid-conjugated fluorescent pH sensors for monitoring pH changes in reconstituted membrane systems. *Analyst* **2015,** *140* (18), 6313-6320.
77. Kremer, J. R.; Mastronarde, D. N.; McIntosh, J. R., Computer visualization of three-dimensional image data using IMOD. *J Struct Biol* **1996,** *116* (1), 71-76.
78. Jin, S. W.; Beis, D.; Mitchell, T.; Chen, J. N.; Stainier, D. Y., Cellular and molecular analyses of vascular tube and lumen formation in zebrafish. *Development* **2005,** *132* (23), 5199-5209.
79. Ellett, F.; Pase, L.; Hayman, J. W.; Andrianopoulos, A.; Lieschke, G. J., mpeg1 promoter transgenes direct macrophage-lineage expression in zebrafish. *Blood* **2011,** *117* (4), e49-56.
80. Schindelin, J.; Arganda-Carreras, I.; Frise, E.; Kaynig, V.; Longair, M.; Pietzsch, T.; Preibisch, S.; Rueden, C.; Saalfeld, S.; Schmid, B.; Tinevez, J. Y.; White, D. J.; Hartenstein, V.; Eliceiri, K.; Tomancak, P.; Cardona, A., Fiji: an open-source platform for biological-image analysis. *Nat Methods* **2012,** *9* (7), 676-682.
81. Schneider, C. A.; Rasband, W. S.; Eliceiri, K. W., NIH Image to ImageJ: 25 years of image analysis. *Nat Methods* **2012,** *9* (7), 671-675.

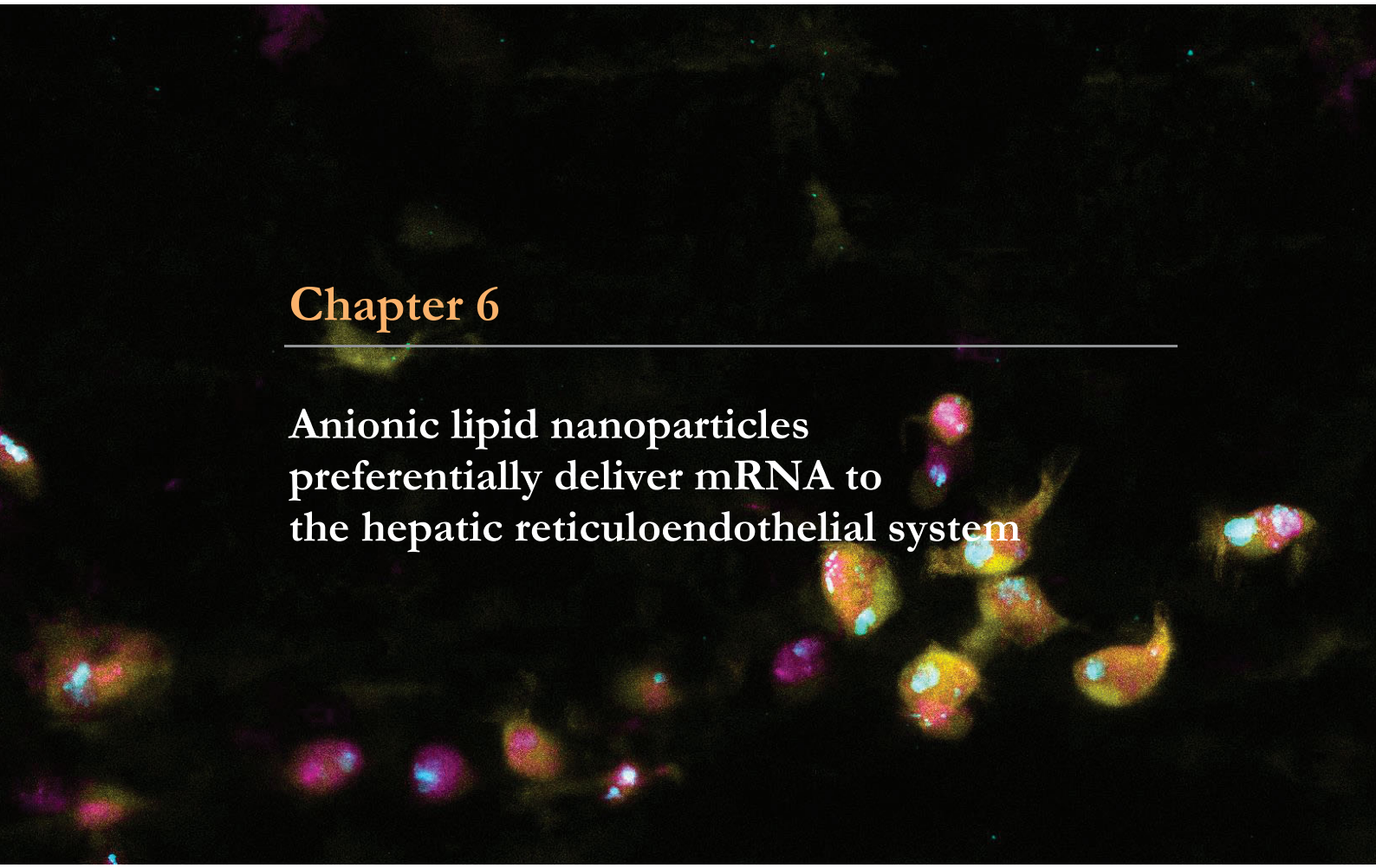

Chapter 6

Anionic lipid nanoparticles preferentially deliver mRNA to the hepatic reticuloendothelial system

Submitted:

Pattipeiluhu, R*; **Arias-Alpizar, G.***; Basha, G.; Bussmann, J.; Sharp, T.H.; Moradi, M.A.; Sommerdijk, N.; , J.; Cullis, P.R.; Kros, A.; Campbell, F. Anionic Lipid Nanoparticles Preferentially Deliver mRNA to the Hepatic Reticuloendothelial System. **Submitted.**

These authors contributed equally*

Image: Macrophages (in magenta) expressing GFP (in yellow) delivered by srLNP (in cyan) in a stabilin-1 & -2 double knockout zebrafish.

6.1 Abstract

Lipid nanoparticles (LNPs) are the leading non-viral technology for the delivery of exogenous RNA to target cells *in vivo*. These delivery platforms are exemplified by Onpattro®, a clinically approved LNP-based RNA interference (RNAi) therapy, indicated for polyneuropathies resulting from transthyretin-mediated amyloidosis, administered systemically, and targeted to parenchymal liver cells. The discovery of LNP technologies capable of preferential RNA delivery to liver cell types beyond hepatocytes has, however, proved more challenging. Here, preceded by a comprehensive mechanistic understanding of nanoparticle biodistribution and clearance, we design an LNP-based mRNA delivery platform capable of preferentially targeting the hepatic reticuloendothelial system (RES). Evaluated in embryonic zebrafish, validated in mice and compared to LNP-mRNA systems based on the lipid composition of Onpattro®, RES-targeted LNPs show significantly enhanced mRNA expression both globally within the liver and specifically within hepatic RES cell types. LNP redirection to the hepatic RES requires switching of LNP surface charge from neutral to anionic, achieved through just a single lipid change within the lipid composition of Onpattro®. Not only does this technology open up new opportunities to treat diseases in which RES cell types play a central role but it cements the view that rational development of advanced RNA therapies must be preceded by a thorough understanding of the nano-bio interactions involved.

6.2 Introduction

RNA therapy relies on cytosolic delivery of exogenous (therapeutic) RNA molecules, *e.g.* mRNA, siRNA, or miRNA, to gain precise control of gene expression within target cells.[1, 2] This requires delivery systems to protect, transport and deliver highly charged, immunogenic and membrane impermeable RNA payloads within target cells and tissues in the body. To this end, lipid nanoparticles (LNPs) have emerged as the state-of-the-art, non-viral RNA delivery system for *in vivo* application.[3-5] These technologies are exemplified by Onpattro®, a clinically approved LNP-based RNA interference (RNAi) therapy, administered intravenously (*i.v.*) and used to treat polyneuropathies resulting from transthyretin-mediated amyloidosis (hATTR).[6, 7] Onpattro® functions by transiently silencing (siRNA delivery) the expression of transthyretin (TTR) specifically within hepatocytes.[8] Hepatocyte targeting is mediated through the adsorption of soluble apolipoprotein E (apoE) to the surface of a circulating LNP.[8, 9] This, in turn, promotes LNP binding to the low density lipoprotein receptor (LDLr),[10] a receptor heavily expressed on the sinusoidal surface of hepatocytes. ApoE-LDLr binding leads to LNP endocytosis and consequent cytosolic siRNA delivery, which is enhanced by the protonation of ionizable (cationic) lipids within the endosome and subsequent disruption of the endosomal membrane.[11]

Following systemic administration, harnessing apoE-mediated LNP specificity for the delivery of RNA therapeutics (siRNA or mRNA) to hepatocytes is relatively common.[5, 10, 12-15] Expanding the scope of LNP-based gene therapies to other hepatic cell types (or non-hepatic cells), and therefore access a much greater diversity of disease states, however, has proved more challenging. To meet this challenge, high throughput empirical screening of DNA-barcoded LNPs has revealed formulations that preferentially target extra-hepatic tissues (*e.g.* bone marrow)[16] and cells (*e.g.* T-cells),[17] as well as individual hepatic (*e.g.* liver endothelial) cell types.[18, 19] However, while these empirical discoveries have undoubtedly enriched our understanding of the structure-activity landscape of LNP technologies, they have not revealed the biological mechanisms underpinning LNP transport and preferential cellular uptake *in vivo*. Only this knowledge enables the rational design of new LNP-based RNA therapies with target cell specificity.[5, 20]

Besides hepatocytes (comprising ~80% liver volume), the liver is composed of non-parenchymal liver cells, including Kupffer cells (KCs) and liver sinusoidal endothelial cells (LSECs).[21] Hepatic blood vessels, or sinusoids, connecting the

hepatic artery and portal vein to the central vein of the liver, are primarily composed of LSECs (~70%) and KCs (~20%).[22, 23] Together these two cell types make up the hepatic reticuloendothelial system (RES) whose primary role is to maintain blood homeostasis through the scavenging of macromolecular waste and pathogens from blood.[24, 25] LSECs, in particular, are specialized scavenger endothelial cells (SECs) and have one of the highest endocytic activities of any cell type in the body.[26] These cells are responsible for the clearance of endogenous macromolecules, such as oxidized low-density lipoprotein and hyaluronic acid,[25, 27, 28] as well as blood borne pathogens.[29, 30] In large part, LSEC clearance of macromolecular and pathogenic waste is mediated through an array of scavenger receptors (*e.g.* Hyaluronan- and Stabilin- receptors), heavily expressed on luminal membrane of LSECs.[31-33] As therapeutic target, LSECs not only play a crucial role in liver homeostasis, regeneration following acute injury, and in the pathogenesis of various liver diseases,[26, 34] but, as antigen presenting cells, are also key regulators of hepatic adaptive immunity and systemic immunotolerance.[35]

Guided by previous observations that *i.v.* administered anionic nanoparticles are extensively recognized and cleared by RES cell types,[36] here, we design anionic LNPs capable of preferentially targeting and transfecting the hepatic RES, *i.e.* scavenger receptor LNPs (srLNPs). This redirection required just a single lipid compositional change from the lipid formulation of Onpattro®. Evaluated within embryonic zebrafish *(Danio rerio),*[37] we qualitatively describe LNP biodistribution, mRNA delivery and expression of a fluorescent protein at cellular resolution, *in vivo* and in real time, with particular focus on relative LNP uptake and mRNA expression within SECs, macrophages and hepatocytes of the embryo. Furthermore, we confirm scavenger receptors, Stabilin-1 and -2, mediated uptake of anionic LNPs by SECs. Finally, we validate preferential LNP-mediated mRNA transfection of the hepatic RES in mice.

6.3 Results

Design and characterization of anionic srLNPs

Previously, we have shown that *i.v.* administered, anionic nanoparticles (ranging in size from 10-150 nm) are rapidly and extensively cleared from circulation by scavenging endothelial cells (SECs) within the posterior cardinal vein (PCV), caudal hematopoietic tissue (CHT) and caudal vein (CV) of a two day old zebrafish embryo. In teleost fish (*i.e.* zebrafish), and other aquatic vertebrates,

SECs are not located primarily in the liver, as for LSECs in mammals, but reside in various other organs including scavenging (venous) blood vessels.[38] Mechanistically, anionic nanoparticle recognition and uptake by SECs is mediated by the scavenger receptors, Stabilin-1 (*stab1*) and Stabilin-2 (*stab2*).[36] Stabilin-1 and Stabilin-2 are heavily expressed by LSECs in the mammalian liver[39] and *i.v.* injection of anionic liposomes in (young) adult mice results in extensive nanoparticle uptake within these cell types. In addition to SECs, anionic nanoparticles are also scavenged by blood resident macrophages, both within the CHT of the embryonic zebrafish and within the mouse liver (*i.e.* within KCs).[36, 40] All together, these observations indicate that the embryonic zebrafish can be used to qualitatively predict *in vivo* nanoparticle interactions with mammalian RES cell types.

Here, we aimed at rationally designing an anionic LNP system enabling genetic manipulation in hepatic RES cells. In general, LNPs consist of five structural components (four lipid reagents and an oligonucleotide payload) that self-assemble to form discrete nanostructures ranging from ~30 to ~150 nm in size (**Figure 1a**).[41] The "hydrophobic" core of an LNP is rich in ionizable lipids (*e.g.* DLin-MC3-DMA (50 mol%) *[in the case of Onpattro®]), cholesterol (38.5 mol%*) and an oligonucleotide payload. The LNP surface (*i.e.* lipid-water interface), in contrast, is rich in helper phospholipids (*e.g.* DSPC, 10 mol%*) and lipid-PEG conjugates (*e.g.* DMG-PEG2k, 1.5 mol%*).[42] We, therefore, hypothesized that switching the helper phospholipid of Onpattro®, from zwitterionic, 1,2-distearoyl-*sn*-glycero-3-phosphocholine (DSPC) to anionic, 1,2-distearoyl-*sn*-glycero-3-phosphoglycerol (DSPG), would render the LNP surface anionic. In turn, an anionic surface charge would redirect LNP targeting and functional RNA delivery from hepatocytes to the hepatic RES, by promoting Stabilin- mediated LNP recognition and uptake in LSECs whilst simultaneously inhibiting hepatocyte apoE-LDLr interactions (**Figure 1b,c**).[43] Hereafter, we refer to DSPG-containing LNPs as srLNPs and LNPs based on the lipid composition of Onpattro® as DSPC-LNPs (**Figure 1d**). In all cases, a nitrogen to phosphate (N/P) ratio of 6 was used, as is typical for larger nucleic acid payloads.[44]

Following microfluidic assembly, cryo-electron transmission microscopy (cryoTEM) revealed LNPs with a typical electron dense core structure (**Figure 1e**).[45-48] Within DSPC-LNPs (47.0 nm ± 13.9 nm), both amorphous and lamellar core structures were present, whereas the core structure of srLNPs (66.6 nm ± 22.0 nm) contained a mixture of amorphous, unilamellar and polymorphic

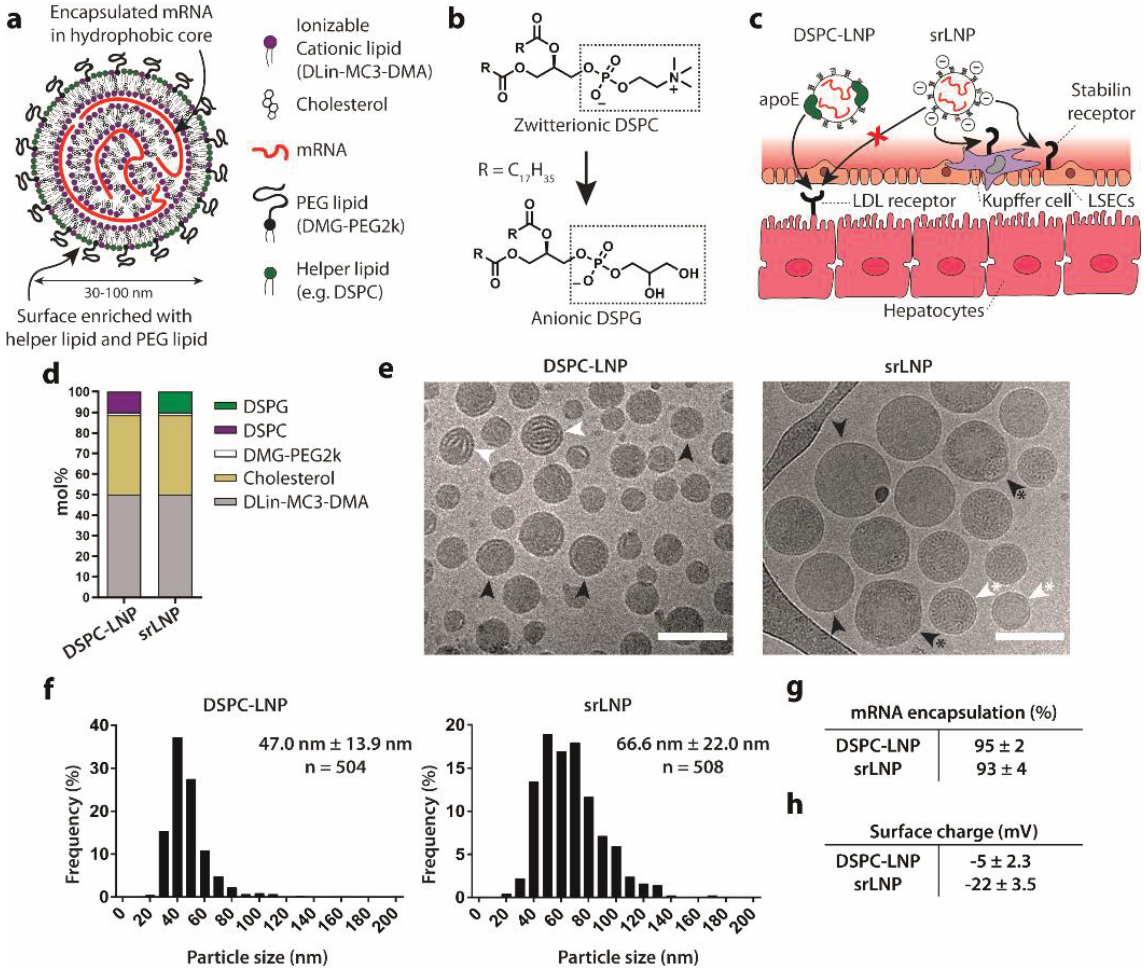

Figure 1 . Design and characterization of srLNPs. (a) Schematic of the structural organization of an LNP containing mRNA, as described previously.[42] Helper phospholipids (typically incorporated at 10 mol%) are enriched at the LNP surface. **(b,c)** Within the liver sinusoids, switching of the helper phospholipid from zwitterionic DSPC (as in Onpattro®) to anionic DSPG creates anionic srLNPs that are directed to the hepatic RES, *via* Stabilin receptor mediated recognition and uptake in LSECs. srLNP uptake within hepatic RES cells is further enhanced by the inhibition of apoE-LDLr interactions mediated by anionic phospholipids (*e.g.* DSPG).[43] The mechanism of recognition and uptake of srLNPs by blood resident macrophages (*i.e.* KCs) is not known. **(d)** Lipid composition of DSPC-LNPs (*i.e.* Onpattro®) and srLNPs. **(e)** CryoTEM images of DSPC-LNPs and srLNPs (entrapping capped mRNA-eGFP) show solid lipid nanoparticle structures. Scale bars: 100 nm. Internal structures indicated with arrows: lamellar (white), amorphous (black), polymorphous (black*) and unilamellar (white*) **(f)** Size distribution of DSPC-LNPs and srLNPs, as determined by cryoTEM. The values derived from the frequency distribution graphs represent the mean ± standard deviation. **(g)** mRNA encapsulation efficiency within DSPC-LNPs and srLNPs, as determined by RiboGreen assay. **(h)** Surface charge of DSPC-LNPs and srLNPs, as determined by zeta potential measurements. See **Supplementary Table 1** for full biophysical characterization of all formulations used in this study.

structures, as has been previously reported for LNP-mRNA systems.[49, 50] Particle sizes of both DSPC-LNPs and srLNPs (determined through cryoTEM image analysis) were comparable to the number-weighted average, as determined by dynamic light scattering (**Figure 1f** and **Supplementary Table 1**), and, in all cases, mRNA encapsulation efficiencies were >95% (**Figure 1g**). Importantly, however, srLNPs possessed a significantly more anionic (ζ-potential ~ -20 mV) surface charge compared to DSPC-LNPs (ζ-potential ~ -5 mV), indicative of DSPG exposed at the lipid-water interface (**Figure 1h**). For detailed biophysical characterization (*i.e.* size, surface charge, encapsulation efficiencies) of all formulations used in this study, please refer to **Supplementary Table 1**.

Biodistribution of LNPs in embryonic zebrafish

To assess LNP biodistribution, DSPC-LNPs and srLNPs, containing a fluorescent lipid probe (DOPE-LR, 0.2 mol%) and encapsulating fluorescent mRNA (capped and Cy5-labelled), were injected (*i.v.,* ~10 mM lipid, ~0.2 mg/kg mRNA) in wildtype zebrafish embryos at two days post-fertilisation (dpf) (**Figure 2a**). Confocal imaging of entire live embryos, as well as high resolution, tissue level views to include key scavenging cell types of the embryo within the CV and CHT (**Figure 2b**), revealed distinct biodistribution patterns for both LNP-mRNA formulations at 1.5 hour post injection (hpi) (**Figure 2c-f**). In the case of DSPC-LNPs, particles were mostly freely circulating, with both lipid and mRNA associated dyes confined to, and homogenously distributed throughout, the vasculature of the embryo (**Figure 2c,d**). In addition, a small fraction of DSPC-LNPs accumulated in blood-resident macrophages, within the CHT of the embryo, indicative of low level recognition and uptake by the RES (white arrowheads, **Figure 2d**; confirmed in *mpeg:*mCherry embryos**, Supplementary Figure 1a-c**). In the case of srLNPs, the majority of injected particles were cleared from circulation at 1.5 hpi, with highly selective accumulation observed within SECs and blood-resident macrophages within the PCV, CHT and CV of the two day old embryo (**Figure 2e,f**; macrophage uptake confirmed in *mpeg1:*mCherry embryos, **Supplementary Figure 1d-f**).

The selective accumulation of srLNPs within scavenging (venous) blood vessels of the embryonic zebrafish closely mirrored previously observed biodistributions of anionic liposomes, polymersomes and inorganic nanoparticles, in which nanoparticle uptake within SECs was mediated by the Stabilin scavenger receptors.[36] To confirm Stabilin-mediated uptake, srLNPs were injected (*i.v.*) in established *stab1*$^{-/-}$*/stab2*$^{-/-}$ double knockout (KO) zebrafish (2 dpf),[51] (described in **Chapter 3**). Within these mutant, srLNPs

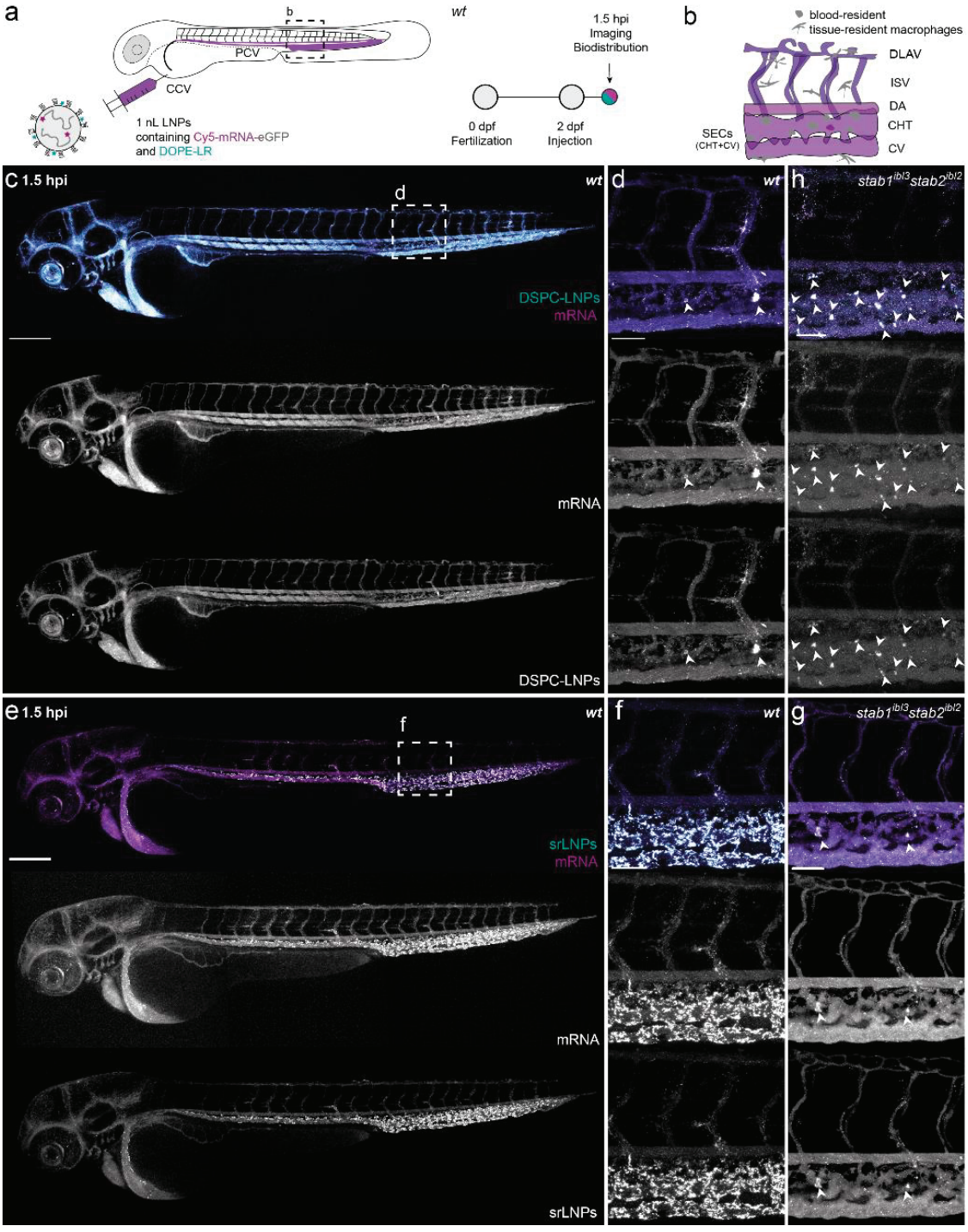

Figure 2. Biodistribution of DSPC-LNPs and srLNPs in two-day old embryonic zebrafish at 1.5 hpi. (a) Schematic showing the site of LNP injection (*i.v*) within embryonic zebrafish (2 dpf) and imaging timeframe. LNPs contained DOPE-LR (cyan, 0.2 mol%) as fluorescent lipid probe and Cy5-labelled eGFP mRNA (magenta) as fluorescent mRNA probe. Injected dose: ~10 mM lipid, ~0.2 mg/kg mRNA. Injection volume: 1 nl. Major venous blood vessels: CCV – common cardinal vein; PCV – posterior cardinal vein. **(b)** Tissue level schematic of a dorsal region of the embryo containing scavenging cell types (*i.e.* SECs and blood resident macrophages). Blood vessels: DA – dorsal aorta, CHT –

caudal hematopoietic tissue; CV – caudal vein; ISV – intersegmental vessel; DLAV - dorsal longitudinal anastomotic vessel**. (c,d)** Whole embryo (10x magnification) and tissue level (40x magnification) views of DSPC-LNP biodistribution within wildtype (*AB/TL)* embryonic zebrafish (2 dpf) at 1.5 hpi. DSPC-LNPs are mostly freely circulating, confined to, and distributed throughout, the vasculature of the embryo. Low level phagocytotic uptake within blood resident macrophages is highlighted by white arrowheads. **(e,f)** Whole embryo (10x magnification) and tissue level (40x magnification) views of srLNP biodistribution within wildtype embryonic zebrafish (2 dpf) at 1.5 hpi. srLNPs are mainly associated with SECs within the PCV, CHT and CV of the embryo and are largely removed from circulation at 1.5 hpi. Phagocytotic uptake of both DSPC-LNPs and srLNPs within blood resident macrophages at 1.5 hpi was confirmed by analogous LNP injections in Tg(*mpeg1*:mCherry) zebrafish embryos, stably expressing mCherry within macrophages (**Supplementary Figure 1**). **(g)** Tissue level (40x magnification) view of srLNP biodistribution within double knockout (*stab1*^{ibl3}*stab2*^{ibl2})[51] zebrafish embryos at 1.5 hpi. Within Stabilin KOs, srLNPs are now mostly freely circulating, with low level phagocytotic uptake within blood resident macrophages highlighted by white arrowheads**. (h)** Tissue level (40x magnification) view of DSPC-LNP biodistribution within double knockout (*stab1*^{ibl3}*stab2*^{ibl2})[51] zebrafish embryos at 1.5 hpi. Within *stabilin* KOs, DSPC-LNPs remain mostly freely circulating, with low level phagocytotic uptake within blood resident macrophages highlighted by white arrowheads. Scale bars: 200 μm (whole embryo) and 50 μm (tissue level).

predominantly remained in circulation at 1.5 hpi with a small fraction accumulating within blood-resident macrophages of the CHT (**Figure 1g** for the whole embryo and **Supplementary Figure 2**). This confirmed srLNPs selectively accumulate within RES cell types of the embryonic zebrafish and that recognition and uptake of srLNPs within SECs, but not macrophages, is mediated by Stabilin receptors. Analogous injections of DSPC-LNPs, within double KO embryos, did not alter DSPC-LNP biodistribution, with the majority of DSPC-LNPs remaining in circulation (**Supplementary Figure 1h** and **Supplementary Figure 2**). In all cases, both lipid and mRNA fluorescent probes, appear fully colocalized at 1.5 hpi, suggesting mRNA remains stably entrapped within the core of both DSPC- and srLNPs in circulation, as well as during (early) cellular recognition and uptake. Under the standard confocal microscope setups used in this study, it was not possible to resolve potential separation of lipid and mRNA fluorescent probes following endosomal rupture and cytosolic mRNA release.

LNP-mediated mRNA delivery and expression in embryonic zebrafish

To assess LNP-mediated delivery of functional mRNA within the embryonic zebrafish, it was first necessary to switch to unlabeled eGFP mRNA (capped, **Figure 3a**), as we consistently observed low mRNA expression levels using Cy5-labeled eGFP (capped) mRNA payloads. This alteration did not significantly

change the structure, surface charge or mRNA encapsulation efficiency of srLNPs (see **Supplementary Table 1**). At 1.5 hpi, srLNPs (~10 mM lipid, ~0.2 mg/kg mRNA) again associated with SECs and blood-resident macrophages within the PCV, CHT and CV of the embryonic zebrafish (**Figure 3b,c**). Given the intrinsic timeframe for mRNA delivery, expression and maturation of eGFP,[52, 53] low level green fluorescence observed at 1.5 hpi, within the yolk sac and iridophores (pigment cells) of the embryo, can be attributed to embryo autofluorescence in the GFP channel.[54] At 24 hpi, however, intense eGFP fluorescence was observed specifically within SECs and blood-resident macrophages of the embryo (**Figure 3d,e**). This timeframe is consistent with reported eGFP-mRNA delivery and expression timeframes using analogous lipid-based delivery systems,[52] whereby the onset of eGFP maturation and fluorescence (*in vitro)* occurs 2-7 h post-incubation and expression levels (fluorescence intensity) continually increase up to 24 h post-treatment.[55] Within *stab1*$^{-/-}$*/stab2*$^{-/-}$ KO embryos, srLNP-mediated eGFP expression, at 24 hpi, was observed only within blood-resident macrophages and not SECs, confirming macrophage uptake of srLNPs, as for other anionic nanoparticles, is not dependent on Stabilin receptors (**Supplementary Figure 3**).

For srLNPs, the exogenous eGFP expression pattern mirrored srLNP biodistribution at 1.5 hpi (**Figure 2e,f**), confirming successful transport, uptake and cytosolic delivery of functional mRNA within these cells. This is particularly remarkable given SECs have one of the highest endo/lysosomal activities of any cell type in the body,[28, 33] and are therefore primed to breakdown fragile RNA molecules. Endosomal escape and cytosolic delivery of RNA is widely recognized as one of the major obstacles in the development of effective RNA therapies,[56] with <2% of internalized siRNA (complexed within LNPs based on the lipid composition of Onpattro®) reaching the cytoplasm of HeLa cells *(in vitro)* and hepatocytes *(in vivo)*.[57, 58] Indeed, the acute extent of mRNA degradation within SECs (as well as potential mRNA degradation in circulation), was, in part, confirmed by injection (*i.v.*) of free eGFP-mRNA (capped; both cy5-labeled and unlabeled) within the zebrafish embryo. This resulted in no significant expression of eGFP within SECs at 24 hpi despite extensive accumulation within these cells at 1.5 hpi (presumably *via* scavenger receptor-mediated uptake of circulating, polyanionic RNA)[59] (**Supplementary Figure 4**).

In the case of DSPC-LNP (~10 mM lipid, ~0.2 mg/kg mRNA) mediated mRNA delivery, widespread eGFP fluorescence was observed throughout the wildtype embryo at 24 hpi (**Supplementary Figure 5**). Combined with the evident lack of cellular accumulation at 1.5 hpi (**Figure 2c,d**), this indicates low-level, non-

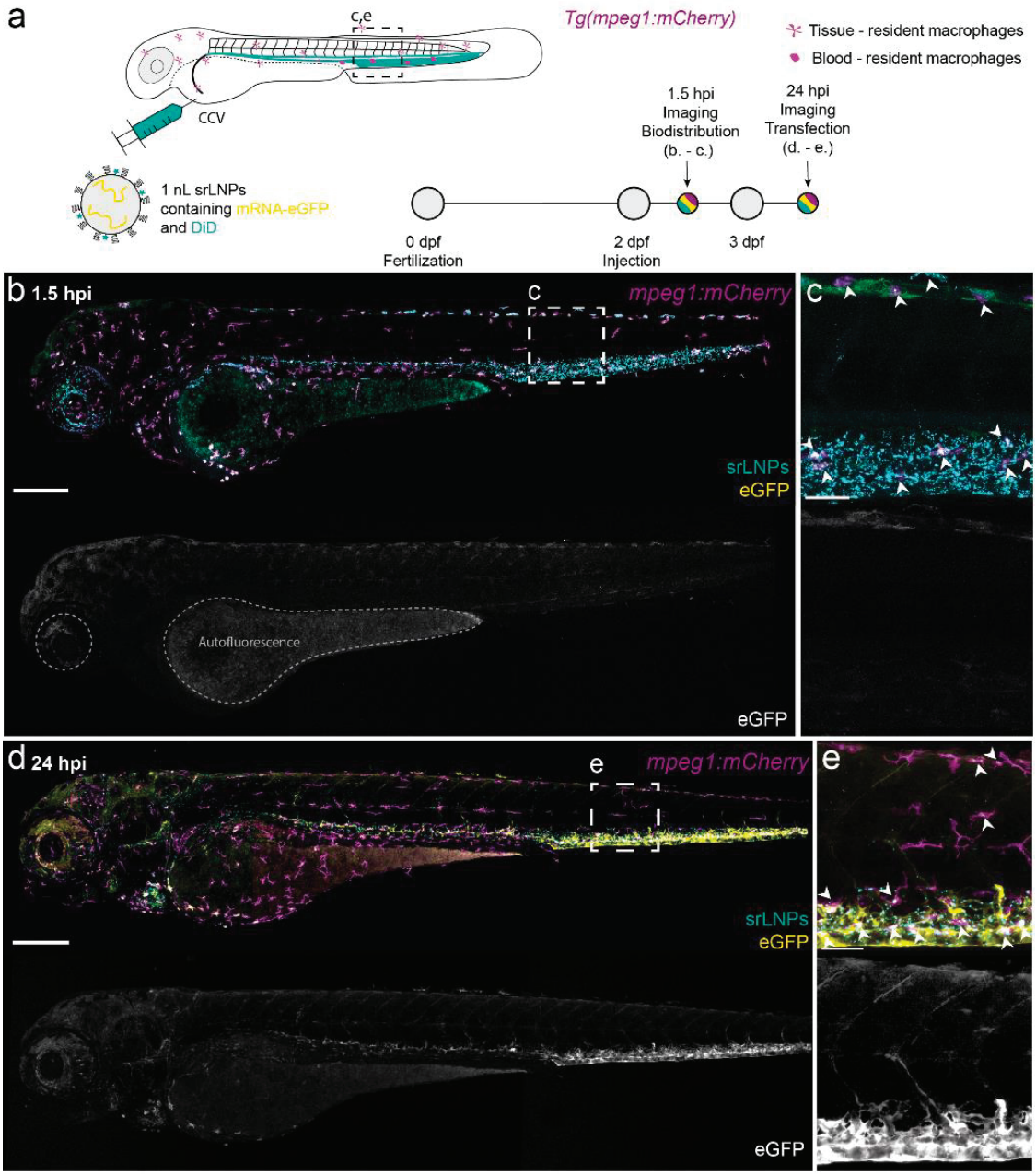

Figure 3. srLNP biodistribution, eGFP-mRNA delivery and eGFP expression within *mpeg1:*mCherry transgenic zebrafish embryos at 1.5 and 24 hpi. (a) Schematic showing the site of srLNP injection (*i.v.*) within embryonic zebrafish (2 dpf) and imaging timeframe. srLNPs contained DiD (cy5, 0.1 mol%) as fluorescent lipid probe and unlabeled, eGFP mRNA (capped) payload. Injected dose: ~10 mM lipid, ~0.2 mg/kg mRNA. Injection volume: 1 nl. Tg*(mpeg1*:mCherry*)* zebrafish embryos stably express mCherry (magenta) within all macrophages**. (b,c)** Whole embryo (10x magnification) and tissue level (40x magnification) views of srLNP biodistribution and eGFP expression within the embryonic zebrafish at 1.5 hpi. srLNPs were associated with SECs and blood resident macrophages (white arrowheads) within the PCV, CHT and CV of the embryo. Low level autofluorescence in the GFP channel is highlighted within the yolk sac and pigment cells of the embryo. **(d,e)** Whole embryo and tissue level views of srLNP

biodistribution and eGFP expression within the embryonic zebrafish at 24 hpi. At this timepoint, srLNPs remain associated with SECs and blood resident macrophages (white arrowheads) within the PCV, CHT and CV of the embryo. However, intense eGFP expression was now observed specifically within the PCV, CHT and CV confirming successful cytosolic delivery and translation of functional eGFP mRNA within SECs and blood resident macrophages. Scale bars: 200 μm (whole embryo) and 50 μm (tissue level).

specific cellular uptake of LNPs, based on the lipid composition of Onpattro®, with concurrent mRNA expression across a broad range of cell types, including SECs and blood-resident macrophages. Importantly, however, at 2 dpf, the liver of the embryonic zebrafish has yet to develop.[60, 61] To assess *in vivo* LNP interactions with a functional liver system, and potentially corroborate reported hepatocyte targeting of Onpattro® in adult mammals, it was therefore necessary to switch to LNP injections in older zebrafish embryos.

Hepatocyte targeting and mRNA expression in older zebrafish embryos

From approximately 55 hours post-fertilisation (hpf), the liver of the embryonic zebrafish undergoes a dramatic growth phase. New intrahepatic blood vessels are formed, with blood circulation detected from 72 hpf,[62] and the localised expression of key hepatocyte markers, including transferrin (Tf)[63] and liver fatty acid binding protein (L-FABP),[64] evidently marking maturation of functional hepatoctyes. During this growth phase, anatomical features, characteristic of the mammalian liver, and important for the correct processing of lipid nanoparticles, also emerge, including a Space of Disse,[65] the likely presence of a fenestrated endothelium,[66] and a functional biliary network (connected to the blood vasculature *via* hepatocytes).[60] These features, combined with a conserved repertoire of lipid transport proteins,[67, 68] including apoE, and lipoprotein receptors, including LDLR,[69, 70] suggest older (> 72 hpf) zebrafish embryos may offer an attractive *in vivo* model to assess endogenous lipid transport mechanisms, including lipid processing disorders,[71] and mechanistically probe their prospective role in the fate of LNPs in higher order mammalian systems.

To verify liver developmental timeframes, and to assess the suitability of the embryonic zebrafish as a predictive *in vivo* model for hepatocyte targeting of nanomedicines, non-PEGylated liposomes (~100 nm), co-formulated with cholesterol-conjugated, human apoE target peptides (Chol-NH-apoE peptide, 5 mol%,), were administered within 3 and 4 day old zebrafish embryos (*L-FABP:*eGFP transgenic line, stably expressing L-FABP-eGFP fusion proteins within hepatocytes) (**Figure 4a,b**).

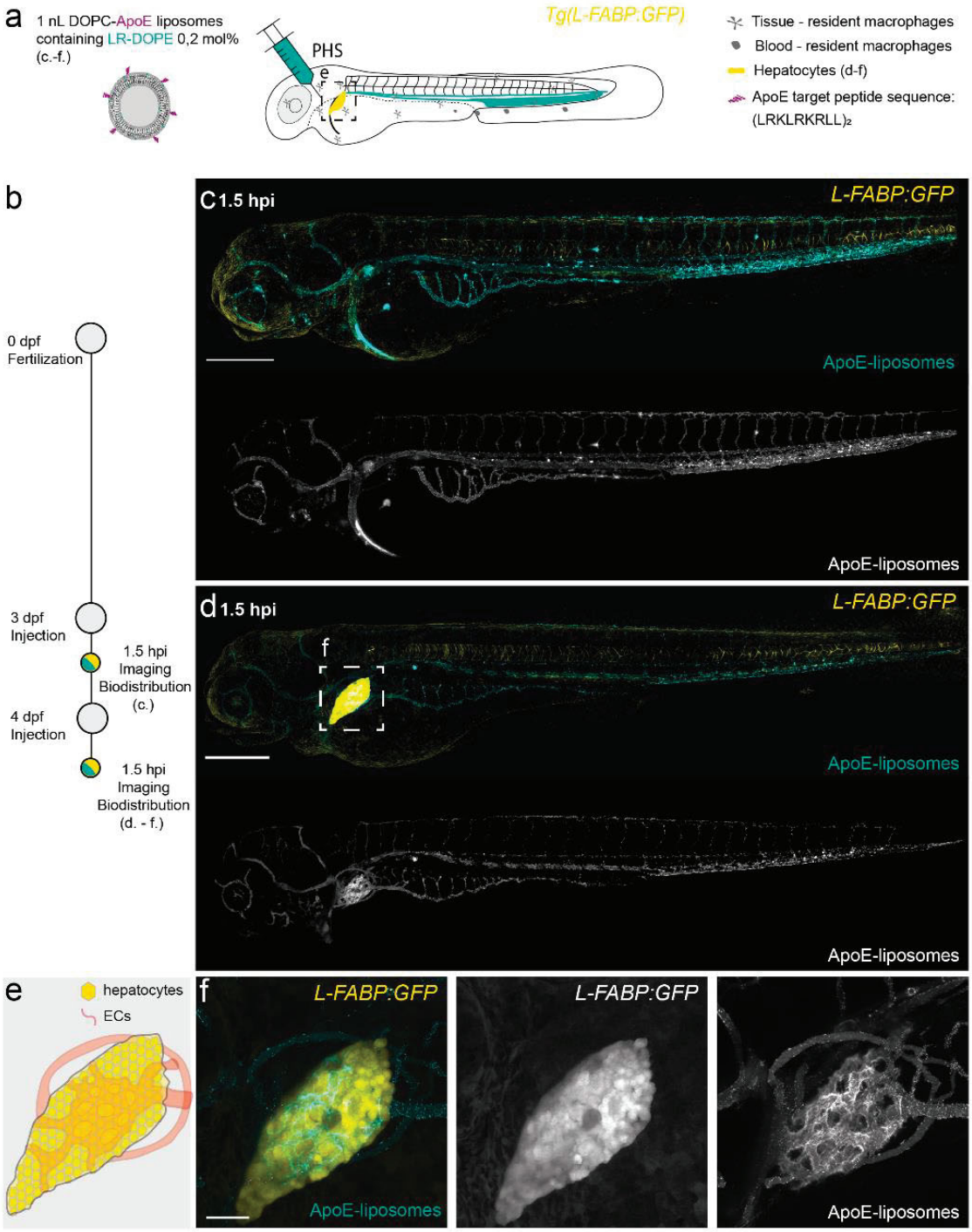

Figure 4. Biodistribution of apoE-targeted liposomes in three- and four-day old zebrafish embryos. (a) Schematic showing the site of apoE-targeted liposome injection (*i.v.*) within embryonic zebrafish (at 3 and 4 dpf). Liposomes contained 0.2 mol% DOPE-LR as fluorescent lipid probe (cyan). Injected dose: ~5 mM lipid, ~5 mol% ApoE target ligand (amino acid primary sequence: $(LRKLRKRLL)_2$), Injection volume: 1 nl. Tg(*L-FABP:*eGFP) zebrafish embryos stably express eGFP (yellow) within hepatocytes. PHS – primary head sinus. **(b)** Injection and imaging timeframe**. (c,d)** Whole embryo (10x magnification) views of apoE-targeted liposome biodistribution within **(c)** three- and **(d)**

four-day old embryonic zebrafish at 1.5 hpi. **(e)** Tissue level schematic of the embryonic liver at 4 dpf**. (f)** Tissue level (40x magnification) views of apoE-targeted liposome biodistribution within the liver of a four-day old embryo. Within the embryonic liver, liposomes appear predominantly associated with ECs and not hepatocytes. Scale bars: 200 μm (whole embryo) and 50 μm (tissue level).

Nanoparticle/macromolecule-conjugated, human apoE target peptides (*amino acid sequence*: $(LRKLRKRLL)_2$; tandem-repeat LDLR target sequence (residues 159-167) of human apoE) have been previously shown to interact with LDLr, as well as the low-density lipoprotein receptor-related proteins, LRP1 and LRP2.[72-74] Following liposome (~5 mM) administration within a zebrafish embryo (3 dpf), no significant fluorescence (eGFP) was observed in the region of the developing liver and apoE-targeted liposomes were mostly freely circulating (**Figure 4c**). At 4 dpf, however, the liver of the embryo, delineated by transgenic eGFP-*L-FABP* fluorescence, became evidently present and *i.v.* administered apoE-targeted liposomes now clearly accumulated within the liver vasculature (**Figure 4d-f**). Interestingly, at 1.5 hpi, we observed no significant colocalization of apoE-targeted liposomes and hepatocytes within the liver. This may be due to liposome stockpiling within the Space of Disse, as has also been described for the hepatic clearance of albumin within embryonic zebrafish (12 dpf).[66] Crucially, however, unmodified DOPC liposomes did not accumulate within the embryonic liver of either a three- or four-day old embryo, confirming liver accumulation of apoE-targeted liposomes within a four-day old zebrafish embryo is exclusively mediated by apoE target peptides (**Supplementary Figure 6**). Overall, these observations corroborate the reported timeframe for both hepatic development and hepatocyte maturation within the zebrafish embryo and confirm apoE-mediated targeting of nanoparticles to the liver of the zebrafish embryo is possible from 4 dpf.

Having verified apoE-mediated liver targeting of liposomes, we next injected DSPC-LNPs (~10 mM, ~0.2 mg/kg mRNA, Figure 5a-e; ~30 mM, ~0.6 mg/kg mRNA, **Figure 5f-i**) and srLNPs (~30 mM, ~0.6 mg/kg mRNA, **Supplementary Figure 7**) in four day old zebrafish embryos. In the case of srLNPs, particles remained largely associated within the PCV, CV and CHT of the 4 day old embryo at 1.5 hpi, and exogenous eGFP expression was primarily restricted within ECs of these venous blood vessels at 24 hpi. No significant srLNP accumulation (at 1.5 hpi) or mRNA expression (at 24 hpi) was observed within the liver, confirming RES targeting of srLNPs remains predominant even in the presence of a functional liver system and functional hepatocytes. In the case of DSPC-LNPs (~10 mM), no significant LNP liver accumulation (1.5 hpi) nor liver specific eGFP

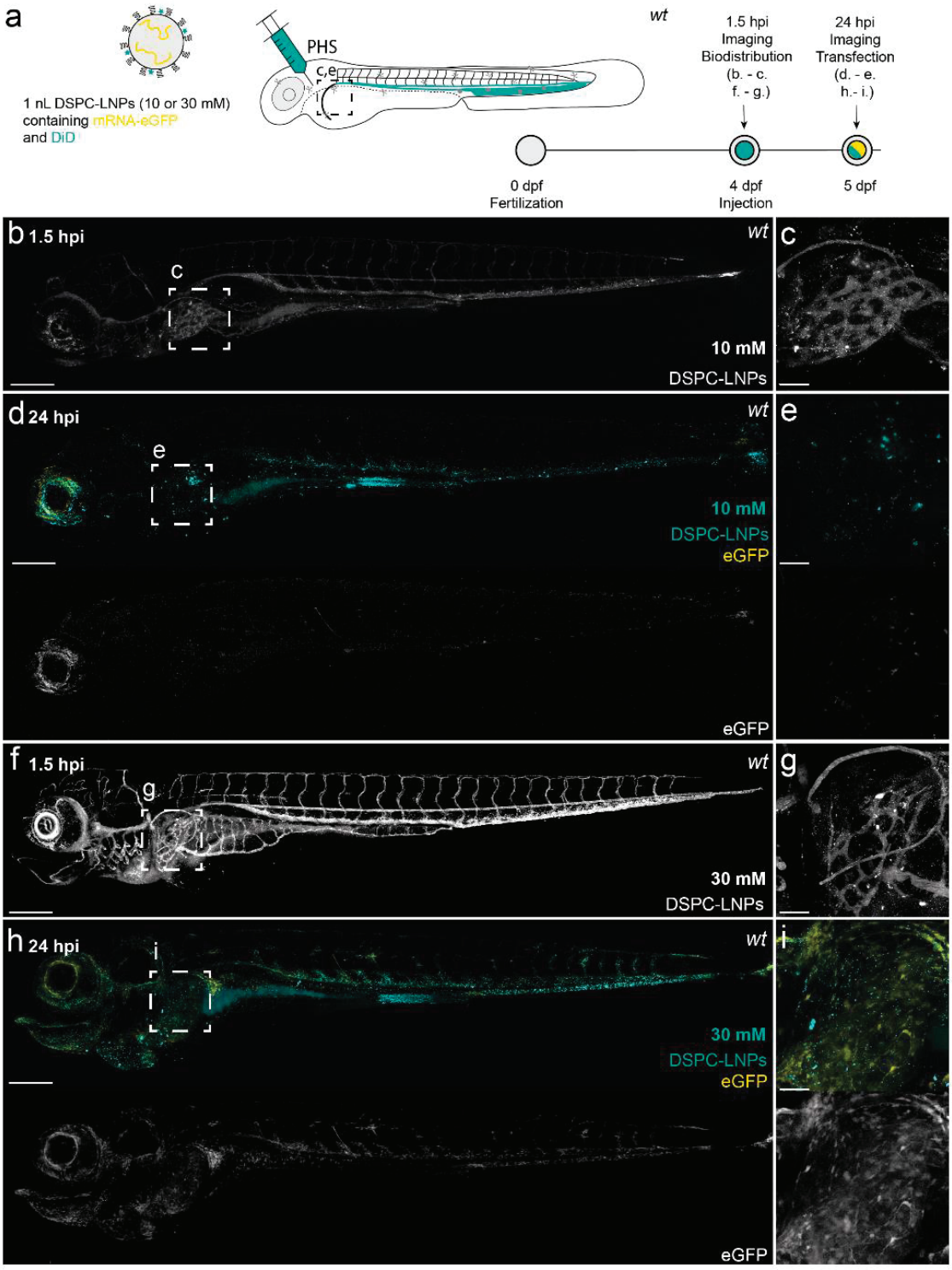

Figure 5. DSPC-LNP (10 and 30 mM) biodistribution and mRNA expression within, four-day old, wildtype (AB/TL) embryonic zebrafish. (a) Schematic showing the site of DSPC-LNP injection (*i.v.*) within embryonic zebrafish (4 dpf). DSPC-LNPs contained DiD (0.1 mol%) as fluorescent lipid probe and unlabeled, eGFP mRNA (capped) payload. Injection and imaging timeframe. Injection volume: 1 nL. PHS – primary head sinus. **(b,c)** Whole embryo (10x magnification) and tissue level (liver region, 40x magnification) views of DSPC-LNP biodistribution at 1.5 hpi. Injected dose: ~10 mM lipid, ~0.2 mg/kg

mRNA. LNPs were mostly freely circulating with no significant accumulation in the liver at 1.5 hpi. Intense fluorescent punctae within the liver region are likely due to macrophage uptake. **(d,e)** Whole embryo (10x magnification) and tissue level (liver region, 40x magnification) views of eGFP expression at 24 hpi. **(f,g)** Whole embryo (10x magnification) and tissue level (liver region, 40x magnification) views of DSPC-LNP biodistribution at 1.5 hpi. Injected dose: ~30 mM lipid, ~0.6 mg/kg mRNA. At both dosages, LNPs were mostly freely circulating with no significant accumulation in the liver observed at 1.5 hpi. Intense fluorescent punctae within the liver region are likely due to macrophage LNP uptake. **(h,i)** Whole embryo (10x magnification) and tissue level (liver region, 40x magnification) views of eGFP expression at 24 hpi. At 30 mM dosage, low level eGFP fluorescence is observed throughout the embryo, including within the liver region. Confocal microscope settings were identical across all experiments. Scale bars: 200 μm (whole embryo) and 50 μm (tissue level).

expression (24 hpi) was observed within the four day old embryo (**Figure 5b-e**). Increasing the dose threefold (~30 mM), however, did result in significant eGFP expression throughout the entire embryo, including the region of the liver (**Figure 5f-i**). Again, with no apparent targeting of DSPC-LNPs within the liver at 1.5 hpi, these observations indicate that DSPC-LNPs ineffectively target functional hepatocytes of the embryonic zebrafish *via* endogenous apoE-mediated lipid trafficking pathways and are instead liable to low-level non-specific uptake, with concurrent mRNA delivery and expression across a wide range of cell types.

LNP-mediated mRNA delivery and expression in mice

Having demonstrated RES specific mRNA transfection in embryonic zebrafish, we finally validated LNP biodistribution and LNP-mediated mRNA expression patterns in (young) adult mice. In particular, we focused on cell-specific LNP distribution and mRNA expression within the murine liver, the largest RES organ in mammals. For all mice experiments, LNP-mRNA formulations were injected (*i.v.*) in C57BL/6 mice (**Figure 6a**). To assess LNP distribution and functional mRNA delivery within individual hepatic and non-hepatic (*i.e.* spleen) RES cell types following *i.v.* administration, mice were anesthetized, a trans-cardiac collagenase perfusion performed, (parenchymal and non-parenchymal hepatic) cells separated, and individual cell types detected using cell-specific antibodies (**Supplementary Figure 8** for representative flow cytometry density plots). To monitor LNP biodistribution across RES cell types and tissues, LNP-mRNA formulations, containing a non-exchangeable, fluorescent lipid probe (DiD, 0.5 mol%), were administered (**Figure 6b**). At 2 hpi, for both DSPC- and srLNPs (42.75 mg/kg total lipid), we observed striking LNP accumulation within mouse liver cell types (**Figure 6c**) compared to those of the spleen (**Supplementary**

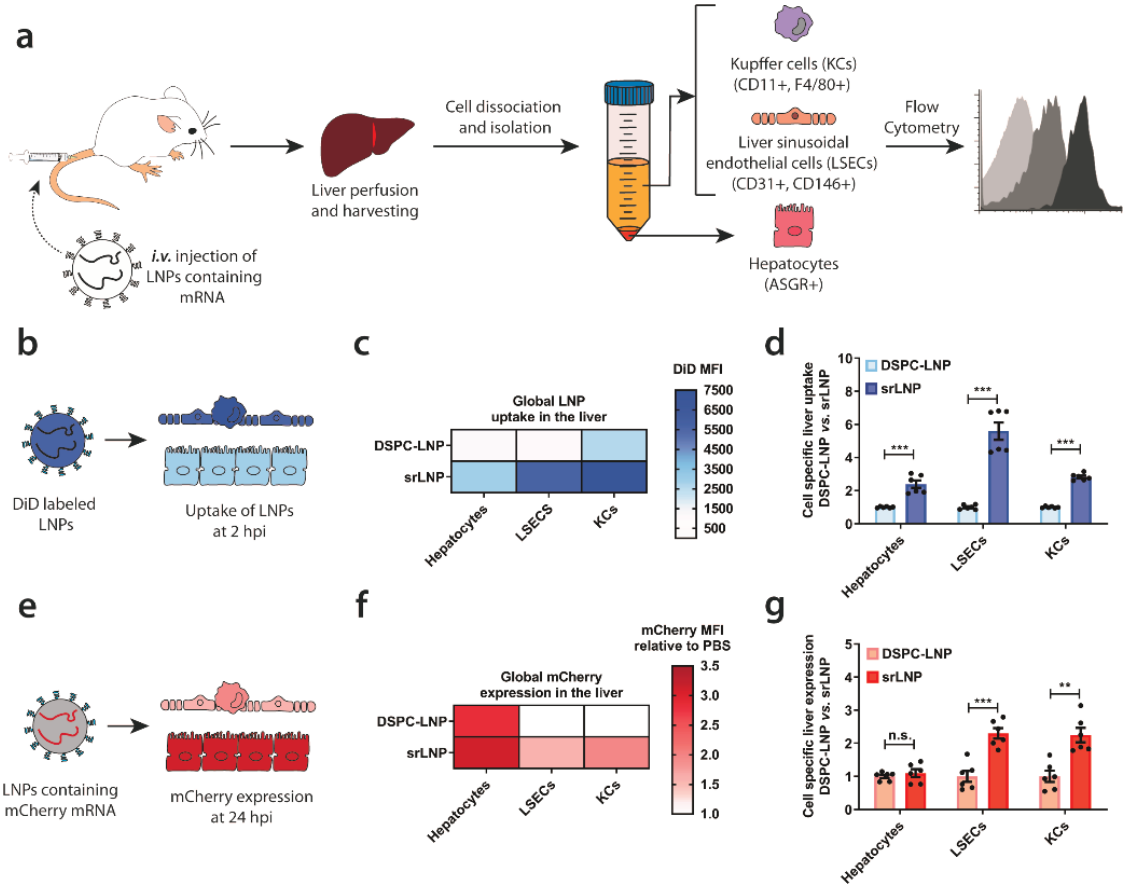

Figure 6. LNP uptake and functional mRNA delivery within different hepatic cell types. (a) Schematic illustrating the procedure to isolate different hepatic cell types and determine LNP-mRNA targeting and functional mRNA delivery. Following intravenous LNP-mRNA injection (*i.v.*) the liver was perfused with collagenase IV, hepatic cells were isolated and stained with specific antibodies, and flow cytometry was used to analyze LNP uptake and gene expression. Specific antibody markers used to uniquely identify hepatocytes, LSECs and KCs, respectively, are defined in parentheses. **(b)** For intrahepatic biodistribution studies, LNPs contained DiD (0.5 mol%) as fluorescent lipid probe. Cellular uptake of DSPC-LNP and srLNP was assessed following mouse sacrifice at 2 hpi. Injected dose: 42.75 mg/kg total lipid. **(c)** Heatmap of global LNP uptake in the liver determined by absolute DiD fluorescence. srLNP demonstrate significantly enhanced LNP uptake within all hepatic cell types, and significant re-direction to hepatic RES compared to DSPC-LNPs**. (d)** Cell specific liver uptake normalized to DSPC-LNP for each cell type**. (e)** For gene expression experiments, LNPs contained capped, mCherry-mRNA. Functional mRNA delivery was assessed based on mCherry fluorescence levels following mouse sacrifice at 24 hpi**. (f)** Heatmap of mCherry expression in different liver cell types following functional mRNA delivery using DSPC-LNP and srLNP. Injected dose: 0.25 mg/kg mRNA. **(g)** Cell specific mCherry expression normalized to DSPC-LNP for each cell type. In all cases, n=6 represents 3 separate liver tissue samples from 2 mice sorted into individual cell types. Bars and error bars in **d** and **g** represent mean ± s.e.m. The data was normalized to the average uptake and expression of DSPC-LNPs within each cell type. Statistical significance was evaluated using a two-tailed unpaired Student's t-test. n.s.= not significant, ** $p < 0.01$, *** $p < 0.001$. Exact P values for **d**: Hepatocytes P= 0.00011, LSECs P= $1.12*10^{-5}$, KCs P= $3.62*10^{-9}$. Exact P values for **g**: Hepatocytes P= 0.464, LSECs P= 0.00064, KCs P= 0.0023.

Figure 9), which although smaller than the liver is a highly efficient unit of the mononuclear phagocyte system.[75] Notably, both LNP formulations distributed to all individually isolated cell types within the liver, as has previously been described for LNP formulations based on Onpattro®.[76, 77] However, srLNPs demonstrated significantly enhanced uptake ($P < 0.001$) within all liver cell types relative to DSPC-LNPs (**Figure 6d**). This confirmed that incorporating anionic DSPG into LNP-mRNA delivery systems not only enhances liver tropism in general but also leads to a significant shift towards LNP targeting and cellular uptake within hepatic RES cell types.

To confirm functional mRNA delivery to hepatic RES cells, LNPs entrapping capped mCherry-mRNA (0.25 mg/kg mRNA) were administered in C57BL/6 mice (**Figure 6e**). This dosage is in line with other systemically administered LNP-mRNA therapies, including those currently in clinical trials (*e.g.* NCT03829384).[78] Following organ isolation and cell separation at 24 hpi, both srLNPs and DSPC-LNPs yielded comparable mCherry protein expression in hepatocytes, as well as within splenic RES cell types (**Figure 6f** and **Supplementary Figure 9**). In contrast, srLNPs yielded significantly enhanced functional mRNA delivery to hepatic RES cell types relative to DSPC-LNPs ($P < 0.001$) (**Figure 6g**). Importantly, for both srLNPs and DSPC-LNPs, absolute mCherry expression levels within hepatocytes were significantly higher than any other cell type analyzed. This apparent disparity between LNP cellular targeting and functional mRNA expression is likely explained, at least in part, by the adverse (high) endosomal activity within LSECs and KCs (leading to significant mRNA degradation despite extensive LNP internalization), combined with the extremely high translational proficiency of hepatocytes (leading to significant mRNA expression despite comparably low LNP internalization).[79] Interestingly, a four-fold dosage increase (1 mg/kg mRNA) resulted in significantly enhanced absolute mRNA expression within LSECs relative to hepatocytes and KCs, indicative perhaps of dynamic competition between these cell types in recognizing and internalizing LNPs (**Supplementary Figure 10**). Given no LNP technology has yet demonstrated exclusive targeting to a single cell type *in vivo*, these findings reaffirm the importance of considering not only LNP biodistribution but also cellular physiology (both in the healthy and diseased state) in the development of new LNP technologies with novel targeting function.

Overall, our data confirm that charge modifications to an LNP surface leads to preferential targeting of the hepatic RES and a significant increase in the absolute levels of functional mRNA expression within these cell types.

6.4 Discussion and Conclusion

Founded on prior knowledge of the fundamental mechanisms of anionic nanoparticle clearance *in vivo*,[36] (**Chapter 1 & 2**) we develop an LNP platform capable of preferentially targeting the hepatic RES, leading to enhanced mRNA expression within hepatic RES cell types. Given the importance of the hepatic RES in establishing and maintaining the liver microenvironment, as well as the pathogenesis of many liver,[26, 80] blood and (auto)immune diseases,[35] it is our belief that anionic LNP formulations should form the basis of future RNA gene therapies, against acquired and inherited diseases in which hepatic RES cell types play a central role.[34] Here, it is also important to recognize the extensive refinement of both ionizable[81-83] and sterol lipid components of LNPs[50] (primarily to promote endosomal rupture/escape and cytosolic RNA delivery), as well as chemical modifications to RNA (to improve stability, translation proficiency and reduce immunogenicity), that have already been made.[84-86] Incorporated within LNPs, these reagents can improve transfection efficiency >10-fold, compared to LNP systems based on the lipid composition of Onpattro®.[81, 82] These reagents are fully transferable to anionic, srLNP formulations and, if necessary, could be retrofitted to widen any potential therapeutic window.

Existing LNP technologies that have demonstrated preferential RNA delivery to non-parenchymal hepatic cell types and/or non-hepatic cells. Importantly, these technologies have all been discovered through bottom-up empirical screens and have not revealed the biological mechanisms underpinning any observed cellular preference. Preferential delivery of mRNA to liver ECs has, for example, been achieved through replacement of cholesterol with either cholesteryl oleate or oxidized cholesterol components.[18, 19] While these observations may conform to a charge-dependent, Stabilin-mediated mechanism of uptake within LSECs, as has been observed for both OxLDL and AcLDL,[27, 87] in the absence of reported zeta potentials and given both sterol reagents likely predominate within the LNP core, this may equally point to an alternative, viable mechanism of LNP recognition and uptake within hepatic RES cell types. Alternatively, exclusive LNP-mediated RNA delivery to the spleen has been achieved through the addition of the anionic phospholipid, 18PA (up to 30 mol%), added to the lipid composition of Onpattro®.[88]

Assuming the measured surface charge of these formulations is also anionic (and given srLNPs showed negligible accumulation within the spleen), this suggests

simply rendering an LNP anionic does not necessarily guarantee preferential uptake within hepatic RES cell types. Overall, these studies highlight the complex interplay between LNP compositional makeup, biophysical properties and structure, and the implications these factors have in determining the fate of an LNP *in vivo*. Given the vast exploitable chemical space of an LNP, the targeting of innate immune cells and hepatocytes – primed to recognize and internalize waste and/or pathogenic (lipid) particles – may therefore reflect the low-hanging fruit of preferential LNP tropisms. Therefore, the discovery of new LNP platforms capable of preferential targeting beyond RES cells and/or hepatocytes will likely benefit from a more focused and informed screening approach.

To this end, the elucidation and exploitation of the fundamental mechanisms dictating both endogenous and exogenous lipid particle fate *in vivo* can focus and direct empirical screens for novel LNP formulations. It is worth emphasizing that all cells rely, to some extent, on systemic lipid transport to ensure correct function. In light of this, we believe the embryonic zebrafish is a powerful addition to the discovery pipeline for new LNP technologies, both as a screening platform and as a tool to probe fundamental biology. As a screening and optimization tool, zebrafish embryos permit real-time, *in vivo* visualization of total LNP injected doses at cellular resolution. Furthermore, with a conserved repertoire of RES cell types, hepatocytes, soluble lipid transport proteins and receptors, the data acquired within these animals can offer qualitative predictions of cell specific LNP recognition and uptake within key mammalian RES organs. Furthermore, up to 5 dpf, the number of different LNP formulations that can be screened is limited only by practical considerations of time and capacity. As a fundamental tool to elucidate biological mechanisms underpinning LNP transport and RNA delivery, the short generational time of the zebrafish (approx. 3 months), the extensive repertoire of established (fluorescent) transgenic lines and antibodies,[89, 90] optimized techniques for genetic manipulation (including CRISPR/Cas9)[91] and advanced imaging techniques, enable key nano-bio interactions underpinning LNP fate *in vivo* to be comprehensively assessed and rapidly confirmed.

In conclusion, the widespread evaluation of LNP-based mRNA therapies as potential prophylactic vaccines,[92, 93] most notably against COVID-19,[94-97] has provided further proof of the broad therapeutic potential of these platform mRNA technologies. However, despite the obvious differences in therapeutic target, mode of action and injection site, all LNP-mRNA vaccine candidates closely resemble the lipid composition of Onpattro®. In particular, LNP surface lipids (*i.e.* "helper" phospholipids and PEG lipids), cholesterol content and overall

lipid composition are strikingly similar between different clinical formulations. Based on our observations, these vaccine candidates can be expected to elicit broad mRNA expression profiles. Indeed, following intramuscular (*i.m.)* injection of an LNP-mRNA COVID-19 vaccine candidate, mRNA (coding for the receptor binding domain (RBD) of SARS-CoV-2) expression was observed across a broad spectrum of cell types, including intramuscular and hepatic immune cells, as well as hepatocytes.[94] However, while the ability to leverage a wide array of cell types to produce a therapeutic protein may be safe and effective as a systemic secreted therapy (*i.e.* suitable for vaccine applications), the lack of LNP designs capable of preferentially delivering RNA to specific diseased cells and tissues in the body remains a major limitation. Although cell specificity, and therefore therapeutic windows, of LNP-mRNA systems can be enhanced, for example, through microRNA regulation of mRNA expression,[98] these technologies still rely on LNPs reaching and delivering functional mRNA within target cells at therapeutically relevant doses. To this end, we believe a top-down approach to LNP discovery, based on pre-existing knowledge of the nano-bio interactions, can guide and focus (high throughput) empirical screening. This will expedite the discovery of new LNP designs with inherent tropisms for specific and varied cell types.

6.5 Materials and Methods

Materials and Reagents

Dimethylformamide (DMF), piperidine, acetic anhydride, pyridine, trifluoroacetic acid (TFA) and acetonitrile (MeCN) were purchased from Biosolve (Valkenswaard, The Netherlands). N,N-diisopropylethylamine (DIPEA), and Oxyma were obtained from Carl Roth GmbH & Co (The Netherlands). Dichloromethane (DCM) and diethyl ether were supplied by Honeywell (Amsterdam, The Netherlands). Fmoc-Rink Amide AM resin was obtained from IRIS Biotech GmbH (Marktredwitz, Germany). All amino acids were supplied by NovaBioChem, (Zwijndrecht, The Netherlands), a subsidiary of Merck. 1,2-distearoyl-*sn*-glycerol-3-phosphocholine (DSPC), 1,2-distearoyl-*sn*-glycero-3-phospho-(1'-rac-glycerol) (DSPG), 1,2-dioleyl-*sn*-glycerol-3-phosphocholine (DOPC) and 1,2-dimyristoyl-rac-glycero-3-methoxypolyethylene glycol-2000 (DMG-PEG2k) were purchased from Avanti Polar Lipids (Alabaster, AL, US) or Lipoid GmbH (Ludwigshafen, Germany). All other chemicals were purchased from Merck (Zwijndrecht, The Netherlands). (6Z,9Z,28Z,31Z)-heptatriaconta-6,9,28,31-tetraen-19-yl-4-(dimethylamino) butanoate (DLin-MC3-DMA) was synthesized as described.[99] 3-azido-5-cholestene (**1**) was synthesized as

described.[100] CleanCap eGFP (5moU) mRNA, CleanCap mCherry (5moU) mRNA and CleanCap Cyanine 5 eGFP (5moU) mRNA were purchased from TriLink Biotechnologies (San Diego, CA) or Tebu-bio (Heerhugowaard, The Netherlands).

Liposome Formulation

DOPC liposomes (with and without incorporated Chol-NH-ApoE-peptide, 5 mol%) were formulated in 20 mM HEPES buffer (pH = 7.3) at a total lipid concentration of 5 mM. DOPC and Chol-NH-ApoE-peptide, as stock solutions in chloroform (10mM), were combined to the desired molar ratios and dried to a film, first under a stream of N_2 followed by the removal of trace solvents *in vacuo* for >1 h. Lipid films were hydrated and large unilamellar vesicles formed through extrusion at room temperature (Mini-extruder, Avanti Polar Lipids, Alabaster, US). Hydrated lipids were passed 11 times through a 100 nm polycarbonate (PC) membrane (Nucleopore Track-Etch membranes, Whatman). All liposome dispersions were stored at 4^{o}C and used within 2 days.

Lipid Nanoparticle (LNP) Formulation

Lipid nanoparticles entrapping mRNA were formulated as previously described.[5] In brief, lipid components (MC3, cholesterol, DSPC or DSPG, and PEG-lipid) were dissolved in ethanol. For biodistribution studies, the non-exchangeable tracer DiD or DOPE-LR was added to lipid mixtures at a concentration of 0.1 mol% or 0.2 mol% respectively. The mRNA was dissolved in 25 mM sodium acetate or sodium citrate buffer (pH 4). The two solution were rapidly mixed (N/P ratio of 6) using a T-junction mixer (total flow rate of 20 mL/min, flow rate ratio of 3:1 v/v). The resulting LNP formulation was dialyzed overnight against PBS (pH 7.4), sterile filtered, and concentrated using 10K MWCO centrifugal filters (Amicon® Ultra, Merck). Entrapment efficiency and mRNA concentration were analyzed using the Quant-iT Ribogreen RNA assay (Life Technologies, Burlington, ON). Total lipid concentrations were measured using the Cholesterol E Total-Cholesterol assay (Wako Diagnostics, Richmond, VA). mRNA doses within embryonic zebrafish were calculated using an estimated average weight of 1 mg per embryo, independent of developmental stage, and an injection volume of 1 nl.

LNP and liposome biophysical characterization

LNP and liposome sizes and zeta potentials were measured using a Malvern Zetasizer Nano ZS (software version 7.13, Malvern Panalytical). For DLS (operating wavelength = 633 nm), measurements were carried out at room temperature in 20 mM HEPES buffer (pH = 7.3) for liposomes, and in 1x PBS (pH = 7.4) for LNPs, at a total lipid concentration of approx. 100 µM. Zeta potentials were measured at 500 µM total lipid concentration, using a dip-cell electrode (ZEN1002, Malvern) for liposomes and in a folded capillary cell (DTS1070, Malvern) for LNPs, at room temperature. All reported DLS measurements and zeta potentials are the average of three measurements.

CryoTEM Imaging and Quantification

Vitrification of concentrated (~10 mM) LNPs was performed using a Leica EM GP operating at 21°C and 95% RH. Sample suspensions were placed on glow discharged 100 µm lacey carbon films supported by 200 mesh copper grids (Electron Microscopy Sciences). Optimal results were achieved using a 60 second pre-blot and a 1 second blot time. After vitrification, sample grids were maintained below −170 ◦ C and imaging was performed on a Tecnai T12 (ThermoFisher) with a biotwin lens and LaB6 filament operating at 120 keV equipped with an Eagle 4K x 4K CCD camera (ThermoFisher). Images were acquired at a nominal underfocus of -2 to -3 µm (49,000× magnification) with an electron dose of ~2000 e^{-}·nm^{-2}. Images were processed and particle size was quantified using the Fiji distribution of ImageJ.[101] For quantification, particle sizes were determined on particles present in amorphous vitrified water and obtained from a triplicate of assemblies (~150-200 particles per assembly per formulation). Generation of frequency distribution graphs was performed using GraphPad Prism (v 6.0).

Zebrafish Husbandry and Injections

Zebrafish (*Danio rerio*, strain *AB/TL*) were maintained and handled according to the guidelines from the Zebrafish Model Organism Database (http://zfin.org) and in compliance with the directives of the local animal welfare committee of Leiden University. Fertilization was performed by natural spawning at the beginning of the light period, and eggs were raised at 28.5 °C in egg water (60 µg/ mL Instant Ocean sea salts). In addition to wild-type (*AB/TL*) embryos, previously established Tg(*mpeg1*:mCherry)^{gl23} [102] and *stab2*^{ibl2}*stab1*^{ibl3} [51] (described in **Chapter 3**) zebrafish lines were also used in this study.

Fluorescently labelled LNPs were injected into 54-96 hours post fertilization (hpf) zebrafish embryos using a modified microangraphy protocol.[103] Embryos were anesthetized in 0.01% tricaine and embedded in 0.4% agarose containing tricaine before injection. To improve reproducibility of microangiography experiments, 1 nl volume were calibrated and injected into the common cardinal vein (2-3 dpf) or primary head sinus (4 dpf). A small injection space was created by penetrating the skin with the injection needle and gently pulling the needle back, thereby creating a small pyramidal space in which the liposomes or LNPs were injected. Successfully injected embryos were identified through the backward translocation of venous erythrocytes and the absence of damage to the yolk ball. Selected zebrafish embryos successfully injected were kept in egg water at 28.5 degrees until later imaging (1.5 or 24 hours post injection).

Zebrafish confocal imaging acquisition and processing

Zebrafish embryos were randomly picked from a dish of 10-30 successfully injected embryos to be imaged after 1.5 or 24 h post injection (hpi). Confocal z-stacks were captured on a Leica TCS SPE or SP8 confocal microscope, using a 10x air objective (HCX PL FLUOTAR), a 40x water-immersion objective (HCX APO L) or 63x water-immersion objective (HC PL APO CS). For whole-embryo views, 3 or 4 overlapping z-stacks were captured to cover the complete body. Laser intensity, gain and offset settings were identical between stacks and when comparing samples per experiment. Images were processed using the Fiji distribution of ImageJ.[101] Confocal image stacks (raw data) are available upon reasonable request.

Mouse husbandry, injection protocol and cell isolation

All mouse protocols were approved by the Canadian Animal Care Committee and conducted in accordance with relevant guidelines and regulations. Mice were maintained on a regular 12-hour light/12- hour dark cycle in a specific pathogen-free animal facility at UBC. C57Bl6 male mice aged between 8 to 10 weeks were used throughout. These mice were divided into groups of 2 and either received intravenous (*i.v*) injection of LNP-mRNAs (either DSPC-LNPs or srLNPs) or PBS as a negative control. For biodistribution studies, LNPs entrapping luciferase mRNA were labelled with 0.5 mol% DiD as fluorescent lipid marker. Injections were performed at 42.75 mg/kg total lipid and mice were sacrificed at 2 hpi. For gene expression studies, LNPs encapsulating mRNA coding for the fluorescent reporter gene mCherry were used, injections were performed at 0.25 mg/kg mRNA dose, and mice were sacrificed at 24 hpi. Mice were anesthetized using a

high dose of isofluorane followed by CO_2. Trans-cardiac perfusion was performed as follows: once the animals were unresponsive, a 5 cm medial incision was made through the abdominal wall, exposing the liver and heart. While the heart was still beating, a butterfly needle connected to a 30 mL syringe loaded with pre-warmed Hank's Balanced Salt Solution (HBSS, Gibco) was inserted into the left ventricle. Next, the liver was perfused with perfusion medium (HBSS, supplemented with 0.5 mM EDTA, Glucose 10 mM and HEPES 10 mM) at a rate of 3 mL/min for 10 min. Once liver swelling was observed, a cut was performed on the right atrium and perfusion was switched to digestion medium (DMEM, Gibco supplemented with 10% fetal bovine serum (FBS, Gibco) and 1% penicillin streptomycin (Gibco) and 0.8 mg/mL Collagenase Type IV, Worthington) at 3 mL/min for another 10 min. At the end of the perfusion of the entire system, as determined by organ blanching, the whole liver and spleen were dissected and transferred to 50 mL Falcon tubes containing 10 ml ice cold (4°C) perfusion media and placed on ice. Next, isolation of hepatic cell types (*i.e.* hepatocytes, Kupffer cells (KCs) and liver sinusoid endothelial cells (LSECs)) was performed following density gradient-based separation. Briefly, the liver was transferred to a Petri dish containing digestion medium, minced under sterile conditions, and incubated for 20 min at 37°C with occasional shaking of the plate. Cell suspensions were then filtered through a 40 µm mesh cell strainer to eliminate any undigested tissue remnants. Primary hepatocytes were separated from other liver residing cells (LRCs) by low-speed centrifugation at 500 rpm with no brake. The supernatant containing mainly LRCs was pelleted using low speed (3000 rpm) centrifugation at 4°C, aliquoted and washed twice with ice cold PBS containing 2% FBS. The pellet containing mainly hepatocytes was collected, washed at low speed and placed on ice. Phenotypic detection using monoclonal antibodies, assessment of LNP delivery and mRNA expression on liver cells was performed immediately after isolation to avoid changes in gene regulation, polarization and dedifferentiation.[104] LNP biodistribution across individual RES cell types of the spleen (*i.e.* endothelial cells and macrophages) were also characterized. Here, the spleen was also dissected and placed into a 40 µm mesh cell and mashed through the cell strainer into the petri dish using the plunger end of the syringe. The suspended cells were transferred to a 15 mL Falcon tube and centrifuged at 1000 rpm for 5 minutes. The pellet was resuspended in 1 mL ACK lysis buffer (Invitrogen) to lyse the red blood cells, aliquoted in FACS buffer and stained with antibodies as described below to identify splenic endothelial cells and macrophages.

FACS analysis

Cell aliquots were resuspended in 300 µl FACS staining buffer (FBS 2%, Sodium Azide 0.1% and ethylenediaminetetraacetic acid (EDTA 1mM)) followed by staining with fluorescence tagged antibodies. Prior to staining, cells were first labeled with anti-mouse CD16/CD32 (mouse Fc blocker, Clone 2.4G2) (AntibodyLab, Vancouver, Canada) to reduce background. Hepatocytes were detected following staining with primary mouse antibody detecting ASGR1 (8D7, Novus Biologicals) followed by goat polyclonal secondary antibody to mouse IgG2a labeled to PE-Cy7 (BioLegend). Kupffer cells were detected with CD11b – FITC or PE (Invitrogen) and F4/80high labeled to APC, endothelial cells with rabbit polyclonal CD31-PE-Cy7 (Abcam) and LSECs identified with CD146-VioBlue (Miltenyi Biotec) and CD31-PE-Cy7. Spleen macrophages and endothelial cells were detected using appropriate antibodies and identified as CD11bhigh and CD31+ve cells following antibody labeling as described. The data were acquired using a LSRII flow cytometer and the FACSDiva software and analyzed by FlowJo following acquisition of at least 10,000 events after gating on viable cell populations. LNP-mRNA delivery or transfection efficacy were assessed based on the relative mean fluorescence intensity of DiD or mCherry positive cells, respectively, measured on histograms obtained from gated cell populations.

6.6 Abbreviations

acLDL	acetylated low-density lipoprotein
apoE	apolipoprotein E
CCMV VLP	cowpea chlorotic mottle virus derived virus-like particles
CHT	caudal hematopoietic tissue
CryoTEM	cryo-electron transmission microscope
CCV	common cardinal vein
CV	cardinal vein
dpf	days post fertilization
DA	dorsal aorta
DLAV	dorsal longitudinal anastomotic vessel
DMG-PEG2k	1,2-dimyristoyl-rac-glycero-3-methoxypolyethyleneglycol-2k
DOPC	1,2-dioleyl-sn-glycerol-3-phosphocholine
DSPG	1,2-disteraroyl-*sn*-glycero-3-phospho-glycerol
DSPC	1,2-distearoyl-*sn*-glycero-3-phosphocholine
ECs	endothelial cells
fluoHA	fluorescently labeled hyaluronic acid
hpi	hour(s) post injection
i.m.	intramuscularly
ISV	intersegmental vessels
i.v.	intravenously
KCs	Kupffer cells
LDLR	low density lipoprotein receptor
L-FABP	liver fatty acid binding protein
LNPs	lipid nanoparticles
LRP	low-density lipoprotein receptor-related proteins
LSECs	liver sinusoidal endothelial cells
MPS	mononuclear phagocyte system
OxLDL	oxidized low-density lipoprotein
PCV	posterior cardinal vein
PHS	primitive head sinus
RES	reticuloendothelial system
RNAi	RNA interference
srLNPs	scavenger receptor lipid nanoparticles
SECs	scavenging endothelial cells
siRNA	silencing RNA
TTR	transthyretin

6.7 Supporting Information

Supplementary Table 1. Composition, size (as measured by DLS), polydispersity (PDI), surface charge (as measured by zeta potential), RNA encapsulation efficiency (as measured by RiboGreen assay) and reproducibility of all LNP and liposome formulations used in this study.

Formulation	mRNA	Fluorescent lipid	% of Fluorescent Lipid	Avg. Size (nm)	PDI	Zeta Potential (mV)	EE (%)	n
DSPC-LNP	eGFP	DOPE-LR	0.2	82.5 ± 2.0	0.085 ± 0.027	-5.5 ± 1.2	95 ± 2	3
srLNP	eGFP	DOPE-LR	0.2	89.2 ± 5.7	0.094 ± 0.023	-21.9 ± 2.5	88 ± 3	3
DSPC-LNP	eGFP	DiD	0.1	82.5 ± 3.4	0.081 ± 0.026	-4.1 ± 1.6	95 ± 1	3
srLNP	eGFP	DiD	0.1	94.7 ± 4.0	0.102 ± 0.016	-17.5 ± 2.4	91 ± 2	3
DSPC-LNP	eGFP	-	-	82.5 ± 4.0	0.103 ± 0.037	-4.0 ± 0.9	93 ± 1	2
srLNP	eGFP	-	-	86.6 ± 6.7	0.108 ± 0.006	-19.0 ± 1.1	91 ± 4	2
DSPC-LNP	mCherry	DiD	0.1	79.9 ± 5.2	0.072 ± 0.038	-3.7 ± 1.8	94 ± 3	2
srLNP	mCherry	DiD	0.1	92.7 ± 3.5	0.102 ± 0.012	-18.8 ± 2.1	89 ± 4	2
DSPC-LNP	Cy5-mRNA	DOPE-LR	0.2	87.0 ± 3.5	0.090 ± 0.016	-3.9 ± 0.9	95 ± 3	2
srLNP	Cy5-mRNA	DOPE-LR	0.2	94.1 ± 2.3	0.096 ± 0.01	-16.2 ± 1.2	91 ± 2	2
DOPC	-	DOPE-LR	0.2	96.3 ± 4.0	0.095 ± 0.011	-6.1 ± 1.1	-	2
DOPC+ApoE-peptide	-	DOPE-LR	0.2	104.7 ± 3.8	0.075 ± 0.012	14.7 ± 1.6	-	2

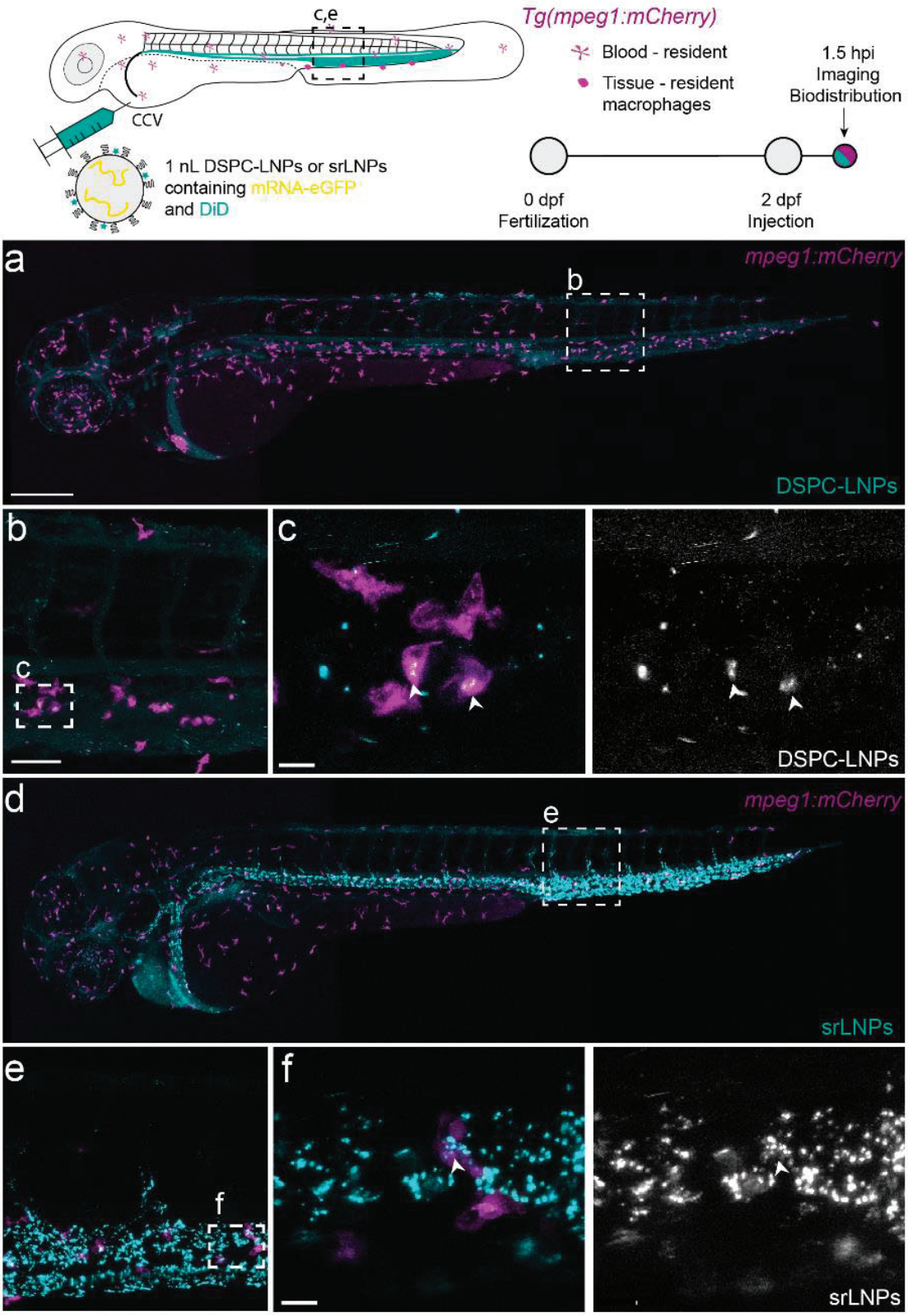

Supplementary Figure 1. Biodistribution of DSPC-LNPs and srLNPs in transgenic *mpeg1:*mCherry zebrafish embryos at 1.5 hpi. Schematic showing the site of LNP injection *(i.v)* within the embryonic zebrafish (2 dpf) and imaging timeframe. LNPs contained DiD (cy5, 0.1 mol%) as fluorescent lipid probe and unlabeled eGFP mRNA.

Tg(*mpeg1:*mCherry*)* zebrafish embryos stably expressing mCherry (magenta) within all macrophages. *Injected dose*: ~10 mM lipid, ~0.2 mg/kg mRNA. *Injection volume*: 1 nl. CCV, common cardinal vein **(a)** Whole embryo view (10x magnification), **(b)** tissue level view (40x magnification) and **(c)** a zoom of a projection of three confocal z-stacks, showing fluorescent co-localisation of DiD (LNP probe) and transgenic mCherry (white arrowheads), confirming low-level DSPC-LNP uptake within these cells. **(d)** Whole embryo view (10x magnification), **(e)** tissue level view (40x magnification) and **(f)** a zoom of a projection of three confocal z-stacks, showing fluorescent colocalisation of DiD (LNP probe) and transgenic mCherry (white arrowheads), confirming simultaneous uptake of srLNPs within both SECs and blood resident macrophages. Scale bars: 200 µm (whole body), 50 µm (tissue level), 10 µm (zoom).

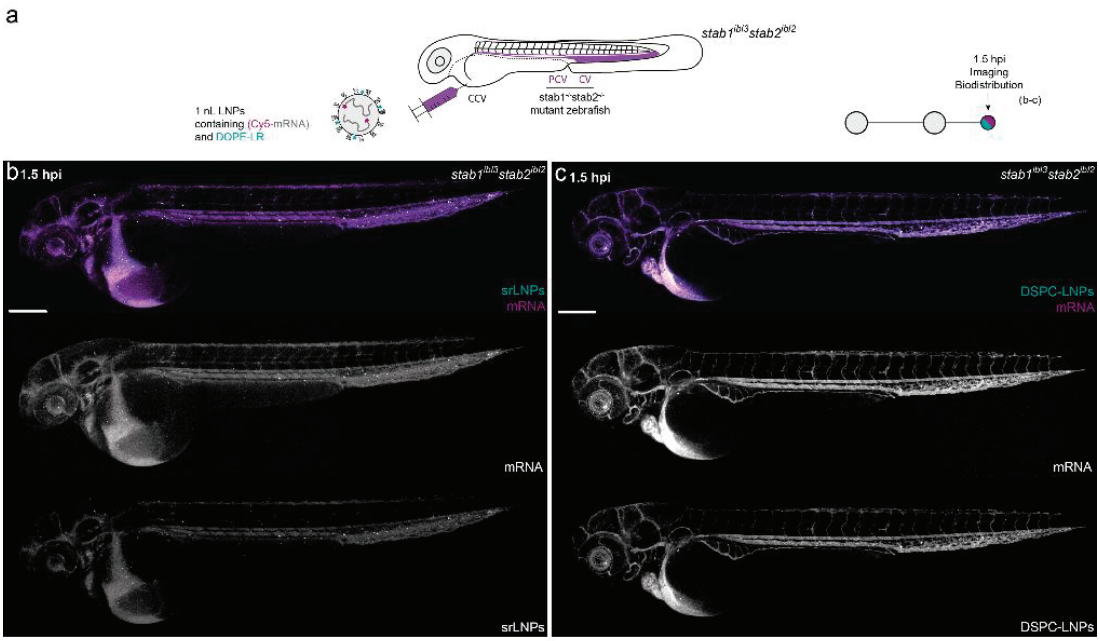

Supplementary Figure 2. Biodistribution of srLNPs and DSPC-LNPs in double knock-out (stab1$^{-/-}$/stab2$^{-/-}$) mutant embryos at 1.5 hpi. **(a)** Schematic showing the site of LNP injection (*i.v*) within double knockout (*stab1^{ibl3}-stab2^{ibl2}*)[51] (described in **Chapter 3**) zebrafish embryos (2 dpf) and imaging timeframe. LNPs contained DOPE-LR (cyan, 0.2 mol%) as fluorescent lipid probe and Cy5-labelled eGFP mRNA (magenta) as fluorescent mRNA probe. Injected dose: ~10 mM lipid, ~0.2 mg/kg mRNA. Injection volume: ~1 nl. CV – cardinal vein; PCV – posterior cardinal vein; CCV – common cardinal vein. **(b,c)** Whole embryo (10x magnification) views of srLNP and DSPC-LNP biodistribution within stab1$^{-/-}$/stab2$^{-/-}$ mutant embryos (2 dpf) at 1.5 hpi. In both cases, LNPs were mostly freely circulating throughout the vasculature of the embryo at 1.5 hpi. Scale bar: 200 µm.

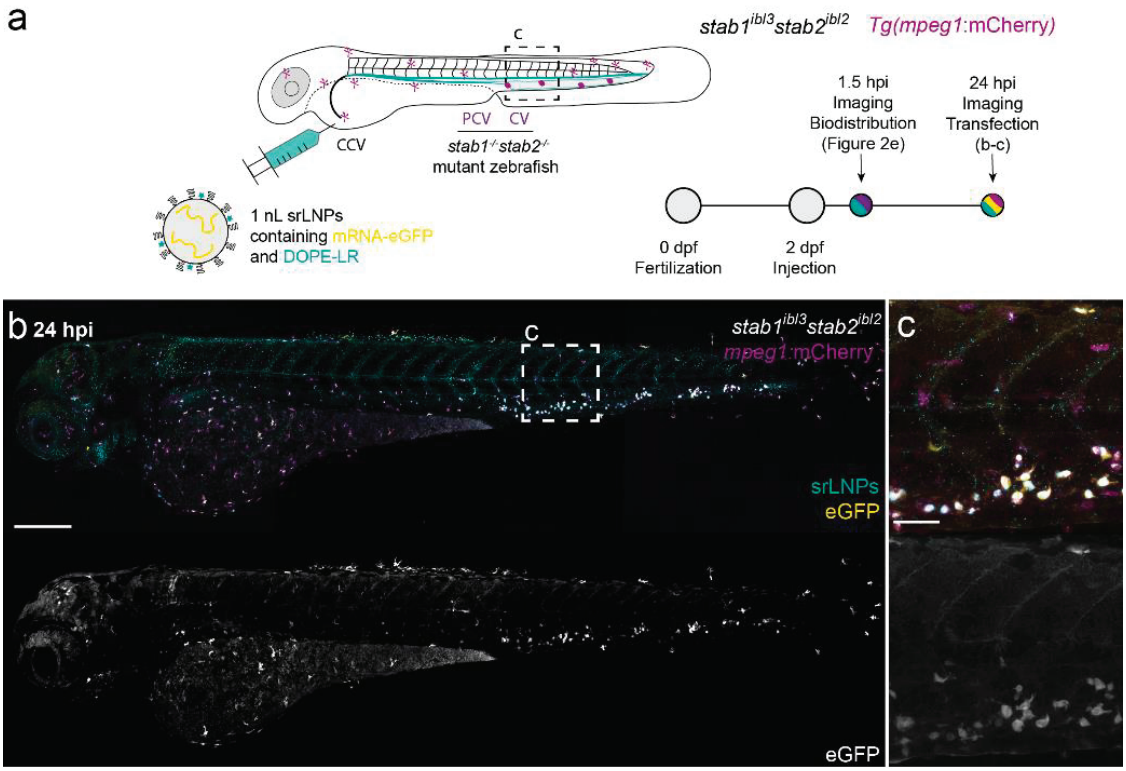

Supplementary Figure 3. srLNP biodistribution and eGFP expression in double knock-out (stab1$^{-/-}$ stab2$^{-/-}$) mutant embryos at 24 hpi. (a) Schematic showing the site of LNP injection (*i.v*) within Tg(*mpeg1*:mCherry), double knockout (*stab1*^{ibl3}*stab2*^{ibl2}) [51] (described in **Chapter 3**) zebrafish embryos (2 dpf) and imaging timeframe. LNPs contained DiD (cy5, 0.1 mol%, cyan) as fluorescent lipid probe and unlabeled eGFP mRNA. Injected dose: ~10 mM lipid, ~0.2 mg/kg mRNA. Injection volume: ~1 nl. CCV – common cardinal vein, CV – cardinal vein; PCV – posterior cardinal vein. **(b,c)** Whole embryo (10x magnification) and tissue level (40x magnification) views of srLNP biodistribution and eGFP expression within stab1$^{-/-}$/stab2$^{-/-}$ mutant embryos at 24 hpi. Within these embryos, srLNP localisation and eGFP expression is observed within blood resident macrophages (magenta) but not SECs at 24 hpi. Scale bars: 200 µm (whole embryo) and 50 µm (tissue level).

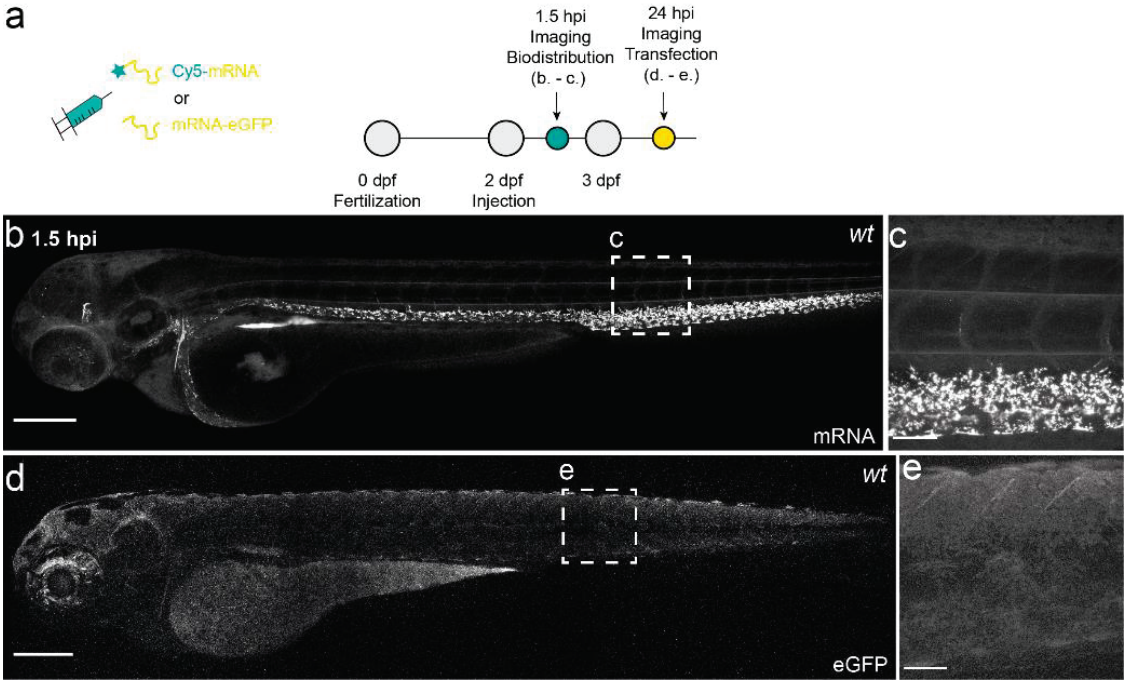

Supplementary Figure 4. Biodistribution and expression of free eGFP mRNA in wildtype (*AB/TL*) embryonic zebrafish. (a) Schematic showing the site of free mRNA injection (*i.v.*; 0.2 mg/kg, 1 nL) within embryonic zebrafish (2 dpf) and imaging timeframe. CCV – common cardinal vein. **(b,c)** Whole embryo (10x magnification) and tissue level (40x magnification) views of free mRNA (cy5-labelled) biodistribution at 1.5 hpi. Free mRNA primarily accumulated within SECs of the embryonic zebrafish at 1.5 hpi, likely mediated by Stabilin receptors.[59] Any phagocytotic uptake of free mRNA within blood resident macrophages cannot be clearly defined within the CHT of the wild-type embryo given the high fluorescence signal (cy5) within overlapping SECs. **(d,e)** Whole embryo (10x magnification) and tissue level (40x magnification) views of eGFP expression (unlabeled mRNA) at 24 hpi. No significant eGFP expression is observed within SECs or blood resident macrophages of the embryonic fish. Scale bars: 200 µm (whole embryo) and 50 µm (tissue level).

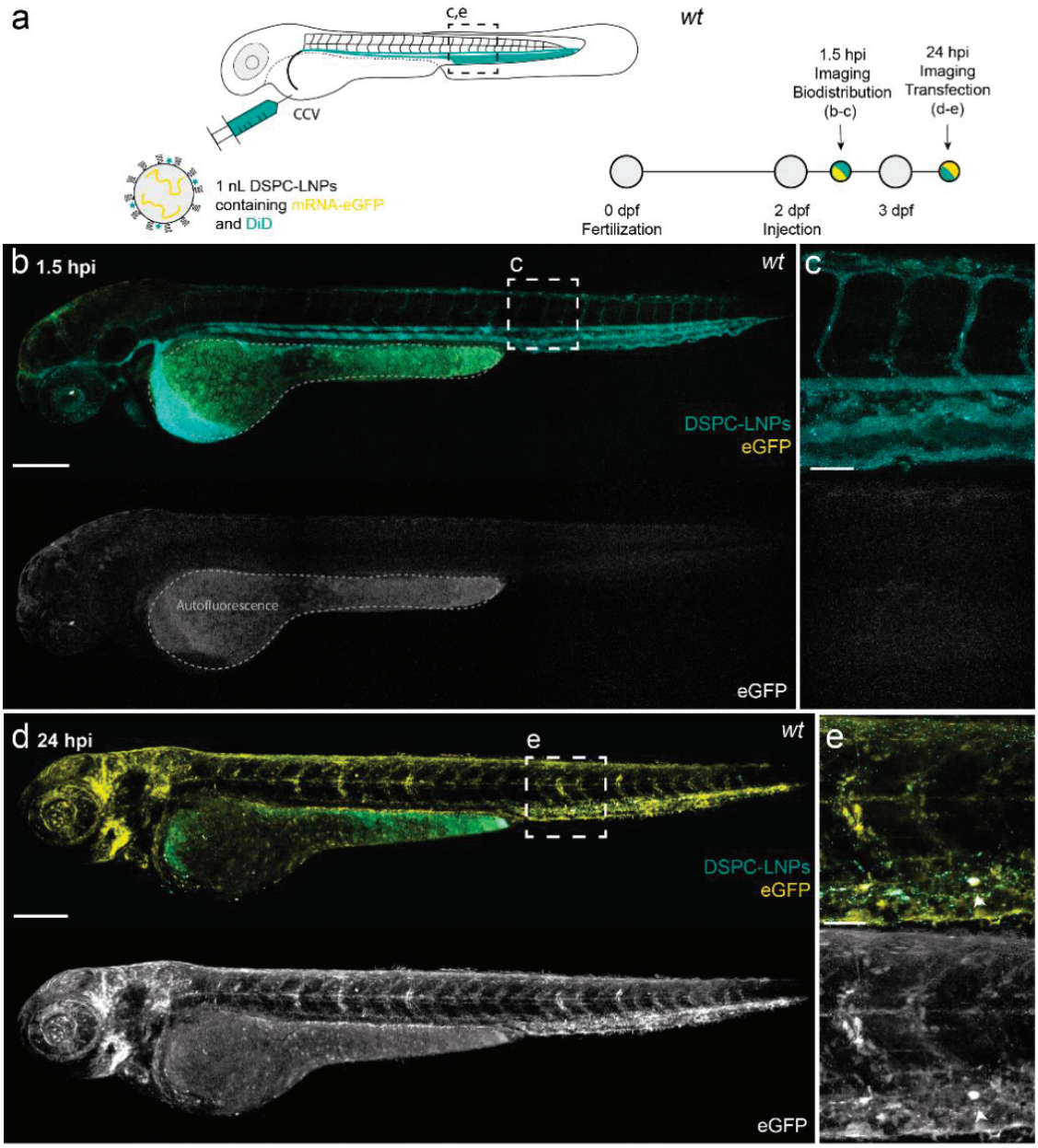

Supplementary Figure 5. DSPC-LNP biodistribution and eGFP expression within wild-type (*AB/TL*) zebrafish embryos at 1.5 and 24 hpi. (a) Schematic showing the site of DSPC-LNPs (*i.v.*) injection within embryonic zebrafish (2 dpf) and imaging timeframe. DSPC-LNPs contained DiD (cy5, 0.1 mol%) as fluorescent lipid probe and unlabelled eGFP mRNA (capped) payload. Injected dose: ~10 mM lipid, ~0.2 mg/kg mRNA. Injection volume: ~1 nl **(b,c)** Whole embryo (10x magnification) and tissue level (40x magnification) views of DSPC-LNP biodistribution and eGFP expression within the embryonic zebrafish at 1.5 hpi. DSPC-LNPs were mostly freely circulating, confined to and homogenously distributed throughout the vasculature of the embryo at 1.5 hpi. Low level embryo autofluorescence (GFP channel) within the yolk sac and pigment cells of the embryo is highlighted. **(d,e)** Whole embryo and tissue level views of DSPC-LNP biodistribution and eGFP expression within the embryonic zebrafish at 24 hpi. eGFP

expression within macrophages (based on location and morphology) highlighted with white arrowheads. Scale bars: 200 µm (whole embryo) and 50 µm (tissue level).

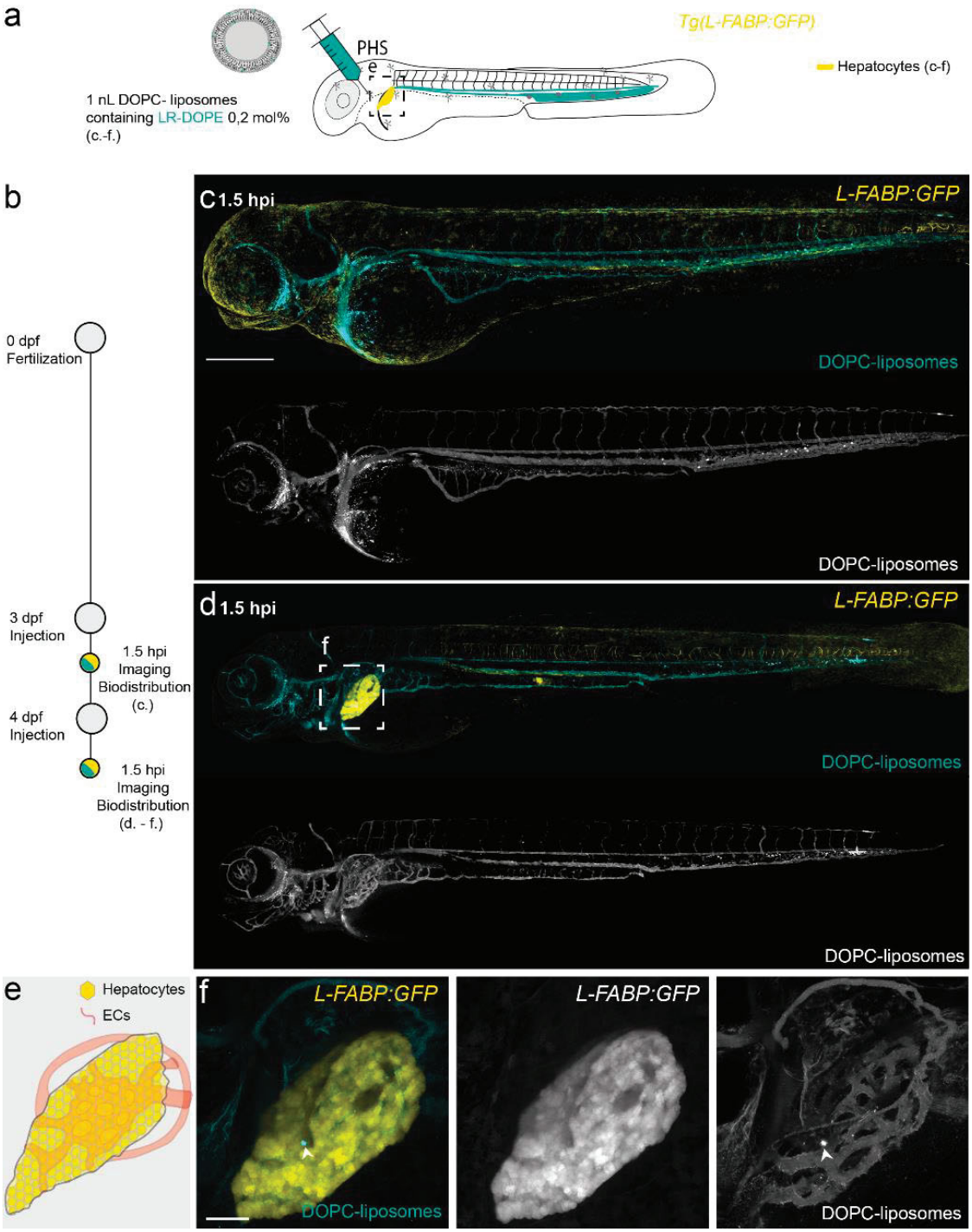

Supplementary Figure 6. DOPC liposome biodistribution in *L-FABP*:eGFP transgenic zebrafish embryos (3 and 4 dpf) at 1.5hpi. (a) Schematic showing the site of liposome injection (*i.v.*) within embryonic zebrafish (3 or 4 dpf). Liposomes contained 0.2 mol% DOPE-LR as fluorescent lipid probe (cyan). Injected dose: ~5 mM lipid. Injection volume: 1 nl. Tg(*LFABP:*eGFP) zebrafish embryos expressing eGFP (yellow) in hepatocytes. PHS – primary head sinus. **(b)** Injection and imaging timeframe. **(c,d)** Whole embryo (10x

magnification) views of DOPC liposome biodistribution within the embryonic zebrafish (3 or 4 dpf) at 1.5 hpi. **(e)** Tissue level schematic of the embryonic liver at 4 dpf. **(f)** Tissue level (40x magnification) views of DOPC liposome biodistribution within the liver of a four-day old embryo. Liposomes freely circulate throughout the liver vasculature and do not associate with either ECs or hepatocytes of the embryonic liver. The single, intense fluorescent (DOPE-LR) punctum (white arrowhead) observed within the liver of the four-day old embryo is most likely due to macrophage uptake. Scale bars: 200 µm (whole embryo) and 50 µm (tissue level).

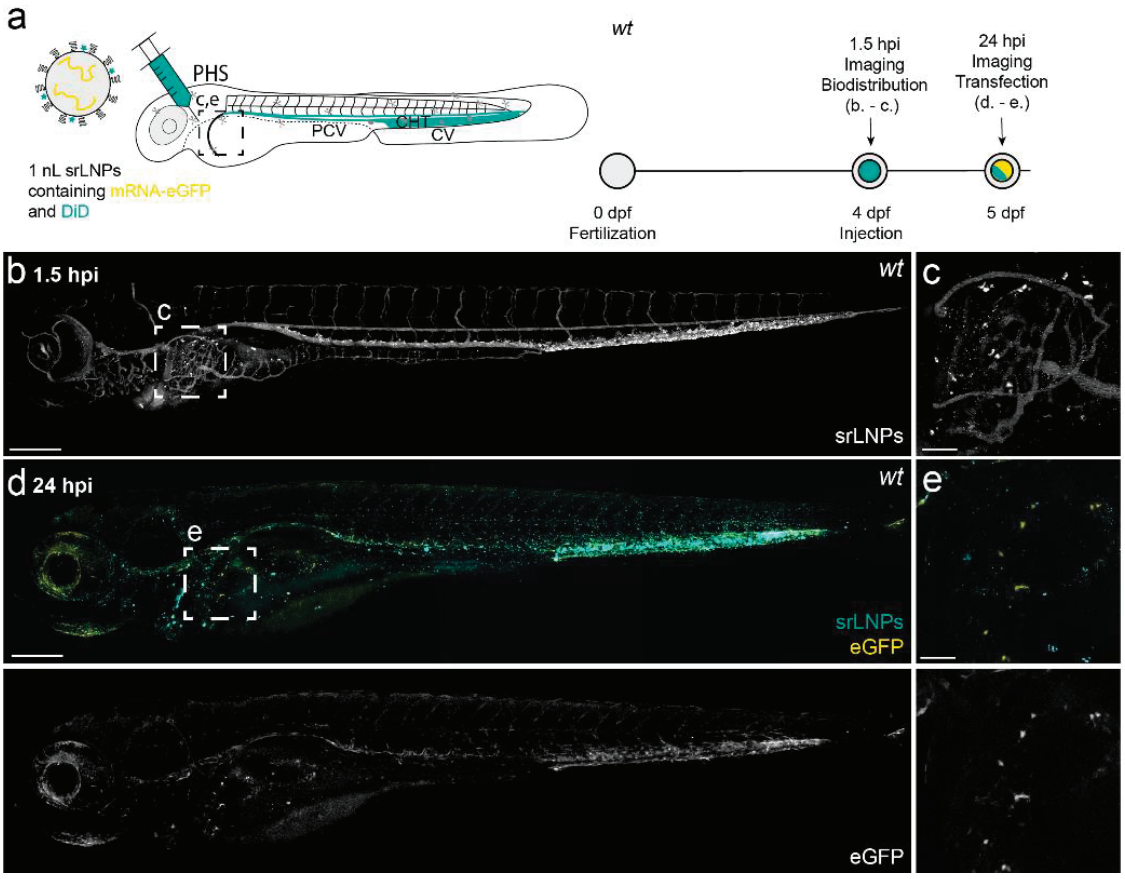

Supplementary Figure 7. srLNP (30mM) biodistribution and mRNA expression within wildtype (*AB/TL*) embryonic zebrafish. (a) Schematic showing the site of srLNP injection (*i.v.*) within embryonic zebrafish (4 dpf). srLNPs contained DiD (approx. 0.1 mol%) as fluorescent lipid probe and unlabeled, eGFP mRNA (capped) payload. Injection and imaging timeframe. Injected dose: ~10 mM lipid, ~0.2 mg/kg mRNA. Injection volume: 1 nl. PHS – primary head sinus. **(b,c)** Whole embryo (10x magnification) and tissue level (40x magnification, liver region) views of srLNP biodistribution (DiD, cyan) at 1.5 hpi. srLNPs were mainly associated with SECs within the PCV, CV and CHT of the four-day old embryo at 1.5 hpi. Due to the higher injected dosage, a significant fraction of srLNPs are also observed in circulation, possibly due to saturation of Stabilin receptors. Within the liver region, individual fluorescent punctae associated with srLNP accumulation are most likely due to macrophage uptake. **(d,e)** Whole embryo (10x magnification) and tissue level (40x magnification, liver region) views of srLNP biodistribution and eGFP expression within the embryonic zebrafish at 24 hpi. srLNPs remain predominantly localized within the PCV, CV and CHT at 24 hpi, with exogenous

eGFP expression mainly restricted to this region of the five day-old embryo. Within the liver region, eGFP fluorescence is restricted to a handful of individual cells and does not evidently colocalize with srLNP-associated fluorescence (DiD). From these images, it is not clear whether eGFP fluorescence within the liver is due to macrophage uptake (possibly distal from the liver, and following macrophage migration), embryo autofluorescence or uptake within an alternative cell type. Scale bars: 200 µm (whole embryo) and 50 µm (tissue level).

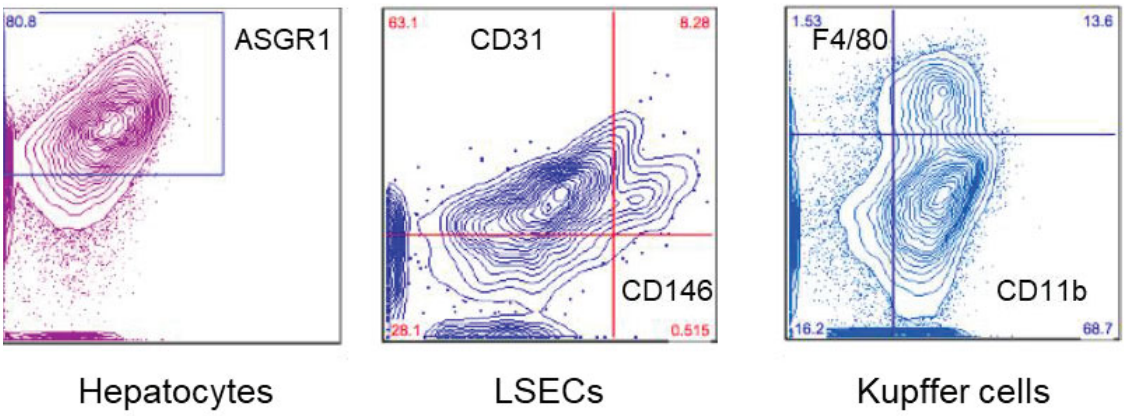

Supplementary Figure 8. Detection of major cell types in the liver microenvironment. Representative flow cytometry density plots illustrate the detection of specific hepatic cell types following liver perfusion and cell harvesting.

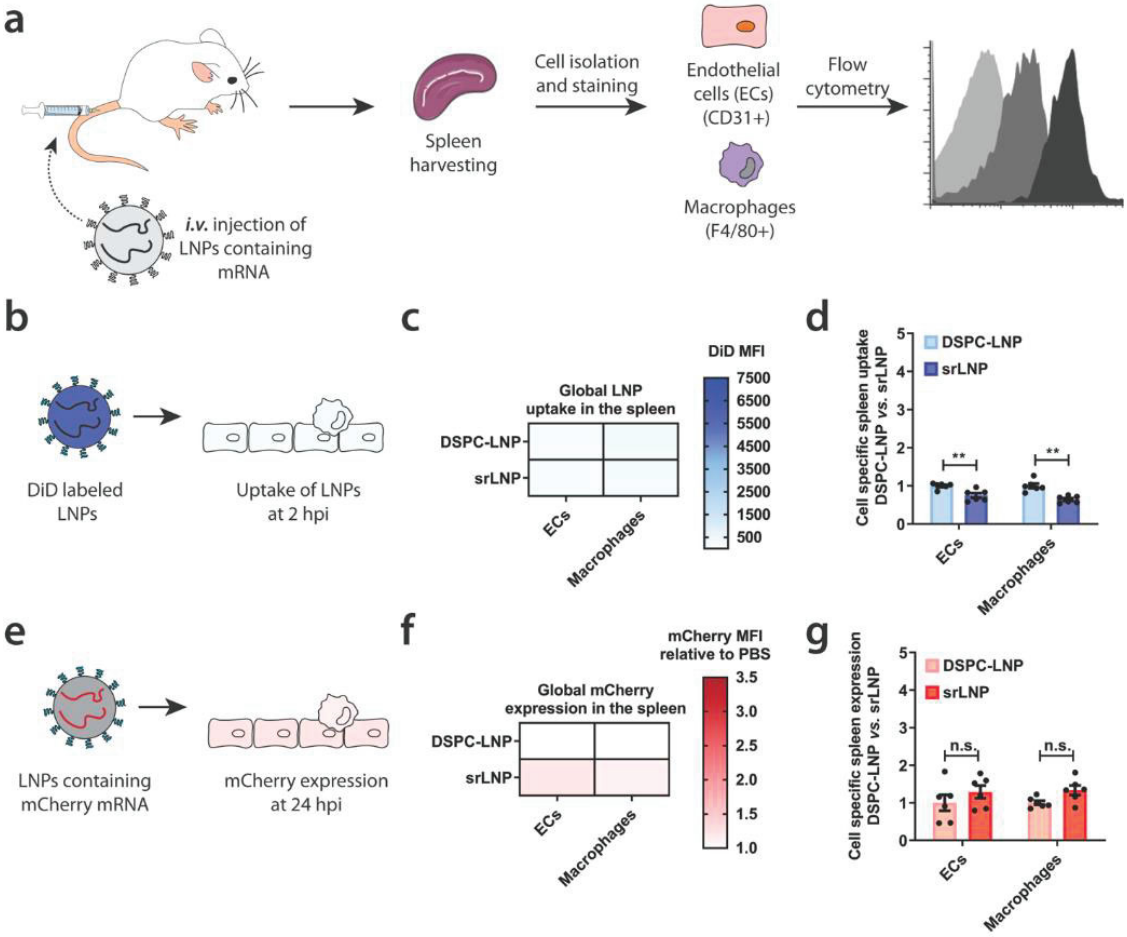

Supplementary Figure 9. LNP uptake and functional mRNA delivery within different splenic cell types. (a) Schematic illustrating the procedure to isolate different splenic cell types and determine LNP-mRNA targeting and functional mRNA delivery. Following intravenous LNP injection (*i.v*), splenic cells were isolated and stained with specific antibodies (in parentheses), and flow cytometry used to analyze LNP uptake or gene expression. **(b)** For biodistribution studies, LNPs contained DiD (0.5 mol%) as fluorescent probe. Cellular uptake of DSPC-LNP and srLNP was assessed 2 hpi. Injected dose: 42.75 mg/kg total lipid. **(c)** Heatmap of global LNP uptake in the spleen determined by absolute DiD fluorescence. **(d)** Cell specific spleen uptake normalized to DSPC-LNP for each cell type. **(e)** For gene expression experiments, LNPs contained mCherry-mRNA. Functional mRNA delivery was assessed based on mCherry reporter gene expression levels at 24 hpi. **(f)** Heatmap of mCherry expression in different spleen cell types using DSPC-LNP or srLNP. Injected dose: 0.25 mg/kg mRNA. srLNP show no significant mCherry expression compared to DSPC-LNP in splenic RES cells. **(g)** Cell specific mCherry expression normalized to DSPC-LNP for each cell type. In all cases, n = 6 represents 3 separate spleen tissue samples from 2 mice sorted into individual cell types. Bars and error bars in **c** represent mean ± s.e.m. The data was normalized to the average expression of DSPC-LNPs within each cell type. Statistical significance was evaluated using a two-tailed unpaired Student's t-test. n.s. = not significant, ** $p < 0.01$, *** $p < 0.001$. Exact P values for **d**: ECs P= 0.0039, Macrophages P= 0.0011. Exact P values for **g**: ECs P= 0.308, Macrophages P= 0.074.

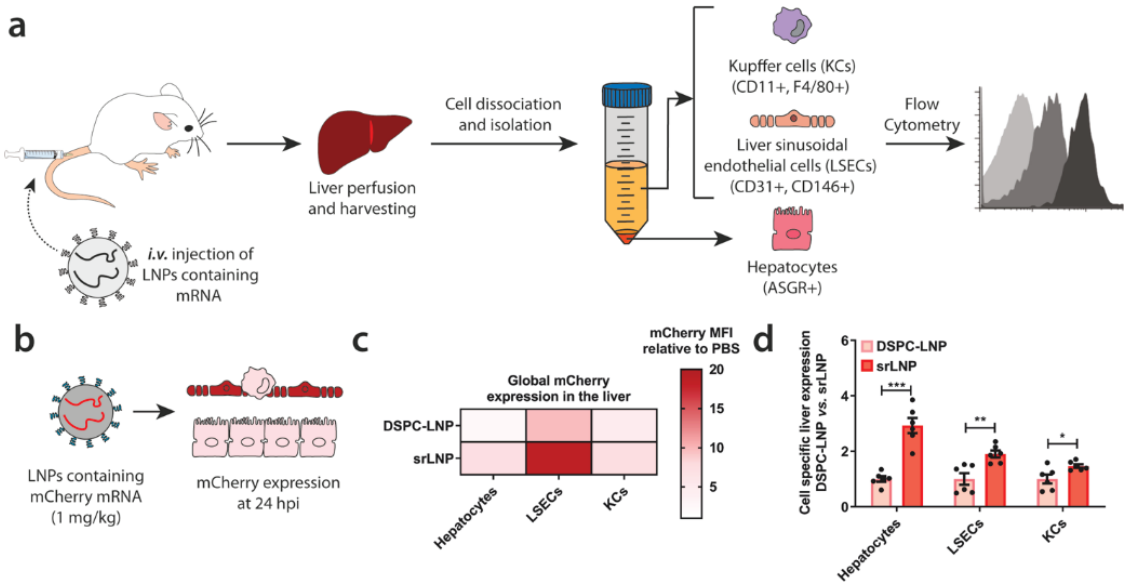

Supplementary Figure 10. Functional mCherry mRNA delivery to hepatic RES cell types at an injected mRNA dose of 1 mg/kg. (a) Schematic illustrating the procedure to isolate different hepatic cell types and determine LNP-mRNA targeting and functional mRNA delivery. Following intravenous LNP injection (*i.v*) the liver was perfused with collagenase IV, hepatic cells were isolated and stained with specific antibodies, and flow cytometry was used to analyze LNP uptake and gene expression. Specific antibody markers used to uniquely identify hepatocytes, LSECs and KCs, respectively, are defined in parentheses. **(b)** LNPs contained mCherry-mRNA. Functional mRNA delivery was assessed based on mCherry reporter gene expression levels at 24 hpi. **(c)** Heatmap of mCherry expression in different liver cell types enabled by mRNA delivery using DSPC-LNP and srLNP. Injected dose: 1 mg/kg mRNA. srLNPs led to enhanced gene expression in hepatic RES cells, predominantly in LSECs. **(d)** Cell specific mCherry expression normalized to DSPC-LNP for each cell type. In all cases, n = 6 represents 3 separate liver tissue samples from 2 mice sorted into individual cell types. Bars and error bars in c and e represent mean ± s.e.m. Statistical significance was evaluated using a two-tailed unpaired Student's t-test. * $p < 0.05$, ** $p < 0.01$, *** $p < 0.001$. Exact P values for **d**: Hepatocytes P= 0.00018, LSECs P= 0.0083, KCs P= 0.025.

6.8 References

1. Delivering the promise of RNA therapeutics. *Nature Medicine* **2019,** *25* (9), 1321-1321.
2. Dammes, N.; Peer, D., Paving the Road for RNA Therapeutics. *Trends in Pharmacological Sciences* **2020,** *41* (10), 755-775.
3. Yin, H.; Kanasty, R. L.; Eltoukhy, A. A.; Vegas, A. J.; Dorkin, J. R.; Anderson, D. G., Non-viral vectors for gene-based therapy. *Nature Reviews Genetics* **2014,** *15* (8), 541-555.
4. Cullis, P. R.; Hope, M. J., Lipid Nanoparticle Systems for Enabling Gene Therapies. *Molecular Therapy* **2017,** *25* (7), 1467-1475.
5. Kulkarni, J. A.; Witzigmann, D.; Chen, S.; Cullis, P. R.; van der Meel, R., Lipid Nanoparticle Technology for Clinical Translation of siRNA Therapeutics. *Accounts of Chemical Research* **2019,** *52* (9), 2435-2444.
6. Akinc, A.; Maier, M. A.; Manoharan, M.; Fitzgerald, K.; Jayaraman, M.; Barros, S.; Ansell, S.; Du, X.; Hope, M. J.; Madden, T. D.; Mui, B. L.; Semple, S. C.; Tam, Y. K.; Ciufolini, M.; Witzigmann, D.; Kulkarni, J. A.; van der Meel, R.; Cullis, P. R., The Onpattro story and the clinical translation of nanomedicines containing nucleic acid-based drugs. *Nature Nanotechnology* **2019,** *14* (12), 1084-1087.
7. Adams, D.; Gonzalez-Duarte, A.; O'Riordan, W. D.; Yang, C. C.; Ueda, M.; Kristen, A. V.; Tournev, I.; Schmidt, H. H.; Coelho, T.; Berk, J. L., et al., Patisiran, an RNAi therapeutic, for hereditary transthyretin amyloidosis. *New England Journal of Medicine* **2018,** *379* (1), 11-21.
8. Kumar, V.; Qin, J.; Jiang, Y.; Duncan, R. G.; Brigham, B.; Fishman, S.; Nair, J. K.; Akinc, A.; Barros, S. A.; Kasperkovitz, P. V., Shielding of Lipid Nanoparticles for siRNA Delivery: Impact on Physicochemical Properties, Cytokine Induction, and Efficacy. *Molecular therapy. Nucleic acids* **2014,** *3* (11), e210-e210.
9. Mui, B. L.; Tam, Y. K.; Jayaraman, M.; Ansell, S. M.; Du, X.; Tam, Y. Y. C.; Lin, P. J.; Chen, S.; Narayanannair, J. K.; Rajeev, K. G.; Manoharan, M.; Akinc, A.; Maier, M. A.; Cullis, P.; Madden, T. D.; Hope, M. J., Influence of Polyethylene Glycol Lipid Desorption Rates on Pharmacokinetics and Pharmacodynamics of siRNA Lipid Nanoparticles. *Molecular therapy. Nucleic acids* **2013,** *2* (12), e139-e139.
10. Akinc, A.; Querbes, W.; De, S.; Qin, J.; Frank-Kamenetsky, M.; Jayaprakash, K. N.; Jayaraman, M.; Rajeev, K. G.; Cantley, W. L.; Dorkin, J. R., et al., Targeted delivery of RNAi therapeutics with endogenous and exogenous ligand-based mechanisms. *Molecular Therapy* **2010,** *18* (7), 1357-1364.
11. Nguyen, J.; Szoka, F. C., Nucleic acid delivery: the missing pieces of the puzzle? *Accounts of chemical research* **2012,** *45* (7), 1153-1162.
12. Sato, Y.; Matsui, H.; Yamamoto, N.; Sato, R.; Munakata, T.; Kohara, M.; Harashima, H., Highly specific delivery of siRNA to hepatocytes circumvents endothelial cell-mediated lipid nanoparticle-associated toxicity leading to the safe and efficacious decrease in the hepatitis B virus. *Journal of Controlled Release* **2017,** *266* (September), 216-225.
13. DeRosa, F.; Guild, B.; Karve, S.; Smith, L.; Love, K.; Dorkin, J. R.; Kauffman, K. J.; Zhang, J.; Yahalom, B.; Anderson, D. G.; Heartlein, M. W., Therapeutic efficacy in a hemophilia B model using a biosynthetic mRNA liver depot system. *Gene therapy* **2016,** *23* (10), 699-707.
14. Ramaswamy, S.; Tonnu, N.; Tachikawa, K.; Limphong, P.; Vega, J. B.; Karmali, P. P.; Chivukula, P.; Verma, I. M., Systemic delivery of factor IX messenger RNA for protein replacement therapy. *Proceedings of the National Academy of Sciences of the United States of America* **2017,** *114* (10), E1941-E1950.
15. Chen, S.; Tam, Y. Y. C.; Lin, P. J. C.; Leung, A. K. K.; Tam, Y. K.; Cullis, P. R., Development of lipid nanoparticle formulations of siRNA for hepatocyte gene silencing following subcutaneous administration. *Journal of Controlled Release* **2014,** *196*, 106-112.
16. Sago, C. D.; Lokugamage, M. P.; Islam, F. Z.; Krupczak, B. R.; Sato, M.; Dahlman, J. E., Nanoparticles That Deliver RNA to Bone Marrow Identified by in Vivo Directed Evolution. *Journal of the American Chemical Society* **2018,** *140* (49), 17095-17105.
17. Lokugamage, M. P.; Sago, C. D.; Gan, Z.; Krupczak, B. R.; Dahlman, J. E., Constrained Nanoparticles Deliver siRNA and sgRNA to T Cells In Vivo without Targeting Ligands. *Advanced Materials* **2019,** *31* (41), 1902251-1902251.
18. Paunovska, K.; Gil, C. J.; Lokugamage, M. P.; Sago, C. D.; Sato, M.; Lando, G. N.; Gamboa Castro, M.; Bryksin, A. V.; Dahlman, J. E., Analyzing 2,000 in vivo Drug Delivery Data Points Reveals Cholesterol Structure Impacts Nanoparticle Delivery. *ACS Nano* **2018,** *12*, 8341-8349.

19. Paunovska, K.; Da Silva Sanchez, A. J.; Sago, C. D.; Gan, Z.; Lokugamage, M. P.; Islam, F. Z.; Kalathoor, S.; Krupczak, B. R.; Dahlman, J. E., Nanoparticles Containing Oxidized Cholesterol Deliver mRNA to the Liver Microenvironment at Clinically Relevant Doses. *Advanced materials (Deerfield Beach, Fla.)* **2019,** *31* (14), e1807748-e1807748.
20. Witzigmann, D.; Hak, S.; van der Meel, R., Translating nanomedicines: Thinking beyond materials? A young investigator's reply to 'The Novelty Bubble'. *Journal of Controlled Release* **2018,** *290* (October), 138-140.
21. Trefts, E.; Gannon, M.; Wasserman, D. H., The liver. *Current Biology* **2017,** *27* (21), R1147-R1151.
22. Wisse, E., An electron microscopic study of the fenestrated endothelial lining of rat liver sinusoids. *Journal of Ultrastructure Research* **1970,** *31* (1), 125-150.
23. Braet, F.; Wisse, E., Structural and functional aspects of liver sinusoidal endothelial cell fenestrae: a review. *Comparative hepatology* **2002,** *1* (1), 1-1.
24. Smedsrod, B.; Pertoft, H.; Gustafson, S.; Laurent, T. C., Scavenger functions of the liver endothelial cell. *Biochem J* **1990,** *266* (2), 313-327.
25. Sørensen, K. K.; Simon-Santamaria, J.; McCuskey, R. S.; Smedsrød, B., Liver sinusoidal endothelial cells. *Comprehensive Physiology* **2015,** *5* (4), 1751-1774.
26. Poisson, J.; Lemoinne, S.; Boulanger, C.; Durand, F.; Moreau, R.; Valla, D.; Rautou, P. E., Liver sinusoidal endothelial cells: Physiology and role in liver diseases. *J Hepatol* **2017,** *66* (1), 212-227.
27. Diep, C. Q.; Ma, D.; Deo, R. C.; Holm, T. M.; Naylor, R. W.; Arora, N.; Wingert, R. A.; Bollig, F.; Djordjevic, G.; Lichman, B.; Zhu, H.; Ikenaga, T.; Ono, F.; Englert, C.; Cowan, C. A.; Hukriede, N. A.; Handin, R. I.; Davidson, A. J., Identification of adult nephron progenitors capable of kidney regeneration in zebrafish. *Nature* **2011,** *470* (7332), 95-100.
28. Smedsrod, B., Clearance function of scavenger endothelial cells. *Comp Hepatol* **2004,** *3 Suppl 1*, S22.
29. Ganesan, L. P.; Mohanty, S.; Kim, J.; Clark, K. R.; Robinson, J. M.; Anderson, C. L., Rapid and Efficient Clearance of Blood-borne Virus by Liver Sinusoidal Endothelium. *PLOS Pathogens* **2011,** *7* (9), e1002281-e1002281.
30. Mates, J. M.; Yao, Z.; Cheplowitz, A. M.; Suer, O.; Phillips, G. S.; Kwiek, J. J.; Rajaram, M. V. S.; Kim, J.; Robinson, J. M.; Ganesan, L. P.; Anderson, C. L., Mouse Liver Sinusoidal Endothelium Eliminates HIV-Like Particles from Blood at a Rate of 100 Million per Minute by a Second-Order Kinetic Process. 2017; Vol. 8, pp 35-35.
31. Sørensen, K. K.; McCourt, P.; Berg, T.; Crossley, C.; Couteur, D. L.; Wake, K.; Smedsrød, B., The scavenger endothelial cell: a new player in homeostasis and immunity. *American Journal of Physiology-Regulatory, Integrative and Comparative Physiology* **2012,** *303* (12), R1217-R1230.
32. Schledzewski, K.; Géraud, C.; Arnold, B.; Wang, S.; Gröne, H.-J.; Kempf, T.; Wollert, K. C.; Straub, B. K.; Schirmacher, P.; Demory, A.; Schönhaber, H.; Gratchev, A.; Dietz, L.; Thierse, H.-J.; Kzhyshkowska, J.; Goerdt, S., Deficiency of liver sinusoidal scavenger receptors stabilin-1 and -2 in mice causes glomerulofibrotic nephropathy via impaired hepatic clearance of noxious blood factors. *The Journal of Clinical Investigation* **2011,** *121* (2), 703-714.
33. McCourt, P. A. G.; Hansen, B.; Svistuonov, D.; Johansson, S.; Longati, P.; Schledzewski, K.; Kzhyshkowska, J.; Goerdt, S.; Johansson, S.; Smedsrød, B., The liver sinusoidal endothelial cell hyaluronan receptor and its homolog, stabilin-1 - Their roles (known and unknown) in endocytosis. *Comparative hepatology* **2004,** *3* (Suppl 1), S24-S24.
34. Wilkinson, A. L.; Qurashi, M.; Shetty, S., The Role of Sinusoidal Endothelial Cells in the Axis of Inflammation and Cancer Within the Liver. 2020; Vol. 11, pp 990-990.
35. Shetty, S.; Lalor, P. F.; Adams, D. H., Liver sinusoidal endothelial cells — gatekeepers of hepatic immunity. *Nature Reviews Gastroenterology & Hepatology* **2018,** *15* (9), 555-567.
36. Campbell, F.; Bos, F. L.; Sieber, S.; Arias-Alpizar, G.; Koch, B. E.; Huwyler, J.; Kros, A.; Bussmann, J., Directing Nanoparticle Biodistribution through Evasion and Exploitation of Stab2-Dependent Nanoparticle Uptake. *ACS Nano* **2018,** *12* (3), 2138-2150.
37. Sieber, S.; Grossen, P.; Bussmann, J.; Campbell, F.; Kros, A.; Witzigmann, D.; Huwyler, J., Zebrafish as a preclinical in vivo screening model for nanomedicines. *Advanced Drug Delivery Reviews* **2019,** *151-152*, 152-168.
38. Seternes, T.; Sørensen, K.; Smedsrød, B., Scavenger endothelial cells of vertebrates: a nonperipheral leukocyte system for high-capacity elimination of waste macromolecules. *Proceedings of the National Academy of Sciences of the United States of America* **2002,** *99* (11), 7594-7597.

39. Smedsrod, B., Scavenger function of liver sinusoidal endothelial cells. *The FASEB Journal* **2009,** *23* (S1), 66.61-66.61.
40. Hayashi, Y.; Takamiya, M.; Jensen, P. B.; Ojea-Jiménez, I.; Claude, H.; Antony, C.; Kjaer-Sorensen, K.; Grabher, C.; Boesen, T.; Gilliland, D.; Oxvig, C.; Strähle, U.; Weiss, C., Differential Nanoparticle Sequestration by Macrophages and Scavenger Endothelial Cells Visualized in Vivo in Real-Time and at Ultrastructural Resolution. *ACS Nano* **2020,** *14* (2), 1665-1681.
41. Evers, M. J. W.; Kulkarni, J. A.; Meel, R. V. D.; Cullis, P. R.; Vader, P.; Schiffelers, R. M., State-of-the-Art Design and Rapid-Mixing Production Techniques of Lipid Nanoparticles for Nucleic Acid Delivery. *Small methods* **2018,** *1700375*, 1-20.
42. Arteta, M. Y.; Kjellman, T.; Bartesaghi, S.; Wallin, S.; Wu, X.; Kvist, A. J.; Dabkowska, A.; Székely, N.; Radulescu, A.; Bergenholtz, J.; Lindfors, L., Successful reprogramming of cellular protein production through mRNA delivered by functionalized lipid nanoparticles. *Proceedings of the National Academy of Sciences of the United States of America* **2018,** *115* (15), E3351-E3360.
43. Yamamoto, T.; Ryan, R. O., Anionic phospholipids inhibit apolipoprotein E—Low-density lipoprotein receptor interactions. *Biochemical and Biophysical Research Communications* **2007,** *354* (3), 820-824.
44. Kulkarni, J. A.; Witzigmann, D.; Leung, J.; Tam, Y. Y. C.; Cullis, P. R., On the role of helper lipids in lipid nanoparticle formulations of siRNA. *Nanoscale* **2019,** *11* (45), 21733-21739.
45. Kulkarni, J. A.; Darjuan, M. M.; Mercer, J. E.; Chen, S.; van der Meel, R.; Thewalt, J. L.; Tam, Y. Y. C.; Cullis, P. R., On The Formation and Morphology of Lipid Nanoparticles Containing Ionizable Cationic Lipids and siRNA. *ACS Nano* **2018,** *12* (5), 4787-4795.
46. Leung, A. K. K.; Hafez, I. M.; Baoukina, S.; Belliveau, N. M.; Zhigaltsev, I. V.; Afshinmanesh, E.; Tieleman, D. P.; Hansen, C. L.; Hope, M. J.; Cullis, P. R., Lipid nanoparticles containing siRNA synthesized by microfluidic mixing exhibit an electron-dense nanostructured core. *Journal of Physical Chemistry C* **2012,** *116* (34), 18440-18450.
47. Kulkarni, J. A.; Witzigmann, D.; Leung, J.; van der Meel, R.; Zaifman, J.; Darjuan, M. M.; Grisch-Chan, H. M.; Thöny, B.; Tam, Y. Y. C.; Cullis, P. R., Fusion-dependent formation of lipid nanoparticles containing macromolecular payloads. *Nanoscale* **2019,** *11* (18), 9023-9031.
48. Crawford, R.; Dogdas, B.; Keough, E.; Haas, R. M.; Wepukhulu, W.; Krotzer, S.; Burke, P. A.; Sepp-Lorenzino, L.; Bagchi, A.; Howell, B. J., Analysis of lipid nanoparticles by Cryo-EM for characterizing siRNA delivery vehicles. *International journal of pharmaceutics* **2011,** *403* (1-2), 237-244.
49. Eygeris, Y.; Patel, S.; Jozic, A.; Sahay, G., Deconvoluting Lipid Nanoparticle Structure for Messenger RNA Delivery. *Nano Letters* **2020,** *20* (6), 4543-4549.
50. Patel, S.; Ashwanikumar, N.; Robinson, E.; Xia, Y.; Mihai, C.; Griffith, J. P.; Hou, S.; Esposito, A. A.; Ketova, T.; Welsher, K.; Joyal, J. L.; Almarsson, Ö.; Sahay, G., Naturally-occurring cholesterol analogues in lipid nanoparticles induce polymorphic shape and enhance intracellular delivery of mRNA. *Nature Communications* **2020,** *11* (1), 983-983.
51. Arias-Alpizar, G.; Koch, B.; Hamelmann, N. M.; Neustrup, M. A.; Paulusse, J. M. J.; Jiskoot, W.; Kros, A.; Bussmann, J., Stabilin-1 is required for the endothelial clearance of small anionic nanoparticles. *Nanomedicine* **2021,** *34*, 102395.
52. Reiser, A.; Woschée, D.; Mehrotra, N.; Krzysztoń, R.; Strey, H. H.; Rädler, J. O., Correlation of mRNA delivery timing and protein expression in lipid-based transfection. *Integrative Biology* **2019,** *11* (9), 362-371.
53. Balleza, E.; Kim, J. M.; Cluzel, P., Systematic characterization of maturation time of fluorescent proteins in living cells. *Nature Methods* **2018,** *15* (1), 47-51.
54. Lopes, S.; Yang, X.; Müller, J.; Carney, T.; McAdow, A.; Rauch, G.-J.; Jacoby, A.; Hurst, L.; Delfino-Machin, M.; Haffter, P.; Geisler, R.; Johnson, S.; Ward, A.; Kelsh, R., Leukocyte Tyrosine Kinase Functions in Pigment Cell Development. *PLoS genetics* **2008,** *4*, e1000026-e1000026.
55. Leonhardt, C.; Schwake, G.; Stögbauer, T. R.; Rappl, S.; Kuhr, J.-T.; Ligon, T. S.; Rädler, J. O., Single-cell mRNA transfection studies: Delivery, kinetics and statistics by numbers. *Nanomedicine: Nanotechnology, Biology and Medicine* **2014,** *10* (4), 679-688.
56. Patel, S.; Kim, J.; Herrera, M.; Mukherjee, A.; Kabanov, A. V.; Sahay, G., Brief update on endocytosis of nanomedicines. *Advanced Drug Delivery Reviews* **2019,** *144*, 90-111.
57. Gilleron, J.; Querbes, W.; Zeigerer, A.; Borodovsky, A.; Marsico, G.; Schubert, U.; Manygoats, K.; Seifert, S.; Andree, C.; Stöter, M., et al., Image-based analysis of lipid nanoparticle–mediated siRNA delivery, intracellular trafficking and endosomal escape. *Nature Biotechnology* **2013,** *31* (7), 638-646.

58. Sahay, G.; Querbes, W.; Alabi, C.; Eltoukhy, A.; Sarkar, S.; Zurenko, C.; Karagiannis, E.; Love, K.; Chen, D.; Zoncu, R.; Buganim, Y.; Schroeder, A.; Langer, R.; Anderson, D. G., Efficiency of siRNA delivery by lipid nanoparticles is limited by endocytic recycling. *Nature biotechnology* **2013,** *31* (7), 653-658.
59. Miller, C. M.; Donner, A. J.; Blank, E. E.; Egger, A. W.; Kellar, B. M.; Østergaard, M. E.; Seth, P. P.; Harris, E. N., Stabilin-1 and Stabilin-2 are specific receptors for the cellular internalization of phosphorothioate-modified antisense oligonucleotides (ASOs) in the liver. *Nucleic Acids Research* **2016,** *44* (6), 2782-2794.
60. Wilkins, B. J.; Pack, M., Zebrafish models of human liver development and disease. *Comprehensive Physiology* **2013,** *3* (3), 1213-1230.
61. Wang, S.; Miller, S. R.; Ober, E. A.; Sadler, K. C., Making It New Again: Insight Into Liver Development, Regeneration, and Disease From Zebrafish Research. *Current topics in developmental biology* **2017,** *124*, 161-195.
62. Korzh, S.; Pan, X.; Garcia-Lecea, M.; Winata, C. L.; Pan, X.; Wohland, T.; Korzh, V.; Gong, Z., Requirement of vasculogenesis and blood circulation in late stages of liver growth in zebrafish. *BMC developmental biology* **2008,** *8*, 84-84.
63. Mudumana, S. P.; Wan, H.; Singh, M.; Korzh, V.; Gong, Z., Expression analyses of zebrafish transferrin, ifabp, and elastaseB mRNAs as differentiation markers for the three major endodermal organs: liver, intestine, and exocrine pancreas. *Developmental dynamics : an official publication of the American Association of Anatomists* **2004,** *230* (1), 165-173.
64. Her, G. M.; Chiang, C.-C.; Chen, W.-Y.; Wu, J.-L., In vivo studies of liver-type fatty acid binding protein (L-FABP) gene expression in liver of transgenic zebrafish (Danio rerio). *FEBS letters* **2003,** *538* (1-3), 125-133.
65. Yin, C.; Evason, K. J.; Maher, J. J.; Stainier, D. Y. R., The basic helix-loop-helix transcription factor, heart and neural crest derivatives expressed transcript 2, marks hepatic stellate cells in zebrafish: analysis of stellate cell entry into the developing liver. *Hepatology (Baltimore, Md.)* **2012,** *56* (5), 1958-1970.
66. Cheng, D.; Morsch, M.; Shami, G. J.; Chung, R. S.; Braet, F., Albumin uptake and distribution in the zebrafish liver as observed via correlative imaging. *Experimental cell research* **2019,** *374* (1), 162-171.
67. Otis, J. P.; Zeituni, E. M.; Thierer, J. H.; Anderson, J. L.; Brown, A. C.; Boehm, E. D.; Cerchione, D. M.; Ceasrine, A. M.; Avraham-Davidi, I.; Tempelhof, H.; Yaniv, K.; Farber, S. A., Zebrafish as a model for apolipoprotein biology: comprehensive expression analysis and a role for ApoA-IV in regulating food intake. *Disease models & mechanisms* **2015,** *8* (3), 295-309.
68. Babin, P. J.; Thisse, C.; Durliat, M.; Andre, M.; Akimenko, M.-A.; Thisse, B., Both apolipoprotein E and A-I genes are present in a nonmammalian vertebrate and are highly expressed during embryonic development. *Proceedings of the National Academy of Sciences* **1997,** *94* (16), 8622 LP-8627.
69. Liu, C.; Kim, Y. S.; Kim, J.; Pattison, J.; Kamaid, A.; Miller, Y. I., Modeling hypercholesterolemia and vascular lipid accumulation in LDL receptor mutant zebrafish. *Journal of lipid research* **2018,** *59* (2), 391-399.
70. O'Hare, E. A.; Wang, X.; Montasser, M. E.; Chang, Y.-P. C.; Mitchell, B. D.; Zaghloul, N. A., Disruption of ldlr causes increased LDL-c and vascular lipid accumulation in a zebrafish model of hypercholesterolemia. *Journal of lipid research* **2014,** *55* (11), 2242-2253.
71. Schlegel, A., Zebrafish Models for Dyslipidemia and Atherosclerosis Research. 2016; Vol. 7, pp 159-159.
72. Wang, D.; El-Amouri, S. S.; Dai, M.; Kuan, C.-Y.; Hui, D. Y.; Brady, R. O.; Pan, D., Engineering a lysosomal enzyme with a derivative of receptor-binding domain of apoE enables delivery across the blood-brain barrier. *Proceedings of the National Academy of Sciences of the United States of America* **2013,** *110* (8), 2999-3004.
73. Jiang, Y.; Zhang, J.; Meng, F.; Zhong, Z., Apolipoprotein E Peptide-Directed Chimeric Polymersomes Mediate an Ultrahigh-Efficiency Targeted Protein Therapy for Glioblastoma. *ACS Nano* **2018,** *12* (11), 11070-11079.
74. Böckenhoff, A.; Cramer, S.; Wölte, P.; Knieling, S.; Wohlenberg, C.; Gieselmann, V.; Galla, H.-J.; Matzner, U., Comparison of five peptide vectors for improved brain delivery of the lysosomal enzyme arylsulfatase A. *The Journal of neuroscience : the official journal of the Society for Neuroscience* **2014,** *34* (9), 3122-3129.

75. Mayer, L. D.; Cullis, P. R.; Bally, M. B., Designing therapeutically optimized liposomal anticancer delivery systems: Lessons from conventional liposomes. Elsevier Science B.V.: Amsterdam, 1998; pp 231-257.
76. Sago, C. D.; Krupczak, B. R.; Lokugamage, M. P.; Gan, Z.; Dahlman, J. E., Cell Subtypes Within the Liver Microenvironment Differentially Interact with Lipid Nanoparticles. *Cellular and molecular bioengineering* **2019,** *12* (5), 389-397.
77. Shi, B.; Keough, E.; Matter, A.; Leander, K.; Young, S.; Carlini, E.; Sachs, A. B.; Tao, W.; Abrams, M.; Howell, B.; Sepp-Lorenzino, L., Biodistribution of small interfering RNA at the organ and cellular levels after lipid nanoparticle-mediated delivery. *The journal of histochemistry and cytochemistry : official journal of the Histochemistry Society* **2011,** *59* (8), 727-740.
78. Moderna Announces Positive Phase 1 Results for the First Systemic Messenger RNA Therapeutic Encoding a Secreted Protein (mRNA-1944). 2019.
79. Schulze, R. J.; Schott, M. B.; Casey, C. A.; Tuma, P. L.; McNiven, M. A., The cell biology of the hepatocyte: A membrane trafficking machine. *The Journal of cell biology* **2019,** *218* (7), 2096-2112.
80. Ni, Y.; Li, J.-M.; Liu, M.-K.; Zhang, T.-T.; Wang, D.-P.; Zhou, W.-H.; Hu, L.-Z.; Lv, W.-L., Pathological process of liver sinusoidal endothelial cells in liver diseases. *World journal of gastroenterology* **2017,** *23* (43), 7666-7677.
81. Rietwyk, S.; Peer, D., Next-Generation Lipids in RNA Interference Therapeutics. **2017,** *11* (8), 7572-7586.
82. Miao, L.; Li, L.; Huang, Y.; Delcassian, D.; Chahal, J.; Han, J.; Shi, Y.; Sadtler, K.; Gao, W.; Lin, J.; Doloff, J. C.; Langer, R.; Anderson, D. G., Delivery of mRNA vaccines with heterocyclic lipids increases anti-tumor efficacy by STING-mediated immune cell activation. *Nature Biotechnology* **2019,** *37* (10), 1174-1185.
83. Hassett, K. J.; Benenato, K. E.; Jacquinet, E.; Lee, A.; Woods, A.; Yuzhakov, O.; Himansu, S.; Deterling, J.; Geilich, B. M.; Ketova, T.; Mihai, C.; Lynn, A.; McFadyen, I.; Moore, M. J.; Senn, J. J.; Stanton, M. G.; Almarsson, Ö.; Ciaramella, G.; Brito, L. A., Optimization of Lipid Nanoparticles for Intramuscular Administration of mRNA Vaccines. *Molecular Therapy - Nucleic Acids* **2019,** *15* (April), 1-11.
84. Khvorova, A.; Watts, J. K., The chemical evolution of oligonucleotide therapies of clinical utility. *Nature Biotechnology* **2017,** *35* (3), 238-248.
85. Ku, S. H.; Jo, S. D.; Lee, Y. K.; Kim, K.; Kim, S. H., Chemical and structural modifications of RNAi therapeutics. *Advanced Drug Delivery Reviews* **2016,** *104*, 16-28.
86. Shen, X.; Corey, D. R., Chemistry, mechanism and clinical status of antisense oligonucleotides and duplex RNAs. *Nucleic Acids Research* **2017,** *46* (4), 1584-1600.
87. De Rijke, Y. B.; Biessen, E. A.; Vogelezang, C. J.; van Berkel, T. J., Binding characteristics of scavenger receptors on liver endothelial and Kupffer cells for modified low-density lipoproteins. *The Biochemical journal* **1994,** *304* (Pt 1), 69-73.
88. Cheng, Q.; Wei, T.; Farbiak, L.; Johnson, L. T.; Dilliard, S. A.; Siegwart, D. J., Selective organ targeting (SORT) nanoparticles for tissue-specific mRNA delivery and CRISPR–Cas gene editing. *Nature Nanotechnology* **2020,** *15* (4), 313-320.
89. Staudt, N.; Müller-Sienerth, N.; Fane-Dremucheva, A.; Yusaf, S. P.; Millrine, D.; Wright, G. J., A panel of recombinant monoclonal antibodies against zebrafish neural receptors and secreted proteins suitable for wholemount immunostaining. *Biochemical and biophysical research communications* **2015,** *456* (1), 527-533.
90. Burket, C. T.; Montgomery, J. E.; Thummel, R.; Kassen, S. C.; LaFave, M. C.; Langenau, D. M.; Zon, L. I.; Hyde, D. R., Generation and characterization of transgenic zebrafish lines using different ubiquitous promoters. *Transgenic research* **2008,** *17* (2), 265-279.
91. Varshney, G. K.; Pei, W.; LaFave, M. C.; Idol, J.; Xu, L.; Gallardo, V.; Carrington, B.; Bishop, K.; Jones, M.; Li, M.; Harper, U.; Huang, S. C.; Prakash, A.; Chen, W.; Sood, R.; Ledin, J.; Burgess, S. M., High-throughput gene targeting and phenotyping in zebrafish using CRISPR/Cas9. *Genome research* **2015,** *25* (7), 1030-1042.
92. Pardi, N.; Hogan, M. J.; Porter, F. W.; Weissman, D., mRNA vaccines — a new era in vaccinology. *Nature Reviews Drug Discovery* **2018,** *17* (4), 261-279.
93. John, S.; Yuzhakov, O.; Woods, A.; Deterling, J.; Hassett, K.; Shaw, C. A.; Ciaramella, G., Multi-antigenic human cytomegalovirus mRNA vaccines that elicit potent humoral and cell-mediated immunity. *Vaccine* **2018,** *36* (12), 1689-1699.

94. Zhang, N.-N.; Li, X.-F.; Deng, Y.-Q.; Zhao, H.; Huang, Y.-J.; Yang, G.; Huang, W.-J.; Gao, P.; Zhou, C.; Zhang, R.-R., et al., A Thermostable mRNA Vaccine against COVID-19. *Cell* **2020,** *182* (5), 1271-1283.e1216.
95. Jackson, L. A.; Anderson, E. J.; Rouphael, N. G.; Roberts, P. C.; Makhene, M.; Coler, R. N.; McCullough, M. P.; Chappell, J. D.; Denison, M. R.; Stevens, L. J., et al., An mRNA Vaccine against SARS-CoV-2 — Preliminary Report. *New England Journal of Medicine* **2020,** *383*, 1920-1931.
96. McKay, P. F.; Hu, K.; Blakney, A. K.; Samnuan, K.; Brown, J. C.; Penn, R.; Zhou, J.; Bouton, C. R.; Rogers, P.; Polra, K.; Lin, P. J. C.; Barbosa, C.; Tam, Y. K.; Barclay, W. S.; Shattock, R. J., Self-amplifying RNA SARS-CoV-2 lipid nanoparticle vaccine candidate induces high neutralizing antibody titers in mice. *Nature Communications* **2020,** *11* (1), 3523-3523.
97. Lu, J.; Lu, G.; Tan, S.; Xia, J.; Xiong, H.; Yu, X.; Qi, Q.; Yu, X.; Li, L.; Yu, H.; Xia, N.; Zhang, T.; Xu, Y.; Lin, J., A COVID-19 mRNA vaccine encoding SARS-CoV-2 virus-like particles induces a strong antiviral-like immune response in mice. *Cell Research* **2020,** *30* (10), 936-939.
98. Jain, R.; Frederick, J. P.; Huang, E. Y.; Burke, K. E.; Mauger, D. M.; Andrianova, E. A.; Farlow, S. J.; Siddiqui, S.; Pimentel, J.; Cheung-Ong, K.; McKinney, K. M.; Köhrer, C.; Moore, M. J.; Chakraborty, T., MicroRNAs Enable mRNA Therapeutics to Selectively Program Cancer Cells to Self-Destruct. *Nucleic acid therapeutics* **2018,** *28* (5), 285-296.
99. Jayaraman, M.; Ansell, S. M.; Mui, B. L.; Tam, Y. K.; Chen, J.; Du, X.; Butler, D.; Eltepu, L.; Matsuda, S.; Narayanannair, J. K.; Rajeev, K. G.; Hafez, I. M.; Akinc, A.; Maier, M. A.; Tracy, M. A.; Cullis, P. R.; Madden, T. D.; Manoharan, M.; Hope, M. J., Maximizing the potency of siRNA lipid nanoparticles for hepatic gene silencing in vivo. *Angew Chem Int Ed Engl* **2012,** *51* (34), 8529-8533.
100. Sun, Q.; Cai, S.; Peterson, B. R., Practical synthesis of 3beta-amino-5-cholestene and related 3beta-halides involving i-steroid and retro-i-steroid rearrangements. *Org Lett* **2009,** *11* (3), 567-570.
101. Schindelin, J.; Arganda-Carreras, I.; Frise, E.; Kaynig, V.; Longair, M.; Pietzsch, T.; Preibisch, S.; Rueden, C.; Saalfeld, S.; Schmid, B.; Tinevez, J. Y.; White, D. J.; Hartenstein, V.; Eliceiri, K.; Tomancak, P.; Cardona, A., Fiji: an open-source platform for biological-image analysis. *Nat Methods* **2012,** *9* (7), 676-682.
102. Ellett, F.; Pase, L.; Hayman, J. W.; Andrianopoulos, A.; Lieschke, G. J., mpeg1 promoter transgenes direct macrophage-lineage expression in zebrafish. *Blood* **2011,** *117* (4), e49-56.
103. Weinstein, B. M.; Stemple, D. L.; Driever, W.; Fishman, M. C., Gridlock, a localized heritable vascular patterning defect in the zebrafish. *Nat Med* **1995,** *1* (11), 1143-1147.
104. Severgnini, M.; Sherman, J.; Sehgal, A.; Jayaprakash, N. K.; Aubin, J.; Wang, G.; Zhang, L.; Peng, C. G.; Yucius, K.; Butler, J.; Fitzgerald, K., A rapid two-step method for isolation of functional primary mouse hepatocytes: cell characterization and asialoglycoprotein receptor based assay development. *Cytotechnology* **2012,** *64* (2), 187-195.

Chapter 7

Zebrafish embryos as a predictive animal model to study nanoparticle behavior *in vivo*

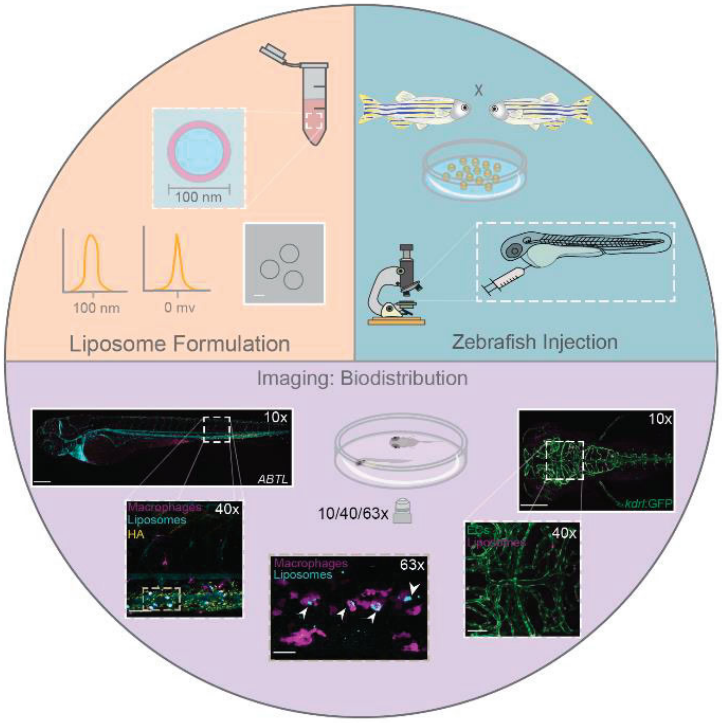

Published:

Arias-Alpizar, G.; Bussmann, J.; Campbell, F. Zebrafish as a predictive animal model to study nanoparticle behavior *in vivo*. *Bio-Protocols.* **2021.** DOI:10.21769/BioProtoc.4173.

7.1 Abstract

A failure to fully understand the complex *in vivo* behavior of systemically administered nanomedicines has stymied clinical translation. To bridge this knowledge gap, new *in vivo* tools are needed to rapidly and accurately assess the nearly infinite array of possible nanoparticle designs. Zebrafish embryos are small, transparent, and easily manipulated animals that allow for whole organism visualization of fluorescently labeled nanoparticles in real time and at cellular resolution using standard microscope setups. Furthermore, key nano-bio interactions present in higher vertebrates are fully conserved in zebrafish embryos, making these animal models a highly predictive and instructive addition to the nanomedicine design pipeline. Here, we present a step-by-step protocol to intravenously administer, image and analyze nanoparticle behavior in zebrafish embryos and highlight key nano-bio interactions within the embryonic zebrafish corresponding to those commonly found within the mammalian liver. In addition, we outline practical steps required to achieve light-triggered activation of nanoparticles within the transparent embryo.

7.2 Introduction

The embryonic zebrafish is a predictive, convenient and cost effective animal model to study the complex *in vivo* behaviour of systemically administered nanoparticles and to characterize key nano-bio interactions at a molecular level.[1-6] In contrast to conventional research animal models (*e.g.* mice and rats), zebrafish embryos are small (1-3 mm), optically transparent and readily available in large numbers. These features enable real-time visualization of nanoparticle injected doses using simple fluorescence microscopy setups, at cellular resolution and over large sample sets. In addition, the extensive range of fluorescent transgenic lines (*e.g.* *mpeg1*:GFP[7] -macrophages; *kdrl*:GFP[8] -endothelial cells), short generational timeframes (approximately 3 months), and the ease of genetic manipulation (*e.g.* CRISPR/Cas9 gene editing),[9, 10] facilitates mechanistic understanding of nanoparticle fate *in vivo*. Crucially, key biological mechanisms underpinning nanoparticle behaviour in higher order vertebrates (*e.g.* rodents and humans) are conserved and functional in zebrafish embryos. In particular, the embryonic zebrafish can accurately predict nanoparticle interactions within the mammalian liver.[3, 6] These interactions account for the (unwanted) clearance of up to 99% of systemically administered nanoparticles.

Here, we provide a step-by-step protocol for the intravenous administration, imaging and analysis of nanoparticles within zebrafish embryos. This protocol describes the use of liposomes but is appropriate for any nanoparticle. In addition, we detail how UV light can be applied to trigger the release of chemical photocages within the embryo *in situ* and *in vivo*. As an example, we have recently used UV light to switch the surface charge of liposomes (from neutral to cationic) within the embryonic zebrafish, revealing new insight into the behaviour of differently charged nanoparticles *in vivo.*[5] In practical terms, a skilled person can inject and mount several hundred zebrafish embryos in a day, and the throughput is generally limited by imaging timeframes. In our experience, confocal imaging (*i.e.* multi-colour whole embryo, 10x objective + 40x/63x ROI), as described below, takes approximately 1 h per embryo. Overall, the embryonic zebrafish is a uniquely powerful addition to the pre-clinical nanomedicine discovery pipeline.

7.3 Procedure

Formulation of fluorescently labelled nanoparticles.

1. Prepare liposomes (or other nanoparticles) using a preferred method (for example, extrusion, ethanol injection or microfluidic preparation[11, 12] for lipid nanoparticles). For fluorescently labelled nanoparticles, ensure that the incorporated dye does not adversely affect nanoparticle biophysical properties but can be easily detected above background autofluorescence within the embryo.

   Preparation of photoactive liposomes, as **Chapter 4** (containing 1 mol% fluorescent lipid probe, 1,2-dioleoyl-*sn*-glycero-3-phosphoethanolamine-N-(lissamine rhodamine B sulfonyl, DOPE-LR) by extrusion is briefly described. Any aqueous buffer can be used.

   i. Formulate liposomes in 10 mM HEPES buffer at a total lipid concentration of 1-5 mM. Generally, liposomes can be formulated by manual extrusion up to a lipid concentration of approx. 30 mM. Final liposome concentration is typically reported as a total lipid concentration.
   ii. Prepare individual lipid stock solutions (1-10 mM) in chloroform.
   iii. In a glass vial, combine lipids to the desired molar concentration and dry to a film, first under a stream of N_2 then > 1 h under vacuum using a bench-top vacuum desiccator. This is to ensure complete removal of residual chloroform. In the highlighted study, various molar ratios of lipids were used. For instance, to test the effect of increasing positive surface charge (**Figure 2**, **Chapter 4**),[5] liposomes were formulated at 1:1, 1:3 and 1:9 molar ratios of cationic lipids (1-3) and zwitterionic 1,2-dioleoyl-sn-glycero-3-phosphocholine (DOPC).
   iv. Manually extrude above phase transition temperature (Tm) of all lipids to form large unilamellar vesicles.
   v. Hydrate lipids to create a suspension. Add aqueous buffer to the lipid film to achieve the desired final lipid concentration. **Note:** In the setup described, we recommend using 0.5-1 mL to avoid sample loss in the 'dead' volume (approx. 50 μL) within the mini-extruder block. In the highlighted example, 1 ml of a 10 mM storage solution was added to achieve a final lipid concentration of 1 mM.
   vi. Warm solution above Tm of all lipids. Vortex the solution vigorously to create a homogenous lipid suspension. There should be no visible film or visible aggregates remaining in the solution. Depending on the lipid mixture and concentration, a lipid suspension may appear cloudy or

transparent.

vii. Load suspension into syringe and fit to one side of extruder block. Fit a clean, empty syringe on other side of extruder block. Heat extruder block to desired temperature (*i.e.* 5-10 °C above Tm of all lipids).

viii. Pass 11 times through 2 x 400 nm polycarbonate (PC) membranes– always end in clean syringe to avoid particulate contamination (*e.g.* dust).

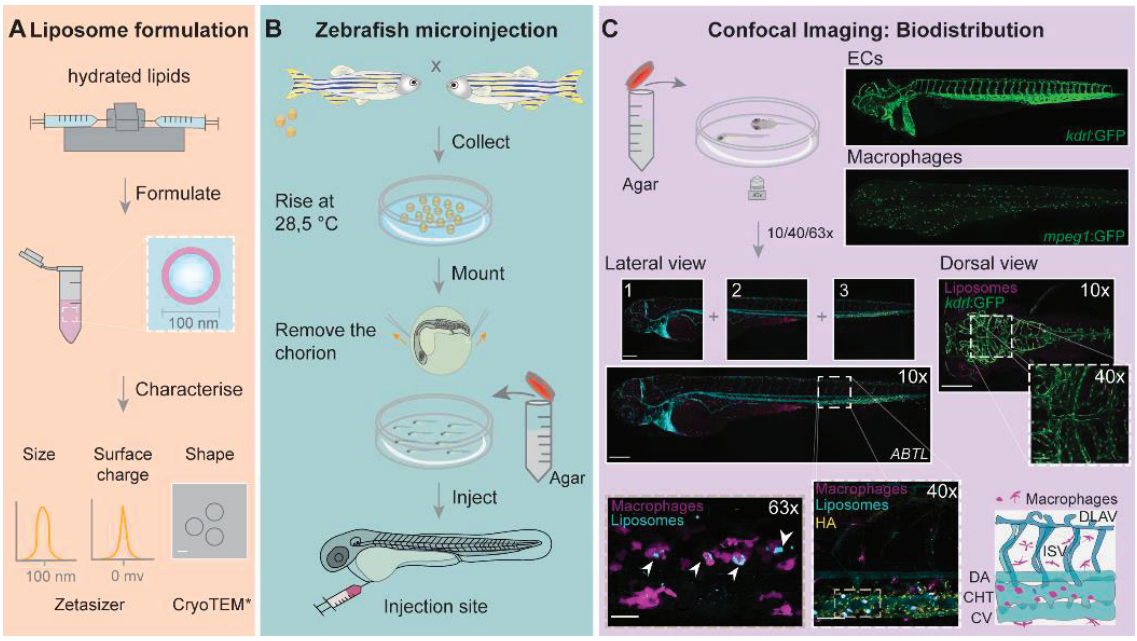

Figure 1. Protocol for intravenous nanoparticle administration, imaging and analysis in zebrafish embryos. (a). Nanoparticle formulation – *e.g.* extrusion of hydrated lipid solution. Following formulation and biophysical characterization, liposomes should be stored at 4 °C. *CryoTEM is optional but recommended. Immediately prior to injection, confirm, at the very least, nanoparticle size. Wherever possible, we recommend using freshly prepared nanoparticles. If this is not possible, confirm nanoparticle stability over time **(b). Zebrafish microinjection**. Cross adult zebrafish (male and female, specific transgenic line if required) to obtain zebrafish eggs by external fertilisation. Raise embryos at 28 °C until the desired stage (*i.e.* ~56 h post fertilisation, hpf). Remove the chorion if embryos have not yet hatched. Mount embryos with agarose gel (0,4% agarose + 0,01% tricaine). Intravenously inject (fluorescently labelled) nanoparticles within the sinus venosus/duct of Cuvier (at 2 dpf). For more details about the injections site see **Figure 2. (c). Confocal imaging nanoparticle biodistribution.** 10x objective to visualise whole body nanoparticle distribution (3-4 overlapping images), 40x objective to visualise tissue level distribution (example shows tail region containing scavenger endothelial cells of the CHT and CV as well as blood resident macrophages), 63x objective to visualise cellular level distribution (example shows liposomes accumulated within macrophages). Liposomes in cyan, macrophages in magenta and fluorescently labelled hyaluronic acid (as a marker for scavenger endothelial cells) in yellow. CV – caudal vein, CHT – caudal hematopoietic tissue, DA – dorsal aorta, DLAV – dorsal longitudinal anastomotic vessel and ISV – intersegmental vessels. Scale bars: 200 µm (10x), 50 µm (40x). Lateral view images are adapted from. [5]

ix. Pass 11 times through 2 x 100 nm PC membranes.
x. Collect the formulated liposomes in a clean glass vial and store in the dark at 4 °C until further use, time depends on liposome stability. We highly recommend using freshly prepared liposomes; however, if using stored liposomes, always confirm size (DLS measurement) immediately prior to use.
xi. (Optional) To analyze light activated liposomes *in vitro*, irradiate liposomes (370 ± 7 nm, 202 mW cm^{-2}) in quartz cuvettes with the LED mounted at a distance of 1 cm from the sample.

2. Characterize the physicochemical properties of the (freshly prepared) liposomes. Size and surface charge are measured using a Malvern Zetasizer Nano ZS. If using stored liposomes, always confirm size immediately prior to injection in embryonic zebrafish.
3. (Optional) CryoTEM analysis to confirm liposome morphology, size and structure [13-16] is strongly advised for any new nanoparticle, in particular, if unusual/unexpected biodistribution is observed in the zebrafish embryo.

Preparation of zebrafish embryos

Note: These steps require a specific license and corresponding approval by regulatory authorities (see *ethics* section below).

1. Breed adult zebrafish by setting up crosses in pairs in breeding tanks during the afternoon, separating male and female with a plastic and transparent divider and use a lid to prevent the zebrafish escaping from the tank.
2. The following morning, remove the divider at the beginning of the light period to allow and control breeding time.
3. Collect zebrafish eggs with a strainer and transfer to petri dishes containing egg water (see *recipes*) (~50-70 embryos per petri dish).
4. Remove unfertilized eggs (remain at a single stage and acquire an irregular shape over time) or dead embryos.
5. Raise eggs in an incubator at 28.5 °C. Replenish with fresh egg water every day.
6. (Optional) Add 25 µl PTU (see *recipe* below) to a petri dish containing 50 ml egg water and around 50-70 embryos, to prevent pigmentation at ~24 h post fertilization.

Microinjection of zebrafish embryos/larvae

1. Remove the chorion protecting zebrafish embryos, if the embryos have not hatched yet, at 56 h post fertilization (hpf). Under a microscope, use a pair of stainless steel tip tweezers to carefully remove the chorion by making a tear in the chorion and pulling opposite sides until the chorion is removed and the embryo is released. Avoid direct contact of tweezers with the embryo to avoid damage to the embryo. **Note:** Pronase treatment is a common alternative for dechorionation; however, we recommend the use of tweezers to avoid unnecessary exposure of the embryo to proteolytic enzymes. If high throughput is required, automated chorion removal using pronase can be performed.[17]
2. Prepare an agarose solution (0.4% agarose in egg water and add tricaine, 0.01% final concentration) to embed the zebrafish embryo. Submerge container in a water bath at 36-40 °C to prevent agarose gelation. Caution: be careful with the temperature control at this step, overheating can damage the zebrafish embryo during mounting steps.
3. Prepare injection microneedles by pulling glass needles with filament according to the instructions of the micropipette puller machine.
4. Transfer approx. 20 embryos, anesthetized in 0.01% tricaine, with a plastic transfer pipette and place them in a clean, empty plastic petri dish.
5. Remove any excess egg water and pipette in prepared agarose solution (~3 ml). Embryos should be evenly distributed and preferably on the bottom surface of the petri dish. Carefully use tweezers to manipulate embryos into the desired position (preferably in lateral view, see **Figure 2** for more detail). Allow agarose gel to cool for a few minutes to solidify.
6. Proceed with the microinjection.
    a. Load fluorescently labelled nanoparticles (~3 µl) in a glass microneedle with a pipette and insert needle into the arm of the injector.
    b. Calculate the injection volume (1 nl volume is recommended).
    c. Cut the length of the microneedle with stainless steel tip tweezers (removing a section of the thinner part of the pre-pulled microneedle tip).
    d. Press the foot pedal to expel one droplet.
    e. Measure the size of a droplet under the microscope. The incorporation of a scale into the ocular of the microscope (or a stage micrometer, *e.g.* agar scientific AGL4079, as an alternative) allows the measurement of a droplet equivalent to 1 nl (*i.e.* 100 µm at 40x).
    f. Adapt the volume accordingly by adjusting the micromanipulator

setting (*i.e.* pressure). **Note:** Repeat this step periodically during injections to ensure injection volume is consistent.

g. Position the microneedle towards the sinus venous/duct of Cuvier (**Figure 2**). **Note:** To reach the zebrafish embryo the needle must be carefully moved 'in and out' once inserted in the agar.

h. Penetrate the skin with the injection needle. **Note:** Be careful not to touch the yolk sac with the tip needle to avoid over-insertion of the microneedle that can lead to unsuccessful *i.v.* injection.

i. Once the needle is inside the duct of Cuvier, gently pull the needle back, creating a small pyramidal space and inject nanoparticle solution (1 nl). At the time of injection, a backward flow/spreading of circulating blood cells should be observed. (See videos in Notes section below, to differentiate between successful and unsuccessful injection).

7. Once injected, carefully remove the microneedle from the embryo.
8. Release the zebrafish embryo from the agarose gel. First, add egg water (~5 ml) on top of the agarose gel. Second, use tweezers to carefully separate the embryo from the agarose (without touching the embryo).
9. Once the embryo is released and able to swim, transfer the injected fish with a plastic transfer pipette to a clean petri dish containing fresh egg water and 0.01% tricaine to proceed with screening for successfully injected fish.

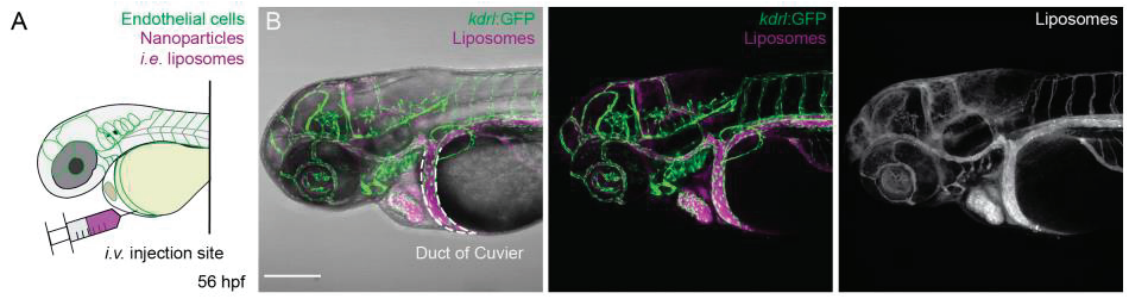

Figure 2. Microinjection site of zebrafish embryo/larvae. (a) Schematic of a zebrafish embryo showing intravenous injection site within the sinus venosus/duct of Cuvier at 56 hpf. **(b)** Zebrafish embryo Tg(*kdrl*:GFP) after injection of fluorescently labelled liposomes (in magenta/grey) at 56 hpf, 1 hpi. Volume of injection: 1 nl. Scale bar 200 μm (10x).

Screening of successfully injected embryos

1. Make a selection of well-injected zebrafish embryos under a fluorescent stereo microscope. Well-injected embryos show fluorescent nanoparticles in circulation (**Figure 3a**).

2. Discard any embryo that does not show nanoparticles in circulation, *i.e.* injected in the yolk sac, pericardial space, *etc.* (**Figure 3b-d**).
3. Ensure fish look healthy with no physical damage (*i.e.* from injection needle).

Imaging

1. Transfer the zebrafish embryo with a plastic transfer pipette to a petri dish containing fresh egg water (with no tricaine added) and keep the zebrafish embryo at 28.5 °C until further use (*i.e.* imaging).
2. (Optional step) Applying UV light after intravenous injection, as **Chapter 4**, of photoactive liposomes. In this case, a LED (375-nm) lamp driven by a custom-built LED driver (I = 350 mA), is used as UV light source.

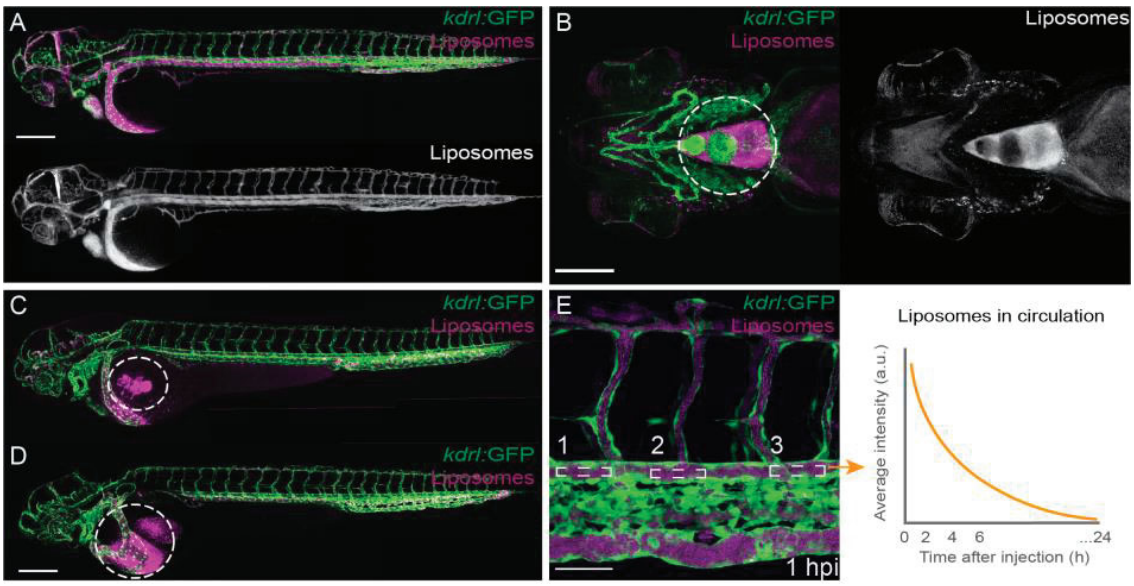

Figure 3. Selection of injected zebrafish embryos. (a). Successfully injected zebrafish embryos, nanoparticles are clearly in circulation, homogeneously distributed throughout the vasculature of the embryo. **(b-d). Unsuccessful injections**, nanoparticles accumulated in the pericardial space **(b),** zebrafish embryo in ventral view) or in the yolk sac **(c)**, within dashed circles) or a combination of both **(d)** and only partial volume of nanoparticles are in circulation. Do not use these embryos as representative of nanoparticle biodistribution. **Note:** For clarity, confocal images are shown here. Screening for successful injection should be done quickly under a stereo microscope. **(e) Nanoparticles in circulation** (in magenta, within boxes) in the dorsal aorta. Intensity values measured in this area can be used to calculate the liposome circulation life at different time points (*i.e.* 1-24 h post injection, hpi). We recommend to use n=6 for each point. All zebrafish embryo shown are 2 days post fertilisation, dpf; Tg(*kdrl*:GFP) 1 hpi. Scale bars: 200 µm (a-d), 50 µm (e).

   a. Determine the power density (in mW cm^{-2}) of the light source and calculate light doses (J per embryo) by multiplying the optical power density by the irradiation time.
   b. For embryo irradiation, the UV source (wavelength 370 ± 7 nm) was positioned approximately 1.5 cm above the agar-embedded embryo (~90 mW cm^{-2}).[5] A minimum irradiation dose of ~2.4 J per embryo was used.
3. Embedding of embryos/larvae in agarose solution (0.4% + 0.01% tricaine) for confocal imaging.
   a. Use a glass bottom dish suitable for confocal imaging.
   Note: This must be able to contain liquid agarose before gel formation, and therefore generic glass slides are not suitable.
   b. Randomly select at least six successfully injected zebrafish embryos to image and transfer them with a plastic transfer pipette into a glass bottom plate.
   c. Place ~3 ml of agarose solution into the glass bottom dish. Make sure the agarose covers the surface of the whole bottom dish and gently position the zebrafish embryos into the correct position for desired imaging (*i.e.* lateral, dorsal, *etc.*) with the help of the tweezers. Allow the gel to cool and solidify over a few minutes.
4. Mounted embryos (*i.e.* in dorsal or lateral view) can now be used for imaging. We recommend to add egg water on top of the agarose to prevent the sample drying out if the time of imaging is extensive (>3 h). After imaging, transfer the fish into petri dishes containing fresh egg water and allow to swim freely at 28.5 °C for at least ~24 h to monitor possible effects after injection and/or for further analysis.
5. Confocal imaging of nanoparticle biodistribution and identification of specific cellular interactions. For nanoparticle assessment, we recommend using transgenic zebrafish lines Tg(*kdrl*:GFP)[8] and Tg(*mpeg1*:GFP)[7] to identify endothelial cells and macrophages respectively. **Note:** the fluorescent nanoparticle probe must not overlap with transgenic fluorescence emission.
   a. Capture confocal z-stacks using a 10x air objective (HCX PL FLUOTAR), a 40x water-immersion objective (HCX APO L) or 63x water-immersion objective (HC PL APO CS).
   b. For whole-embryo views, maximum projections of three overlapping z-stacks (10x) were captured to cover the complete embryo.
   c. Figures 3, 4, 6 and 7c and Supplementary Figures 1-3, 7-9 in

Chapter 4[5] illustrate the use of confocal imaging after intravenous administration of liposomes in zebrafish embryo.

6. Identification of nanoparticle interactions with scavenger endothelial cells (SECs, *i.e.* analogous to liver sinusoidal endothelial cells in mammals), can be assessed using fluorescent hyaluronic acid (fluoHA) as a specific and non-competitive marker of SECs (**Figure 1c**)[3]. In addition, the involvement of the key scavenger receptors – Stabilin-2 and -1 –can be easily-assessed through co-injection of dextran sulfate within the embryonic zebrafish.[3, 6] Furthermore, *stabilin-2*, *stabilin-1,* and *stabilin-1* and *-2* knockout embryos have been generated, described in **Chapter 2 & 3**.[3, 6]

7. 4 Materials and Reagents

Zebrafish breeding tanks with divider (Tecniplast, Italy)
Stainless steel tip tweezers (IDEAL-TEK, catalog number: 3480641)
Borosilicate glass microneedles with filament, 10 cm (Science Products, Sutter Instruments, catalog number: BF100-78-10)
Microloader 20 µl (Eppendorf, catalog number: 5242956003)
Disposable petri dishes, 92 x 16 mm with cams (SAERSTEDT, catalog number: 82.1473.001)
Plastic transfer pipettes (SAERSTEDT, catalog number: 86.1171)
Glass bottom dishes (WillCo-dish, catalog number: GWST-5040)
Low-melting-point agarose (Sigma-Aldrich, catalog number: A9414)
Instant Ocean sea salt for aquariums (Instant Ocean, catalog number: SS15-10)
Fluorescent nanoparticles (*e.g.* liposomes as described below. Store in dark)
N-Phenylthiourea (PTU)* (Sigma Aldrich, catalog number: P7629. See Recipes. Store at room temperature)
Tricaine (ethyl 3-aminobenzoate methanesulfonate) (Sigma Aldrich, catalog number: A5040) (See recipe below, store at 4 °C and dark once diluted)
Adult zebrafish (wildtype (AB/TL) or transgenic line of interest)
Lipids (Avanti Polar Lipids, Lipoid GmbH and/or Sigma Aldrich)
Formulation buffer (*e.g.* HEPES* (10 mM), See Recipes, store at room temperature)
Glass vials, 5 ml (VWR international, catalog number: 548-0555)
Polycarbonate membranes, 400 and 100 nm pore size (Nucleopore Track-Etch membranes, Whatman, catalog numbers: 7065257, 6257028)
Chloroform (Sigma Aldrich, catalog number: 67-66-3)Egg water (See Recipes)
Ethanol* (Honeywell, catalog: 67-63-0)
Agarose gel (See Recipes) *Optional

Equipment

Mini-extruder (Avanti Polar Lipids, catalog number: 610000)
Syringes 1000 µl (Avanti Polar lipds, catalog number: 610017)
Vacuum desiccator (Fisher Scientific, model: Pirex 1594/02D)
Bench-top vortex (Scientific Industries, model: G-560E)
Nanosizer (Malvern Zetasizer Nano ZS)
LED-UV light source (wavelength 370 nm, FWHM = 13.4 nm; H2A1-H375-S, Roithner Lasertechnik)
Stereo microscope (Leica, model: MS5)
Micropipette puller (Sutter Instruments Co, model: P-97)
Injector (Eppendorf, FemtoJet, catalog number: 524702135) attached to a manual micromanipulator (World Precision Instruments, WPI model M3331R) on a steel base plate (WPI, code 5052) with a magnetic stand (WPI, code M10)
Incubator (Heraeus, model: B15)
Water bath (ELBANTON, Julabo, model: MWB)
Fluorescent stereomicroscope (Leica, model: M205 FA-2)
Confocal microscope (Leica Microsystems, model: SP8/SPE)
Fully approved zebrafish facility (See Ethics section below)

Software

Zetasizer Software Version 7.13.
Fiji distribution of ImageJ; Versions 1.51p and 1.52p[18, 19].
Confocal microscopy data were processed using Leica Software (Leica Application Suite X software, version 3.5.5.19976).

Data analysis

Process the images using the Fiji distribution of ImageJ[18, 19]. Adjust brightness and contrast, rotate and crop the image if needed. For the whole embryo view, stitch the maximum projection of 3 or 4 images at an appropriate overlapping point (**Figure 1c**). For comparison and/or quantification laser intensity, gain and offset settings must be identical between stacks and between experiments. Quantification of liposome circulation lifetime decay (n=3-6) shown in **Figure 4g** and **Supplementary Figures 7-8** in **Chapter 4**[5] was calculated using a previously described macro for ImageJ[3] using the measured nanoparticle fluorescent intensity within the dorsal aorta, as illustrated in **Figure 3e**.

Notes

These studies require knowledge, license and basic skills in zebrafish husbandry and handling. Good zebrafish husbandry practices are critical throughout this protocol to ensure the health and comfort of the zebrafish is maintained at all times. Reproducibility is essential. Repeat all experiments at least twice. Use different zebrafish lines, if possible, and always repeat with new batches of (freshly prepared) nanoparticles. In case of light application, do not irradiate excessive numbers of embryos simultaneously to avoid embryo-to-embryo variations in light dose. For experiments monitoring changes in liposome biodistribution following light activation, always image the same embryo before and after UV irradiation. Intravenous injections can be performed at any point between 2 and 4 dpf. Ethical approval is required for any experiment in zebrafish after 5 dpf.

Ethics

All animal experiments must be in accordance with institutional regulations. In this case, zebrafish (*Danio rerio*, strain *AB/TL*) were maintained and handled in accordance with guidelines from the European Convention on the protection of vertebrate animals used for experimental and other scientific purposes,[20] and in compliance with the directives of the local animal welfare committee of Leiden University.

Recipes

Egg water

Mix 60 µg of instant Ocean sea salts per ml. Store at room temperature.

N-Phenylthiourea (PTU)

Mix PTU powder in 85% ethanol solution to a final concentration of 3% (w/v). Store at room temperature and in the dark.

Agarose gel

In a clean glass container, mix low melting agar powder in egg water to a final concentration of 0.4%. Melt the agarose mixture in a microwave, shake until dissolved and keep it in a water bath at 36-40 °C. Add tricaine to a final concentration of 0.01%.

HEPES buffer

HEPES (10 mM) adjusted to pH 7.4 with 1 m aqueous NaOH. Ultrapure MilliQ® water, purified by a MilliQ Advantage A10 water purification system from MilliPore. Store at room temperature.

Tricaine

Mix 400 mg tricaine powder with 97.9 ml of deionized water, and adjust to pH 7 with 2.1 ml of 1 M Tris (pH 9). Store in the dark at 4 °C. Mix 1 ml of stock solution with 9 ml of egg water for the working solution.

7.5 Abbreviations

CRISPR/Cas9	clustered regularly interspaced short palindromic repeat/Cas9
CryoTEM	Cryo-transmission electron microscopy
CV	caudal vein
dpf	day(s) post fertilization
DOPE-LR	1,2-dioleoyl-*sn*-glycero-3-phosphoethanolamine-N-(lissamine rhodamine B sulfonyl)
DSPC	1,2-distearyl-*sn*-glycero-3-phosphocholine
fluoHA	fluorescent hyaluronic acid
hpi	hour(s) post injection
hpf	hour(s) post-fertilization
i.v.	Intravenously
SEC	scavenging endothelial cells
PC	polycarbonate
PTU	N-Phenylthiourea

7.6 References

1. Sieber, S.; Grossen, P.; Bussmann, J.; Campbell, F.; Kros, A.; Witzigmann, D.; Huwyler, J., Zebrafish as a preclinical in vivo screening model for nanomedicines. *Adv Drug Deliv Rev* **2019,** *151-152*, 152-168.
2. Sieber, S.; Grossen, P.; Uhl, P.; Detampel, P.; Mier, W.; Witzigmann, D.; Huwyler, J., Zebrafish as a predictive screening model to assess macrophage clearance of liposomes in vivo. *Nanomedicine* **2019,** *17*, 82-93.
3. Campbell, F.; Bos, F. L.; Sieber, S.; Arias-Alpizar, G.; Koch, B. E.; Huwyler, J.; Kros, A.; Bussmann, J., Directing Nanoparticle Biodistribution through Evasion and Exploitation of Stab2-Dependent Nanoparticle Uptake. *ACS Nano* **2018,** *12* (3), 2138-2150.
4. Hayashi, Y.; Takamiya, M.; Jensen, P. B.; Ojea-Jimenez, I.; Claude, H.; Antony, C.; Kjaer-Sorensen, K.; Grabher, C.; Boesen, T.; Gilliland, D.; Oxvig, C.; Strahle, U.; Weiss, C., Differential Nanoparticle Sequestration by Macrophages and Scavenger Endothelial Cells Visualized in Vivo in Real-Time and at Ultrastructural Resolution. *ACS Nano* **2020,** *14* (2), 1665-1681.
5. Arias-Alpizar, G.; Kong, L.; Vlieg, R. C.; Rabe, A.; Papadopoulou, P.; Meijer, M. S.; Bonnet, S.; Vogel, S.; van Noort, J.; Kros, A.; Campbell, F., Light-triggered switching of liposome surface charge directs delivery of membrane impermeable payloads in vivo. *Nat Commun* **2020,** *11* (1), 3638.
6. Arias-Alpizar, G. K., B.; Hamelmann, N.M.; Neustrup, M.A.; Paulusse, J.M.J.; Jiskoot, W.; Kros, A.; and Bussmann, J., Stabilin-1 is required for the endothelial clearance of small anionic nanoparticles. *Nanomedicine: NBM* **2021,** *In press*.
7. Ellett, F.; Pase, L.; Hayman, J. W.; Andrianopoulos, A.; Lieschke, G. J., mpeg1 promoter transgenes direct macrophage-lineage expression in zebrafish. *Blood* **2011,** *117* (4), e49-56.
8. Jin, S. W.; Beis, D.; Mitchell, T.; Chen, J. N.; Stainier, D. Y., Cellular and molecular analyses of vascular tube and lumen formation in zebrafish. *Development* **2005,** *132* (23), 5199-5209.
9. Varshney, G. K.; Pei, W.; LaFave, M. C.; Idol, J.; Xu, L.; Gallardo, V.; Carrington, B.; Bishop, K.; Jones, M.; Li, M.; Harper, U.; Huang, S. C.; Prakash, A.; Chen, W.; Sood, R.; Ledin, J.; Burgess, S. M., High-throughput gene targeting and phenotyping in zebrafish using CRISPR/Cas9. *Genome Res* **2015,** *25* (7), 1030-1042.
10. Suster, M. L.; Kikuta, H.; Urasaki, A.; Asakawa, K.; Kawakami, K., Transgenesis in zebrafish with the tol2 transposon system. *Methods Mol Biol* **2009,** *561*, 41-63.
11. Zhang, H., Thin-Film Hydration Followed by Extrusion Method for Liposome Preparation. In *Liposomes: Methods and Protocols*, D'Souza, G. G. M., Ed. Springer New York: New York, NY, 2017; pp 17-22.
12. Yu, B.; Lee, R. J.; Lee, L. J., Chapter 7 - Microfluidic Methods for Production of Liposomes. In *Methods in Enzymology*, Academic Press: 2009; Vol. 465, pp 129-141.
13. Baxa, U., Imaging of Liposomes by Transmission Electron Microscopy. In *Characterization of Nanoparticles Intended for Drug Delivery*, McNeil, S. E., Ed. Springer New York: New York, NY, 2018; pp 73-88.
14. Crawford, R.; Dogdas, B.; Keough, E.; Haas, R. M.; Wepukhulu, W.; Krotzer, S.; Burke, P. A.; Sepp-Lorenzino, L.; Bagchi, A.; Howell, B. J., Analysis of lipid nanoparticles by Cryo-EM for characterizing siRNA delivery vehicles. *Int J Pharm* **2011,** *403* (1-2), 237-244.
15. Almgren, M., Mixed micelles and other structures in the solubilization of bilayer lipid membranes by surfactants. *Biochim Biophys Acta* **2000,** *1508* (1-2), 146-163.
16. Frederik, P. M.; Hubert, D. H., Cryoelectron microscopy of liposomes. *Methods Enzymol* **2005,** *391*, 431-448.
17. Mandrell, D.; Truong, L.; Jephson, C.; Sarker, M. R.; Moore, A.; Lang, C.; Simonich, M. T.; Tanguay, R. L., Automated zebrafish chorion removal and single embryo placement: optimizing throughput of zebrafish developmental toxicity screens. *J Lab Autom* **2012,** *17* (1), 66-74.
18. Schindelin, J.; Arganda-Carreras, I.; Frise, E.; Kaynig, V.; Longair, M.; Pietzsch, T.; Preibisch, S.; Rueden, C.; Saalfeld, S.; Schmid, B.; Tinevez, J. Y.; White, D. J.; Hartenstein, V.; Eliceiri, K.; Tomancak, P.; Cardona, A., Fiji: an open-source platform for biological-image analysis. *Nat Methods* **2012,** *9* (7), 676-682.
19. Schneider, C. A.; Rasband, W. S.; Eliceiri, K. W., NIH Image to ImageJ: 25 years of image analysis. *Nat Methods* **2012,** *9* (7), 671-675.
20. Alestrom, P.; D'Angelo, L.; Midtlyng, P. J.; Schorderet, D. F.; Schulte-Merker, S.; Sohm, F.; Warner, S., Zebrafish: Housing and husbandry recommendations. *Lab Anim* **2020,** *54* (3), 213-224.

Chapter 8

General Discussion & Concluding Remarks

Image: Tissue resident macrophage (in magenta) expressing eGFP (in yellow) after delivery of mRNA with srLNPs (cyan) looking at a non-transfected macrophage.

8.1 General discussion

Despite remarkable advances in nanomedicine, (*i.e.* increasing the therapeutic index of delivered carriers, protecting cargos), this field has been full of expectations with relatively slow progress, hampered by underestimated challenges (*i.e.* clinical translation). This situation is reflected in the limited amount of nanoparticles that reached the final approval to be used as therapeutics. Over the past decades, most studies have been mainly concentrated in the design of new (and sometimes very complex) systems to achieve targeted drug delivery, often disregarding the fundamental and mechanistic behavior of nanoparticles *in vivo* and the corresponding biological interactions in health and diseases states.

Conventional *in vivo vs. in vitro* nanoparticle assessment

In vitro and *in vivo* studies have been traditionally proposed to assess the effect of nanoparticles in biological systems. Nowadays, *in vitro* technologies that aim to simulate the physiological environment (*i.e.* organ-on-a-chip, extracellular matrix) are emerging. However, *in vitro* tests relying on the exposure of nanoparticles to culture cells is still frequently used. This strategy favors the rapid test of many formulations but unfortunately, prediction of the *in vivo* behavior of nanoparticles and translation of data obtained only by *in vitro* studies, is often unsuccessful.

Static conditions of *in vitro* studies do not consider dynamic key processes affecting the fate of nanoparticles, for instance blood-proteins adsorbed on the nanoparticle surface, or the sequestration and clearance of nanoparticles by immune (*i.e.* macrophages) and other cell types. In addition, the rapid dedifferentiation of particular cells in culture, such as LSECs,[1] not only limit long-term culture but also changes the profile and functionality *in vitro,* affecting receptor-nanoparticle interactions*.* For these reasons and considering the diversity of nanoparticle systems, it becomes clear that in depth analysis of nanoparticle-bio interactions strictly requires *in vivo* experiments. To date, rodents are the conventional and required biological system used to test stability in blood, circulation life-time and delivery efficiency of their cargos. Frequently nanoparticles tested in rodents are unable to deliver (therapeutic relevant) drugs to the desired tissue, often without a proper understanding of the reason(s) for the failure. This reveals the challenging task of translating nanomedicines to the clinic and the need for additional model(s) that could allow

nanoparticle pre-screening to obtain improved nanomedicine formulations and contribute in the comprehensive recognition of involved biological interactions.

Zebrafish as an accurate model in nanomedicine research

In this thesis, the accuracy and efficacy of the zebrafish embryo in nanomedicine is demonstrated and applied to design new strategies for preferential targeting. The zebrafish represents a suitable alternative, to bridge the knowledge gap between *in vitro* and *in vivo* studies, by investigating the complex journey of nanocarriers and their potential interactions after systemic administration. Therefore, an useful addition to the design of improved drug delivery systems.

The practicality and the unique advantage of optical transparency of the zebrafish enable imaging techniques to track fluorescently labeled nanoparticles in real time, thereby, the screening of big nanoparticle libraries. These characteristics not only offer the opportunity to correlate the physicochemical properties of designed nanoparticles (and variations) to the behavior in an multiorgan system, but also gives the possibility to discover novel (unexpected) nanomedicines. Furthermore, most of the biological processes controlling the uptake of nanoparticles can be resolved in the zebrafish due to the overall conservation at a cellular level of physiological processes involved. Besides the fundamental behavior of engineered nanoparticles, processes that can be studied in this model include: the correlation between physicochemical properties and cellular responses, pharmacokinetics, biodistribution of (functionalized) nanoparticles, dynamic processes in real time such as endocytic routes, phagocytosis by macrophages, delivery of payloads (*i.e.* small molecules, genetic material), mechanisms of clearance, and preferential targeting. From the functional point of view, the ease to generate mutants or transgenic lines, by using CRISPR/Cas9 or *Tol2* respectively, facilitates the study of molecular interactions with cell-types and/or receptors by comparing the interaction of nanoparticles in the absence or presence of the functional protein of interest.

Additional innovative techniques can be exploited in combination with the zebrafish model used in this thesis, especially in the field of genetics and microscopy, which are constantly evolving and introducing breakthroughs. For example, more detailed transcriptomics data that allows information about the zebrafish gene expression at different stages, from 1 to 5 dpf, in a transcriptomics atlas[2] will contribute to the improvement of the zebrafish in the nanomedicine field once a specific receptor is targeted. Additionally, advancements in microscopy techniques applied to a zebrafish, such as improvements in the

tracking of (single) nanoparticles with high-resolution images, or the combination of serial sectioning cryo-preserved zebrafish tissue with scanning electron microscopy that determines the cellular fate of electron-dense particles[3], will directly benefit and make a more powerful zebrafish model for developing better nanomedicines.

It would be, however, wrong to pretend that the zebrafish replaces rodent experiments. Instead, as an *in vivo* pre-screening tool of nanomedicines, zebrafish is intended to be used as a model to optimize the infinite amount of nanomedicine platforms and mechanistically understand fundamental interactions. Importantly, differences between embryonic stages, compared to adults, or between organisms (*e.g.* ratio between cell types, genetic expression) should be considered. Therefore, validation with rodents once a nanomedicine formulation is optimized, is still required. In this way, the use of additional adult animals or mammal studies could be significantly decreased, supporting the ethical guidelines of the 3 R's (replacement, refinement, reduction) in the use of experimental animals. Furthermore, long term (>5 dpf) zebrafish experiments for the study of adaptive immune responses (*i.e.* in the development of vaccines) require, as mice, ethical approval of the regulatory animal experiment agencies.

Key biological mechanisms underpinning nanoparticle behavior and applications

The biological mechanisms investigated throughout this thesis includes the effect of physicochemical properties (*e.g.* surface charge, size, chemistry) on the biodistribution of nanoparticles, endothelial cell uptake, and clearance by the hepatic RES (*e.g.* LSECs and KCs). Especial attention was dedicated to anionic nanoparticles and their uptake mediated by interaction with scavenging receptors Stabilin-1 and Stabilin-2, described in **Chapters 2** and **3**.[4, 5] This process is of vital importance, because it represents one of the main hepatic clearance routes of nanoparticles after systemic administration, for exogenous nanoparticles (*e.g.* polymeric, inorganic, virus-like). **Chapter 2** and **3** provides a relevant model to study the effect of these two scavenging proteins by generating the *stabilin 1- stabilin 2* double knockout zebrafish with CRISPR/Cas9. To note, double knockout experiments in mice are limited due to the low viability as a result of a kidney failure.[6] Here, it was shown that prevention in the clearance of LSECs enhances the pharmacokinetics of anionic nanoparticles; whereas targeting of LSECs allows the development of nanotherapies of liver-related diseases.

Convinced that a proper understanding of mechanisms related with uptake and clearance of nanoparticles represents a solid foundation to design simple and effective nanosystems, we implemented the fundamental knowledge acquired during the previous studies, described in the first part of the thesis, to rationally design two new liposomal formulations with targeting specificity or control over cell uptake. In **Chapter 4**, to control the cargo delivery with an external stimulus, long circulating liposomes composed of two lipids were studied.[7] Upon applying a light trigger, the surface charge changed, from near-neutral to cationic, and internalization of endothelial cells was observed with concomitant delivery of the cargo. This study revealed interesting mechanistic aspects associated with the rapid switching of the surface charge in real time *in vivo*, the behavior of cationic liposomes (*i.e.* interactions with macrophages and endothelial cells) and the importance of selecting a correct light dose to induce efficient photolysis and, thereby, a more efficient and controlled drug delivery system. Clinical relevance of light-based technologies have been proven and reviewed.[8] In this proof of concept study UV-light, which has a limited penetration depth, was used. However, longer wavelength sensitive photocleavable lipids can be used to circumvent this limitation.

A screening of nanoparticles formulated with a library of synthetic lipids resulted in the serendipitously discovery of a novel formulation able to target brain endothelial cells in zebrafish larvae. These liposomes are composed of only two lipids, with no additional targeting functionality and characterized by a phase-separated morphology as revealed by CryoTEM. By systematically varying the lipid composition, it was shown that a protrusion is required for selective liposome accumulation in the zebrafish. Moreover, the challenge of understanding the mechanism led us to compare the liposome fate with endogenous lipid transport. The involvement of a triglyceride lipase mechanism was shown and emphasizes the importance to look into endogenous lipid transport processes to comprehend mechanisms related with the uptake of lipid-based nanoparticles. Validation in rodents, injected with a radiolabeled formulation to allow PET imaging, supported our findings in wildtype mice; however, further studies will be required to further investigate the mechanism. This preferential targeting of endothelial cells via triglyceride lipase mechanism is described in **Chapter 5.**

Recently, mRNA-based therapies used LNPs as a carrier were designed and approved to treat the world-wide COVID-19 pandemic caused by SARS-CoV-2 (**see Chapter 8.2**). In **Chapter 6**, a simple lipid change in the already clinical approved Onpattro® LNP formulation results in the preferential targeting of

hepatic RES in mice. The rationale behind the lipid change was based on the knowledge acquired to preferentially target LSEC *via* Stabilin-1 and Stabilin-2 receptors using anionic nanoparticles. Biodistribution and cellular interactions of these two formulations were first studied in the zebrafish, including the previously generated *stabilin* double knockout to confirm the mechanism. Finally, the key findings were validated in mice demonstrating successful translation and the challenging task of preferentially target delivery.

In general, the findings in this thesis contribute in the comprehension of nano delivery systems *in vivo*. Liver-associated diseases (*e.g.* hepatic RES or EL as key players) are candidates for possible applications of nanoparticles, administered intravenously, described in this work. The target of other tissues or cell types than the liver becomes more challenging, due to off-targeting effects of particles accumulated in organs involved in clearance. Besides their applications, it is important to highlight the tendency to redirect the research in nanomedicine to a more rational design mediated by the understanding of the biological mechanisms occurring *in vivo*. This, undoubtedly, strengthens the knowledge needed to further apply it to the improvement of, not only new, but also existing therapies.

8.2 Concluding remarks

Deliver a cargo to the right place in a living system is not a simple job and requires a thorough understanding of the complete route and interactions that could hamper/help in the main task. The identification, in the early stages of research, of biological interactions with nanoparticles, at cellular resolution and in real time, and the comprehensive *in vivo* behavior provide opportunities to improve existing and new nanotherapies.

The investigation in this thesis has contributed to a better understanding of the fundamental and mechanistic behavior of the nanoparticles *in vivo* by using the zebrafish as a highly predictive and convenient model. Furthermore, most of the key findings were validated in rodents, indicating its suitability and predictability when translation is required. Many challenges remain though, novel molecular interactions to be discovered such as the role of other scavenger receptors and macrophages in the process of nanoparticles, understanding of the exact role of specific proteins adsorbed on the internalization of nanoparticles, identification of proteins that induce nanoparticle selective targeting (*e.g.* tumors, specific cell-types -especially outside of the liver-), effective strategies to

prevent/target macrophage uptake and the manipulation of nanoparticle interactions with immune cells to trigger immune responses.

Recently, after years of study, the approval of the first nanoparticle-based gene therapy drug in the clinic acknowledges the significant potential of nanotechnology. This new drug paved the way to a new era where nanomedicine vaccines were developed rapidly as a strategy to control a global pandemic situation. Nanomedicine platforms delivering a mRNA genetic sequence encoding for the stabilized viral spike (S) protein to the host cells with LNP as a carrier have demonstrated, so far, an innovative, efficient and accurate prophylactic strategy against the SARS-CoV-2 virus. Delivered mRNA antigenic proteins into the cytosol enables the antibody production that strengthens the immunological system to attack the virus if required. LNPs represents the most suited example of the new direction that nanomedicine is experiencing. This unique current situation, were two LNP-mRNA vaccines[9, 10] are approved by the World Health Organization and other nanotechnologies[11] show the ability of nanomedicine to design targeted drug delivery technologies. Likewise, it opens opportunities in the development of other vaccines, that are being developed, to treat lethal virus-caused diseases (*i.e.* Ebola, seasonal flu, cytomegalovirus), rated with high mortality worldwide and it indicates a shift of the nanotechnology towards a more advanced biotechnology application to provide personalized medicine such as protein replacement, gene editing applications specific sequences of target disease-causing genes, and cancer nanovaccines. Overall, in this new era of nanomedicine, zebrafish represents a robust model in the pre-screening and optimization of LNPs, as demonstrated in this thesis.

Finally, advances in parallel research fields like genetics, epigenetics, imaging techniques in combination with *in vivo* models as research tools, such as the zebrafish presented in this thesis, reinforce strategies to continue the fascinating research of molecular interactions affecting the behavior and uptake of NPs and that will contribute to the improvement of nano-therapies.

8.3 References

1. Geraud, C.; Schledzewski, K.; Demory, A.; Klein, D.; Kaus, M.; Peyre, F.; Sticht, C.; Evdokimov, K.; Lu, S.; Schmieder, A.; Goerdt, S., Liver sinusoidal endothelium: a microenvironment-dependent differentiation program in rat including the novel junctional protein liver endothelial differentiation-associated protein-1. *Hepatology* **2010,** *52* (1), 313-326.
2. Farnsworth, D. R.; Saunders, L. M.; Miller, A. C., A single-cell transcriptome atlas for zebrafish development. *Dev Biol* **2020,** *459* (2), 100-108.
3. Vidavsky, N.; Akiva, A.; Kaplan-Ashiri, I.; Rechav, K.; Addadi, L.; Weiner, S.; Schertel, A., Cryo-FIB-SEM serial milling and block face imaging: Large volume structural analysis of biological tissues preserved close to their native state. *J Struct Biol* **2016,** *196* (3), 487-495.
4. Campbell, F.; Bos, F. L.; Sieber, S.; Arias-Alpizar, G.; Koch, B. E.; Huwyler, J.; Kros, A.; Bussmann, J., Directing Nanoparticle Biodistribution through Evasion and Exploitation of Stab2-Dependent Nanoparticle Uptake. *ACS Nano* **2018,** *12* (3), 2138-2150.
5. Arias-Alpizar, G.; Koch, B.; Hamelmann, N. M.; Neustrup, M. A.; Paulusse, J. M. J.; Jiskoot, W.; Kros, A.; Bussmann, J., Stabilin-1 is required for the endothelial clearance of small anionic nanoparticles. *Nanomedicine* **2021,** *34*, 102395.
6. Schledzewski, K.; Geraud, C.; Arnold, B.; Wang, S.; Grone, H. J.; Kempf, T.; Wollert, K. C.; Straub, B. K.; Schirmacher, P.; Demory, A.; Schonhaber, H.; Gratchev, A.; Dietz, L.; Thierse, H. J.; Kzhyshkowska, J.; Goerdt, S., Deficiency of liver sinusoidal scavenger receptors stabilin-1 and -2 in mice causes glomerulofibrotic nephropathy via impaired hepatic clearance of noxious blood factors. *J Clin Invest* **2011,** *121* (2), 703-714.
7. Arias-Alpizar, G.; Kong, L.; Vlieg, R. C.; Rabe, A.; Papadopoulou, P.; Meijer, M. S.; Bonnet, S.; Vogel, S.; van Noort, J.; Kros, A.; Campbell, F., Light-triggered switching of liposome surface charge directs delivery of membrane impermeable payloads in vivo. *Nat Commun* **2020,** *11* (1), 3638.
8. Yun, S. H.; Kwok, S. J. J., Light in diagnosis, therapy and surgery. *Nature Biomedical Engineering* **2017,** *1* (1), 0008.
9. Anderson, E. J.; Rouphael, N. G.; Widge, A. T.; Jackson, L. A.; Roberts, P. C.; Makhene, M.; Chappell, J. D.; Denison, M. R.; Stevens, L. J.; Pruijssers, A. J., et al., Safety and Immunogenicity of SARS-CoV-2 mRNA-1273 Vaccine in Older Adults. *N Engl J Med* **2020,** *383* (25), 2427-2438.
10. Sahin, U.; Muik, A.; Derhovanessian, E.; Vogler, I.; Kranz, L. M.; Vormehr, M.; Baum, A.; Pascal, K.; Quandt, J.; Maurus, D., et al., COVID-19 vaccine BNT162b1 elicits human antibody and TH1 T cell responses. *Nature* **2020,** *586* (7830), 594-599.
11. Moitra, P.; Alafeef, M.; Dighe, K.; Frieman, M. B.; Pan, D., Selective Naked-Eye Detection of SARS-CoV-2 Mediated by N Gene Targeted Antisense Oligonucleotide Capped Plasmonic Nanoparticles. *ACS Nano* **2020,** *14* (6), 7617-7627.

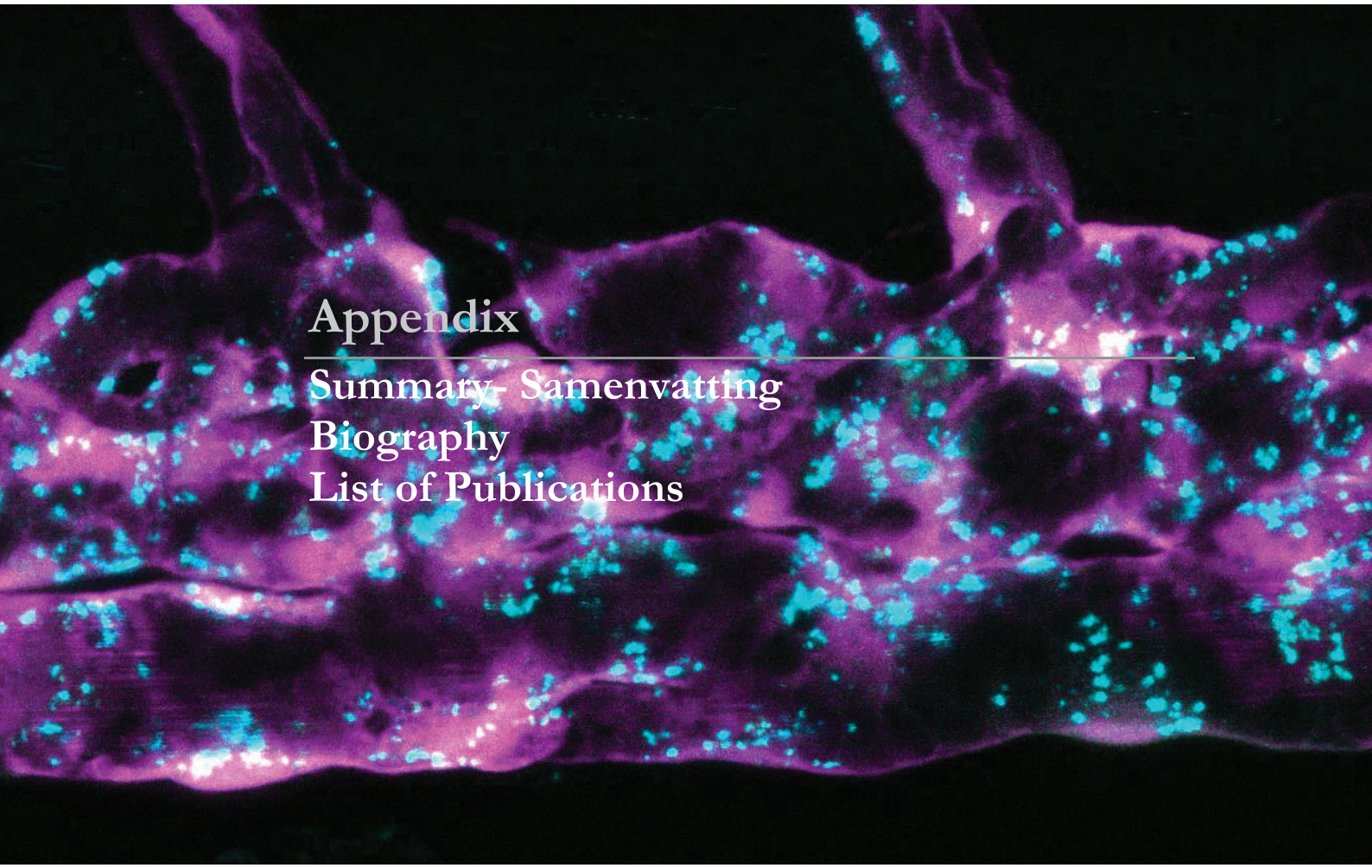

Appendix

Summary- Samenvatting
Biography
List of Publications

Image: Venous endothelium (magenta) after intravenous injection of fluorescently labelled nanoparticles (cyan) in Tg(*lyve1*:DsRed) zebrafish embryo.

Summary

Clinical translation of efficient and targeted drug delivery nanosystems is challenging, partially due to an insufficient knowledge of the mechanisms influencing nanoparticle circulation, uptake and the identification of molecular components in these mechanisms. Due to the dynamic nature of the involved mechanisms, an *in vivo* assessment is strictly required. The work described in this dissertation contributes to the mechanistic understanding of the behavior of primarily lipid-based nanoparticles *in vivo*. To achieve that goal, we used the zebrafish as an *in vivo* pre-screening model of nanoparticles, by studying the biodistribution and to unravel specific interactions at the cellular level. As the main strategy, fluorescently labeled nanoparticles were injected in zebrafish embryos and imaged with confocal microscopy to track the intravenously administered nanoparticles. This approach enables the investigation of the fundamental behavior of nanoparticles, correlation of the physicochemical properties of the formulated lipid-based nanoparticles with their biodistribution and identification of important nano-bio interactions. Zebrafish established transgenic lines expressing fluorescent proteins in specific cell-types were used to study specific interactions. In addition, genetically modified zebrafish applying CRISPR/Cas9 were generated. These strategies not only show key mechanistic features of nanoparticles in circulation, but also promote the rational design of more efficient nanoparticles systems, able to preferentially target specific cell-types *in vivo*.

Chapter 1 introduces the field of nanomedicine, describes the design and properties of the lipid-based nanoparticles and provides a list of the clinically approved intravenously (*i.v.*) administered lipid-based drug delivery systems. This overview revealed the necessity of *in vivo* models to support the selection of appropriate delivery nanotechnologies and improve the success rate in the clinical translation of nanomedicines. Comprehension of the nanoparticle journey and associated nano-bio interactions to reach the desired target is required to achieve this goal. In this chapter, the physiological barriers encountered by nanoparticles in circulation (interaction with immune cells, clearance of particles, *etc.*) are described. In addition, the zebrafish model is proposed to visualize and investigate the nanoparticle journey *in vivo*. **Chapter 1** highlights key features of the zebrafish, such as optical transparency and ease of genetic manipulation, making them an attractive model for the development of more efficient nanomedicines.

In **Chapter 2**, the embryonic zebrafish is established as a model to study the *in vivo* behavior of nanoparticles. The combination of the transparency of this organism

with fluorescent labeled nanocarriers and visualization by confocal microscopy revealed fundamental aspects in the behavior of a wide range of nanoparticles used. Here, biodistribution studies and identification of cellular interactions with nanoparticles were analyzed in the caudal region of the zebrafish. Importantly, this region displays a subset of endothelial cells that are in close homology to liver sinusoidal endothelium in mammals. This was confirmed by the conserved uptake of oxidized LDL, lithium carmine, DOPG liposomes and fluorescent hyaluronic acid allowing translation to mice. In addition, **Chapter 2** revealed the identification of Stabilin-2 receptor in the uptake of primarily anionic nanoparticles. Stabilin-2 is a scavenger receptor that recognizes and removes biomolecules, bacteria, and other ligands from circulation. As shown in this chapter, the Stabilin-2-nanoparticle interaction is of particular importance to nanomedicine delivery since it can be either blocked by inhibitors (*i.e.* dextran sulfate) increasing the circulation life time of nanoparticles or exploited to target a specific liver cell-type (*e.g.* liver sinusoidal endothelial cells, LSECs).

In **Chapter 3**, other scavenger receptors abundantly expressed in mice liver endothelium and in the caudal vein region of the zebrafish embryo were investigated to study the clearance of anionic nanoparticles. CRISPR/Cas and *in situ* hybridization methodologies were applied to successfully generate and characterize a single *stabilin-1* mutant and a double *stabilin-1* and *stabilin-2* zebrafish mutant. The role of Stabilin-1 receptor on the uptake of nanoparticles was studied, revealing that nanoparticle size is one of the key parameters determining the differential uptake between the two Stabilin receptors. Stabilin-1 was identified as responsible for the clearance and uptake of small anionic nanoparticles (6-30 nm). In addition, this investigation revealed that both Stabilin receptors contribute to the clearance of anionic nanoparticles with diameter of ~100 nm. Finally, we identified an endogenous Stabilin ligand, the endotoxin lipopolysaccharide, responsible for toxicity and immune activation in mammals. This ligand was found to be cleared from host circulation by Stabilin-1 and Stabilin-2.

Preceded by an understanding of the influence of the surface charge in the behavior of nanoparticles, the research in **Chapter 4** focuses on the design of a nano-system capable of delivering a cargo triggered by an external stimulus. Generally, this approach is attractive because it offers a better spatiotemporal control for delivery of the cargo. Here, liposomes capable of switching the surface charge *in situ* and *in vivo* using light as an external trigger were developed. Liposomes were composed of a neutral lipid facilitating circulation and a photoactive lipid that, upon stimulus, switches the surface charge from near-

neutral to cationic. This change in the surface properties results in endocytosis and delivery of the liposomal content. After formulation and biophysical characterization, the liposomes were intravenously administered in zebrafish. Liposomes freely circulated allowing access to any vascularized tissue. Upon exposure to UV light, the liposomes adhered rapidly to all endothelial cells followed by internalization. This demonstrated stimulus-controlled endocytosis and payload delivery. Furthermore, dynamic and simultaneous interactions of the liposomes with endothelial cells and macrophages were found during the transition of the surface charge.

Chapter 5 a serendipitously found liposomal formulation targeting the brain vasculature of the zebrafish was studied. Here, cryo transmission electron microscopy (CryoTEM) analysis and *in vivo* biodistribution studies were combined to understand the observed tissue specificity. Liposomes, named PAP3, composed of two lipids (DSPC and DOaG) showed accumulation in brain endothelial cells (bECs) in the zebrafish. Biophysical characterization of PAP3 liposomes with CryoTEM revealed an uncommon 'parachute' morphology. This can be attributed to the observed phase separation between DOaG and DSPC lipids. Furthermore, the presence of phase separation domains in the liposomes was required to obtain the specific targeting in the zebrafish larvae. Mechanistically, it was also demonstrated that the recognition and binding of PAP3 liposomes are inhibited by heparin and decreased by the endothelial lipase inhibitor XEN445. This data suggests that PAP3 liposomes hijack an endogenous triglyceride lipase-mediated pathway of plasma lipid transport and metabolism, targeting endothelial cells expressing endothelial lipase (*LIPG*), highly expressed in bECs in zebrafish embryo. In mice, liposomes predominantly accumulated within the liver and spleen, matching with the high expression of endothelial lipase within these metabolic organs and opening the opportunity to further study this behavior in mice.

In **Chapter 6,** a rationally designed lipid nanoparticle (LNP) formulation containing mRNA able to preferentially target the hepatic reticuloendothelial system (RES) was developed. To design srLNPs, a single zwitterionic lipid (DSPC) within the lipid composition of the clinically approved Onpattro®, was replaced with DSPG. This replacement changes the surface charge of the LNPs, from neutral to anionic, resulting in redirecting preferentially targeting to the hepatic RES. The *in vivo* behavior of LNP formulations were compared showing that mRNA was preferentially delivered using srLNP formulation intravenously administrated in the zebrafish embryo. Biodistribution of srLNPs and cytoplasmic delivery of the mRNA in zebrafish demonstrated the selective expression of a fluorescent protein in hepatic cell types at cellular resolution. This study revealed that srLNPs

effectively target scavenging endothelial cells (SECs) mediated by scavenger receptors Stabilin-1 and Stabilin-2. This was confirmed with the help of our previously established *stabilin* double knockout (described in Chapter 3). Furthermore, validation in mice confirmed the srLNP biodistribution, uptake, cytosolic delivery and protein expression of hepatic RES mice cells, opening up opportunities to treat diseases associated with RES.

Chapter 7 provides a step-by-step protocol for the intravenous administration of nanoparticles in the zebrafish embryo, a technique used throughout the studies described in this thesis. This chapter highlights the importance, cost effectivity and versatility of the zebrafish to study nanomedicine, provides a list of the materials and equipment required to ensure reproducibility of a range of experiments. This includes liposome formulation, detailed description of how to perform intravenous injection in a zebrafish embryo, application of UV-light to trigger the release of photocages in the zebrafish embryo, imaging and analysis of nanoparticles in primarily the caudal vein region of the zebrafish.

The last chapter, **Chapter 8**, combines all studies presented in this dissertation in a general discussion resulting in some concluding remarks.

Samenvatting

De klinische toepassing van doelgerichte, efficiënte nanosystemen voor geneesmiddelentoediening is een grote uitdaging. Een belangrijke oorzaak hiervan is onvoldoende kennis van de mechanismen die de circulatie en opname van nanodeeltjes beïnvloeden en de identificatie van de relevante moleculaire componenten. Voor een beter begrip van dit complexe probleem is een *in vivo* evaluatie strikt vereist. Het werk beschreven in dit proefschrift draagt bij tot een gedetailleerd begrip van het gedrag van lipide-gebaseerde nanodeeltjes *in vivo*. Hiertoe werd de zebravis als een *in vivo* pre-screening model van nanodeeltjes gebruikt, door de biodistributie te bestuderen en specifieke interacties op cellulair niveau te ontrafelen. Als belangrijkste strategie werden fluorescent gelabelde nanodeeltjes geïnjecteerd in zebravisembryo's en gevisualiseerd door middel van confocale microscopie om de intraveneus toegediende nanodeeltjes te volgen. Deze benadering maakt het mogelijk het fundamentele gedrag van nanodeeltjes te onderzoeken, de fysisch-chemische eigenschappen van de geformuleerde lipide-gebaseerde nanodeeltjes te correleren met hun biodistributie en belangrijke nano-bio interacties te identificeren. Transgene lijnen van zebravissen die fluorescente eiwitten tot expressie brengen in verschillende celtypes werden gebruikt om specifieke interacties te bestuderen. Daarnaast hebben we genetisch gemodificeerde zebravissen gecreëerd met CRISPR/Cas9. Deze technieken tonen niet alleen de belangrijkste mechanistische eigenschappen van nanodeeltjes in circulatie, maar bevorderen ook het rationele ontwerp van efficiëntere nanodeeltjes-systemen, met een voorkeur voor specifieke celtypen *in vivo*.

Hoofdstuk 1 introduceert het gebied van de nanogeneeskunde, beschrijft het ontwerp en de eigenschappen van de lipide-gebaseerde nanodeeltjes en geeft een lijst van de klinisch goedgekeurde (*i.v.*) lipide-gebaseerde geneesmiddelafgifte-systemen. Uit dit overzicht blijkt de behoefte aan *in vivo* modellen ter ondersteuning van de selectie van geschikte toedieningsnanotechnologieën en ter verbetering van de succeskans bij de klinische vertaling van nanomedicijnen. Om dit doel te bereiken is inzicht nodig in het traject van de nanodeeltjes en de bijbehorende nano-bio interacties om het gewenste doel te bereiken. In dit hoofdstuk worden de fysiologische barrières beschreven waarmee nanodeeltjes in circulatie te maken krijgen (interactie met immuuncellen, klaring van deeltjes, *etc.*). Daarnaast wordt het zebravismodel voorgesteld om de reis van nanodeeltjes *in vivo* te visualiseren en te onderzoeken. **Hoofdstuk 1** belicht belangrijke eigenschappen van de zebravis, zoals optische transparantie en het gemak van

genetische manipulatie, waardoor ze een aantrekkelijk model zijn voor de ontwikkeling van efficiëntere nanomedicijnen.

In **Hoofdstuk 2** wordt de embryonale zebravis gebruikt als een model om nanodeeltjes te bestuderen. De combinatie van de doorzichtigheid van dit diermodel met fluorescent gelabelde nanodeeltjes die geobserveerd kunnen worden met confocale microscopie onthulde fundamentele aspecten in het gedrag van een breed scala van geteste nanodeeltjes. In dit hoofdstuk werden biodistributiestudies en identificatie van cellulaire interacties met nanodeeltjes geanalyseerd in de staartregio van de zebravis. Belangrijk is dat in deze regio een deel populatie van de bloedvatcellen (endotheel) homologie vertoont met het sinusoïdale endotheel van de lever bij zoogdieren. Dit werd bevestigd door de geconserveerde opname van geoxideerd LDL, lithiumkarmijn, DOPG-liposomen en fluorescerend hyaluronzuur, waardoor translatie naar muizen bewezen werd. Deze studie maakte de identificatie mogelijk van de Stabiline-2 receptor die verantwoordelijk is voor de opname van voornamelijk anionische nanodeeltjes. Stabiline-2 is een zogenaamde 'scavenger' receptor die macromoleculen, bacteriën en andere liganden herkent en verwijdert uit de circulatie. Zoals aangetoond in dit hoofdstuk, is de Stabiline-2-nanodeeltje interactie van bijzonder belang voor nanogeneeskunde, omdat het ofwel geblokkeerd kan worden door remmers (*b.v.* dextran sulfaat) die de circulatielevensduur van nanopartikels verlengen, ofwel benut kan worden om een specifiek lever celtype (*b.v.* lever sinusoïdale endotheliale cellen, LSECs) te targeten.

In **Hoofdstuk 3** werden andere scavenger receptoren, die tot expressie komen in het leverendotheel van muizen en in de staart regio van het zebravisembryo, onderzocht om de opname van anionische nanodeeltjes te bestuderen. CRISPR/Cas en *in situ* hybridisatie werden toegepast om met succes een enkelvoudige *stabiline-1* mutant en een dubbele *stabiline-1* en *stabiline-2* zebravismutant te genereren en te karakteriseren. De rol van de Stabiline-1 receptor op de opname van nanodeeltjes werd bestudeerd, waarbij bleek dat de grootte van het nanodeeltje één van de belangrijkste parameters is die de differentiële opname tussen de twee Stabiline receptoren bepaalt. De Stabiline-1 receptor is verantwoordelijk voor de opname van kleine anionische nanodeeltjes (6-30 nm). Bovendien bleek uit dit onderzoek dat beide Stabiline-receptoren bijdragen aan de opname van anionische nanodeeltjes met een diameter van ~100 nm. Tenslotte werd een endogeen Stabiline ligand geïdentificeerd, het endotoxine lipopolysaccharide, welke verantwoordelijk is voor toxiciteit en immuunactivatie bij zoogdieren. Dit ligand bleek uit de circulatie te worden verwijderd door zowel Stabiline-1 als Stabiline-2.

Hoofdstuk 4 richt zich op het ontwerp en van een nanosysteem dat in staat is een lading af te leveren onder controle van een externe stimulus. Over het algemeen is dit type geneesmiddel afgifte systeem aantrekkelijk omdat het een betere controle biedt voor de afgifte van de lading. Hiervoor werden liposomen ontwikkeld die in staat zijn de oppervlaktelading *in situ* en *in vivo* te veranderen onder invloed van licht als externe trigger. Liposomen werden geformuleerd met een neutraal lipide die zorgt voor goede circulatie en een fotoactieve lipide die de oppervlaktelading verandert van bijna-neutraal naar kationisch onder invloed van een lichtpuls. Deze verandering in de oppervlakte-eigenschappen leidt tot endocytose en afgifte van de liposomale inhoud. Na biofysische karakterisering werden de liposomen intraveneus toegediend in zebravissen. De liposomen circuleerden vrij in de bloedbaan en hadden toegang tot gevasculariseerd weefsel. Na blootstelling aan UV-licht hechtten de liposomen zich snel aan alle endotheelcellen, gevolgd door internalisatie. Dit toonde het principe van stimulus-gecontroleerde endocytose en afgifte van de lading aan. Bovendien werden dynamische en gelijktijdige interacties van de liposomen met endotheelcellen en macrofagen gevonden tijdens de verandering van de oppervlaktelading.

In **Hoofdstuk 5** werd een bij toeval gevonden liposomale formulering bestudeerd met een sterke voorkeur voor de hersenvasculatuur van zebravissen. In dit hoofdstuk werden cryo-transmissie elektronenmicroscopie (CryoTEM) analyse en *in vivo* biodistributie studies gecombineerd om de waargenomen weefselspecificiteit te begrijpen. Liposomen, PAP3 genaamd, samengesteld uit twee lipiden (DSPC en DOaG) accumuleerde in hersenendotheelcellen (bECs) van zebravissen. Biofysische karakterisering van deze PAP3-liposomen met CryoTEM onthulde een ongewone 'parachute'-morfologie. Dit kan worden toegeschreven aan fasescheiding tussen DOaG en DSPC lipiden. Bovendien bleek de aanwezigheid van fasescheidingsdomeinen in de liposomen vereist om de specifieke targeting in de zebravislarven te verkrijgen. In vervolgstudies werd aangetoond dat de herkenning en binding van PAP3 liposomen worden geremd door heparine en verminderd door de endotheliale lipase inhibitor XEN445. Deze waarnemingen suggereren dat PAP3 liposomen een endogene triglyceride lipase-gemedieerde route van plasma lipide transport en metabolisme gebruikt die voorkomt in endotheelcellen met endotheliale lipase (LIPG) expressie. In muizen werden de liposomen vooral aangetroffen in de lever en de milt, welke correleert met de hoge expressie van endotheliaal lipase in deze metabolische organen.

In **Hoofdstuk 6** werd een rationeel ontworpen lipide nanodeeltje (LNP) formulering voor mRNA afgifte met voorkeur voor het lever reticuloendotheliale

systeem (RES) ontwikkeld. Om deze zogenaamde srLNPs te ontwerpen, werd één zwitterionische lipide (DSPC) in de klinisch goedgekeurde Onpattro® formulering, vervangen door het DSPG. Deze aanpassing verandert de oppervlaktelading van de LNPs, van neutraal naar anionisch, met als resultaat dat de srLNPs zich bij voorkeur bevinden in de lever-RES. Het *in vivo* gedrag van de LNP formuleringen werd vergeleken en toonde aan dat mRNA beter werd afgeleverd met srLNPs intraveneus toegediend in het embryo van de zebravis. Biodistributie studies in zebravissen toonden de selectieve expressie aan van een fluorescerend eiwit in leverceltypes met cellulaire resolutie. Deze studie toonde aan dat srLNPs zich effectief richten op scavenging endotheelcellen (SECs) gemedieerd door scavenger receptoren Stabiline-1 en Stabiline-2. Dit werd bevestigd met behulp van de eerder beschreven Stabiline double knockout (zie Hoofdstuk 3). Validatie in muizen bevestigde de biodistributie, opname, cytosolische afgifte en eiwitexpressie van srLNP in hepatische RES cellen, wat mogelijkheden opent voor de behandeling van ziekten die geassocieerd worden met RES.

Hoofdstuk 7 beschrijft een stap-voor-stap protocol voor de intraveneuze toediening van nanodeeltjes in een zebravisembryo, een techniek die gebruikt wordt in de studies van dit proefschrift. Dit hoofdstuk benadrukt het belang, de kosteneffectiviteit en de veelzijdigheid van de zebravis als *in vivo* model voor geneeskunde. In dit hoofdstuk wordt een lijst van de materialen en apparatuur nodig om de reproduceerbaarheid deze experimenten gegeven. Dit hoofdstuk behandeld liposoom formulering, en geeft een gedetailleerde beschrijving van hoe intraveneuze injectie in een zebravis embryo uit te voeren, het gebruik van licht als externe trigger, data acquisitie en analyse van nanodeeltjes in de zebravis.

In **Hoofdstuk 8** werden alle studies die in dit proefschrift zijn gepresenteerd gecombineerd in een algemene discussie en werden enkele conclusies getrokken.

Biography

Gabriela Arias Alpízar was born on April 22, 1984 in San José, Costa Rica. In 2005, she obtained a Bachelor of Science in Pharmacy degree followed by a Licentiate (Master's) degree in Pharmacy in 2008, from the University of Medical Sciences (Universidad de Ciencias Médicas, UCIMED) in Costa Rica. Subsequently, she worked as a pharmacist for about 2 years and represented GlaxoSmithKline as a medical advisor for almost a year.

After moving from Costa Rica to The Netherlands and motivated to contribute as a scientific researcher, she obtained a Master's degree in "Drug Discovery and Safety" in the research track of "Target Finding" at the *Vrije* University Amsterdam in 2015. During this program, two masters internships were performed at the Amsterdam Institute for Molecules, Medicines and Systems (AIMMS), in the Division of BioAnalytical Chemistry Department and in the Division of Medicinal Chemistry Department, *Vrije* University Amsterdam. The first focused on the optimization and validation of an at-line high resolution screening methodology to separate and identify bioactive compounds from complex mixtures. In the second internship, radioligand binding assays and functional assays were optimized and validated to pharmacologically characterize zebrafish histamine3-like receptors and compare them to human orthologues.

In February 2016, she started a PhD research in the Supramolecular & Biomaterials Chemistry group in Leiden Institute of Chemistry (LIC), Leiden University under supervision of Prof. Dr. Alexander Kros, Dr. Jeroen Bussmann and in close collaboration with the Institute of Biology Leiden (IBL), under supervision of Prof. Dr. Herman Spaink. She focused on understanding the fundamental behavior of nanoparticles *in vivo* and investigating interactions associated by using the zebrafish embryo as a model, as described in this thesis. She presented parts of the work described in this dissertation in several (inter)national meetings and conferences and was awarded in two occasions with a poster prize. During her PhD, she also supervised Bachelor and Master students and was involved in teaching of practical academic courses.

Since June 2020, Gabriela has been working as a research scientist in the Leiden Academic Centre for Drug and Research (LACDR), at the Biotherapeutic Division with Prof. Dr. Wim Jiskoot and Dr. Jeroen Bussmann, where she will continue the research identifying the role of other receptors in the mechanism of nanoparticles in circulation using different *in vivo* models.

This work was presented at the following meetings:

Oral Presentations

Nanobio&Med, Barcelona **2019**. "Fundamental behavior of nanoparticles revealed in zebrafish".
CHAINS, Veldhoven **2019**. "Liposomes targeting the BBB *in vivo*"
ESM-EVBO European Vascular Biology meeting, Maastricht **2019.** "Unraveling the selective accumulation of unusual liposomes to the BBB in the zebrafish".
CHAINS, Veldhoven **2017.** "Selective blood vessel deletion through Stabilin2-dependent nanoparticle uptake *in vivo*".

Poster Presentations

CHAINS, Veldhoven **2019.**
Belgian-Dutch Biopharmacy, Ghent **2019**.
CHAINS, Veldhoven **2018**. (**Awarded**).
Germany-Dutch Microvascular biology meeting, Amsterdam **2018**. (**Awarded**).
FIGON Innovative Drug Research, Ede **2018**.
ZDM11 Zebrafish Disease Models Congress, Leiden **2018.**
FIGON Innovative Drug research, Ede **2017**.
The European zebrafish meeting, Budapest **2017.**
Annual BBBnedwork meeting "Barrier of the brain in ageing", Leiden **2017.**
Reedijk Symposium, Leiden **2017.**

List of publications

Manuscripts described in this thesis:

Arias-Alpizar, G.*; Papadopoulou, P.*; Rios, X.; Moradi, M.A.; Pattipeiluhu, R.; Bussmann, J.; Sommerdijk, N.; Llop, J.; , J.; Kros, A.; Campbell, F., Phase-Separated, "Parachute" Liposomes Hijack a Triglyceride Lipase-Mediated Lipid Transport and Metabolism Pathway to Selectively Target Endothelial Cells *in vivo*. **Manuscript in preparation.**

Pattipeiluhu, R.*; **Arias-Alpizar, G.***; Basha, G.; Bussmann, J.; Sharp, T.H.; Moradi, M.A.; Sommerdijk, N.; Cullis, P.R.; Kros, A.; Campbell, F., Anionic Lipid Nanoparticles Preferentially Deliver mRNA to the Hepatic Reticuloendothelial System. **Submitted.**

Arias-Alpizar, G.; Bussmann, J.; Campbell, F., Zebrafish as a predictive animal model to study nanoparticle behavior *in vivo*. *Bio-Protocols.* **2021,** 4173.

Arias-Alpizar, G.; Koch, B.; Hamelmann, N. M.; Neustrup, M. A.; Paulusse, J. M. J.; Jiskoot, W.; Kros, A.; Bussmann, J., Stabilin-1 is required for the endothelial clearance of small anionic nanoparticles. *Nanomedicine: Nanotechnology, Biol. Med.* **2021**, 34, 102395.

Arias-Alpizar, G.*; Kong, Li*; Vlieg, R.; Rabe, A.; Papadopoulou, P.; Meijer, M.S.; Bonnet, S.; Vogel, S.; van Noort, J.; Kros, A.; Campbell, F., Light-triggered switching of liposome surface charge directs the intracellular delivery of membrane impermeable payloads *in vivo*. *Nat Comm* **2020,** 11 (1), 3638.

Campbell, F.; Bos, F. L.*; Sieber, S*.; **Arias-Alpizar, G.***; Koch, B. E.; Huwyler, J.; Kros, A.; Bussmann, J., Directing Nanoparticle Biodistribution through Evasion and Exploitation of Stab2-Dependent Nanoparticle Uptake. *ACS Nano* **2018,** 12, 2138-2150.

*These authors contributed equally.

Other publications:

Saez Talens*, V.; **Arias-Alpizar, G***.; Makurat, D. M. M.; Davis, J.; Bussmann, J.; Kros, A.; Kieltyka, R. E., Stab2-Mediated Clearance of Supramolecular Polymer Nanoparticles in Zebrafish Embryos. *Biomacromolecules* **2020,** *21*, 1060-1068.

Otvos, R. A.*; Mladic, M.*; **Arias-Alpizar, G.**; Niessen, W. M.; Somsen, G. W.; Smit, A. B.; Kool, J., At-Line Cellular Screening Methodology for Bioactives in Mixtures Targeting the Alpha7-Nicotinic Acetylcholine Receptor. *J Biomol Screen* **2016,** *21*, 459-467.

* These authors contributed equally.